



107

**Preparation and Characterization of Magnetic and Non-magnetic
Nanosized Spinel Oxides, Nickel Nanoparticles and
Nickel-Polymer Nanocomposites**

**Thesis submitted to
Cochin University of Science and Technology
in partial fulfilment of the requirements for the award of the degree of**

Doctor of Philosophy

**by
E. Muhammad Abdul Jamal**

**Department of Physics
Cochin University of Science and Technology
Cochin – 682 022
India**

June 2009

DECLARATION

Certified that the present work in this thesis entitled “Preparation and Characterization of Magnetic and Non-magnetic Nanosized Spinel Oxides, Nickel Nanoparticles and Nickel-Polymer Nanocomposites” is based on the original research work carried out by me under the guidance and supervision of Prof. M. R. Anantharaman, Department of Physics, Cochin University of Science and Technology, Cochin – 22 and has never been included in any other thesis submitted previously for the award of any degree

Cochin -22

08-06-2009



E Muhammad Abdul Jamal



Prof. M R Anantharaman
, Department of Physics
Cochin University of Science and Technology
Cochin – 682 022 India

CERTIFICATE

Certified that the work presented in this thesis entitled “Preparation and Characterization of Magnetic and Non-magnetic Nanosized Spinel Oxides, Nickel Nanoparticles and Nickel-Polymer Nanocomposites” is based on the bonafide research work done by Mr E. Muhammad Abdul Jamal under my guidance, at the Magnetics Laboratory, Department of Physics, Cochin University of Science and Technology, Cochin – 22, and has not been included in any other thesis submitted previously for the award of any degree

Prof. M. R. Anantharaman
(Supervising Guide)

Cochin-22

08-06-2009

Acknowledgements

A number of people have directly and indirectly assisted and contributed to the successful completion of this Ph. D work and I thank them all. In particular I wish to mention my guide Professor M. R. Anantharaman for all the support and encouragement extended to me in addition to the superb guidance he provided throughout this project. It was a big blessing for me to get to know him and to work with him.

I express my gratitude to Dr Philip Kurian of Department of Polymer Science and Rubber Technology, and Dr Jacob Philip, Director of STIC, CUSAT for their guidance and sustained support for the project.

I thank UGC of India for the fellowship granted to me under the faculty improvement programme

I am indebted to the faculty and scientists in various institutions around the world for helping me at various stages of this work, particularly Dr P. A. Joy of N. C. L. Pune, Dr P. Mohanan of Department of Electronics, CUSAT, Dr Guntu Rao of IIT, Mumbai, Professor Gunter Schatz of Konstanz University, Germany, Professor D. Sakthi Kumar of Toyo University, Japan, Dr Manfred Albrecht and Dr Denys Makarov of Chemnitz University, Germany and Dr Manoj Raama Verma, RRL, Trivandrum.

I am grateful to Dr K. H. Prema for assisting and encouraging me in all my work related to polymer synthesis.

My thanks are also due to the faculty members of the Department of Physics of Cochin University of Science and Technology for the help they have provided for the completion of this research work.

Magnetics Laboratory was a wonderful place to work in. I am deeply thankful to its past and present members for creating the cordial atmosphere and for their support and help. I remember Dr Mohamed, Dr Joseph, Dr Saravanan, Dr Santhosh Shenoy, Dr Malini, Dr Asha, Dr Solomon, Dr Sajeev, Dr Swapna and Dr Mathew George with deep gratitude and affection. I would also like to mention Veena, Senoy, Narayanan, Vijutha, Reena, Geetha, Vinaya, Hyson, Tom, Sagar, Vasudevan and Anjali.

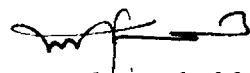
I thank Professor Mohanan, Professor Suresh Babu, Professor M. Chandran, Shri Murali and Shri Aji of Government College, Madapally and Professor Indira of Government College, Koyilandy and Professor Jayakumar of University College, Trivandrum for their help in getting the fellowship under FIP sanctioned by UGC.

I thank Anuerin Salim, Kannan and Sudheesh with whom I shared a house in Cochin for their support and help during my Ph. D course.

I remember with gratitude the help of Dr Shibu Eapen of STIC, Shri Murali of Prompt Engineering, Shri Gurulinga of IISc, Bangalore and Shri Verma of Hill Electronics, Cochin for their technical help at various stages of my work. I express my gratitude to Professor R. Anandan for helping with the editorial work.

I thank all my fellow research scholars of the Department of Physics for the affection and support they provided to me.

Last but not the least, I thank my parents, my wife Sajitha and my children for all their support during the period of this research work and to them I dedicate this Ph. D thesis.



E. Muhammad Abdul Jamal

List of Publications

1. Size-dependent surface plasmon resonance in silver silica nanocomposites Senoy Thomas, Saritha K Nair, **E Muhammad Abdul Jamal**, S H Al-Harhi, Manoj Raama Varma and M R Anantharaman *Nanotechnology* **19** No 7 (20 February 2008) 075710 (7pp)
2. Synthesis of nickel-rubber nanocomposites and evaluation of their dielectric properties, **E.Muhammad Abdul Jamal**, P. A. Joy, Philip Kurian, M. R. Anantharaman *Materials Science and Engineering B*. 156 (2009) 24-31
3. Effect of nickel nano-fillers on the dielectric and magnetic properties of composites based on rubber in the X-band, **E. Muhammad Abdul Jamal**, P. A. Joy, P. Mohanan, Philip Kurian, M. R. Anantharaman (Published online first, *Applied Physics A* DOI 10.1007/s00339-009-5284-1)
4. On the magnetic, mechanical and rheological properties of rubber-nickel nanocomposites, E. **Muhammad Abdul Jamal**, P. A. Joy, Philip Kurian, M. R. Anantharaman (Accepted for publication, *Polymer Bulletin*)
5. On the magnetic and dielectric properties of nickel-neoprene nanocomposites **E.Muhammad Abdul Jamal**, P. A. Joy, Philip Kurian, M. R. Anantharaman (Under Review. *Materials Physics and Chemistry*)
6. Synthesis and characterization of zinc aluminate nanoparticles by sol-gel combustion process **E.Muhammad Abdul Jamal**, D. Sakthi Kumar, M. R. Anantharaman (Under Review, *Bull. Mater. Scien.*)
7. Synthesis of nickel nanoparticles through a new chemical process **E Muhammad Abdul Jamal**, P. A. Joy, D. Sakthi Kumar, Yasuhiko Yoshida, M. R. Anantharaman, International symposium on Frontiers in Nanoscale Science, Technology and Education, August 16-19 (2006), Cochin, India
8. Synthesis of zinc aluminate nanoparticles by sol-gel process. **E. Muhammad Abdul Jamal**, D. Sakthi Kumar, M. R. Anantharaman International conference on Nano-materials and Its Applications (ICNA-2007) 4-6 Feb 2007, NIT, Trichy, India
9. On the dielectric and magnetic properties of rubber-nickel composites in the X band, **E.Muhammad Abdul Jamal**, P.Mohanan, Philip Kurian, M. R. Anantharaman (Cochin Nano-

Preface

The story of magnetism can be traced to the discovery of loadstone around 2000 years ago and since then magnetism and magnetic materials have been playing a lead role in making life more humane. Considering the proliferation of new gadgets and devices based on magnetic materials sooner or later the magnetic industry will outgrow the semiconductor industry. The advent of nanoscience and nanotechnology as a major discipline has provided further impetus to the already burgeoning research activities in the area of magnetic materials. This has given birth to a new area of nanomagnetic materials. With the advances made in nanomagnetic materials, the size of the hard disk has been shrunk, the density of the hard disk has been tripled in accordance with the Moore's predictions, the retrieval rate from a hard disk has been increased several times and a new concept based on magnetic spintronics called MRAM has already become a reality. Such is the pace with which this field is advancing that it is only natural that materials scientists, physicists and chemists delve more and more into these phenomena and materials in order to improve upon the existing and find newer materials to remove obsolescence.

Thus the area of magnetism and magnetics is an evergreen area for the scientists, the more they delve into the physics the more remains to be understood at the bottom! Ferrites played an important role in the 50s and 60s in realizing many devices namely high frequency transformers, radio frequency and microwave antenna, radiation absorbers, magnetic recording media and core memories. In that spinel ferrites played a seminal role. They are sought after because the properties can be tailored to suit various applications by simple chemical means. Spinel ferrites comprises of two types, the normal spinel and the inverse spinels. Normal spinels with cations having tetrahedral site preference were found to be non-magnetic. However these materials have been continuously improved upon since their catalytic properties are of interest to

chemical engineers. The recent findings of many researchers including some of the earlier work carried out in this laboratory has shown that normal spinels when prepared in the nano-regime exhibit magnetic properties. This has been puzzling scientists and many hypotheses needs testing like why a normal spinel which has no A-B interaction should lead to ferrimagnetism or is it because of formation of spin clusters or is it because of cation redistribution? Zinc ferrite and cadmium ferrite are normal spinels in the micron regime and are non magnetic. However, when they are prepared in the nano regime, they are reported to be exhibiting a net magnetization at room temperature. Hence zinc ferrite and cadmium ferrites are ideal templates to test various hypotheses. If a systematic investigation on these materials in the nano regime is conducted, many of the unanswered questions will find suitable answers. It is with this motive that a systematic study on the structural and magnetic properties were envisaged a part of this thesis. Zinc aluminate belongs to a non-magnetic family of spinels and it would be interesting to investigate the structural and electrical properties when they are crystallized in the nano-regime. So zinc aluminate is also investigated with emphasis on finding out possible cation redistribution when prepared in the nano-regime

Magnetic metal nanoparticles have been an attractive material for chemists and physicists alike. Metal nanoparticles like nickel have innumerable applications in the form of magnetostrictive transducers, as filler material in making nanocomposites, and also as catalysts for chemical reactions. The synthesis of nickel nanoparticles is often tricky and details are not available in the literature. Moreover, highly reactive nature of the nanoparticles is a cause of worry since they oxidize to form their corresponding oxides and are rendered useless as far as applications are concerned. Hence one of the objectives of this particular investigation was to prepare self-protected nickel nanoparticles by a novel method and use these particles as filler for preparing nanocomposites based on natural rubber as well as synthetic rubber. This was attempted because the incorporation of nanoparticles like nickel in a matrix like rubber not only imparts the required magnetic property to a lossy dielectric but also reinforces the polymer as well. Thus the incorporation of nickel nanoparticles in polymer matrixes like natural rubber and neoprene rubber will lead to microwave absorbers based on them. So the preparation of

nanocomposites based on rubber and nickel is another objective of this investigation. Any study on the magnetic, electric and structural properties will only be complete if they are properly characterized and results explained based on the analysis of the results. Various models are available for predicting the magnetic and electrical properties of these composites which will lead to the origin of a good electromagnetic wave absorbers. The magnetic permeability and dielectric permittivity in various frequency bands like radiofrequency, S and X are to be evaluated and modeled based on the surface impedance equation. This is another motivation of the present investigation. Thus the objectives of the present work can be summarized and are listed as follows.

1. Preparation and characterization of zinc and cadmium ferrite nanoparticles
2. Evaluation of structural, morphological and magnetic properties on size reduction by high energy ball-milling
3. Synthesis of magnetic nickel nanoparticles
4. Structural, morphological and magnetic studies on nickel nanoparticles
5. Synthesis of rubber-nickel nanocomposites
6. Structural and morphological evaluation
7. Evaluation of dielectric and magnetic properties in rf, S and X band frequencies

Salient features of the present work

1 Studies on sol-gel synthesized and ball milled zinc ferrite and cadmium ferrite

In general the exhibition of room temperature magnetism in nanosized zinc ferrites otherwise non-magnetic in the micron region are attributed to the inversion in spinel structure, and the reason for this inversion with particle size reduction is not clear. Zinc ferrite can be synthesized using conventional ceramic methods, and the size reduction can be achieved by the high energy ball-milling. The structural inversion could be one of the reasons for high magnetic moment at room temperature exhibited by nanosized zinc ferrite. But this inversion can be a consequence of the size reduction of the particles to nanometer regime. This also can be due to the disturbance in equilibrium of lattice energy due to energy transfer during the milling process.

One way of examining this effect is to synthesize normal spinel ferrites like zinc ferrite using methods like sol-gel synthesis in reduced particle size. A sol-gel auto-combustion method has been employed to synthesize spinels. The size-range of the particles obtained is nearly 50 nm for both zinc ferrite and cadmium ferrite. The samples synthesized using sol-gel process have a much reduced grain size even without ball milling. The same effects produced by prolonged high energy ball milling can be brought about faster if the samples are synthesized using this method. This possibility has been looked into in the experimental work presented in this thesis.

Cadmium ferrite and zinc ferrite are two closely similar systems. Both Zn and Cd cations do not have any net magnetic moment since their d shells are completely filled and have no unpaired electrons and no magnetic moment as a result. Their ionic sizes are comparable (0.74 Å and 0.97 Å respectively) and both these atoms have a tetrahedral site preference in spinel structured crystals and form normal spinels. These studies reveal that both zinc and cadmium ferrite in the nano regime exhibit magnetism at room temperature and a plausible mechanism is proposed in the thesis.

2 Synthesis of nickel nanoparticles and rubber-nickel composites and their characterization studies

Nickel assumes an important role among all metallic magnetic elements. Nickel nanoparticles have a number of technological applications. But the synthesis of nickel nanoparticles is normally a time consuming process because of the nature of the chemical processes involved. Precipitation methods can yield very fine nickel particles but the yield is very small. Further these methods require repeated filtering and washing because the particles of nickel are usually formed as a precipitate in an organic solvent.

In these circumstances it has been realized that a dry procedure to synthesize nickel nanoparticles will be very much helpful, especially if nickel is to be used in the preparation of magnetic composites. Literature survey revealed that so far only one report has described the synthesis of nickel nanoparticles in a dry combustion process. This process is a dry method, and nickel nanoparticles are formed in a chemical reaction of the nature of an oxidation, and this

combustion process is assisted by the fuel urea, and initiated by microwaves. The attempt to further simplify the process was successful and a a very simple process had been devised to produce nickel nanoparticles in bulk quantities. The synthesized powder had been thoroughly characterized using various analytical tools and found that these particles are comparable in quality with commercially available samples. These nanoparticles are self protected due to the formation of a small oxide coating at the time of synthesis.

These precharacterized nickel nanoparticles were used in the preparation of rubber-nickel nanocomposites and they have many important technological applications. Two kinds of composites were prepared using two different rubber varieties (natural rubber and neoprene rubber) and they were characterized thoroughly. Their dielectric and magnetic properties in the radio frequencies as well as in the S and X band microwave frequencies were determined and their microwave absorbing properties were evaluated based on the surface impedance equation.

Proposed chapters in the thesis

The thesis is divided into two parts. Part 1 comprises the synthesis and characterization of zinc and cadmium ferrite in the nanoregime, their characterization using various analytical techniques like XRD, TEM, SEM, VSM and SQUID and also deals with the effect of high energy ball-milling on the morphological and magnetic properties of them. Part 2 comprises of the synthesis of nanonickel particles, their characterization and investigations carried out on nanocomposites prepared by incorporating pre-characterized nickel particles in rubber matrixes for various loadings according to a specific recipe in two matrices namely natural rubber and neoprene rubber. These composites are evaluated for their cure characteristics, mechanical properties and static magnetic properties in addition to the evaluation of their complex dielectric permittivity and magnetic permeability in the rf, S and X band frequencies.

The entire research work consists of nine chapters. The division of chapters with a brief outline of the contents is given below

Chapter 1 is the introduction chapter. A brief introduction about the phenomenon of magnetism and the importance of magnetic material is provided in this chapter. The importance on the study

of magnetic metal oxides and magnetic metal nanoparticles and the importance of magnetic composite materials are briefly described.

Chapter 2 is a description about the various important experimental techniques adopted in the studies including the details of some instrumentation and automation carried out for the present study.

Chapter 3 describes the details of the synthesis and characterization of zinc ferrite and cadmium ferrite nanoparticles in sol-gel auto-combustion method and the studies on the dielectric properties of the two mixed oxide nanoparticles

Chapter 4 deals with the studies on the effect of high energy ball-milling (HEBM) on the structural, morphological and magnetic properties of cadmium and zinc ferrites nanoparticles. The effect of HEBM for durations 10, 20, 30, 60 and 120 minutes are presented in this chapter along with the properties of un-milled sample in its pristine polycrystalline phase. Low temperature studies on zinc ferrite using SQUID are also presented in this chapter

Chapter 5 describes the synthesis of nanoparticles of nickel and its characterization by various tools like X-ray diffractometry, transmission electron microscopy, SQUID magnetometry, energy dispersive spectroscopy, zero field-cooled and field-cooled magnetization studies and scanning electron microscopy. These studies were conducted with a view to establishing the size and purity of nickel particles synthesized in a method developed in-house.

Chapter 6 deals with the synthesis of rubber-nickel nanocomposites by incorporating nickel nanoparticles in rubber matrix (both natural rubber and neoprene rubber matrixes). The analysis of cure properties of these two classes of composites is carried out along with studies on their mechanical and magnetic properties.

Chapter 7 describes the studies of dielectric properties of natural-rubber-nickel nanocomposites (NRNCs) and neoprene-nickel-nanocomposites (NNCs) in the frequency range of 100 KHz to 8 MHz (radio frequencies). Analysis of the possible polarization mechanisms operating in this frequency regime in the composites is also dealt with in this chapter.

Chapter 8 deals with the evaluation of complex dielectric permittivity and magnetic permeability of the composites in S and X bands of microwave frequencies. The measurements were done

using cavity perturbation technique. The possibility of using the composites as microwave absorbers in the X band also is inspected by calculating the reflection loss for a given thickness of 2 mm.

Chapter 9 is the conclusion chapter where the summary of all the findings of the present investigations is discussed in detail.

In addition to these chapters listed above, an **annexure** is incorporated, which the gist of the investigations is carried out on zinc aluminate nanoparticles synthesized using sol-gel auto-combustion method. The significance of this study is that, it helped a great deal in optimizing the method of sol-gel combustion method. Zinc aluminate is not a magnetic material, and does not fit into the main theme of the research work and hence its inclusion as an annexure.

Contents

Chapter 1

Introduction

| | | |
|---------|--|----|
| 1.1 | Magnetism and magnetic materials | 1 |
| 1.1.1 | Magnetism | 1 |
| 1.1.2 | Magnetic moments | 2 |
| 1.1.3 | Magnetization | 3 |
| 1.1.4 | Orbital and spin magnetic moments | 3 |
| 1.1.5 | Magnetic behavior of isolated magnetic moments | 4 |
| 1.1.6 | Diamagnetism | 5 |
| 1.1.7 | Paramagnetism | 5 |
| 1.1.8 | Magnetic interactions | 7 |
| 1.1.8.a | Magnetic dipole interaction | 7 |
| 1.1.8.b | Exchange Interaction | 8 |
| 1.1.9 | Types of exchange interactions | 9 |
| 1.1.10 | Magnetic orders in solids | 10 |
| 1.1.11 | Superparamagnetism | 14 |
| 1.1.12 | Magnetic domains | 15 |
| 1.2. | Ferrites and their magnetic properties | 15 |
| 1.2.1 | Spinel structure | 15 |
| 1.2.2 | Normal and inverse spinels | 17 |
| 1.2.3 | Magnetic properties of ferrites | 17 |
| 1.3 | Magnetic metal nanoparticles | 20 |
| 1.3.1 | Nickel nanoparticles | 20 |
| 1.3.2 | Synthesis of nickel nanoparticles | 20 |
| 1.4 | Composite materials | 21 |
| 1.4.1 | Importance of composite materials | 21 |
| 1.4.2 | Nanocomposites | 22 |

| | | |
|-------------------------|---|----|
| 1.4.3 | Magnetic nanocomposites as microwave absorbers | 23 |
| 1.5 | Present work | 24 |
| 1.5.1 | Motivation and objectives of the present work | 24 |
| | References | 26 |
| Chapter 2 | | |
| Experimental techniques | | |
| 2.1 | Introduction | 29 |
| 2.2 | Sol-Gel Synthesis | 29 |
| 2.3 | Dielectric permittivity and ac conductivity studies | 31 |
| 2.3.1 | Basic principles | 31 |
| 2.3.2 | Design of the dielectric cell | 33 |
| 2.4 | Fabrication of ac susceptometer | 34 |
| 2.4.1 | a.c.susceptometry | 34 |
| 2.4.2 | Fabrication of a. c. susceptometer | 35 |
| 2.4.3 | Automation | 37 |
| 2.4.4 | Standardization and validation | 39 |
| 2.4.5 | Studies on LCMO samples | 40 |
| 2.5 | High energy ball-milling | 43 |
| 2.5 | High energy ball-milling | 44 |
| 2.5.2 | Milling parameters | 45 |
| 2.6 | Vibrating sample magnetometry | 47 |
| 2.6.1 | Basic principles | 47 |
| 2.6.2 | Working principles of a VSM | 48 |
| 2.7 | Cavity perturbation technique | 49 |
| 2.7.1 | Principle | 49 |
| 2.8 | SQUID Magnetometer | 51 |
| 2.8.1 | Basic ideas | 51 |
| 2.8.2 | Design of SQUID | 52 |
| 2.9 | Transmission Electron Microscopy | 52 |
| 2.9.1 | Basic features | 52 |

| | | |
|-------|------------------------------|----|
| 2.9.2 | Design of a TEM | 53 |
| 2.10 | Scanning Electron Microscopy | 54 |
| | References | 55 |

Chapter 3

Synthesis and evaluation of dielectric properties of zinc ferrite and cadmium ferrite nanoparticles

| | | |
|-----|--|----|
| 3.1 | Synthesis and structural characterization of zinc ferrite | 57 |
| 3.2 | Synthesis and structural characterization of cadmium ferrite | 58 |
| 3.3 | Dielectric and a.c conductivity studies | 59 |
| 3.4 | Dielectric properties of zinc ferrite | 60 |
| 3.5 | Evaluation of ac conductivity of zinc ferrite | 63 |
| 3.6 | Dielectric studies of cadmium ferrite | 67 |
| 3.7 | Evaluation of ac conductivity of cadmium ferrite | 70 |
| 3.8 | Conclusion | 72 |
| | References | 73 |

Chapter 4

Effect of high energy ball milling on Zinc Ferrite and Cadmium ferrite nanoparticles

| | | |
|------|--|----|
| 4.1 | Sample preparation | 76 |
| 4.2. | XRD analysis of ball-milled samples | 76 |
| 4.3 | The transmission electron micrography | 78 |
| 4.4 | Scanning electron microscopy | 80 |
| 4.5 | Magnetic properties | 84 |
| 4.6 | SQUID magnetization studies | 87 |
| 4.7 | Superparamagnetic behaviour and Langevin fit | 92 |
| 4.8 | Conclusion | 95 |
| | References | 96 |

Chapter 5

Synthesis and characterization of nickel nanoparticles

| | | |
|-----|----------------------|-----|
| 5.1 | Introduction | 99 |
| 5.2 | Experimental | 102 |
| 5.3 | X-ray Diffractometry | 102 |

| | | |
|-----|--|-----|
| 5.3 | Magnetization studies | 103 |
| 5.4 | Temperature dependent magnetization | 105 |
| 5.5 | Transmission Electron Microscopy and EDS | 106 |
| 5.6 | Scanning electron microscopy | 109 |
| 5.7 | Conclusion | 111 |
| | References | 112 |

Chapter 6

Preparation and cure, mechanical and magnetic studies on rubber-nickel nanocomposites

| | | |
|------|---------------------------------------|-----|
| 6.1 | Compounding recipes | 116 |
| 6.2 | Mixing | 116 |
| 6.3 | Cure analysis | 117 |
| 6.4 | Cure characteristics of NRNCs | 119 |
| 6.5 | Cure characteristics of NNCs | 124 |
| 6.6 | Moulding of the composites | 128 |
| 6.7 | X-ray diffractometry | 128 |
| 6.8 | Mechanical properties | 130 |
| 6.9 | Magnetic properties of NRNCs and NNCs | 133 |
| 6.10 | Conclusion | 138 |
| | References | 139 |

Chapter 7

Dielectric properties of rubber-nickel nanocomposites in radio-frequencies

| | | |
|-------|--|-----|
| 7.1 | Properties of composites | 141 |
| 7.2 | Dielectric studies in radiofrequency range | 143 |
| 7.3 | Results and Discussions | 143 |
| 7.3.1 | Dielectric properties of natural-rubber-nickel composites | 143 |
| 7.3.2 | Dielectric properties of neoprene-rubber-nickel composites | 151 |
| 7.4 | Conclusion | 154 |
| | References | 155 |

Chapter 8

Dielectric permittivity and magnetic permeability studies on rubber-nickel composites in the S and X band microwave frequencies

| | | |
|-------------|--|------------|
| 8.1 | Microwave absorbers | 157 |
| 8.2 | Cavity perturbation method | 158 |
| 8.3 | Measurements in the S band | 159 |
| 8.4 | Measurements in the X band | 160 |
| 8.5 | Complex diel. permittivity of natural-rubber-nickel composites | 160 |
| 8.6 | Complex diel. permittivity of neoprene-rubber-nickel composites | 163 |
| 8.7 | Magnetic permeability of the composites | 165 |
| 8.8 | Complex dielectric permittivity in X band | 167 |
| 8.9 | Complex magnetic permeability in the X band | 171 |
| 8.10 | Input impedance and reflection loss | 173 |
| 8.11 | Conclusion | 177 |
| | References | 179 |

Chapter 9

| | |
|-------------------|------------|
| Conclusion | 181 |
|-------------------|------------|

Annexure

| | |
|---|------------|
| On the structural, optical and dielectric properties of zinc aluminate nanoparticles | 185 |
|---|------------|

Chapter 1

Introduction

1.1 Magnetism and magnetic materials

1.1.1 Magnetism

Magnetism and magnetic materials fascinated man from time immemorial. The first documented evidence of the association of man with magnetic materials dates back to more than two thousand years with the discovery of loadstone. The mariners compass was the first device invented by man based on the principles of magnetic properties of material, and this navigational aid helped him in discovering new continents, and is responsible for building up the modern day's world order [1].

Even though the phenomenon of magnetism was known to man for thousands of years, magnetism as a modern branch of science evolved only during the last two centuries. But tremendous advancements have been achieved in the understanding of the phenomenon of magnetism during this period, helped by the theoretical knowledge achieved on the structure of matter. Magnetic materials have become an indispensable part in the modern day technology, and virtually there is no field of technology where such materials do not find a place. This presence is felt in gadgets from ordinary loudspeakers to superconducting magnets. The vast proliferation of personal computers is helped by the availability of high capacity hard disks developed with low grain size magnetic recording particles [2].

The magnetic phenomena can be divided into various types depending on the kind of magnetic interactions that exist in the atomic level leading to different kinds of magnetic materials. The present day knowledge on magnetism is based on the principle of quantum mechanics, and it is often said that the phenomenon of magnetism is a good example for having the presence of quantum mechanics felt in every day life. Though tremendous progress has been

Chapter 1

achieved in the understanding of the phenomenon, the magnetism in condensed matter is an active area of research even today. This interest arises mainly out of two aspects; the first is the difficulties still remaining in understanding certain behaviors of magnetic materials, and secondly the requirement of more and more demanding materials for technological applications [3].

Knowledge of fundamental aspects of the phenomenon of magnetism is essential to understand various kinds of magnetic interactions and the existence of different kinds of magnetic properties. An attempt is made to briefly explain the fundamental aspects of magnetism in the ensuing sections. This will help in further discussions about magnetic behavior of materials.

1.1.2 Magnetic moments

Magnetic moment is the fundamental object in magnetism. Classically every circulating current gives rise to a magnetic moment, and by considering a infinitesimally small current loop of area dS carrying a current, we can define a magnetic moment as~

$$d\mu = Ids \quad (1.1)$$

where $d\mu$ is a vector quantity in the direction of the area dS of the current loop. The magnetic moment is always associated with an angular momentum since all circulating charged particles producing electric current have mass. In atoms the magnetic moment is caused by an orbiting electron. The angular momentum L of that electron is thus proportional to the magnetic moment and we can write

$$\mu = \gamma L \quad (1.2)$$

where γ is the gyromagnetic ratio. Also this association of magnetic moment and angular momentum causes the magnetic moment to undergo a precession when placed in a magnetic field \mathbf{B} . Considering \mathbf{B} along the z axis and μ initially at an angle θ to \mathbf{B} the frequency of precession is given by

$$\omega_L = \gamma B \quad (1.3)$$

and ω_L is known as the Larmor precession frequency.

The ground state ($1s^1$) electron of hydrogen atom has a magnetic moment equal to

$$-\mu_B = -\frac{e\hbar}{2m_e} \quad (1.4)$$

Where μ_B is known as the Bohr magneton and takes a value $9.274 \times 10^{-24} \text{ Am}^2$. This is a convenient unit for describing the size of atomic magnetic moments [3].

1.1.3 Magnetization

The magnetization M of a solid material is defined as the total magnetic moment per unit volume in the solid. The primary reason for the existence of magnetic moment in the solid is the magnetic moment of the atoms or molecules in the solid, and since the size of the atoms are several order smaller than the size of the solid, we make a continuum approximation suggesting M is a smooth vector field continuous everywhere inside the solid, except at its edges. The magnetic field is defined by the vector field \mathbf{B} and \mathbf{H} which are related by

$$\mathbf{B} = \mu_o \mathbf{H} \quad (1.5)$$

Here, $\mu_o = 4\pi \times 10^{-7} \text{ Hm}^{-1}$, \mathbf{B} and \mathbf{H} are scaled versions of each other were \mathbf{B} is measured in Tesla (T) and \mathbf{H} is measured in Am^{-1} .

These quantities are related to each other in a magnetic solid in the form

$$\mathbf{B} = \mu_o (\mathbf{H} + \mathbf{M}), \quad (1.6) \quad \text{and in a linear}$$

material, $\mathbf{M} = \chi \mathbf{H}$ (1.7) where χ is a dimensionless quantity called the magnetic susceptibility.

$$\mathbf{B} = \mu_o (1 + \chi) \mathbf{H} = \mu_o \mu_r \mathbf{H}, \quad (1.8) \quad \text{where}$$

$\mu_r = 1 + \chi$ (1.9) is the relative permeability of the material [3, 4].

1.1.4 Orbital and spin magnetic moments

The electronic angular momentum of a circulating current loop in atomic level is associated with the orbital motion of electron. In a real atom the magnitude of the magnetic moment of such orbiting electrons is dependant on the electronic state occupied by the electron. The component of the orbital angular momentum m_l along a fixed axis is $m_l \hbar$ and the magnitude of the orbital angular momentum is $\sqrt{l(l+1)} \hbar$. Hence the component of magnetic moment due to

Chapter 1

orbital motion along the z axis is $-m_l\mu_B$ and the magnitude of the total magnetic moment is $\sqrt{l(l+1)}\mu_B$ where μ_B is the Bohr magneton. But this is not the only magnetic moment an electron possesses. An electron has an intrinsic magnetic moment which is associated with an intrinsic angular momentum. This intrinsic angular momentum is called the spin. The spin of an electron is characterized by a spin quantum number s , which for an electron takes the value $\frac{1}{2}$. The component of spin angular momentum is $m_s\hbar$ and m_s has only two possible values, $\pm\frac{1}{2}$. The component of angular momentum along a particular axis is $\hbar/2$ or $-\hbar/2$. These two alternatives are generally referred to as up and down spins. The spin angular momentum is associated with a magnetic moment which has a component along a particular axis equal to $-g\mu_B m_s$. Here g is a constant called the g-factor. The g-factor takes a value approximately equal to 2. Thus component of spin magnetic moment along the z axis is $\mp\mu_B$, even though the spin is half integral. The energy of the electron in a magnetic field B is therefore

$$E = g\mu_B m_s B \quad (1.10)$$

As a result the energy level splits in a magnetic field by an amount $g\mu_B m_s B$ which is known as Zeeman splitting.

In general the orbital and spin angular moments combine to give a net angular momentum. The g-factor can take different values in real atoms depending on the contributions from orbital and spin counterparts of angular momenta. But the angular momentum of an electron is always an integral or half integral multiple of \hbar . So it is convenient to drop the factor \hbar in expressions which is equivalent of saying that the angular momentum is expressed in units of \hbar [3,5].

1.1.5 Magnetic behavior of isolated magnetic moments

Only two kinds of magnetic behavior can be expected if we consider the magnetic moments of atoms or molecules separately. They are diamagnetism and paramagnetism. All other magnetic behaviour exhibited by matter arises out of the interactions of magnetic moments between atoms. Diamagnetism and paramagnetism can be understood on the basis of magnetic

susceptibility of individual atoms. When an atom with a magnetic moment interacts with a magnetic field B , the perturbed Hamiltonian is given as

$$\hat{H} = \hat{H}_o + \mu_B (L + gS) \cdot B + \frac{e^2}{8m_e} \sum (B \times r_i)^2 \quad (1.11)$$

the paramagnetic and diamagnetic behavior can be understood and explained on the basis of the above equation [3].

1.1.6 Diamagnetism

Diamagnetism is a weak negative magnetic susceptibility exhibited generally by those atoms with no unfilled electronic shells. The phenomenon of diamagnetism is entirely quantum mechanical and should be treated as such. In the equation 1.11 above, in the case of atoms with unfilled electronic shells, the paramagnetic term can be ignored. Calculation of susceptibility on the basis of first order perturbation theory after ignoring the paramagnetic term gives a negative quantity indicating an antiparallel arrangement of magnetic moments in the atoms with the applied magnetic field B . The expression for susceptibility is given as,

$$\chi = -\frac{N e^2 \mu_o}{V 6m_e} \sum_{i=1}^Z \langle r_i^2 \rangle \quad (1.12)$$

where N is the number of moments available in a given volume V . As the temperature is increased above zero, states above the ground state becomes important but such effects are negligible and diamagnetic susceptibility of an element is generally temperature independent. All materials exhibit diamagnetism. But the magnitude of diamagnetism is so small and can be considered as a weak effect [3].

1.1.7 Paramagnetism

When an external magnetic field is applied certain atoms shows a positive susceptibility i.e. the induced magnetization is in the same direction of the applied field. In the case of diamagnetism we considered material with no unpaired electrons. But atoms with unpaired electrons have a non-zero magnetic moment. These magnetic moments are distributed at random directions and the interaction between them is so weak to cause any alignment in the absence of the magnetic field. The application of a magnetic field causes the individual moments to align

Chapter 1

parallel to the field creating a net magnetization and a positive susceptibility. The degree of the induced magnetization depends on the strength of the magnetic field applied (when temperature remains constant). The paramagnetism has a stronger dependence on temperature compared to the diamagnetism. The ordering effect of the applied magnetic field is destroyed by the thermal vibrations as they try to randomize the spin. So the magnetization of a material is having a dependence on the quantity B/T. The paramagnetic effect is much stronger than the diamagnetic effect. But the diamagnetism is always present in all materials as a weak negative contribution.

The average induced magnetic moment $\langle \mu_z \rangle$ in a paramagnetic material with a magnetic moment μ per atom is given by the relation,

$$\langle \mu_z \rangle = \mu \left(\coth\left(\frac{\mu B}{k_B T}\right) - \frac{1}{\frac{\mu B}{k_B T}} \right), \quad \text{or} \quad (1.13)$$

$$\frac{\langle \mu_z \rangle}{\mu} = \coth y - 1/y, \quad \text{where } y = \left(\frac{\mu B}{k_B T}\right) \quad (1.14)$$

where k_B is the Boltzmann's constant

The function $\coth y - 1/y$ is known as the Langevin function. If there are n atoms in the sample undergoing magnetization the saturation magnetization is given by

$$M_s = n\mu \quad (1.15)$$

And the magnetization at any instant is given by M and

$$M = n\langle \mu_z \rangle, \quad (1.16) \quad \text{So it is}$$

convenient to express the relation 1.15 in terms of M and M_s , i.e.

$$\frac{M}{M_s} = \coth y - 1/y \quad (1.17)$$

This relation demonstrates that paramagnetic susceptibility is inversely proportional to the absolute temperature which is known as the Curie's Law. This equation is obtained by the semi-classical treatment of magnetic moments by assuming that the moments can get oriented to any direction with respect to the applied magnetic field. But this is not true in a strict quantum mechanical sense. Moments can only have certain allowed directions.

If we proceed in a strictly quantum mechanical way, for atoms with a net magnetic moment $J = \frac{1}{2}$, there are only two possible values for the z component of the magnetic moment i.e. $m_J = \pm \frac{1}{2}$. If we proceed by taking this assumption it is possible to show that

$$\frac{M_s}{M} = \tanh\left(\frac{\mu_B B}{k_B T}\right) = \tanh y \quad (1.18)$$

This relation is different from that of 1.17 but the behavior of the function is quite similar to Langevin function.

In the general case, where J can take any integer or half integer value, the paramagnetic induction is given by the relation

$M = M_s B_J(y)$, where $B_J(y)$ is the Brillouin function given by

$$B_J(y) = \frac{2J+1}{2J} \coth\left(\frac{2J+1}{2J} y\right) - \frac{1}{2J} \coth \frac{y}{2J} \quad (1.19)$$

The Brillouin function reduces to a Langevin function when $J = \infty$ and to a tanh function when $J = \frac{1}{2}$. [3, 4]

1.1.8 Magnetic interactions

In a solid material, the nature of the magnetic behavior is determined by the kind of magnetic interaction existing between the atomic magnetic moments. These magnetic interactions are the ways the moments communicate with each other to produce long range order. The collective effects of these interactions give rise to interesting magnetic phenomena in solids, which are different from their individual isolated magnetic moments. All types of magnetic phenomena exhibited by solids are arising due to cooperative behavior of magnetic moments. We can consider various kinds of interactions of magnetic moments that exist in solids.

1.1.8.a Magnetic dipole interaction

This kind of interaction is the first expected interaction which may play a role in the magnetic materials. The energy of two magnetic dipoles μ_1 and μ_2 separated by a distance r is given by the equation

$$E = \frac{\mu_o}{4\pi r^3} \left[\mu_1 \cdot \mu_2 - \frac{3}{r^2} (\mu_1 \cdot r)(\mu_2 \cdot r) \right], \quad (1.20)$$

this energy is very small (of the order of 10^{-23} J) and at ordinary temperatures this is negligible when compared to the thermal energy of the atoms and cannot contribute to any magnetic ordering in solid magnetic materials. But magnetic dipolar interaction can become significant at very low temperatures close to absolute zero.

1.1.8.b Exchange Interaction

In solids, when the atoms are sufficiently close and their wave functions overlap, the exchange force comes into play. This is the kind of interaction which makes the spins of neighboring atoms to align parallel or antiparallel, and purely quantum mechanical in nature, and has no classical counterpart. The basic cause of exchange force is the Coulomb interaction and the preference of atoms for a lower energy state. The exchange interaction is determined by the exchange integral J , and the exchange Hamiltonian of two atoms with overlapping wave functions is written as

$$\hat{H} = -2JS_1 \cdot S_2 \quad (1.21)$$

When J is positive the triplet state $S=1$ (parallel) is favored, and when J is negative the singlet state $S=0$ (antiparallel) is favored by the spins of interacting atoms. Exchange interaction causes the spins to get aligned in parallel or antiparallel fashions without the application of any external magnetic field. This interaction causes the hydrogen molecules to form from two hydrogen atoms by making the spins to align in antiparallel orientations and thus minimizing the exchange energy. But the spins need not align antiparallel in all cases, and there are situations in which the parallel alignment of spins is favored, even though such situations are rare in nature.

In a solid, the exchange forces are not limited to neighboring atoms, but the effect of all atoms in a crystal is to be taken into account. The Hamiltonian can now be written as

$$\hat{H} = -\sum_{i,j} J_{ij} S_i \cdot S_j, \quad (1.22)$$

here the factor 2 is omitted because the summation includes each pair of i and j twice. The calculation of the exchange integral is complicated in general. A positive value of exchange integral is a necessary condition for ferromagnetism to occur [3, 4].

1.1.9 Types of exchange interactions

The exchange interaction can be direct or indirect, depending on the positions of the interacting atoms. In direct exchange, the interaction is in between two neighboring atoms, and proceeds without the need of any intermediary. The neighboring magnetic orbitals should have sufficient overlap for any direct exchange interaction to take place. This overlap is not available in many neighboring atoms, especially in some magnetic rare earths, where the 4f electrons only extend to less than one tenth of the inter-atomic distance. And in such magnetic materials it is necessary to consider some kind of indirect exchange interaction.

If the indirect exchange is mediated through a non-magnetic atom placed in between two magnetic ions, the kind of exchange interaction is called a superexchange. It arises because there is a kinetic energy advantage for antiparallel arrangement. Usually superexchange takes place when two transition metal ions are separated by an oxygen ion. MnO is a good example for superexchange interaction. The crystalline structure of MnO does not allow any direct overlap between the orbitals of Mn^{2+} ions. There is an oxygen atom in between any two Mn atoms and Mn atoms prefer an antiparallel spin orientation due to exchange interaction mediated through oxygen ions.

In oxides showing mixed valency another kind of indirect exchange interaction takes place, which is named as double exchange. Double exchange is a result of hopping of electrons between different valent states, and produces parallel alignment of spins, or ferromagnetic ordering. Double exchange is the type of exchange interaction found in magnetite (Fe_3O_4) which contains Fe^{2+} and Fe^{3+} ions on octahedral sites in equal numbers and the same number of Fe^{3+} ions in tetrahedral sites. Electron hopping between Fe^{2+} states and Fe^{3+} states in the octahedral sites through the oxygen ions favors parallel alignments of spins. But the same time a superexchange interaction takes place between the Fe^{3+} ions in the octahedral and tetrahedral sites, making the spins to align in antiparallel and to have the net magnetic moment to vanish. The net moment is only due to the Fe^{2+} ions. A magnetic moment of $4 \mu_B$ per formula unit is expected and the measurements agree with this expected result.

Another kind of indirect exchange interaction known as the RKKY interaction exists between atoms of metals. This interaction is mediated through the spin polarized conduction

Chapter 1

electrons in the metals. A localized magnetic moment can spin polarize a conduction electron and this polarization can couple to a neighboring isolated magnetic moment which is some distance away. This exchange interaction is indirect in nature. The name RKKY indicates the names of Ruderman, Kittel, Kasuya and Yosida. This interaction can be ferromagnetic or antiferromagnetic (parallel or antiparallel spin) depending on the distance between the interacting moments. This interaction is having an oscillatory nature with a wave length $\frac{\pi}{k_F}$ because of the sharpness of the Fermi surface. The RKKY interaction is the prevalent interaction in spin glass structures [3].

1.1.10 Magnetic orders in solids

Different kinds of exchange interactions and the nature of the exchange integrals cause different kinds of magnetic ordering in solids. The most important of these magnetic orderings are the ferromagnetic and antiferromagnetic kinds, caused by the parallel or antiparallel alignment of spins of neighboring atoms. Also there exists spiral and helical structures in which, the spin undergoes a conical or circular precession as we move from one atom to the next progressively. In addition to these there is another kind of ordering of the moments known as the spin glasses in which spins are randomly oriented in a frozen state.

A ferromagnet has a spontaneous magnetization even in the absence of a magnetic field. All the magnetic moments lie along a single unique direction. In 1907 Weiss explained it in the light of a proposed molecular field existing inside all ferromagnetic materials. But calculation showed that this field should be of the order of 10^3 T in order to explain the behavior of the ferromagnets. The mystery was finally solved in 1924 after Heisenberg explained it on the basis of exchange interaction, which is purely an electrostatic phenomenon. Exchange interaction involves large Coulomb energies, and not a mysterious phenomenon as molecular field. The parallel alignment of spins is disturbed by the thermal vibrations of the atoms in the solids and above a transition temperature T_C the magnetic material becomes paramagnetic, losing its spontaneous magnetization. This transition temperature is known as the Curie temperature and given by the equation.

$$T_C = \frac{n\lambda\mu_{eff}^2}{3k_B} \quad (1.23)$$

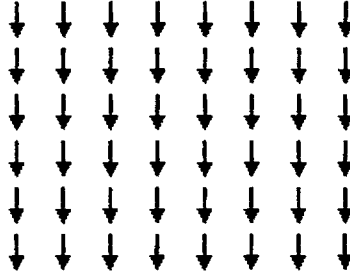


Figure 1.1: Ferromagnetic ordering of moments

and λ is the molecular field constant (as per the Weiss theory). Also the magnetic susceptibility of a ferromagnetic sample at any given temperature T is given by

$$\chi \propto \frac{1}{T - T_C} \quad (1.24)$$

When the exchange integral is negative, an antiparallel arrangement of neighboring spins, and thereby the magnetic moments, is favored resulting in antiferromagnetic ordering. Very often this happens in systems having two sublattices which interpenetrate each other. This antiparallel arrangement of moment is spontaneous inside the solid and affected by thermal energy. Below a transition temperature T_N , which is known as the Neel temperature, the antiparallel arrangement of neighboring magnetic moments is completely disturbed. This temperature is given by a relation,

$$T_N = \frac{n|\lambda|\mu_{eff}^2}{3k_B}, \quad (1.25)$$

where the modulus of the constant λ is taken because the molecular field constant is negative in the case of antiferromagnetism [3].

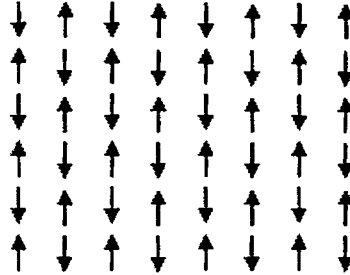


Figure 1.2: Antiferromagnetic ordering

Ferrimagnetism arises when the two sublattices of antiparallel spin alignment are not equivalent. The magnetic moments of adjacent sublattices do not cancel out and the material will have a net magnetization. Ferrimagnetism is shown by ferrites which are spinel structured mixed oxides of iron with a chemical formula AB_2O_4 , where A is a divalent cation like Zn^{2+} , Co^{2+} etc. The molecular field of each sublattice is different in ferrites and the spontaneous magnetization of each sublattice can have different temperature dependence. So the temperature dependence of the magnetization of Ferrimagnetic samples is complicated. The magnetic susceptibilities of ferrimagnets do not follow the Curie Weiss law in general. Other than ferrites another important group of materials exhibiting ferrimagnetism is garnets. They have a chemical formula $R_3Fe_5O_{12}$ where R is a trivalent rare earth atom. Barium ferrite, which has a hexagonal crystal structure, is another important ferrimagnetic material with a chemical formula $BaFe_2O_{10}$. Ferrimagnets are electrical insulators and this property gives them technological importance since it is possible to use them in high frequency applications, for which metallic magnets are not suitable [3, 6].

In certain rare earth metals a peculiar kind of magnetic order exists. In these materials the crystal structure is such that the atoms lie in layers. The moments of neighboring layers make an angle between them, and this angle is not 0 or 180 as in the case of ferromagnetic or antiferromagnetic ordering. Due to the arbitrary nature of angle between the magnetic moments between adjacent layers there is a rotation of the moments as we progressively move through layers. This kind of a magnetic order is known as the helical order or helimagnetism. The pitch of the spiral will not be an integer multiple of the layer distance in general and therefore the magnetic moments in any two layers will not have the same direction. Helical structures are found in rare earth metals like Tb, Dy and Ho. These metals have a hexagonally close packed

structure. The axis of the helix is perpendicular to the hexagonally close packed planes and this direction of helix is known as the c axis. The exchange interaction in rare earth metals is an indirect RKKY interaction [3, 5].

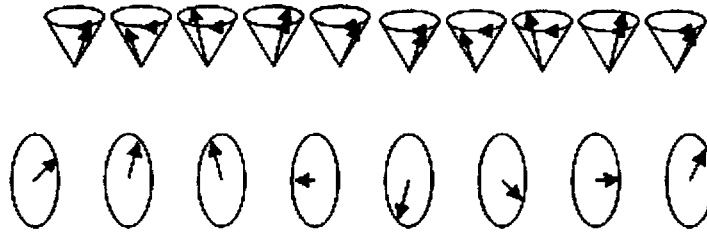


Figure 1.3: Ordering of magnetic moments in helimagnetism

Spin glasses are obtained when a non magnetic (diamagnetic) material is thinly populated with randomly distributed magnetic atoms. The spins freeze randomly and it may appear that no interaction is possible between randomly distributed frozen spins. But this is not true. Some kind of cooperative phenomena takes place inside spin glasses. At high temperatures the spins are not ordered lacking any interaction between the moments. But at a particular temperature T_i known as the freezing temperature some kind of a long range interaction comes to exist and the system gets magnetically ordered. There is a random cooperative freezing of spins at this freezing temperature [3, 7, 8].

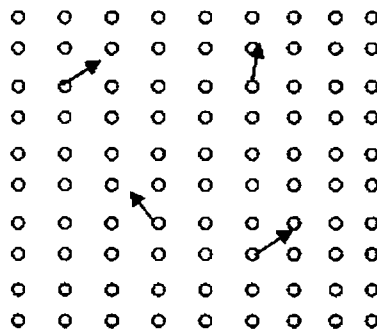


Figure 1.4: Ordering of magnetic moments in spin-glass

1.1.11 Superparamagnetism

As suggested by Frenkel and Dorfmann, all ferromagnetic materials below a critical grain size would consist of a single magnetic domain [9, 10]. This critical particle size for metallic magnetic particles is approximately 15 nm as estimated by Kittel et al [11]. Let us consider a single domain particle, the direction of whose magnetic moment makes an angle θ to the magnetic field. In the absence of any additional anisotropic terms, the energy of this particle can be expressed as

$$E = -\mu H \cos \theta \quad (1.26)$$

If we have a number of such particles in an assembly in thermodynamic equilibrium at temperature T , there will be a Boltzmann distribution of θ 's over the particle assembly. The fraction of the total magnetization which is aligned with the applied magnetic field can be calculated by assuming the Boltzmann distribution of energy at the particular temperature and this will yield the Langevin function

$$L(x) = \coth y - \frac{1}{y}, \quad y = \frac{\mu H}{kT} . \quad (1.27)$$

This treatment is analogous to the Langevin treatment of atomic paramagnetism, but the difference is that in this case a single particle as a whole is treated as the atomic entity instead of a molecule in paramagnetism. This single particle may contain as large as 10^5 molecules. So the magnetization behavior of single domain particles in thermodynamic equilibrium at all fields is identical with that of atomic paramagnetism, except that an extremely large moment is involved. Because of this similarity the thermal equilibrium behavior of single domain particles is termed as superparamagnetism.

There are two requirements for a magnetic sample to behave as superparamagnetic. The magnetization curve should not show any hysteresis and the magnetization curve of an isotropic sample must be temperature dependant so that the curves taken at different temperatures must overlap when plotted against H/T .

1.1.12 Magnetic domains

The magnetic moments inside a ferromagnetic material are all aligned parallel to each other, as a result of the exchange interactions, at temperatures below the Curie point. But if we

examine any ferromagnetic specimen, the magnetic moment will be much less than the saturation moment, and the specimen comes to saturation only on the application of an external magnetic field. The reason for this observation can be explained on the basis of magnetic domains existing in the ferromagnetic specimen.

Ferromagnetic materials are composed of small magnetic regions called domains and within each of such domains the magnetization is saturated because the moments are arranged parallel to each other. But the directions of magnetization of different domains are not parallel. Domains also form in antiferromagnetic and ferrimagnetic specimens. The increase in the gross magnetic moments of such specimens takes place by two independent processes.

- In weak applied fields the volume of favorably oriented domains increases at the expense of unfavorably oriented domains
- In strong applied fields the domain magnetization rotates towards the direction of the field.

A Bloch wall is the transition layer that separates adjacent domains magnetized in different directions. The change in spin directions between domains does not occur in one discontinuous jump but takes place in a gradual way over many atomic planes. The exchange energy is lower when the change is distributed over many spins. In Bloch walls the axis of rotation is such a way that the axis coincides with the plane formed by the aligned spins.

Another type of domain wall exists in ferromagnetic thin films called Neel wall. In this case the spins rotate in the transition region with an axis of rotation lying perpendicular to the plane formed by the aligned spins [4, 5, 12].

1.2. Ferrites and their magnetic properties

1.2.1 Spinel structure

A discussion on spinel structure and ferrites is necessary since a part of the present research work is on the synthesis of ferrite nanoparticles and studies of their various physical properties including the magnetic behaviour.

Name of the crystal structure spinel was derived from the naturally occurring crystal $MgAl_2O_4$ which is commonly known as spinel. More than 140 oxides and 80 sulphides have been

Chapter 1

identified as having this structure. Such a great abundance of crystals with spinel structure indicates the relatively high stability of this structure. Most of the compounds identified to have spinel structure are not naturally occurring, but synthesized in the laboratory. Some of the technologically important natural spinels are gahnite ($ZnAl_2O_4$), magnetite (Fe_3O_4) and spinel ($MgAl_2O_4$) itself [13].

Bragg and Nishikawa separately determined the spinel structure in the year 1915 [13]. The basic structure is formed by a cubic close packed (fcc) array of oxygen atoms. In an fcc crystal structure two kinds of voids or interstitial spaces are available, which are the sites a cation can occupy. One kind of sites has a tetrahedral co-ordination of oxygen atoms and are called the A sites. Other kind of voids has an octahedral co-ordination of oxygen atoms and called the B sites. One eighth of the A sites and one half of the B sites are occupied by cations in a normal spinel structure. The formula unit is represented as AB_2O_4 where A and B are cations occupying A and B sites. The unit cell contains 8 formula units AB_2O_4 , with eight occupied A sites, 16 occupied B sites and 32 oxygen atoms. The space group is $Fd\bar{3}m$. Oxygen atoms have a four fold co-ordination formed by three cations in the B site and one cation in the A site [13].

A spinel unit cell can be diagrammatically represented by taking an A site as the origin, and by dividing the unit cell into 8 cubes of edge $a/2$ to show the arrangement of A and B atoms as shown in figure 1.5

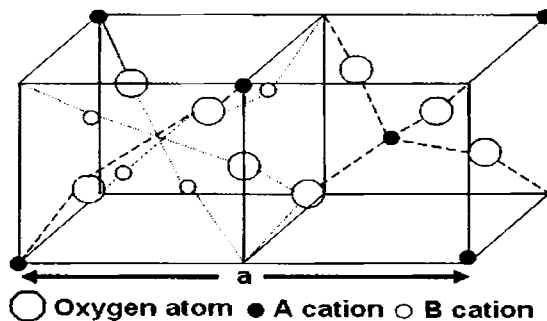


Fig 1.5: Spinel structure

The unit cell can be divided into octants; two octants are shown here.

1.2.2 Normal and inverse spinels

In the spinel ZnFe_2O_4 , Zn cations occupy the A sites and Fe cations the B sites. This cation distribution can be indicated by the formula



where the parenthesis indicates the tetrahedral site occupancy and the square brackets the octahedral site occupancy. This kind of distribution is considered the normal one and the spinels with this distribution are called normal spinels. If D denotes the divalent cations and T the trivalent cations, then another distribution in the form



is possible, and is called an inverse spinel. But in many cases instead of a complete inversion as indicated above, an intermediate cation distribution is observed which can be represented as



where δ is the degree of inversion. Degree of inversion has a value of zero for the normal spinel and one for the completely inverse spinel. The degree of inversion depends on the nature of the sample as well as the preparation techniques. There are reports that inversion can be forcefully imparted in samples which otherwise have a normal spinel structure by mechanical milling and heat quenching. Inversion can influence the physical properties of the spinels and the understanding the degree of inversion of a spinel is extremely important in the study of spinel structured compounds [6, 13].

1.2.3 Magnetic properties of ferrites

Ferrites are mixed oxides of metals of which one is iron. They are not naturally occurring materials. A major portion of all the known ferrites are spinels. Spinel ferrites exhibit antiferromagnetism, i.e. the spins of neighboring atoms are oppositely aligned in the crystal. This causes a cancellation of magnetic moments normally, but can give rise to a net magnetic moment if the magnetic moments of the neighboring atoms are not equal. Antiferromagnetism with unequal magnetic moments is otherwise known as ferrimagnetism as stated earlier.

Superexchange interactions mediated through oxygen atoms exist between metal cations in spinel ferrites. These interactions are negative according to Neel's theory i.e. the spin moment

Chapter 1

are aligned antiparallel to each other by the interactions. Three sets of interactions namely A-A, B-B and A-B are possible in which only A-B interaction is predominant and other two interactions are too weak to overcome thermal energy and to produce antiferromagnetic ordering except at very low temperatures. As a result of A-B interaction the magnetic moments of A sites are held antiparallel to those on B sites and the spontaneous magnetization of the domain is therefore due to the difference in moments at A and B sites. Ferrites are interesting materials in the point of view of magnetic interactions. As already described in article 1.9 the magnetic interaction in ferrite material is explained on the basis of superexchange mediated through oxygen atoms. The only possible exchange interaction in ferrites is the superexchange, since the cation-cation distance is too large to produce any wave function overlapping. There are two kinds of co-ordination existing in spinel ferrites for the cations. They are either in A sites or in B sites. Mediated through the oxygen atoms, three kinds of superexchange interactions are possible in a ferrite. They can be labeled as A-O-A, A-O-B and B-O-B depending on the types of cations participating in the process. Among these interactions, the strongest is the A-O-B interaction followed by B-O-B and A-O-A respectively. Let us label the corresponding superexchange integral as J_{AB} , J_{BB} and J_{AA} [3, 6, 13].

Bulk zinc ferrite has a normal spinel structure. Zn^{2+} is paramagnetic and has a strong preference to tetrahedral (A) sites. The only magnetic interaction present in bulk zinc ferrite is the weak B-O-B superexchange interaction, since the A sites are occupied by Zn^{2+} ions and this interaction is not effective to produce any net magnetic moment at ordinary temperature and zinc ferrite has a Neel temperature 10K [3, 6].

But there are many findings about the magnetic properties of zinc ferrite when the crystallites are synthesized in reduced sizes [14-27]. This size reduction can be achieved by a number of means. Choosing the appropriate synthesis method is one way to reduce the size. In addition to this, a commonly adopted size reduction technique is using mechanical means such as high energy ball-milling.

The size reduction in any magnetic material, especially ferrites, can lead to some novel properties which are different from the bulk. The ferrites can exhibit superparamagnetism due to the fine size of the crystallites. There can be spin canting due to the high surface to volume ratio [28]. Inversion in normal ferrites makes some of the Zn^{2+} ions to migrate to the octahedral sites.

So an equal number of Fe^{3+} ions will be transferred to the tetrahedral sites and it opens up a possibility of superexchange interaction A-O-B between the two sublattices.

There are other reasons suggested by some researchers for the high magnetization of the zinc ferrite with reduced particle size. One reason is the clustering of Fe^{3+} ions and the formation of ferromagnetic ordering. There can be competing ferromagnetic and ferrimagnetic ordering due to Fe^{3+} clustering. Also ball-milling process can break the superexchange bonds due to the oxygen vacancies it creates.

It is also suggested that the existence of non-collinear surface spins can be a reason for room temperature magnetic ordering in zinc ferrites. Non-collinearity is a result of particle size reduction and the resulting high surface to volume ratio. Due to this high surface to volume ratio the spins of the surface cannot be ordered parallel to each other as expected inside of a bulk crystal. The antiferromagnetic ordering between the moments of the Fe^{3+} ions are expected to cancel the net magnetic moment, but on the surface they are not aligned parallel to each other perfectly and produce a net magnetic moment.

Metastable zinc ferrite which exhibited high magnetization even at room temperature was first reported by Pavljukhin in 1984 [51]. In this study mechanical milling was employed for the size reduction. It also suggested that only the surface region of the fine particles formed by milling shows magnetic ordering. Chinnasamy et al showed that zinc ferrite particles exhibiting high magnetic moment even at 300K can be prepared by high energy ball milling [52]. Several reports show that zinc ferrite prepared by co-precipitation method in ultrafine sizes exhibit high magnetism even at room temperature without any mechanical treatment. The occupation of Zn^{2+} ions in octahedral sites is well established by Jayadevan B et al through the method of extended X-ray absorption fine structure [29]. High magnetic ordering of zinc ferrite is also reported in thin films formed by radio frequency sputtering [30]. These reports suggest that the origin of magnetism is the inversion in structure created by high temperature and rapid cooling. These films do not attain magnetic saturation even at a high magnetic field of 5 T. They also suggested glassy behavior of these films on the basis of the ac susceptibility studies.

Cadmium atom is very similar to zinc atom. Both these atoms have an empty d shell with no unpaired electrons and no net magnetic moment. Their ionic sizes are almost the same. Both of these atoms form spinel structured ferrites. (But it may be noted that cadmium aluminate is not

spinel, even though zinc aluminate is). The spinel crystals they form as ferrites have a normal structure, with all cadmium or zinc atoms in tetrahedral sites. Because of these similarities we can expect cadmium ferrite too is paramagnetic at room temperature and it can only show ferrimagnetic properties at a very low temperature. Cadmium ferrite also has a Neel temperature close to 10K [6]. Cadmium ferrite is expected to show similar magnetic properties to zinc ferrite when subjected to high energy ball-milling.

1.3 Magnetic metal nanoparticles

1.3.1 Nickel nanoparticles

Particles of ferromagnetic metals like Fe, Co and Ni attract a lot of interest not only because they offer deviations in physical properties from their bulk counterparts, but also they are used in many technological applications. The changes in physical properties include thermal, optical, electrical and magnetic properties [31].

The synthesis and studies of nickel nanoparticles has been an active field of research for the past many decades. One of the reasons for the increased interest in nickel nanoparticles is that they are chemically stable compared to iron and cobalt particles. Composite materials with nickel as one of the phase also attract very active research interest due to their varied potential technological applications [32-33]. Over the years, numerous methods had been developed and reported for the synthesis of nickel nanoparticles.

1.3.2 Synthesis of nickel nanoparticles

Sodium borohydride and hydrazine hydrate are the common reducing agents used for the preparation of the nickel particles in precipitation methods. In this method a suitable salt of nickel is dissolved in an organic solution like ethylene glycol and the control of pH is usually achieved by adding NaOH solution or liquid ammonia. Size control can be achieved by adding a surfactant like poly vinyl pyrrolidone and nickel particles as small as 10 nm have been synthesized. Size control of the precipitated particles can also be achieved by allowing the chemical reaction to take place in a micro-emulsion of oil in water [34-39].

Polyol method is also commonly used for the synthesis of nickel nanoparticles in which ethylene glycol acts as a solvent as well as reducing agent. Again, particles of size smaller than 10 nm are synthesized in this method also. Reflexion of the solution for long time, typically four to six hours, is required to complete the reaction [40].

There are many reports for the preparation of nickel nanoparticles in spray pyrolysis method. A fine spray of nickel nitrate salt is sent to a reducing atmosphere like gaseous hydrogen or nitrogen, or a combination of both. This method is useful if a large quantity of nickel particles is required. A continuous production of nickel particles is possible in this method. A similar technique is employed in the gas-phase reduction synthesis of nickel nanoparticles from nickel chloride. Some of the important methods in gas-phase reduction are laser assisted gas-phase photonucleation and hydrogen plasma metal reduction [41-43].

Recently a combustion method has been reported for the synthesis of nickel nanoparticles. Here nickel nanoparticles are synthesized from nickel nitrate salt by the method of microwave assisted combustion, using urea as the combustion agent. This is different from other methods since the nickel particles are not formed as a precipitate [44].

In our experimental studies it has been found that a sol-gel combustion method can produce nickel nanoparticles from nickel nitrate. Ethylene glycol can be used as the combustion agent. This new method, developed completely in house, can give reasonably large quantities of nickel nanoparticles compared to the precipitation methods. The controlling parameters like pH of the solution, temperature of the reaction, initial concentration etc are optimized, to synthesize pure nickel particles of the size of 25 to 40 nm in size. The particles have good shelf life, and not easily oxidized when exposed to atmospheric oxygen. Also we have suggested a possible chemical reaction explaining the formation of nickel particles in this method. Details of the preparation methods and characterization are described in detail in chapter 4.

1.4 Composite materials

1.4.1 Importance of composite materials

As technology progresses, natural materials become insufficient for the demanding properties of materials for newer and newer technological applications. The increasing demand of

Chapter 1

new materials with specific physical properties can only be met by the synthesis of composite materials. Composite materials are made of two or more naturally available materials [45]. They usually contain two different phases in them. One of these phases is a continuous medium in general and is called as the matrix. The second phase is in the form of particles or fibers dispersed in the matrix and generally called as the fillers. Ceramic materials, polymers and metals are the commonly used matrix materials and a wide range of materials are used as fillers depending on the kind of properties the composite is expected to achieve. The purpose of making a composite is to enhance the property of the matrix material, without losing its characteristic functionalities [45]. For example, carbon black is incorporated in natural rubber to increase the electrical conductivity of rubber [46]. The characteristic properties of rubber, such as its flexibility and mouldability, which give it the advantage of the ease of production into various shapes and sizes, are not affected by filling rubber matrix with carbon black. So rubber carbon black composite is useful for a number of technological applications, in which rubber or carbon black taken separately is not useful. Another example is the incorporation of fibers in resins like epoxies and polyesters. Compared to most metals, the mechanical properties of resins are not very high and due to this resins are not suitable for applications where high mechanical strength is required. But at the same time resins can be easily moulded into complex shapes. A fiber resin composite can give the resins the kind of mechanical strength suitable for applications, keeping its mouldability intact.

1.4.2 Nanocomposites

A composite material with at least one of the constituent components is in nanometric size is a nanocomposite. It is a well known fact that the properties of materials show a marked deviation when they are in the nano regime in comparison to the properties of the bulk samples. Generally materials with a grain size less than 100 nm are termed as nanomaterials. Nanocomposites are made by incorporating nanoparticles in matrices like polymers, ceramics or metals. Better dispersion of fillers in a matrix material can be achieved by using nanoparticles [47]. Such a better dispersion can produce composite material with uniform physical properties even in scale of sub micron dimensions. Such material can offer better bonding between the matrix and fillers. These composites open up the possibility of synthesizing multifunctional

materials with unique properties that cannot be achieved with traditional materials and methods of preparation. There are numerous examples for nanocomposites in natural biological systems. One good example is the bone of animals [45]. They are composites made of ceramic materials like calcium carbonates, with organic binders in a strictly nano scale dimension. It is the nanoscale bonding that gives the bone its special strength and elastic properties. Scientists and engineers world over are trying to mimic the biological nanocomposites, to tailor-make composites with specific properties for specialized applications.

1.4.3 Magnetic nanocomposites as microwave absorbers

The interest in electromagnetic absorbers in the microwave region has increased in recent times due to the significant expansion in applications using electromagnetic waves in this frequency band. There are numerous electronic gadgets operating in the microwave frequencies like mobile phones, wireless local area networks, radar systems etc and the problem of electromagnetic interference has worsened significantly, necessitating the use of microwave absorbers [48, 49]. A good absorber has to have low or negligible reflection, sufficiently large attenuation and good heat dissipation characteristics because the absorbed energy is converted to heat within the material. In stealth technology, which is another important field of application of microwave absorption, total absorption of electromagnetic waves without any reflection is essential since the device should go undetected by radar signals.

The complex dielectric permittivity and magnetic permeability of a material together defines its electromagnetic wave absorbing characteristics and hence the importance of magnetic dielectric materials. Various kinds of magnetic dielectric materials have been developed over the years to find application as microwave absorbers such as ferrites, ferrite-polymer composites and composites containing metallic magnetic particulates [50]. In comparison to ferrites, metallic magnetic composites have several advantages like high saturation magnetization, tunability of magnetic permeability by controlling the volume fraction of metallic particles, mechanical flexibility of the host material of the composite etc. One major disadvantage of metallic magnetic composite is the drop in magnetic permeability at higher applied frequencies due to skin effect and eddy current loss developed in the particulates. However, this drawback can be overcome by

using particles of size smaller than the skin-depth of the metal with respect to the frequency of operation [50].

1.5 Present work

1.5.1 Motivation and objectives of the present work

Zinc ferrite and cadmium ferrite belongs to the class of normal spinels where the Zn and Cd cations have an exclusive tetrahedral site preference. However in the nanoregime zinc ferrite and cadmium ferrite is known to exhibit ferrimagnetism and many hypothesis and theories exist. It is believed that cation redistribution is responsible for the net magnetism exhibited by these ferrites where some of the Zn/Cd cation prefers to occupy the octahedral sites instead of the tetrahedral sites thus pushing the same number of Fe cations to the tetrahedral sites. However some others believe that surface magnetism is responsible for the net magnetization exhibited by the ferrites. Thus an investigation on the finite size effects on the magnetic properties of normal spinel is an interesting proposition not only from a theoretical point of view but also from an applied perspective. The surface magnetism can lead to metastable states and this can find practical applications. Zinc ferrite and cadmium ferrite can be synthesized phase pure and the size can be reduced by high energy ball-milling. This gives scope for investigating the size effects on the magnetic and electric properties. Various analytical tools like XRD, TEM, VSM and SQUID etc can aid in the understanding their magnetic and structural variations. So zinc and cadmium ferrites will be synthesized in the nanoregime by sol-gel combustion synthesis method and they will be subjected to high energy ball-milling for size reduction.

Metallic nanoparticles like nickel are difficult to be synthesized and it was thought that a simple process for the synthesis of Ni particles could be developed and the incorporation of such particles in rubber matrix could lead to nanocomposites that would eventually help in synthesizing magnetic nanocomposites for microwave applications. The precise tuning of the particle size of metal nanoparticles is essential since the size of the metal fillers decide the Snoek's limit. This enables tuning of microwave characteristics of these materials for microwave absorption. Preparation of nanocomposites necessitates that they be

prepared according to a specific recipe. This would be carried out by trial and error and other optimization experiments. Finally these materials are to be tested for their performance characteristics and modeled. The complex dielectric permittivity and magnetic permeability of these composites are to be determined in the microwave frequency regime to investigate the usability of them in the frequency band as absorbers.

Thus the objectives of the present work can be summarized and are listed as follows.

1. Preparation and characterization of zinc and cadmium ferrite nanoparticles
2. Evaluation of structural, morphological and magnetic properties on size reduction by high energy ball-milling
3. Synthesis of magnetic nickel nanoparticles
4. Structural, morphological and magnetic studies on nickel nanoparticles
5. Synthesis of rubber-nickel nanocomposites
6. Structural and morphological evaluation
7. Evaluation of dielectric and magnetic properties in rf, S and X band frequencies

References:

1. Chin-Wen Chen, Magnetism and Metallurgy of Soft Magnetic Materials: North Holland Publishing Company (1997), Amsterdam
2. C. Radhakrishnamurty, Magnetism and Basalts, Geological Society of India (1993), Bangalore
3. Stephen Blundell, Magnetism in Condensed Matter, Oxford University Press (2001) Oxford
4. B. D. Cullity, Introduction to Magnetic Materials, Addison Wesley Publishing Company (1972), London
5. Soshin Chikazumi, Physics of Magnetism, John Wiley and Sons, Inc (1964), New York
6. R. Valenzuela, Magnetic Ceramics, Cambridge University Press, (1994) London
7. K. H. Fischer, J. Hertz, Spin Glasses, Cambridge University Press (1993)
8. Debashish Chowdhary, Spin Glasses and Other Frustrated Systems, World Scientific (1986), London
9. J. Frenkel, J. Dorfman: Nature, 126 (1930) 274
10. C. P. Bean, J. D. Livingston, J. Appl. Phys, Supplement to 30 (4) (1959) 120S-129S
11. C. Kittel, Phys. Rev. 70 (1946) , 965
12. D. Hadfield, Permanent Magnets and Magnetism, John Wiley and Sons (1962), London
13. V. R. K. Murthy, B. Viswanathan, Ferrite Materials, Science and Technology, Narosa Publishing House (1962), New Delhi
14. H. H. Hamdeh, J. C. Ho, S. A. Oliver, R. J. Wiley, G. Oliveri, G. Busca: J. Appl. Phys 81 (4) (1997) 1851
15. Z. H. Zhou, J. M. Xue , Chan H. S. O., J. Appl. Phy, 90 (2001) 4169
16. M. Tada et al. J. Appl. Phys. 93 (2003) 7566
17. A. Kundu, S. Anand, H.C. Verma, Powder. Technol. 132 (2003) 131
18. J. S. Jiang et al. Nano. Stru. Mater. 12 (1999) 143

19. F. S. Li, L. Wang, J. B. Wang, Q. G. Zhou, X. Z. Zhou, H. P. Kunkel, G. Williams, *J. Magn. Magn. Mater.* 268 (2004) 332
20. L. D. Tung, V. Kolesnichenko, G. Caruntu, D. Caruntu, Y. Remond, V. O. Golub, C. J. O'Connor, L. Spinu, *Physica B*, 319 (2002),116
21. A.Kundu ,C. Upadhyay H. C. Verma H C *Phys. Lett. A* 311 (2003) 410
22. S.D. Shenoy, P. A.Joy, M. R. Anantharaman, *J. Magn. Magn. Mater* 269 (2004) 217
23. H. Ehrhardt, S.J. Capbell, M. Hofmann, *J. Alloys Compounds* 339 (2002) 255
24. P. M. G. Nambissan, C. Upadhay, H.C.Verma, *J. Appl. Phys.* 93 (2003) 6320
25. H. H. Hamdeh, J. C. Ho, S. A. Oliver, R. J. Wiley, J. Kramer, Y. Y. Chen, S. H. Lin, Y. D. Yao, M. Daturi, G. Busca: *IEEE Trans. Magnetics*, 31 (6) (1995) 3808 (15orig)
26. W. Schiessl, W. Potzel, H. Karzel, M. Steiner, G. M. Kalvius: *Phy. Rev. B* 53 (14) 1996 9143
27. F. K. Lotgering,: *J. Phys. Chem. Solids*, 27 (19996) 139 9 (17 orig)
28. S. A. Oliver, H. H. Hamdeh, J. C. Ho: *Phys. Rev. B* 60 (5) (1999) 3400
29. B. Jayadevan, K. Tohiji, K. Nakatsuka: *J. Appl. Phys.* 76 6325
30. S. Nakashima, K. Fujita, K. Tanaka, K. Hirao, T. Yamamoto, I. Tanaka: *Phys. Rev. B*, 75 (2007) 174443
31. Harisingh Nalwa, *Nanostructured materials and nanotechnology*, Academic Press London
32. K. Akamatsu, K. Nakashahi, S. Ikeda, H. Nawafune: *Eur. Phys. J. D.* 24 (2003) 377
33. M. Lieberthal, W. D. Kaplan: *Mater. Sci. Engg. A* 302 (2001), 83
34. W. Xu, K. Y. Liew, H. Liu, T. Huang, C. Sun, Y. Zhao: *Mater. Lett.* 62(17-18) (2008) 2571-73 Microwave assisted synthesis of nickel nanoparticles
35. M. L. Singla, A. Negi, V. Mahajan, K. C. Singh, D. V. S. Jain: *Applied Catalysis A*, 323 (2007) 51-57
36. E. A. Abcdel-Aal, S. M. Malekzadeh, M. M. Rashad, A. A. El-Midany, H. El-Shall: *Powder Technology*, 171 (1) (2007) 63-68

Chapter 1

37. D.E. Zhang, X.M. Ni, H.G. Zheng, Y. Li, X.J. Zhang, Z.P. Yang: *Materials Letters*, 59, (16) (2005), 2011-2014
38. J. W. Park, E. H. Chae, S. H. Kim, J. H. Lee, J. W. Kim, S. M. Yoon, J. Y. Choi: *Mater. Chem. Phys.* 97 (2006) 371
39. Z. Li, C. Han, J. Shen: *J. Mater. Sci.* 41 (2006) 3473
40. S. Ayyappan, G.N. Subbanna, R. S. Gopalan, C.N.R. Rao, *Solid State Ionics* 84 (1996) 271
41. W. Wang, Y. Itoh, I. W. Lenggaoro, K. Okuyama, *Mater. Sci.Engg. B* 111 (2004) 69
42. H.T. Zang, G. Wu, X.H. Chen, X.G. Qiu *Materials research bulletin* 41 (2006) 495
43. Y. Duan, J. Li: *Mater. Chem. Phys.* 87 (2004) 452
44. R. K. Sahu, A. K. Ray, A. J. Kailath, L. C. Pathak: *J. Mater. Res.* 21 (7) (2006) 1664
45. P. M. Ajayan, L. S. Schadler, P. V. Braun: *Nanocomposite Science and Technology*, Wiley-VCH (2003), New York.
46. R. Bandhopadhyaya, W. Rong, S. K. Friedlander: *Chem. Mater.* 16 (2004) 3147
47. X. Wang, J. E. Hall, S. Warren, J. Krom, J. M. Magistrelli, M. Rackaitis, G. G. A. Bohm: *Macromolecules* 40 (2004) 499
48. B. Zhang, Y. Feng, J. Xiong, Y. Yang, H. Lu: *IEEE Trans. Magnetics*, 42 (7) (2006) 1778
49. A. N. Yusoff, M. H. Abdullah, S. H. Ahmed, S. F. Jusoh, A. A. Mansorand, S. A. A. Hamid: *J. Appl. Phys.* 92 (2002) 215
50. L. Bao-Wen, S. Yang, Y. Zhen-Xing, N. Ce-Wen, *Appl. Phys. Lett.*, 89 (2006) 132504
51. V. Sepelak, K. Tkacova, *Acta Montanistica Slovaca*, 3 (1997), 266
52. C. N. Chinnasamy, A. Narayanasamy, N. Ponpandian, K. Chattopadyah, H. H Gu'erault, J. M. Greneche, *J. Phys. Condens. Mater.* 12 (2000) 7795

Chapter 2

Experimental techniques

2.1 Introduction

Synthesis of phase pure compounds forms part of any research in the regime of materials science. The emergence of novel preparation techniques namely sol-gel synthesis need special mention in this context since they can be effectively employed to tune the particle size which are also essential for research in nanoscience. These methods of preparation come in handy as far as preparation of nanoparticles is concerned. After preparation of these samples proper characterization is necessary, which require several analytical techniques. Any investigation in material science is then about preparation, optimization of the conditions and characterization at appropriate stages. This chapter gives an overview of the various methods employed for the preparation of precursory materials and their characterization. The fabrication of an ac susceptometer in-house also is described in this chapter along with standardization experiments and inter-laboratory correlation data.

2.2 Sol-Gel Synthesis

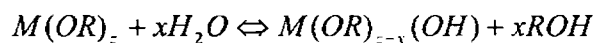
Sol-gel process is emerging as an important method of preparation for the synthesis of metal oxide nanoparticles in which a solution of metal salts in an organic solvent (sol) is allowed to undergo a gelation process to form a highly porous gel and metal oxides are formed from this. Highly porous metal hydroxides are formed in the initial stage of sol-gel process using metal salts and organic alcohols like ethylene glycol or xylene. Chemical reaction in the first stage of the process leads to the formation of a network of metal hydroxides and gelation takes place when all the hydroxide species are linked in a single network like structure. This gel is a thick and porous solid structure surrounding the interconnecting pores and is a polymer of hydroxides, formed in three dimensions. By heating the solvent can be removed completely and highly porous and

Chapter 2

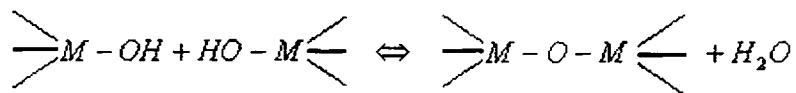
ultrafine metal hydroxide powder will be obtained. Metal oxides are formed from this ultrafine metal hydroxide powder by heat treatment [1].

In certain cases heating the gel under ambient conditions at a temperature of around 100°C can result in the combustion of the gel assisted by the organic material remaining in the gel. Metal oxide powder then formed is of nanometer size. Such a process is generally called a sol-gel combustion process. A variety of organic combustion agents can be used for the automatic combustion of the gel. Urea, citric acid, ethylene glycol, diethylene glycol etc are the commonly used combustion agents. But normally, metal oxides are synthesized by calcinating the gel in temperature controlled furnaces for specified time durations at temperatures ranging from 300°C to 1000°C depending on the nature of metal oxide to be formed.

The chemical reactions at the various stages of the sol-gel process can be generalized as follows. The metal alkoxides formed after dissolving the metal salt in the organic solvent undergoes hydrolysis in the first stage of the reaction. This is depicted as follows



And condensation occurs when the hydroxide molecules bind together as they release water molecules and a gel network of the hydroxide is formed and is shown below.



The rate of hydrolysis and condensation are important parameters that affect the properties of the final product. Slower and more controlled hydrolysis leads to smaller particles possessing unique properties.

As a result of the metal-oxygen bonds in the corresponding alkoxides precursor, sol-gel process has been found useful for preparing only metal oxides and the gel formed during the process of synthesis is essentially metal hydroxides. But studies have revealed that particles other than oxides can be synthesized in some cases. Spherical SiC particles have been synthesized employing a sol-gel process in an inert atmosphere of argon gas [1].

There are many reports on the synthesis of mixed oxides like ferrites and aluminates using sol-gel method [2-5]. In our studies, sol-gel method is utilized for the synthesis of zinc ferrite and cadmium ferrite nanoparticles. Monodispersed nanoparticles of zinc ferrite and cadmium

ferrite were prepared using sol-gel method. Sol-gel technique has a number of advantages over other techniques for synthesizing metal oxide ceramics. The possibility of the production of ultrafine porous powder is the main advantage. Since the precursor metal salts are dissolved in an organic liquid medium, homogeneity of very high degree is ensured. Also sol-gel process opens up the possibility of industrially large scale production of oxides on a commercial basis.

2.3 Dielectric permittivity and ac conductivity studies

2.3.1 Basic principles

The evaluation of dielectric parameters namely dielectric permittivity and dielectric loss provide insight into the polarization process that takes place in materials. Dielectric behavior of a material is arising from the dielectric polarization when the material is under the influence of an external electric field. When an electric field is applied across the sample, there is a shift of charges and electric dipoles are formed inside the material. This shift of charges inside the material causes a net charge to accumulate on the electrodes introducing a capacitance in the system.

When the applied electric field is removed the net dielectric dipole moment formed in the material is supposed to vanish immediately. But this will not happen in reality. Depending on the material there is a delay in coming back to the zero dipole moment state. This delay is due to the various frictional or dissipative forces present in the material. These damping forces cause a power loss and this is termed as the dielectric loss. When a sinusoidally changing electric field is applied across the sample the resulting polarization in the material is lagged by a fixed phase angle due to the dielectric loss. This gives rise to two components of polarization inside the material, one is in phase and the other is 90° out of phase. These two components can be considered the real and imaginary components of the polarization when represented in a complex plane. Accordingly there are two components for the dielectric permittivity of the material when a sinusoidally varying electric field is applied [6].

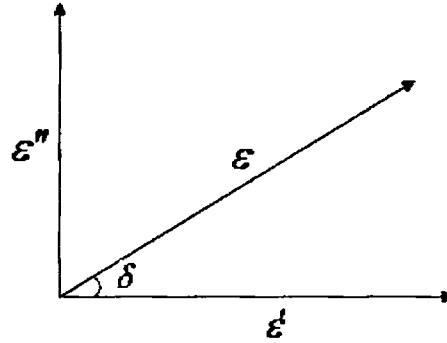


Figure 2.1: Representation of complex permittivity

$$\varepsilon' = \varepsilon \cos \delta \quad (2.1)$$

$$\varepsilon'' = \varepsilon \sin \delta \quad (2.2)$$

$$\tan \delta = \frac{\varepsilon''}{\varepsilon'} \quad (2.3)$$

here $\tan \delta$ is the tangent of the loss angle and called as the loss tangent of the material. The loss tangent is dependant on the frequency of the applied electrical field. The total dielectric permittivity can be treated as a complex quantity, i.e.

$$\varepsilon = \varepsilon' - j\varepsilon'' \quad (2.4)$$

$$\varepsilon_r = \frac{\varepsilon}{\varepsilon_0} = \frac{\varepsilon' - j\varepsilon''}{\varepsilon_0} \quad (2.5)$$

Where, ε_r is the relative permittivity of the material, ε is the total permittivity, ε' is the real part of the complex permittivity and ε'' is the imaginary part of the complex permittivity of the material. Here ε_0 is the permittivity of free space [6].

The dielectric measurements, which are described in chapters to follow, were carried out using an LCR meter model HP 4285A and a home-made dielectric cell [7]. Capacitance and dielectric loss are measured for frequencies of applied electric field varying from 100 kHz to 8 MHz. Samples were placed inside the dielectric cell in the form of pellets of diameter 12 mm and thickness in the range of 1.8 to 2.2 mm. temperature of the sample was made to vary using an electric heater attached to the dielectric cell and an automatic temperature controller. Temperature

variation in the range of 300K to 393K is possible with the home-made setup. Ac conductivity (σ_{ac}) of the samples were determined from the dielectric loss using the relation

$$\sigma_{ac} = 2.\pi.f.D.\epsilon_0.\epsilon_r \quad (2.6)$$

where D is the loss tangent of the material

The entire measurement set-up was automated using a commercial data acquisition package called labVIEW. Automation programs were developed in house using the package and desktop computer running on Windows 2000 operating system. Data points were acquired at intervals of 100 kHz of frequency and 20 K intervals of temperature. Measurements of dielectric permittivity and ac conductivity were carried out from a frequency range of 100 kHz to 8 MHz.

2.3.2 Design of the dielectric cell

The dielectric cell used for the dielectric and a c conductivity studies are fabricated in-house [7]. The schematic design of the cell employed for dielectric measurements is given in figure 2.2. The cell is made up of mild steel with a cylindrical stem having provisions for fixing various attachments such as electrical connections and vacuum gauges. The cell is connected to a rotary pump to maintain a pressure of 10^{-2} Torr inside the chamber. The inner diameter of the cell is about 18cm, and has a length of 30cm. The sample holder is fixed at the bottom of a one-end closed metallic tube to be embedded to the top flange. For the electrical conductivity and dielectric measurements the thin film sample is spring loaded to a sample holder and inserted into the conductivity cell. For bulk samples pellets are mounted on the sample holder consisting of two copper disc electrodes in between which the palletized samples are loaded. The sample holder can be heated using a temperature-controlled heater. The details of the dielectric/conductivity cells are depicted in figure 2.2.

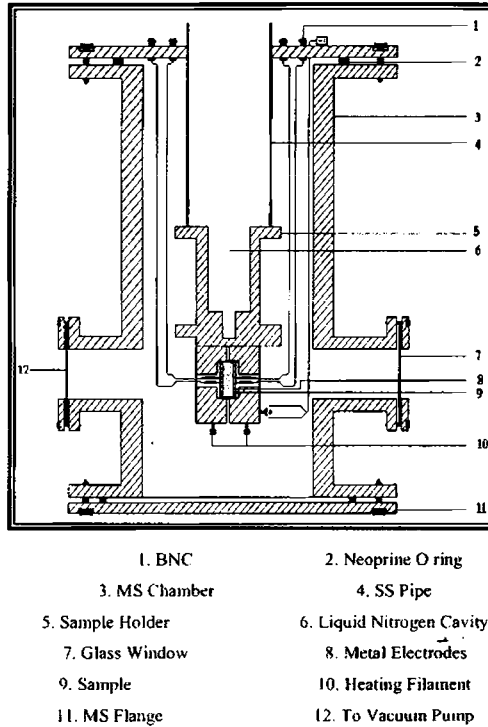


Figure 2.2: Cell for the dielectric and conductivity measurements.

2.4 Fabrication of ac susceptometer

2.4.1 a.c.susceptometry

The measurement of ac magnetic susceptibility is a convenient tool in the characterization of many magnetic and superconducting samples [8-12]. Usually very expensive superconducting quantum devices are required for such studies [13]. But in many measurements, the relative variation of the magnetic moment with temperature assumes more importance than the absolute magnetic moment, because such measurements are sufficient to reveal the presence of various kinds of magnetic transitions exhibited by the sample. Keeping this point in mind, an ac susceptometer was fabricated with the capability of giving accurate results on the relative variations in the magnetic moment of samples with temperature and is useful in the studies of

many perovskite and spinel samples showing ferromagnetic to paramagnetic phase transition as well as superparamagnetic transitions in a temperature range of 120K to 300K [14-16]. The accuracy of the susceptometer in recording the relative a c magnetic susceptibility can be validated with samples whose magnetization graph against temperature is already reported. For example it is well known that the paramagnetic oxide of gadolinium (Gd_2O_3) has a strict linear dependence of its magnetic moment on the temperature in the range 130-300K [17-19]. Pure samples of gadolinium oxide were used to standardize the susceptometer, in terms of the relative changes in magnetization.

2.4.2 Fabrication of a. c. susceptometer

The setup is basically a three coil system consists of a single primary coil and two secondary coils. The primary coil is wound over the outer cavity of the of the double walled brass cylinder, and has a total of 8000 turns wound over a length of 12 cm with tapings at 3000 and 5000 turns, wound using 24 swg copper wire. It can produce a field of 1000 gauss when a current of 1A flows through the primary coil. When a potential difference of 5 volts is applied across the coil of 1000 turns it can produce nearly 100 gauss at the centre of the inner cavity. Two secondary windings are placed inside the inner brass cavity, wound in opposite directions, which consists of 1200 turns each, wound with 32 swg wire. Total length of the secondary windings is 8 cm, each coil having a length of 4 cm each. The two coils are perfectly balanced, producing an emf very close to zero when an ac voltage is applied on the primary. A few turns from one of the secondary coil is unwound carefully to make the two coils balancing. The sample is placed inside the secondary coil and the introduction of the sample produces imbalance of inductance in the secondary coil system, and this in turn produces a net induced emf. This induced emf is proportional to the magnetization of the sample placed inside the secondary coil.

The outer cavity of the double walled cylinder has a diameter of 75 mm and a length of 60 cm. The inner cavity has a diameter of 50mm. The secondary windings are done on a nylon spool with a diameter of 14 mm inner and 12 mm outer diameter. Samples in the form of pellets of diameter 12 mm can be placed inside the secondary coil. The secondary coils are attached on a polymer rod connected on the outer lid of the double walled cylinder. The outer lid closes both the cavities without gas leakage with the help of O-rings. A copper rod of diameter 50mm is

Chapter 2

riveted with the inner cavity and the external end of the copper rod is made in the form of an open cavity for the purpose of introducing liquid nitrogen for cooling the inner cavity.

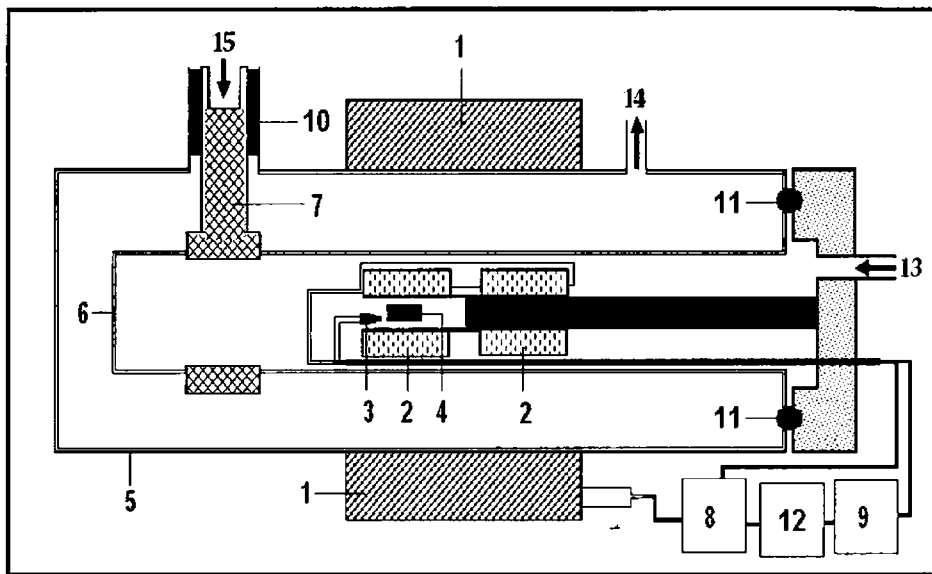


Figure 2.3: Schematic of the ac susceptometer

1. Primary coil 2. Secondary coil. 3. Temperature sensor. 4. Sample 5. Outer jacket 6 Inner jacket 7 Copper rod 8 Lock-in amplifier 9 Temperature sensor 10 Polymer insulation 11 O-rings 12 Interfacing computer 13 Inlet of dry nitrogen 14 Outlet to vacuum pump 15 Inlet for liquid nitrogen

Polymer insulation is given in the space between the copper rod and the outer cavity to prevent heat loss. The entire setup is placed horizontally at the time of measurements.

The temperature variation inside the inner cavity is achieved by the method of heat exchange using dry nitrogen gas, filled inside the inner cavity, after evacuation. The lowest temperature that can be attainable in the set up is 120K. This is because of some heat loss due to the imperfections in the insulation near the edge of the copper rod exposed to atmosphere. Temperature is allowed to rise by natural heating and recorded using the Cryocon temperature controller with the help of a platinum resistance temperature sensor which is positioned inside the secondary coil very close to the sample. A heater is attached with the copper rod for the purpose

of controlling the temperature and for the heating of the sample above room temperature. The space between the inner and outer cavities of the susceptometer is evacuated using a rotary vacuum pump for better cooling and for minimizing the consumption of liquid nitrogen and is maintained in dynamic vacuum during the measurement.

The primary coil is driven using the built in oscillator of the lock-in amplifier (EG&G model 7260) with sinusoidal voltage of amplitude 500 mV and frequency 159 Hz. It is estimated that a sinusoidal magnetic field of amplitude nearly 10 gauss is produced inside the secondary coils. The induced emf is fed back to the lock-in amplifier. Both the amplitude and phase of the incoming signal is measured and recorded at different temperatures. The amplitude of the induced emf is proportional to the susceptibility of the magnetic sample placed inside the secondary coil.

2.4.3 Automation

The set up was fully automated using the commercial data acquisition software package called LabVIEW. The interfacing was done by IEEE488 GPIB supplied by National Instruments. A program in the language G is written for LabVIEW and this program allows the measurement of emf and phase from the lock-in amplifier at any specified intervals of temperature from 0.05K to 10K. The measured readings are automatically updated in a data file. The flow chart of the program is shown in figure 2.4 The program has an interactive user interface in which the user can set the starting temperature, the stopping temperature and the increment of the temperature between each set of readings in the measurement. The program then acquires the temperature reading from the temperature controller and checks whether the stopping temperature has been achieved. If the temperature is above or equal the stopping temperature the program stops the data acquisition, and otherwise it checks if the temperature is equal to the temperature at which a reading is to be recorded. Again if yes, the out put of the lock-in amplifier is acquired by the program and reading is recorded. The program then increment the temperature by the required amount and the process is repeated. The program runs until the maximum temperature is attained, where the program is terminated. The acquired data is written in a file in ASCII format and can be called by any program for the purpose of analysis. A separate program is used if the temperature is decreasing (cooling), where the increment is to be subtracted to get the new temperature at which the recording of lock-in output is to be done. The measurements are

Chapter 2

recorded while the temperature of the sample is increasing. The sample is first cooled to the required temperature and allowed to gain temperature by natural exchange of heat with the surroundings.

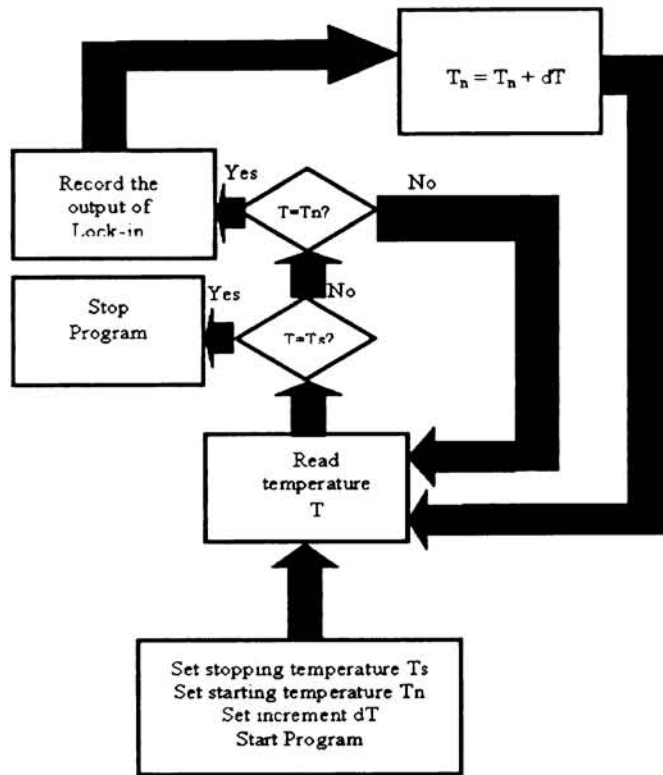


Figure 2.4: The flow chart of data acquisition

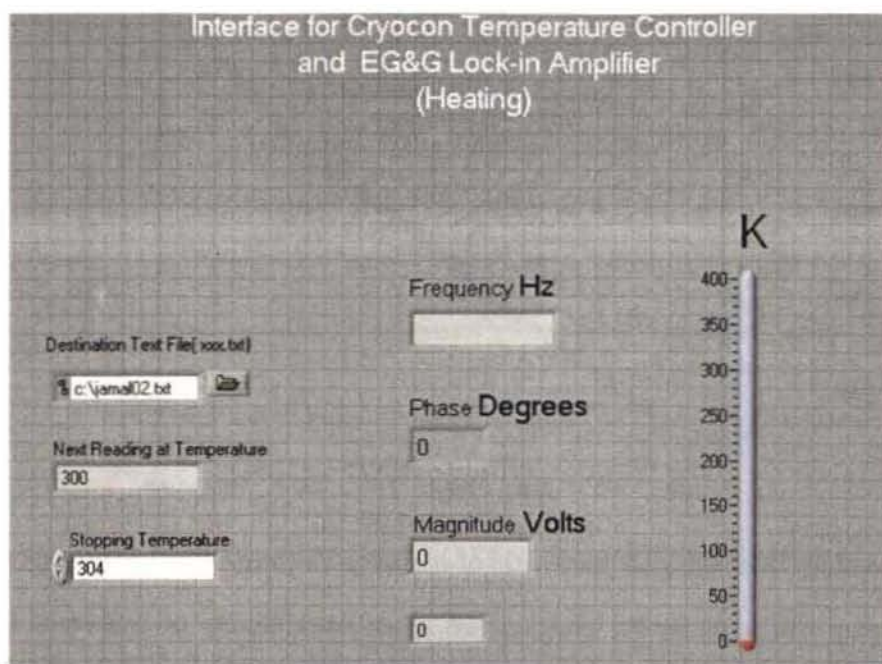


Figure 2.5: The user interface of the data acquisition program

2.4.4 Standardization and validation

Standardization of the instrument is done using paramagnetic oxide of gadolinium, which has a linear variation of magnetization in the range of 200K to 300K. A known mass of the sample was placed inside the secondary coil, and the induced voltages were measured at intervals of 1 K. A graph was plotted between the reciprocal of the induced emf and the temperature. This graph gives the variation of $\frac{1}{\chi}$ with temperature in arbitrary units. The experiment for standardization was repeated for various masses of gadolinium oxide. A base line graph was plotted keeping both the secondary coils free of any sample and this was used for the base line correction. Moreover the instrument is never used to determine the absolute magnetization of samples, but used only to study the relative variations in magnetization with temperature, especially to determine the temperature of transition from paramagnetic phase to ferromagnetic phase in magnetoresistive samples as mentioned earlier.

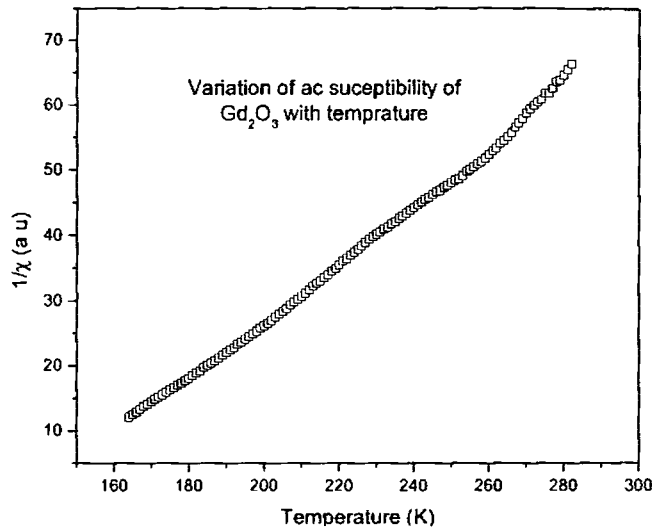


Figure 2.6: Variation of the reciprocal of ac susceptibility of Gd₂O₃ with temperature

The setup was used for the measurement of ac susceptibility of lanthanum calcium manganate (LCMO) nanoparticles as a first verification of its proper working. Lanthanum calcium manganates have a known magnetic transition at a near room temperature and the reported temperatures of such transitions are within the operational temperature range of the home fabricated susceptometer.

2.4.5 Studies on LCMO samples

The LCMO samples were synthesized and provided by Dr Mrs. Asha Mary John, one of the co-researchers in the same research group. Figure 2.7 shows the X-diffraction patterns of the LCMO samples sintered at different temperatures after the initial calcination. The newly fabricated ac susceptometer is used to study the ac susceptibility of the LCMO samples sintered at various temperatures. From previous reports on the magnetic properties of LCMO is well known that this compound has a paramagnetic to ferromagnetic transition at about 260K. In order to study this transition the temperature range is selected from 180K to 300K. The new set up can be easily used for the studies in this temperature range.

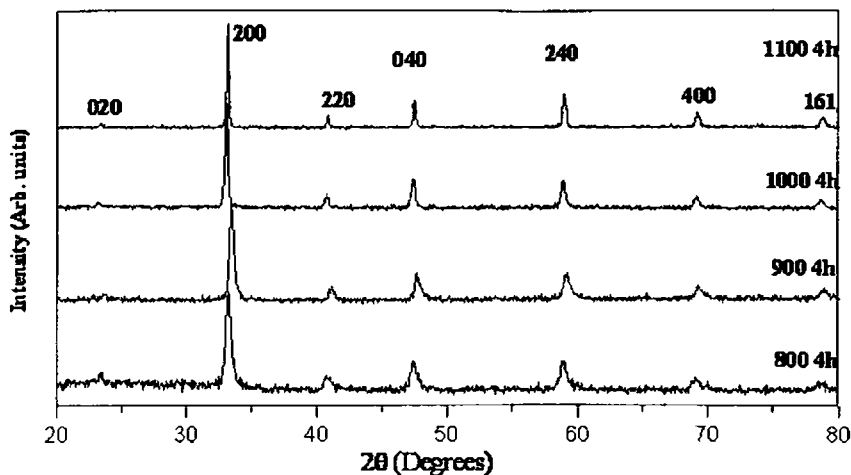


Figure 2.7: XRD of LCMO sintered LCMO samples

. The LCMO sample in the form of thin pellets of size is placed inside one of the secondary coils exactly in the middle. The inner chamber of the susceptometer is first evacuated and then filled with dry nitrogen gas. This is required for preventing condensation of water inside the chamber at low temperature. The oscillator output of the Lock-in amplifier is connected to the primary coil to the 2000 turns winding and the signals from the secondary coil is fed to the Lock-in amplifier. The leads from the temperature sensor are connected to the temperature controller. The lock-in amplifier and the temperature controller are connected to the desktop computer via GPIB cables as mentioned before. Liquid nitrogen is introduced in the copper chamber of the susceptometer setup until the temperature reaches the required value of 180K. The data acquisition program has been started at this point of time. The increment of temperature is set at 1K. The setup is kept without electrical disturbances until the data acquisition is completed. The data is then called to a graph plotting program and data analysis is carried out.

The results of the ac susceptibility studies are summed up in the diagram 2.8. All the graphs are plotted against normalized induced voltage against temperature since the actual magnitude of the susceptibility is not having much importance in this study. Instead the variation of susceptibility against temperature, indicating the magnetic transition is important. A well defined transition from ferromagnetic phase to paramagnetic phase is indicated by a fall in the ac

Chapter 2

susceptibility. This kind of a transition is observed in all the samples as indicated in figure 2.8. The actual transition point is calculated by plotting the reciprocal of susceptibility against temperature and by giving a linear fit to the linear portion indicating a rise in $\frac{1}{\chi}$ as shown in figure 2.9. The intercept of the linear fit on the X axis is the transition temperature. Figure 2.9 gives a typical example for the calculation of the transition temperature. All other transition temperatures are calculated in the same method and the result is tabulated in table 3.1

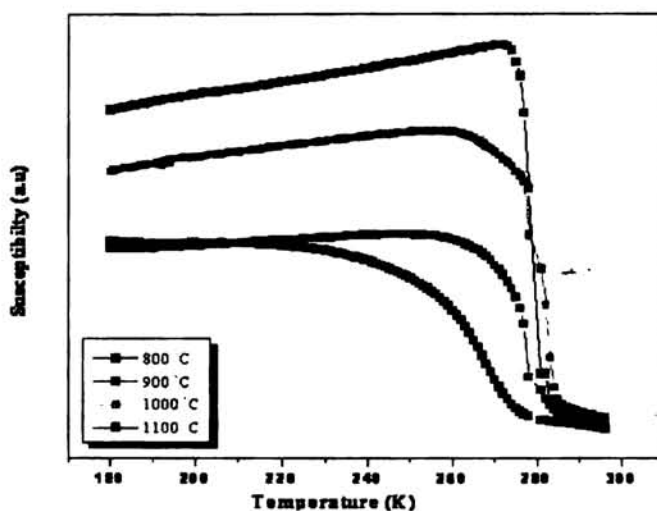


Figure 2.8: Variation of ac susceptibility with temperature of LCMO samples sintered at various temperatures

It can be observed that the transitions are becoming sharper. The sample sintered at 800°C is showing a broad transition whereas the sample sintered at 1100°C is showing a sharp transition. All LCMO samples, after attaining the paramagnetic phase, show a constant magnetic susceptibility on further increase in temperature. The shift in transition temperature is significant between the 800°C and 900°C sintered samples. But after this the transition temperature remains almost a constant

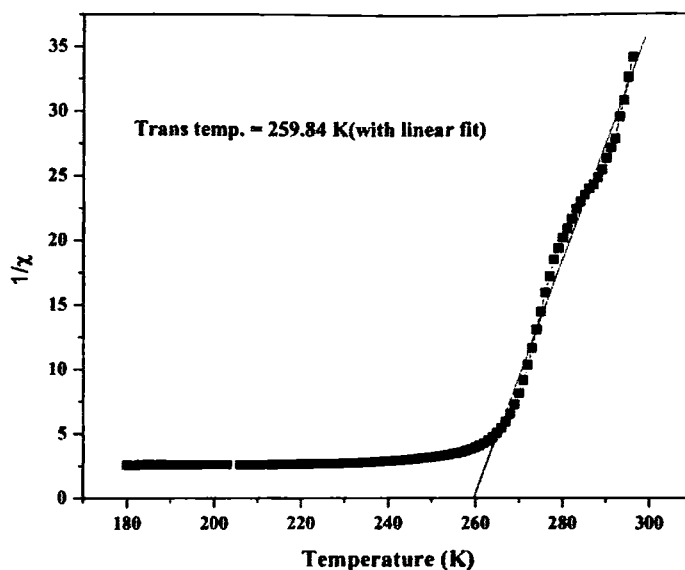


Figure 2.9: Finding the transition temperature by giving linear fit to $\frac{1}{x}$ vs. T graph

| Trial No | Sintering temperature ($^{\circ}\text{C}$) | Transition temperature (K) |
|----------|--|----------------------------|
| 1 | 800 | 259.8 |
| 2 | 900 | 274.1 |
| 3 | 1000 | 278.8 |
| 4 | 1100 | 275.3 |

Table 2.1: Transition temperatures of LCMO samples sintered at various temperatures

2.5 High energy ball-milling

High energy ball-milling (HEBM) was developed in 1970s as an industrial process to synthesize new alloys and phase mixtures. This is a powder metallurgical process which allows the preparation of alloys and composites which cannot be synthesized by conventional techniques. This top-down technique is widely employed in research of nanomaterials mainly to achieve reduced grain sizes of particles. Ball-milling devices (BMDs)

Chapter 2

come in a variety of designs like tumbler mills, attrition mills, shaker mills, vibratory mills, planetary mills etc [20].

2.5.1 Planetary ball-mill

In the present work a planetary type ball-milling device by Fritsch model Pulverisette 7 (figure 2. 10) was used for the HEBM studies on zinc ferrite and cadmium ferrite samples. In a planetary type BMD there are two grinding bowls, with heavy and hard grinding balls inside, fixed on diametrically opposite points of a rotating circular platform and capable of rotating about their own axis. The platform and the bowls rotate in opposite directions. The motion resembles the planetary motion of a planet. The grinding balls inside the bowls are constantly acted by centrifugal force, and due the two simultaneous rotatory motions the direction to which the centrifugal force is acting changes abruptly at regular intervals (figure 2.11). This produces two kinds of motion on the grinding balls. The grinding balls running along the walls of the bowl, and the balls striking the diametrically opposite side of the wall. The first kind of motion produces frictional effect and second kind of motion causes high impact between the balls and the material inside the bowl. The impact energy is many times greater compared to conventional grinding devices resulting excellent grinding performance in a shorter time. After the bowls are charged with the powder, they are sealed with O rings to minimize atmospheric contamination. Wet milling is usually done by introducing an organic fluid in the bowl, in order to prevent wear of the bowls and the sides of the bowls.



Figure 2.10: Planetary ball-milling unit

2.5.2 Milling parameters

The following parameters of a BMD determines the size reduction that can be achieved by milling [21]

- Type of mill
- Milling atmosphere
- Milling media
- Intensity of milling
- Ball to powder weight ratio (BPR)
- Milling time
- Milling temperature

The reduction in grain size is accomplished by the kinetic energy transfer from balls to powder. Since the kinetic energy of the balls depend on their mass and velocity, materials with high density are preferred for the as the balls. Tungsten carbide or steel are the commonly employed material for making grinding balls. In the present study vials with a thick internal coating of tungsten carbide and tungsten carbide balls were used for milling.

Chapter 2

The high density balls (14750 kg/m^3) are suitable for grinding ceramics like zinc and cadmium ferrites.

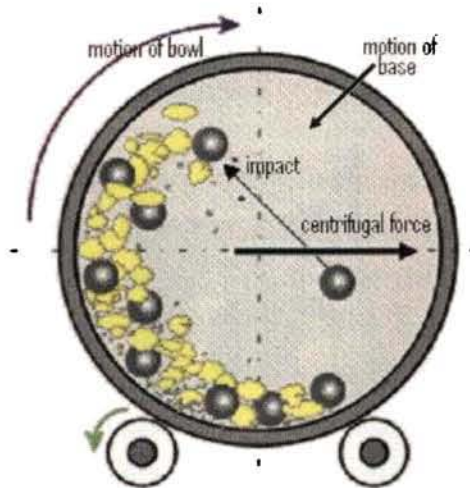


Figure 2.11: Schematic of the ball-movement

In any milling experiment the grain size reduction is rather rapid in the initial stages and slows down after reaching a maximum size reduction. The mechanism of grain size reduction is understood as the result of formation of an array of dislocations produced by atomic level strains caused by kinetic energy transfer. Initially this process extends the entire sample, but after a particular level of size reduction very high stress levels are required to continue the process. In addition to this, temperature developed inside the bowls is a prohibitive factor for size reduction beyond a limit. The impact speed is a decisive factor which determines the kinetic energy transfer. The ball-bowl contact time is given by the relation

$$t = (1 + 1.2e) \sqrt{\frac{\pi m}{30YR}} \quad (2.7)$$

where Y is the yield strength of the bowl, R is the ball radius, e is the coefficient of restitution of the bowl's inner walls and m is the mass of the ball [16].

The details of the HEBM experiments conducted on zinc ferrite and cadmium ferrite samples are described in detail in the chapter 3

2.6 Vibrating sample magnetometry

2.6.1 Basic principles

Magnetic characterization of the composite samples has been carried out using vibration sample magnetometer model EG & G Par 4500. In a VSM, the sample is placed on a vibrating stylus, and introduced into a coil placed between the pole pieces of an electromagnet which produces a strong and uniform magnetic field. A sinusoidal emf is induced in the coil due to the simple harmonic motion of the magnetic sample inside the coil and the amplitude of this ac electrical signal is proportional to the magnetization level of the sample mounted on the end of the stylus [22, 23]

A schematic diagram of VSM is shown in figure 2.12 and in figure 2.13 a simplified block diagram is given.

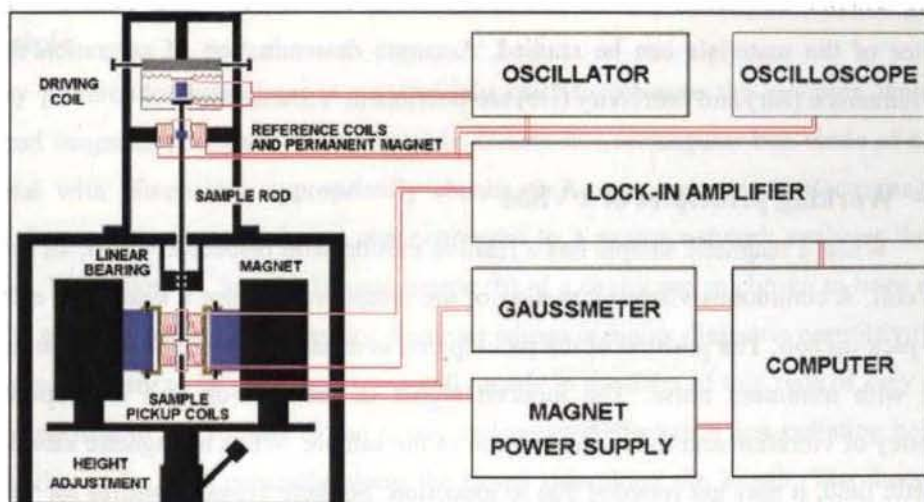


figure 2.12: Schematic diagram of a Vibration Sample Magnetometer

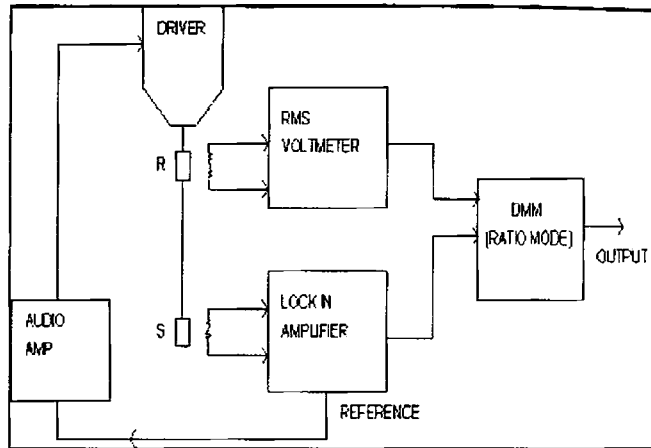


Figure 2.13: Block diagram of a Vibration Sample Magnetometer

VSM is an excellent tool for the characterization of magnetic samples. Magnetization at varying external magnetizing fields can be accurately determined using VSM and the hysteresis behavior of the materials can be studied. Accurate determination of saturation magnetization (M_s), remnance (M_r) and coercivity (H_c) are possible in VSM studies.

2.6.2 Working principles of a VSM

When a magnetic sample has a relative motion with respect to a coil, an emf is induced in the coil. A continuous vibratory motion of the sample can induce a sinusoidal electrical signal in the pick-up coil. The position of the pick-up coil is usually adjusted to have maximum induced signal with minimum noise. The induced signal in the pick-up coil is proportional to the frequency of vibration and the magnetization of the sample. When a magnetic sample moves in a magnetic field, it may get retarded due to induction. So there are possibilities for variation in the frequency of vibration of the sample inside the pick-up coil. In order to maintain a perfect simple harmonic motion with accurate frequency, a servo technique is usually used to maintain the vibration of the sample holder. This servo mechanism continuously tracks the movement of the sample holder and accurately controls the vibration of the sample.

This servo technique uses a vibrating capacitor located beneath the transducer to generate an ac control signal that varies solely with the vibration amplitude and frequency. The signal, which is at the vibration frequency, is fed back to the oscillator where it is compared with the

drive signal so as to maintain constant drive output. It is also phase adjusted and routed to the signal demodulator where it functions as the reference drive signal. The signal developed in the pick up coils is then buffered, amplified and applied to the demodulator. There it is synchronously demodulated with respect to the reference signal derived from the moving capacitor assembly. The resulting dc output is an analog signal, which depends only on the magnitude of the magnetic moment, and not influenced by the amplitude and frequency drift. The cryogenic setup attached to the sample assembly can be used to study the magnetization of samples at low temperatures. The resulting dc output is an analog of the moment magnitude alone, uninfluenced by vibration amplitude changes and frequency drifts. A cryogenic setup attached to the sample permits the low temperature studies.

2.7 Cavity perturbation technique

2.7.1 Principle

Cavity perturbation technique is very widely used to measure the complex dielectric permittivity and magnetic permeability of materials. Cavity is a rectangular box made of a non-magnetic metal with dimensions appropriately chosen to have resonance of electromagnetic waves in the frequency range of interest and connected to a vector network analyzer through coaxial cables. The length (l), breadth (a) and height (b) of a cavity are so chosen to have a pre-determined TE mode to sustain in the cavity. Samples whose complex dielectric permittivity and magnetic permeability are to be measured are usually made in the form of thin rods of very small volume in comparison to the volume of the cavity and inserted through a non-radiating hole (or slot) made on the cavity wall generally along the broad side along the length. The theory for analyzing such measurements was first developed by Bethe and Schwinger [24]. The method has many advantages like it is easy to perform the experiment and it is a non-destructive and contactless. But the volume of the sample must be very small so as to produce a negligible effect on the field configuration in the cavity. The cavity perturbation technique is based on the change in the resonant frequency and quality factor of the cavity due to the insertion of a sample into it at the position of electric field maximum or magnetic field maximum, depending upon the nature of the parameter to be studied. In figure 2.14 a schematic representation of the cavity is shown.

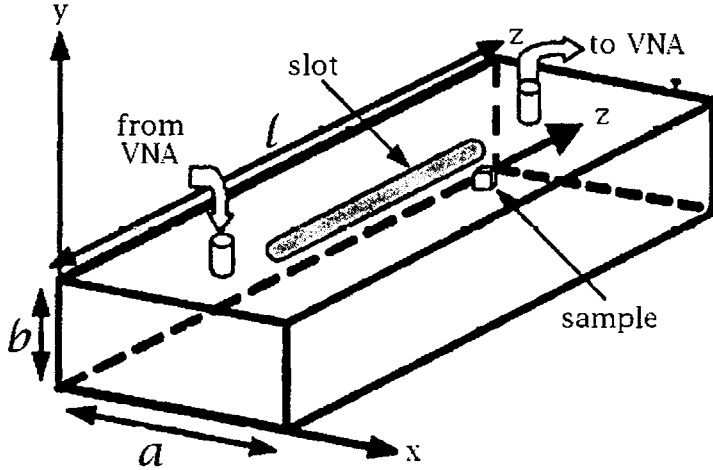


Figure 2.14: Schematic representation of a cavity resonator

2.7.2. Working principles

For a rectangular cavity, real part of the dielectric permittivity can be calculated from the relation [24, 25]

$$\frac{\Delta f}{f_s} = 2 \frac{V_s}{V_c} (\epsilon'_r - 1) \quad (2.8)$$

where Δf is the shift in resonance frequency on introduction of the sample into the cavity and V_s and V_c are the volume of the sample and cavity respectively.

The imaginary part of the dielectric permittivity is given as

$$\left[\frac{1}{2Q_s} - \frac{1}{2Q_c} \right] = 2 \frac{V_s}{V_c} \epsilon''_r \quad (2.9)$$

Q_s and Q_c are the quality factors of the cavity with and without sample, given by

$$Q_s = \frac{f_s}{\Delta f}, \quad Q_c = \frac{f_c}{\Delta f} \quad (2.10)$$

Magnetic permeability was measured by perturbing the cavity by the samples at positions where the electric field is zero. X band measurements were possible only for even modes since this cavity was provided with a hole at the centre of the cavity. The real and imaginary parts of the complex permeability of composite samples were determined using the relations

$$\mu_r' - 1 = \frac{(\lambda_g^2 + 4a^2)}{8a^2} \left(\frac{\Delta f}{f_s} \right) \frac{V_c}{V_s} \quad (2.11)$$

$$\mu_r'' = \frac{(\lambda_g^2 + 4a^2)}{16a^2} \left(\frac{1}{Q_s} - \frac{1}{Q_c} \right) \frac{V_c}{V_s} \quad (2.12) \text{ and}$$

$$\lambda_g = \frac{2l}{p} \quad (2.13) \text{ where } p \text{ is the}$$

number of mode in which the cavity is excited for a particular measurement.

In this study the complex dielectric and magnetic parameters of rubber-nickel nanocomposites were evaluated using the cavity perturbation technique. Further details are given in chapter 8 for the continuity of the discussion where the experimental results are presented.

2.8 SQUID Magnetometer

2.8.1 Basic ideas

Superconducting Quantum Interference Devices (SQUID) are very sensitive magnetometers capable of measuring extremely small magnetic fields typically of the order of 10^{-17} T [26]. They are based on superconducting loops containing Josephson junctions. Their noise levels in a SQUID are extremely low. A Josephson junction is made up of two superconductors, separated by an insulating layer so thin that electrons can pass through it. A SQUID consists of tiny loops of superconductors employing Josephson junctions to achieve superposition: each electron moves simultaneously in both directions. Because the current is moving in two opposite directions, the electrons have the ability to perform as qubits (that theoretically could be used to enable quantum computing). SQUIDs have been used for a variety of testing purposes that demand extreme sensitivity, including engineering, medical, and geological equipment. Because they measure changes in a magnetic field with such sensitivity, they do not have to come in contact with a system that they are testing. The direct current superconducting

2.8.2 Design of SQUID

SQUID consists of two Josephson junctions connected in parallel. When the SQUID is biased with a current greater than the critical current, the voltage across the SQUID is modulated with the flux threading the SQUID at a period of one flux quantum, $\Phi_0 \equiv h/2e$. Therefore, the SQUID is a flux-to-voltage transducer. This special flux-to-voltage characteristic has enabled researchers to use the device to detect small magnetic field, current, voltage, inductance and magnetic susceptibility. SQUIDs are the most sensitive devices in detecting the magnetic flux. Low-Tc SQUID has been used in a wide range of applications, including biomagnetism, susceptometers, nondestructive evaluation, geophysics scanning SQUID microscope, and nuclear magnetic resonance [26]

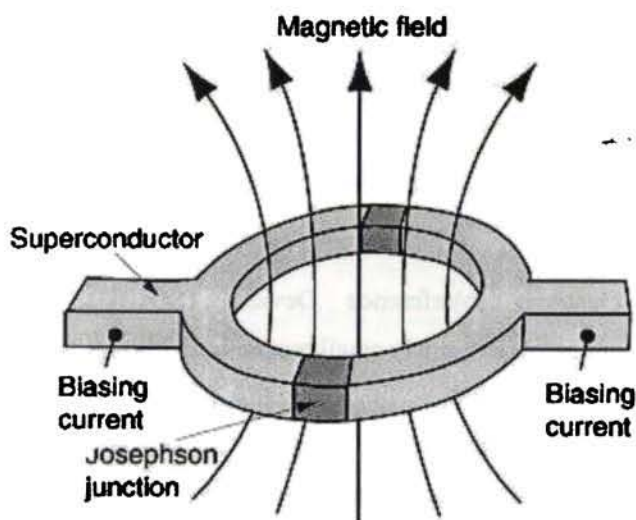


Fig. 2.15: Schematic of a SQUID

2.9 Transmission Electron Microscopy

2.9.1 Basic features

The morphological studies of nanoparticles synthesized in sol-gel method are carried out with the help of transmission electron microscopy. A transmission electron microscope (TEM) is the high frequency counterpart of an optical microscope. Instead of light waves in an optical

microscope, high energy electrons, typically accelerated in a potential of 200 keV is employed in a transmission electron microscope. . Focusing of the electron beams is done by magnetic lenses or condenser lenses. The working of a TEM can be briefly explained with the help of a schematic diagram in fig. 2.16

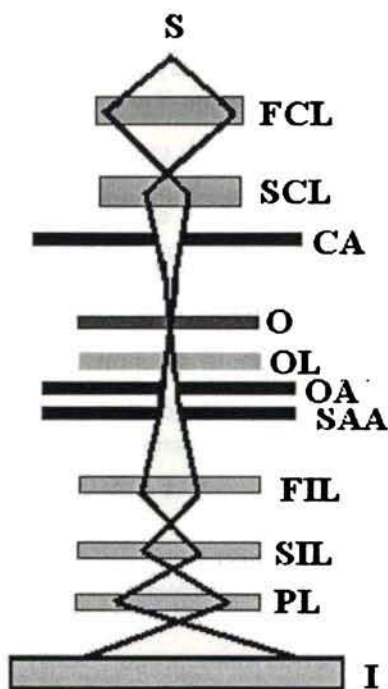


Fig 2.16: Schematic of a TEM

2.9.2 Design of a TEM

The electron gun (S) at the top produces monochromatic beam of electrons and can be compared with the source of light in an optical microscope. The beam of electrons coming out of the electron gun is focused into a collimated beam with the help of two magnetic lenses (or condenser lenses) which are marked as FCL and SCL in the diagram. The advantage of the magnetic lens is that the converging power can be controlled by adjusting the electric current in a magnetic coil. And the specimen can be uniformly illuminated by the electron beam by adjusting the powers of the two lenses FCL and SCL. The specimen whose magnified image is to be recorded is placed in the position immediately after the condenser aperture and the beam of

Chapter 2

electrons transmitted through the specimen is again passed through the objective lens O and two apertures named as the objective aperture (OA) and selected area aperture (SAA). With the help of the first and second intermediate lenses (FIL and SIL) and the projection lens (PL) the magnified image (I) of the specimen is formed on a fluorescent screen or on a photographic plate. The darker areas of the image represent those areas of the sample that fewer electrons were transmitted through (they are thicker or denser). The lighter areas of the image represent those areas of the sample that more electrons were transmitted through (they are thinner or less dense)

A modern day TEM will have many state-of-the-art attachments that provide powerful tools for researchers to study crystal structure, electronic structure, and chemical composition of materials. TEM usually has an energy filter, an x-ray energy dispersive spectrometer, an electron energy-loss spectrometer, and several digital data recording systems. Also a TEM nowadays is equipped with a holography unit, a scanning attachment with chemical mapping resolution better than 1 nm, and cooling and heating in-situ stages that can heat or cool specimens to temperatures ranging from 15K to 1300K.

2.10 Scanning Electron Microscopy

While a TEM allows electrons to get transmitted through the specimen to enable the image formation, a scanning electron microscope (SEM) uses the technique of scanning the specimen with impinging electrons to form an image by the scattered electrons and the emitted electromagnetic radiations [27]. Thermionically emitted electrons from a tungsten or lanthanum hex boride cathode are accelerated through a potential difference of about 100 keV, focused using condenser lenses to a very small spot with the size of 1 to 5 nm and made to fall on the specimen. The energy exchange between the electrons falling on the specimen results in the emission of secondary electrons or electromagnetic radiations which can be detected to produce an image. Secondary electron emissions are detected by a scintillator photomultiplier device to form the image. Steep surfaces in the specimen eject more secondary electrons compared to the flat surfaces and appear brighter in the image. This gives the image a well-defined three dimensional appearance. Using secondary electrons a resolution of 1 nm can be achieved. In addition to the secondary electrons, high energy back-scattered electrons can be used to form the image. Such image formation is important in the detection of areas of different chemical composition from the

difference in the contrast. In certain cases the light emitted by the effect of fluorescence is used to form the image, and by analyzing the wavelengths of the cathodoluminescence is analyzed and images of real color are formed in the detection system.

In our studies compressed pellets of ball-milled nanoparticles of zinc ferrite and cadmium ferrite, synthesized in sol-gel process, are studied using scanning electron microscopy. Very good resolution is obtained in all cases and these studies give a clear cut idea about the particle size of the nanoparticles synthesized and the effect of ball-milling on the particles.

In addition to the experimental techniques described above various other characterization tools were used in the present study like X-ray diffractometry, electron dispersive spectroscopy, ultra-violet visible absorption spectroscopy and so forth. These techniques are well documented and it is felt that detailed descriptions are not required about them.

References:

1. R. Valenzuela: Cambridge University Press (1994)
2. M.R. Barati, S.A.S. Ebrahimi, A. Badii: *J. Non-crystalline Solids* 354 (47-51,)2008 5184-5185
3. A. Pradeep, P. Priyadharsini, G. Chandrasekaran: *Mater. Chem. Phys.* 112 (2) (2008) 572-576
4. B.G. Toksha, S. E. Shirsath, S.M. Patange, K.M. Jadhav: *Solid State Communications* 147(11-12) (2008) 479-483
5. Y. Yuan, C. Liu, Y. Zhang, X. Shan: *Mater. Chem. Phys.* 112(1) (2008) 275-280
6. B. Tareev, *Physics of Dielectrics Materials*, MIR Publishers (1975), Moscow
7. .E. M. Mohammed, M. R. Anantharaman: *J. Instrum. Soc. India* 32 (3) (2002) 165
8. A. Bajpai, A. Banerjee: *Rev. Sci. Instrum.* 68 (11) (1997) 4075
9. S. Miga, A, J. Dec: *Rev. Sci. Instrum.* 78 (2007) 033902
10. S. Ramakrishnan, S. Sundaram, R. S. Pandit, G. Chandra: *J. Phys. E. Sci. Instrum.* 18 (1985)
11. D. X. Chen: *Meas. Sci. Technol.* 15 (2004) 1195
12. P. Vanderbemden: *Cryogenics*, 38 (1998) 839

Chapter 2

13. A. Pasquarelli, C. D. Grattaz, S. D. Penna, S. D. Luzioz, V. Pizzellay, G. L. Romaniz: *Phy. Med. Biol.* 41 (1996) 2533
14. V. Markovich et al: *J. Phys. Condens. Matt.* 19 (2007) 346210
15. P. Dey, T. K. Nath, A. Banerjee: *J. Phys. Condens. Matt.* 19 (2007) 376204
16. S. D. Shenoy, Ph. D. Thesis, Department of Physics, Cochin University of Science and Technology
17. S. L. Bud'ko, P. C. Canfield: *J. Magnetism and Magnetic Mater.* 299 (2006) 281
18. A. Kremenovic, B. Antic, A.S. Nikolic, J. Blanusa, B. Jancar, A. Meden, S. Mentus, *Scripta Materialia*, 57, (12), (2007) 1061
19. Cao Jianli, Liu Li, Wu Xiaofei, Wen Shipeng, Jin Riguang, Zhang Liqun *Journal of Rare Earths*, 24, 1, Supplement 1, (2006), 335
20. H. J. Fetch: Proceedings of the NATO advanced study institute on Nanophase materials synthesis, Properties and applications: Kluwer academic publications (1994) 18 original
21. C. Suryanarayana, G. H. Chen, F. H. S. Froes: *Scripta Metallurgica* 26 (1992) 1727
22. Joseph A. Pesch, *Rev. Sci. Instrum.*, 54, No.4 (1983) 480
23. Simon Foner, *Rev. Sci. Instrum.* 30, No.7 (1959) 548
24. Y. Ye, A. Sklyuyev, C. Akyel, P. Ciureanu, *IEEE Proc. Instrumentation and Measurement Technology Conference, IMTC (2007)* 1-6, DOI: 10.1109/IMTC.2007.379006
25. Mi Lin, Yong Wang; M.N Afsar, *IEEE Proc. 13th International Conference on Terahertz Electronics, Infrared and Millimeter Waves . IRMMW-THz 2005.* 1, 19-23 (2005) 62 - 63 1 DOI: 10.1109/ICIMW.2005.1572407
26. Hong-Chang Yang et al, *Tamkang Journal of Science and Engineering*, 6, No. 1, (2003), 9-18
27. R. F. Egerton, *Physical Principles of Electron Microscopy*, Springer (2005)

Chapter 3

Synthesis and evaluation of dielectric properties of zinc ferrite and cadmium ferrite nanoparticles

Zinc ferrite and cadmium ferrite are technologically important materials employed for a variety of applications [1-3]. In the micron regime they crystallize in the normal spinel structure with Zn/Cd ions occupying the tetrahedral sites exclusively [4]. However when they are prepared in the nano-regime they exhibit altogether different properties and hence they are the subject of investigation for evaluating their properties in the nano regime [5]. The synthesis of nanosized zinc ferrite and cadmium ferrite is thus important and the evaluation of their structural and electric properties assumes significance. This chapter deals with the synthesis of zinc ferrite and cadmium ferrite and their characterization. The ferrite samples were prepared using sol-gel combustion method, the details of which are described in chapter 2 [6].

3.1 Synthesis and structural characterization of zinc ferrite

Zinc nitrate hydrate and ferric nitrate hydrate were taken in stoichiometric proportions and were dissolved in ethylene glycol by adding the solvent slowly and under constant stirring. Sol formed at 70°C was heated at a constant temperature of 120°C until auto-combustion took place and the resulting powder after combustion was analyzed using X-ray diffractometry (using a Rigaku X-ray diffractometer with Cu K-alpha source). The pattern was analyzed by comparing it with the data available in JCPDS files and it was found that there was presence of impurity phases in the form of oxides of zinc indicating that the phase formation of zinc ferrite was not complete. At the same time the peaks corresponding to the spinel $ZnFe_2O_3$ also present in the powder. So it was evident that the formation of solid solution of zinc ferrite was not complete in

Chapter 3

the initial stage of the combustion. It was found that pure zinc ferrite nanoparticles could be prepared by calcination of the powder at a temperature of 700°C for duration of 24 hours.

Figure 3.1 shows the effect of calcination on the phase formation on zinc ferrite particles. The phase formed at 700°C is extremely pure at and the impurity content is minimal as indicated by the X-ray diffraction diffractometry.

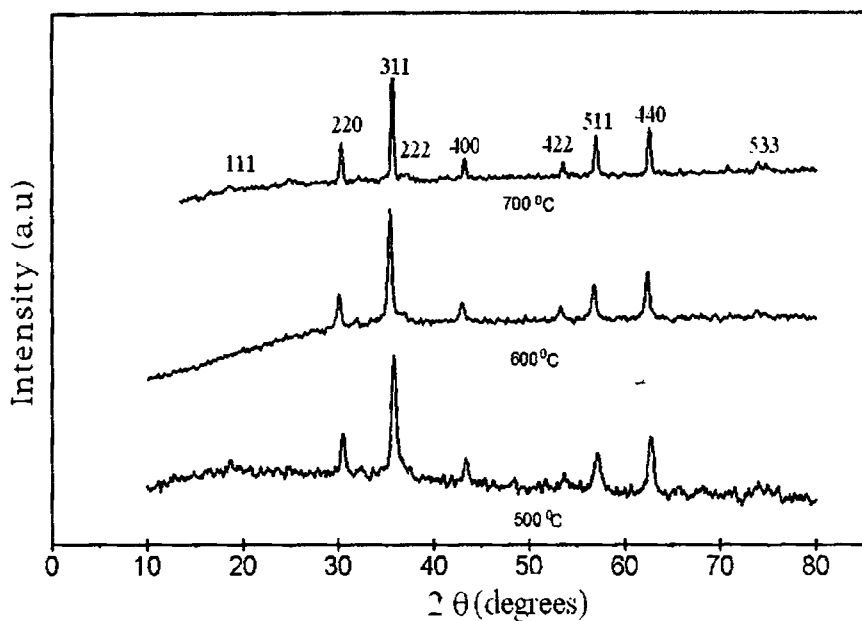


Figure 3.1: Effect of calcination on the phase formation of zinc ferrite particles

3.2 Synthesis and structural characterization of cadmium ferrite

Synthesis of cadmium ferrite was carried out using the same method of sol-gel auto-combustion in a similar fashion as that in the case of zinc ferrite. Here cadmium nitrate and ferric nitrate were employed as precursors for the synthesis of cadmium ferrite. Formation of gel was noted at a temperature of 70 °C followed by combustion at about 120 °C. Samples sintered at 900 °C exhibited phase pure characteristics typically of a normal spinel compound. The powder was calcinated at different temperatures starting from 400 °C to 900 °C in a furnace in an ordinary atmosphere of air. The X-ray diffractogram of samples in the various stages of calcination is shown in figure 3.2. The diffraction peaks corresponding to CdO in the impure samples are

marked in the diagram. Unlike in the case of zinc ferrite, the phase formation in the case of cadmium ferrite was at an elevated temperature of 800-900 °C. The samples for analysis were prepared by calcination at 900 °C for 36 hours. A detailed evaluation of the morphological and magnetic properties of the two ferrite nanoparticles is presented in the ensuing chapter where the effect of high energy ball-milling is described in detail.

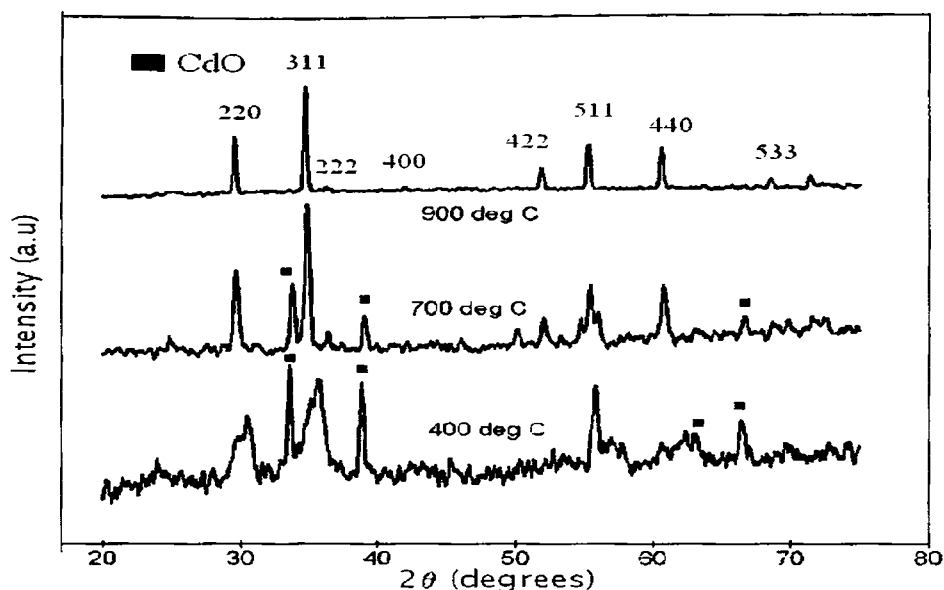


Figure 3.2: Effect of calcination in the phase formation of cadmium ferrite particles

3.3 Dielectric and a.c conductivity studies

Dielectric and ac conductivity studies of zinc and cadmium ferrites were carried out using an HP Impedance analyzer model 4285 A and a home-made dielectric cell under a vacuum of 10^{-3} mbar and at temperatures varying from 30 °C to 120 °C. The fabrication details of the dielectric cell are cited elsewhere [7]. Nanoparticles of zinc and cadmium ferrites were pressed into pellets of size 12 mm in diameter and approximately 2 mm in thickness. These pellets were sintered at a temperature of 700°C for 24 hours to achieve maximum compaction of the particles. In the dielectric cell, a capacitor is created by placing the pellet in between two copper discs of the same diameter and the capacitance was measured using the impedance analyzer in a frequency range of 100 kHz to 8 MHz. The temperature was recorded with a Cryocon temperature controller with

Chapter 3

platinum resistance (PT-100) temperature sensor. The dielectric permittivity of the material was calculated from the measured values of capacitance using the relation

$$\varepsilon' = \frac{C.d}{\varepsilon_0 A} \quad (3.1)$$

and dielectric loss of the material using the equation

$$\varepsilon'' = \varepsilon' \tan \delta \quad (3.2)$$

where, ε' is the dielectric permittivity of the sample (the real part), C is the capacitance of the capacitor formed by inserting the sample between two metal plates, d is the thickness of the sample, ε_0 the permittivity of free space and A is the area of cross section of the sample [8]. The ac conductivity of the sample was determined from the loss tangent by using the relation

$$\sigma_{ac} = 2\pi.f.\varepsilon_0.\varepsilon'.\tan \delta \quad (3.3)$$

where f is the applied frequency [8]

3.4 Dielectric properties of zinc ferrite

The variation in dielectric permittivity (ε') with applied frequency is presented in figure 3.3 as a semi log plot in which log of the frequency is in the x-axis and ε' is in y-axis. It can be observed that there is a steady decrease in ε' with applied frequency. This phenomenon can be understood on the basis of Maxwell-Wagner model of interfacial polarization and Koop's phenomenological theory [9,10]. The zinc aluminate pellets used in this study was made of uniaxially pressed nanoparticles. Every grain of the pellets can be considered having a perfect crystalline characteristic and therefore is expected to exhibit low electrical resistance compared to the grain boundaries. This is exactly the model presented in Koop's theory. Maxwell-Wagner type interfacial polarization exists in the grain boundaries around the grains, because of the accumulation of charges in these high resistance regions. This kind of polarization exists in all poly-crystalline samples which are heterogeneous in nature [11].

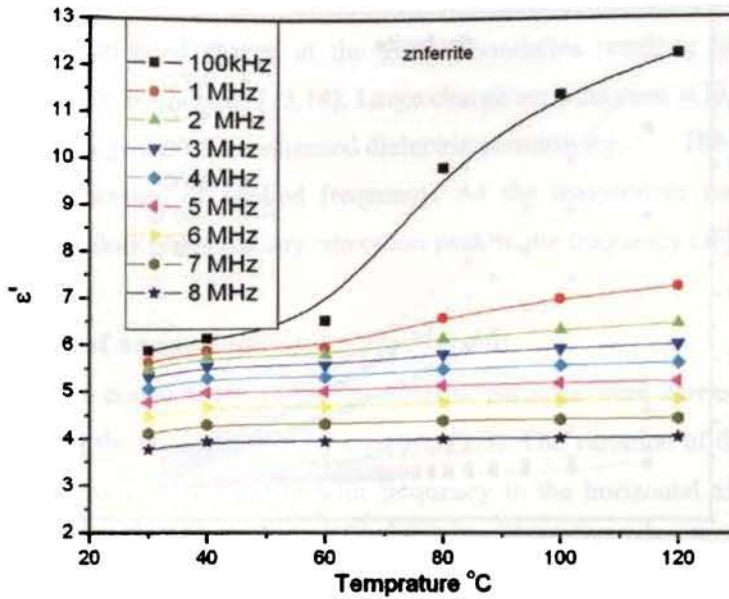


Figure 3.4 Variation of dielectric constant of zinc ferrite with temperature

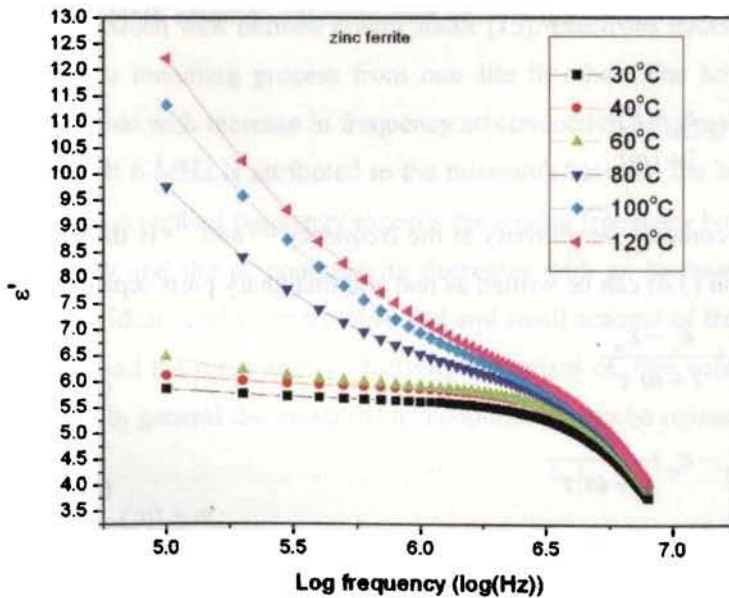


Figure 3.3 Variation of dielectric constant of zinc ferrite with frequency

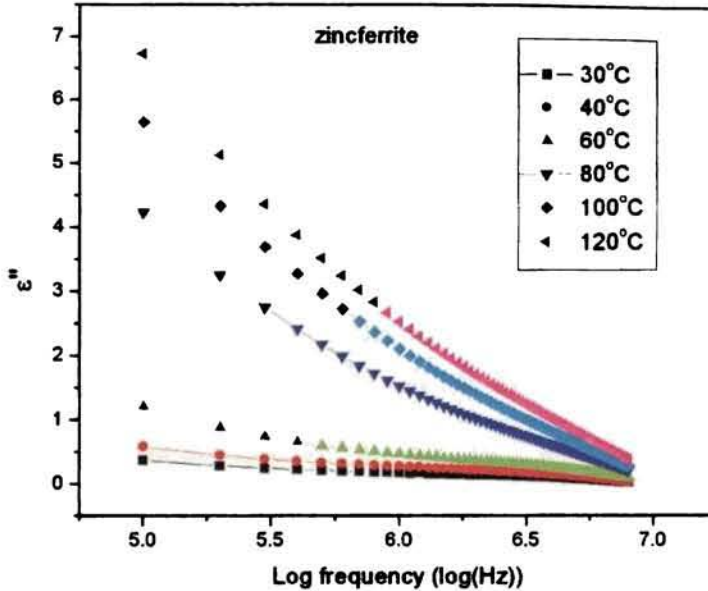


Figure 3.5: Variation of dielectric loss of zinc ferrite with frequency

Applying Debye model of dielectric relaxation the complex dielectric permittivity can be expressed as [12]

$$\epsilon^*(\omega) - \epsilon_\alpha = \frac{\epsilon_s - \epsilon_\alpha}{1 + i\omega\tau} \quad (3.4)$$

where $\epsilon^*(\omega)$ is the complex permittivity at the frequency ω and ϵ_α is the permittivity at optical frequencies. Equation (3.4) can be written as real and imaginary parts separated as

$$\epsilon'(\omega) = \epsilon_\alpha + \frac{\epsilon_s - \epsilon_\alpha}{1 + \omega^2\tau^2} \quad (3.5)$$

and

$$\epsilon''(\omega) = (\epsilon_s - \epsilon_\alpha) \frac{\omega\tau}{1 + \omega^2\tau^2} \quad (3.6)$$

The decrease in dielectric permittivity with increase in applied frequency is in accordance with equation (3.5). The presence of interfacial polarization gives rise to a relaxation process with a high relaxation time compared to electronic or dipolar polarization. This causes a decrease in the dielectric permittivity in the given frequencies. It can be observed from figure 3.4 that there is a steady increase in the permittivity with rise of temperature at all frequencies. With increase in

temperature charge carriers acquire more mobility as a result of thermal activation and this can enhance the accumulation of charge at the grain boundaries resulting in a lower electrical conductivity at the grain boundaries [13,14]. Large charge accumulation at higher temperatures at the interfaces of grains gives rise to enhanced dielectric permittivity. The loss tangent decreases with the increase of applied frequency. As the temperature rises the loss tangent increases steadily and does not show any relaxation peak in the frequency range.

3.5 Evaluation of ac conductivity of zinc ferrite

Studies on ac conductivity of the zinc ferrite particles were carried out from the loss tangent by employing the relation given by equation (3.3). The variation of the ac conductivity is plotted in figure 3.6 as a semi log plot with frequency in the horizontal axis for temperatures beginning from 30°C through 120°C. At all temperatures ac conductivity shows a steady increase with increase of frequency. In a dielectric material we cannot expect any free charge carriers and therefore the contribution of free charge carriers to the dc conductivity can be ruled out. The ac conduction in the material is through a hopping mechanism of bound charges, in which charges hop back and forth between well defined bound states [15]. Electrons undergo hopping between bound states through a tunneling process from one site to other. The hopping mechanism is supported by the fact that with increase in frequency ac conductivity increases [16]. A drop in ac conductivity after about 6 MHz is attributed to the mismatch between the hopping frequency and applied frequency. When applied frequency exceeds the hopping frequency hopping goes out of step with applied frequency and the ac conductivity decreases with an increase in frequency, very often, deviations from ideal conditions are observed and small amount of free charge carriers are present in the system and the measured conductivity comprises of two components, namely the ac and dc conduction. In general the measured ac conductivity can be represented by the relation [17]

$$\sigma_{ac}(\omega)_m = \sigma_{ac}(\omega) + \sigma_{dc} \quad (3.7)$$

where $\sigma_{ac}(\omega)_m$ is the frequency dependant conductivity and $\sigma_{ac}(\omega)$ is the contribution from the ac conductivity and σ_{dc} is the dc conductivity.

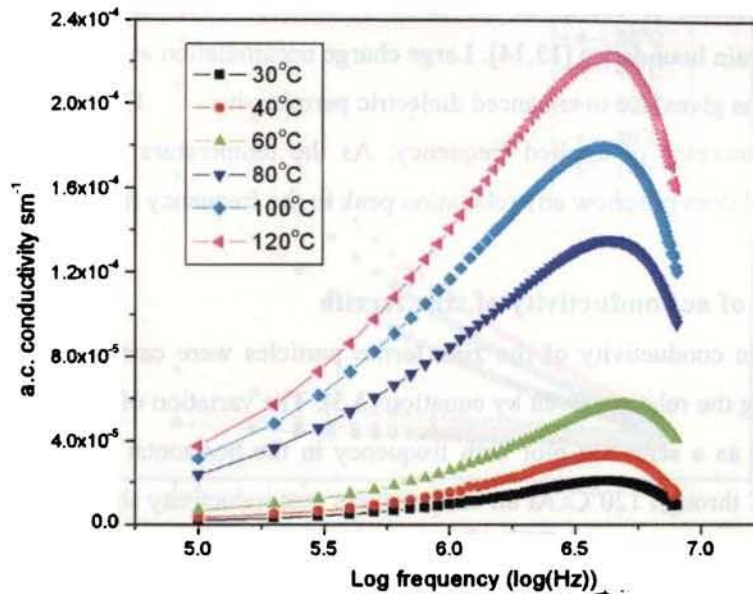


Figure 3.6: Variation in a.c. conductivity of zinc ferrite with frequency

The total conductivity (sum of dc and ac components of conductivity) is dependant on the angular frequency ω of the applied signal. From figure 3.6 it can be observed that the total conductivity is very small at 100 kHz compared to that at higher frequencies. So the static contribution of the dc conductivity to total conductivity is negligible at all temperatures. Further the angular frequency dependence of the ac conductivity can be represented (in the ascending portion of the curve) in the form

$$\sigma_{ac} = \sigma_{dc} + Af^s \quad (3.8)$$

where A and s are coefficients and f is the applied frequency [17,21]. Since the dc conductivity is found to be negligible equation 8 can be written in the form

$$\sigma_{ac} = Af^s \quad (3.9)$$

The values A and s can be determined by plotting log of ac conductivity against log frequency. The plot is a straight line, since

$$\log \sigma_{ac} = \log A + s \log f \quad (3.10)$$

Equation 3.10 is the equation of a straight line with a slope s .

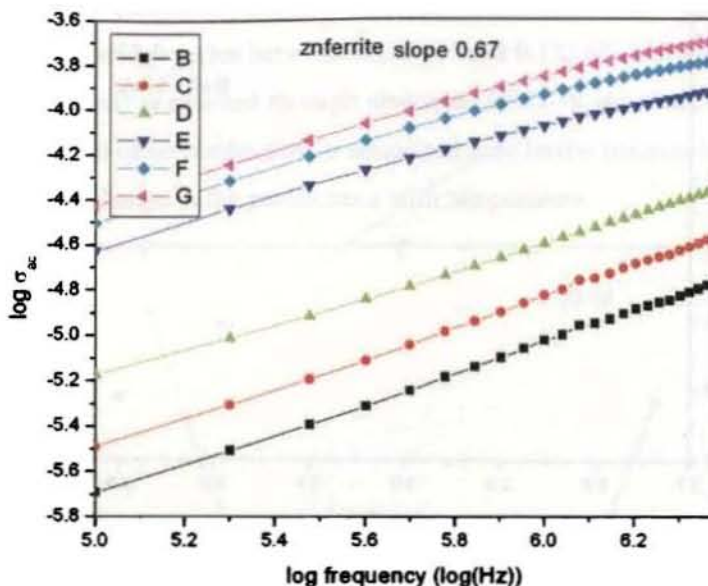


Figure 3.7: Graph between log frequency and log of ac conductivity

The values of s for different temperatures were determined by plotting $\log f$ with $\log \sigma_{ac}$ and by finding the slope of the resulting straight line. The plots are presented in figure 3.7. The plots are parallel to each other and the slope of the straight line region is between 0.67 and 0.68. It is reasonable to assume that the parameter s is independent of temperature. The parameter s can throw light on two distinct conduction mechanisms. The conduction can be through quantum mechanical tunneling (QMT) of charge carriers through barriers separating localized sites and in such a case the parameter s is independent of temperature [18]. Another possible mechanism of conduction is the correlated barrier hopping (CBH) in the same barrier [18]. In CBH a decrease in the parameter s is expected with increase of temperature. For zinc ferrite particles the decrease in s is only nominal.

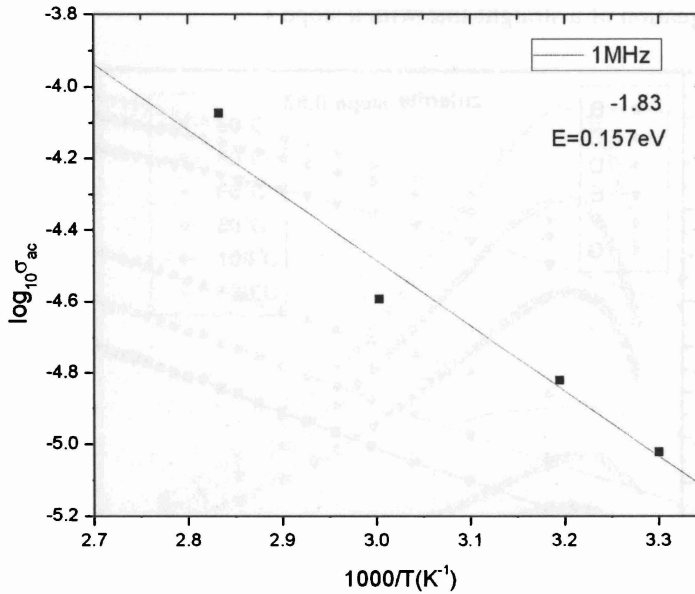


Figure 3.8: Graph of $\log(\sigma_{ac})$ vs. $100/T$. Activation energy is determined from the slope of this graph

The ac conductivity of zinc ferrite was found to increase with temperature because the absorption of heat energy increases the mobility of electrons taking part in the hopping process. The variation of ac conductivity with temperature can be understood on the basis of Arrhenius equation of the form

$$\sigma_{ac} = \sigma_o \exp\left(\frac{-E}{k_B T}\right) \quad (3.11)$$

Where σ_o is the pre-exponential factor, E is the activation energy, k_B is the Boltzmann's constant and T is temperature in Kelvin [19,20]. Activation energy of zinc ferrite particles was estimated by plotting $\log_{10}(\sigma_{ac})$ against $100/T$ and by finding the slope of the straight line obtained by the method of least square linear fit. A typical plot with straight line fit is shown as figure 3.8 for frequency of 1 MHz. The activation energy in eV is given by the equation

$$E = \frac{2.303 \times 1000 \times m.k_B}{e} \quad (3.12)$$

where m is the slope and e is the electronic charge. The activation energy was found to decrease with frequency initially and after 4 MHz it increases with increasing frequency as depicted in figure 3.9. Activation energy varies between 0.135 eV and 0.175 eV and this suggests that the ac conduction in the material is realized through electrons. QMT of electrons between barriers can be a possible mechanism of ac conduction in nanosized zinc ferrite because it has been found that there is no appreciable change in the parameter s with temperature.

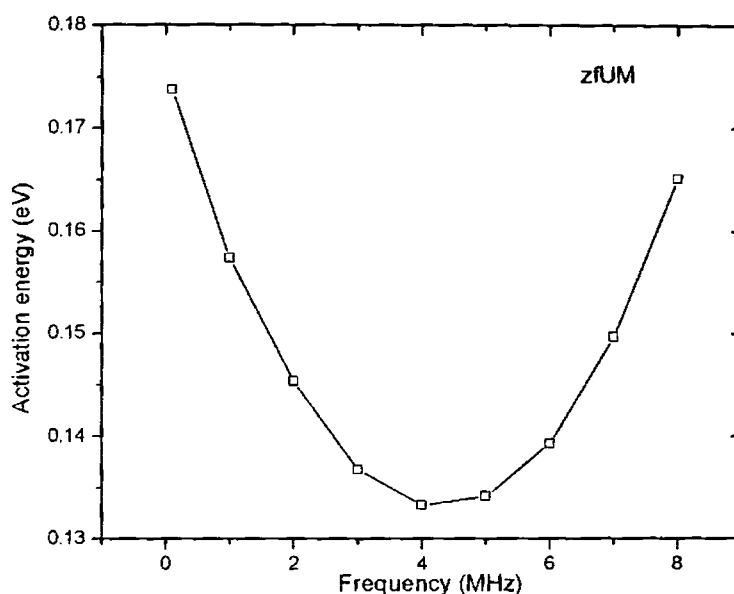


Figure 3.9: Variation of activation energy with frequency (zinc ferrite)

3.6 Dielectric studies of cadmium ferrite

The evaluation of dielectric permittivity and dielectric loss of cadmium ferrite was carried out in a similar fashion. The pellets were pressed uniaxially and sintered at 900 °C for 36 hours for having the required compaction before they were placed in the dielectric cell.

Figure 3.10 depicts the variation of real part of the relative dielectric permittivity of cadmium ferrite with frequency in the frequency range of 100 kHz-8 MHz at various temperatures starting from 30 °C to 120 °C. The dielectric constant of cadmium ferrite at any given frequency and temperature is greater than that of zinc ferrite. The larger lattice constant of cadmium ferrite could be the reason for this increase. The same reason can be applied to the

Chapter 3

smaller dielectric constant of zinc aluminate (which is given as an annexure to this thesis) compared to zinc and cadmium ferrites. The permittivity of cadmium ferrite is found to decrease with the frequency as observed in many ceramic materials. The presence of interfacial polarization is attributed to this dielectric dispersion in this frequency band as already explained in the previous sections of this chapter.

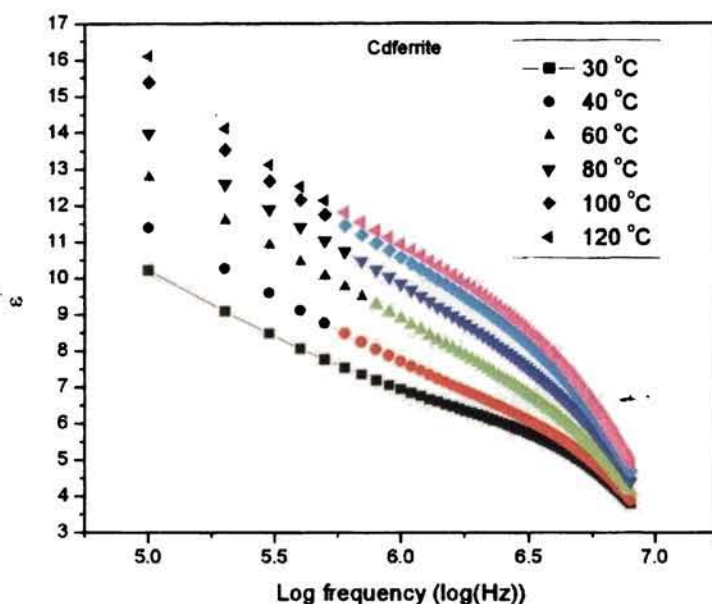


Figure 3.10: Dielectric permittivity of cadmium ferrite with frequency

In figure 3.11 the variation of dielectric permittivity of cadmium ferrite with temperature is shown. There is a steady increase in the dielectric permittivity with rise of temperature at all frequencies in the range. This is expected of a ceramic material and the enhancement in permittivity is attributed to the freedom of movements of individual grains due to thermal energy.

The dielectric loss of cadmium ferrite is plotted against frequency and is shown in figure 3.12. The loss decreases with frequency and does not show any resonance. It can be observed that there is a steady increase in dielectric loss with temperature. The increase in loss with temperature is more pronounced at lower frequencies. At higher frequencies the dielectric loss is almost a constant. It appears that the polarization mechanism operating in the material has a relaxation frequency less than 100 kHz and the loss is not much significant at higher frequencies. This

points to the existence of interfacial polarization in the material due to the presence of grains and grain boundaries.

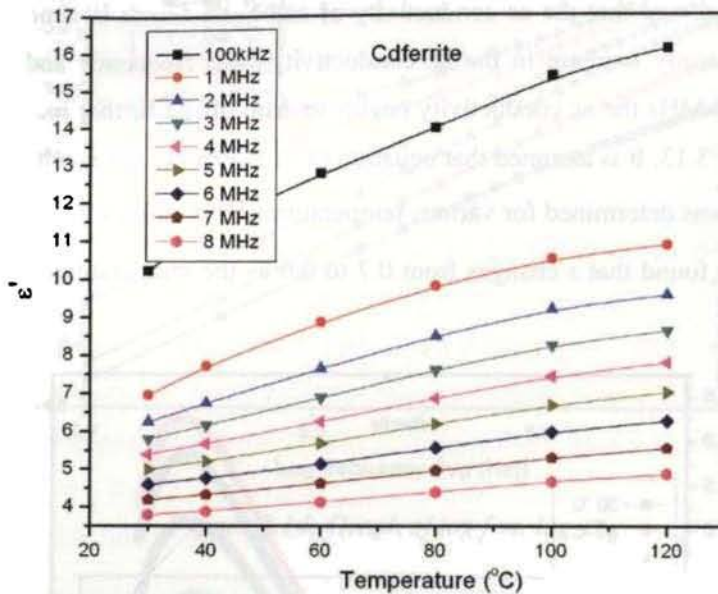


Figure 3.11: Variation of dielectric permittivity with temperature

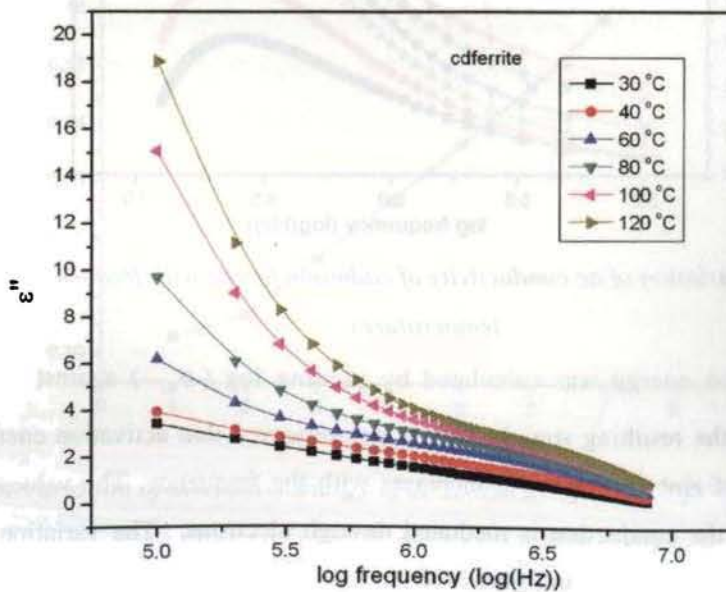


Figure 3.12: Variation of dielectric loss with frequency

3.7 Evaluation of ac conductivity of cadmium ferrite

It can be observed that the ac conductivity of cadmium ferrite is similar to that of zinc ferrite. There is a steady increase in the ac conductivity with frequency and after reaching a maximum at about 6 MHz the ac conductivity begins to drop off on further increase in frequency as depicted in figure 3.13. It is assumed that equation (3.9) is valid in the ascending portion of the curve. The factor s was determined for various temperatures by plotting $\log(f)$ against $\log(\sigma_{ac})$ (figure 3.14). It was found that s changes from 0.7 to 0.6 as the temperature rises from 30 °C to 120 °C.

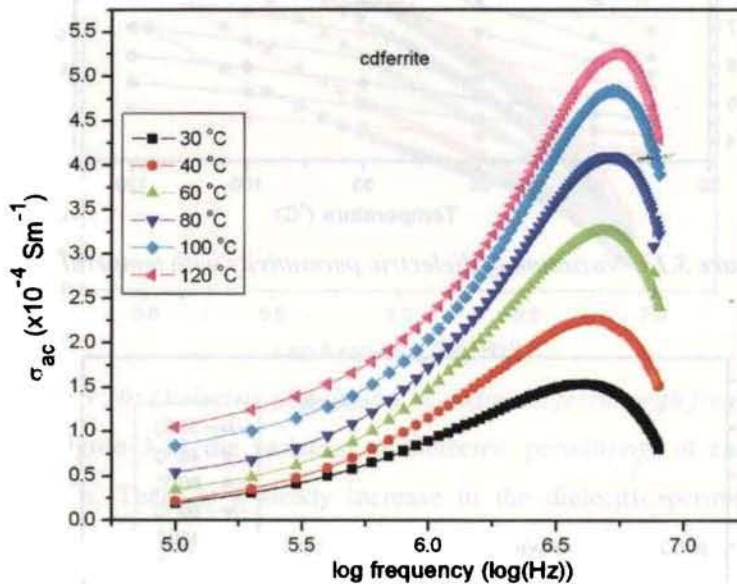


Figure 3.13: Variation of ac conductivity of cadmium ferrite with frequency at various temperatures

The activation energy was calculated by plotting $\log(\sigma_{ac})$ against $1000/T$ and by finding the slope of the resulting straight line. It was observed that activation energy lies in the same range of that of zinc ferrite and it increases with the frequency. The values of activation energy indicate that the conduction is mediated through electrons. The variation in activation energy with frequency is depicted in figure 3.15

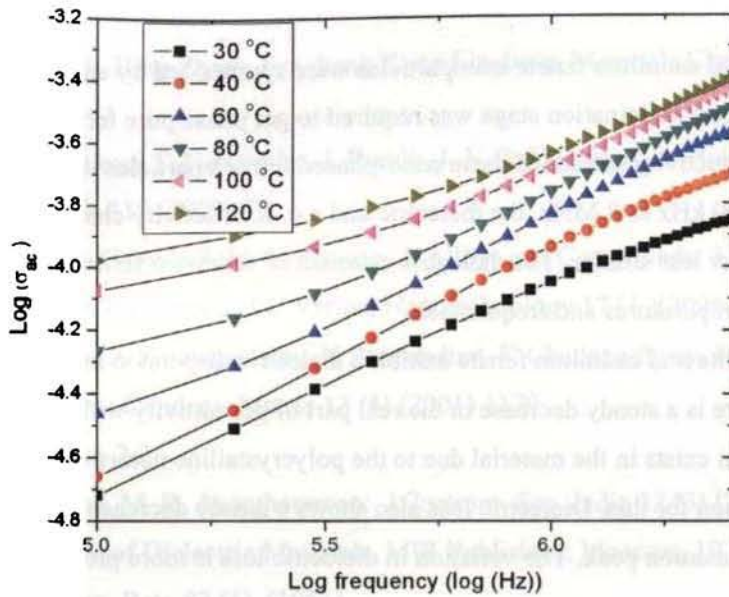


Figure 3.14: Graph of $\log f$ vs. $\log \sigma_{ac}$

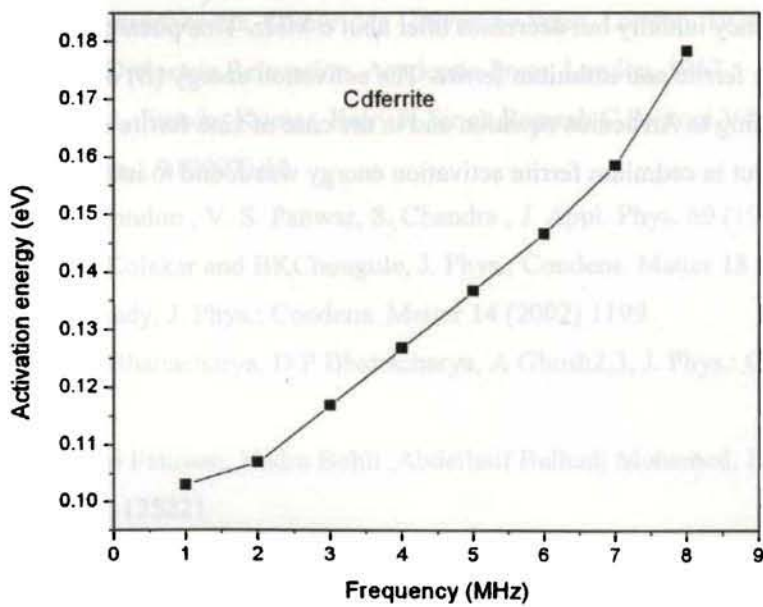


Figure 3.15: Variation of activation energy of ac conductivity with frequency (cadmium ferrite)

3.8 Conclusion

Zinc ferrite and cadmium ferrite nanoparticles were synthesized by employing a sol-gel auto-combustion method. Calcination stage was required to get phase pure ferrite particles. The dielectric and a.c conductivity studies of these nano-phased ferrites particles were carried out in a frequency range of 100 kHz to 8 MHz. the dielectric and a.c. conductivity characteristics of these two ferrites are more or less similar. The dielectric constant of cadmium ferrite is greater than that of zinc ferrite at all temperatures and frequencies.

Both zinc ferrite and cadmium ferrite exhibit a dielectric dispersion in the given frequency range. There is a steady decrease in the real part of permittivity with frequency. Interfacial polarization exists in the material due to the polycrystalline nature of the material is understood as the reason for this. Dielectric loss also shows a steady decrease with frequency and does not show any relaxation peak. The variation in dielectric loss is more pronounced at higher temperatures.

The variation of a.c. conductivity was evaluated for both the materials and found that it increases with frequency initially but decreases after about 6 MHz. This phenomenon was observed in both zinc ferrite and cadmium ferrite. The activation energy (E) of a.c conduction was estimated according to Arrhenius equation and in the case of zinc ferrite E decreases initially and then increases. But in cadmium ferrite activation energy was found to increase with frequency.

References:

- 1 Zhang Tianshu, P. Hing,Zhang Jiancheng Kong Lingbing, *Materials Chemistry and Physics* 61 (1999) 192
- 2 J. Plocek, A. Hutlova, D.Niznansky, J. Bursik, J.-L. Rehspringer, Z. Micka, *J. Non-Crystalline Solids* 315 (2003) 70
- 3 H. Ehrhardt, S. J. Campbell, M. Hoffmann, *J. Alloys and Compounds*, 339 (2002), 255
- 4 M K Roy, Bidyut Haldar and H C Verma, *Nanotechnology* 17 (1)(2006) 232
- 5 C N Chinnasamy, A Narayanasamy, N Ponpandian, K Chattopadhyay, H Gu erault and J-M Greneche, *J. Phys.: Condens. Matter* 13 (5) (2001) 1179
- 6 This thesis section 2.2
- 7 E. M. Mohammed, M. R. Anantharaman: *J. Instrum. Soc. India* 32 (3) (2002) 165
- 8 B.Tareev, *Physics of Dielectric Materials*, MIR Publishers, Moscow, 1975
- 9 C.G.Koopes, *Phys. Rev.* 83 (1), (1951)
- 10 K W Wagner, *Ann. Phys.* 40 (1993), 817
- 11 H.A. Pohl, *Dielectrophoresis*, Cambridge University Press, London, 1978
- 12 Vera.V. Daniel, *Dielectric Relaxation*, Academic Press, London, 1967
- 13 Ramadhar Singh1, Jitendra Kumar, Rajiv K Singh,Ramesh C Rastogi,Vikram Kumar, *New Journal of Physics*, , 9 (2007) 40
- 14 R Singh , R. P. Tandon , V. S. Panwar, S. Chandra , *J. Appl. Phys.* 69 (1991) 2504
- 15 R S Devan, Y DKolekar and BKChougule, *J. Phys.: Condens. Matter* 18 (2006) 9809
- 16 M M El-Samanoudy, *J. Phys.: Condens. Matter* 14 (2002) 1199
- 17 Aloka Ghosh, S Bhattacharya, D P Bhattacharya, A Ghosh2,3, *J. Phys.: Condens. Matter* 20 (2008) 035203
- 18 Fethi Gmati, Arbi Fattoum, Nadra Bohli ,Abdellatif Belhadj Mohamed, *J. Phys.: Condens. Matter* 20 (2008) 125221
- 19 Nadeem Musahwar, M A Majeed Khan, M Husain , M Zulfequar, *J. Phys. D: Appl. Phys.* 40 (2007) 7787
- 20 Mathew George, Swapna S Nair, K A Malini1, P A Joy, M R Anantharaman, *J. Phys. D: Appl. Phys.* 40 (2007) 1593
- 21 Z. M. Elimat, *J. Phys. D: Appl. Phys.* 39 (2006) 2824

Chapter 4

Effect of high energy ball milling on Zinc Ferrite and Cadmium ferrite nanoparticles

This chapter takes a look at the size effects on the structural and magnetic properties of zinc ferrite and cadmium ferrite particles. As discussed in the earlier chapters these ferrites in the micron regime crystallize in the normal spinel form and are found to be antiferromagnetic [1]. The zinc and cadmium cations are believed to be having an exclusive tetrahedral preference [2]. In the nano regime the size effects are more pronounced with the exhibition of ferrimagnetic like properties resulting out of a probable cation re-distribution or due to surface magnetism or spin glass behavior or a combination of two more of the above factors [3-9]. It is well known that sol-gel synthesis results in nanosized particles of cadmium and zinc ferrite [10]. However traces of impurity phases are unavoidable in the final product. Hence calcination at higher temperature is normally resorted to which eventually allows the grain size to grow [11]. This is undesirable as far as the samples for studying size effects are concerned. High energy ball-milling can be employed for the reduction of particle size. For this phase pure samples are prepared via sol-gel synthesis and subsequent calcination and they are subjected to ball-milling for various time durations. The focus of this chapter is laid in understanding the size effect on the various properties of zinc and cadmium ferrites.

Ferrites are ferrimagnetic oxides and represented by the chemical formula AFe_2O_4 , where A is the metal with an oxidation state of 2 [1]. These materials continue to attract lot of interest because of their potential uses in many applications. Many of these materials are good catalysts [12-14]. Zinc ferrite is used in the oxidative dehydrogenation of n-butane to butanes and as a sorbent for high temperature desulphurization of coal gas. In addition to this, ferrites are of interest from a fundamental perspective too. Zinc and cadmium ferrites exhibit normal spinel structure in bulk with Fe atoms occupy the octahedral voids whereas Zn and Cd occupy the

Chapter 4

tetrahedral voids. A deviation from the normal spinel structure to an inverse spinel structure is reported in many cases of these materials, especially when the particle size is below 25 nm. Inversion in spinel structure can lead to magnetic ordering in these structures [6-9]. For these synthesizing ferrite materials in small particle sizes, typically 10 to 15 nm is necessary.

4.1 Sample preparation

Sol-gel synthesis combined with subsequent high energy ball milling can produce ferrite nanoparticles with sizes as low as 14 nm. Further, it is possible to tune the particles to the desired size by controlling the milling parameters like time and speed of rotation.

As-prepared samples of zinc and cadmium ferrites are subjected to high energy ball-milling (HEBM). The ball-milling of the samples had been carried out in a Fritsch P-7 high energy planetary ball milling unit. The entire ball-milling experiments were carried out in a medium of toluene in tungsten carbide coated vials with tungsten carbide balls. The weight ratio of sample to balls was maintained at 1:10 and the milling speed was kept at 450 rotations per minute (rpm). The milled sample was dried in a hot air oven at 100°C in a porcelain bowl, scrapped and dried again at 120°C. The samples were ball-milled for five different durations beginning from 10 minutes and up to 120 minutes. The particles were then subjected to various studies using X-ray diffractometry, vibrating sample magnetometry, transmission electron microscopy and scanning electron microscopy. In addition to this low temperature magnetization measurements were conducted on zinc ferrite samples using a SQUID magnetometer.

4.2. XRD analysis of ball-milled samples

The X-ray diffraction pattern of the milled and unmilled zinc ferrite nanoparticles are depicted in figure 4.1. It is evident from the diagram that the unmilled sample is single phasic and this sample possesses the largest particle size. There is a progressive variation in the broadening of the diffraction peaks and this is clearly visible in the pattern. The line broadening is the maximum for the 120 minutes milled sample. Further milling is not attempted because the sample loses its crystallinity at this point. Many of the peaks other than the main peaks are not visible in the X-ray diffraction diagram of the 120 minute milled sample. In figure 4.2 the X-ray

diffraction patterns of the ball milled cadmium ferrite powder are shown. A similar variation is exhibited in the particle sizes of cadmium ferrite too.

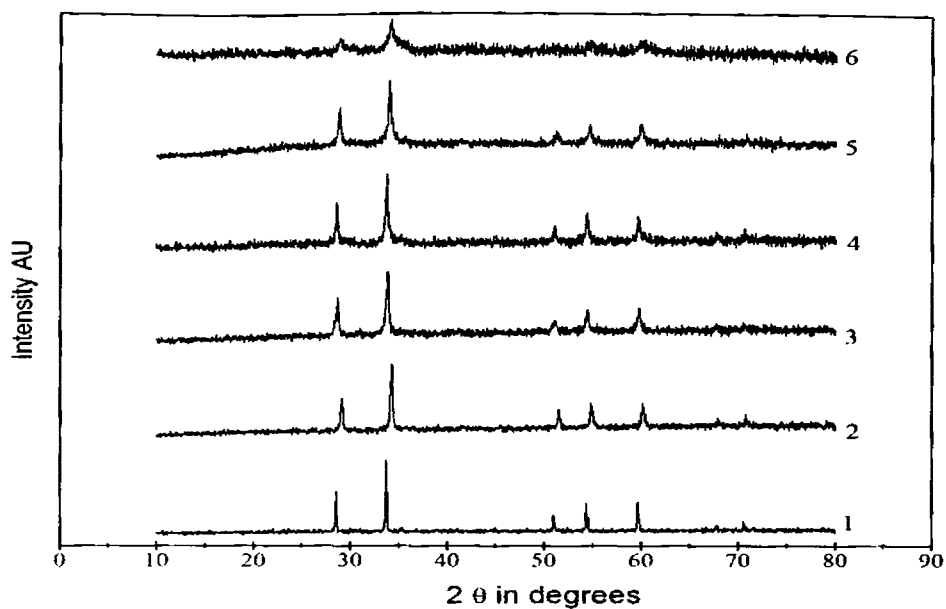


Figure 4.1: X-ray diffraction pattern of ball-milled zinc ferrite particles

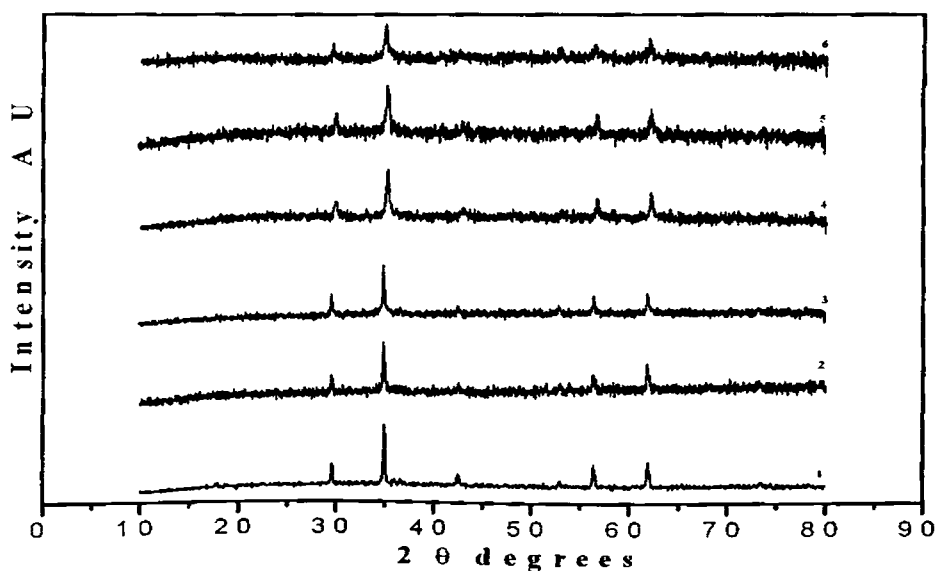


Figure 4.2: X-ray diffraction pattern of ball-milled cadmium ferrite particles

The particle sizes of all the ball-milled samples were estimated by employing Debye-Scherrer equation [15]. There is a progressive decrease in the particle sizes. A size reduction from 46 nm to 18 nm was noticed in the case of zinc ferrite and in the case of cadmium ferrite particles, the particle sizes shrunk from 59 nm to 15 nm. These results are tabulated and are shown in table 4.1

| Milling time (minutes) | Peak index | Zinc Ferrite | | | Cadmium Ferrite | | |
|------------------------|------------|------------------------|---------------------|-------------------------------|------------------------|---------------------|-------------------------------|
| | | Peak position (degree) | Peak width (degree) | Calculated particle size (nm) | Peak position (degree) | Peak width (degree) | Calculated particle size (nm) |
| 0 | 311 | 34.91 | 0.19 | 46 | 33.74 | 0.14 | 59.3 |
| 10 | 311 | 34.92 | 0.20 | 42 | 33.74 | 0.19 | 43 |
| 20 | 311 | 34.91 | 0.22 | 37 | 33.74 | 0.24 | 34 |
| 30 | 311 | 34.90 | 0.32 | 26 | 33.73 | 0.298 | 27 |
| 60 | 311 | 34.90 | 0.35 | 23 | 33.73 | 0.37 | 22 |
| 120 | 311 | 34.9 | 0.45 | 18 | 33.72 | 0.58 | 15 |

Table 4.1: Milling time and particle sizes of zinc ferrite and cadmium ferrite nanoparticles

4.3 The transmission electron micrography

The transmission electron micrographs of the unmilled and 120 min milled zinc ferrite samples are shown in figure 4.3 and 4.4 respectively. The reduction in the size of the crystallites can be clearly seen and comparable. The average particle size determined manually in the case of unmilled zinc ferrite particles is 75 nm. This is in good agreement with that of values calculated from the X-ray diffraction pattern using Debye-Scherrer relation. The sample milled for a

duration of 120 min shows highly reduced particle size. The particle size determined from the micrograph in this case is 12 nm and this also in very good agreement with the result obtained from the analysis of X-ray diffraction peaks. However slight deviation in the sphericity of milled samples is noticeable. Such deviations are reported for many compounds prepared using sol-gel synthesis [10]. These findings are also supported by the scanning electron microscopy of the samples.

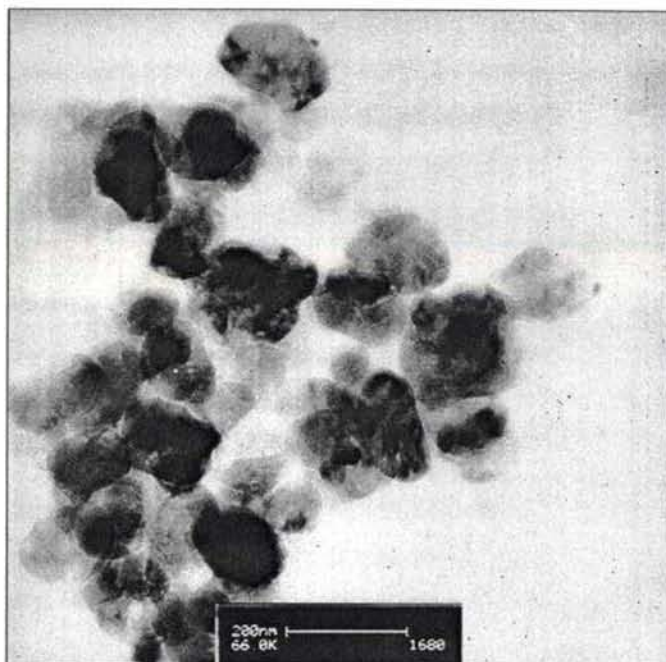


Figure 4.3: TEM of unmilled zinc ferrite particles

Transmission electron microscopy experiments could not be carried out on cadmium ferrite samples. However from a broad conjecture, based on the correlation results on particle size evaluated using XRD and TEM of zinc ferrite samples, it is to be assumed that the relative change in the full width at half maximum (FWHM) of peaks is a good indication of the fact that the particle size derived using XRD analysis are realistic

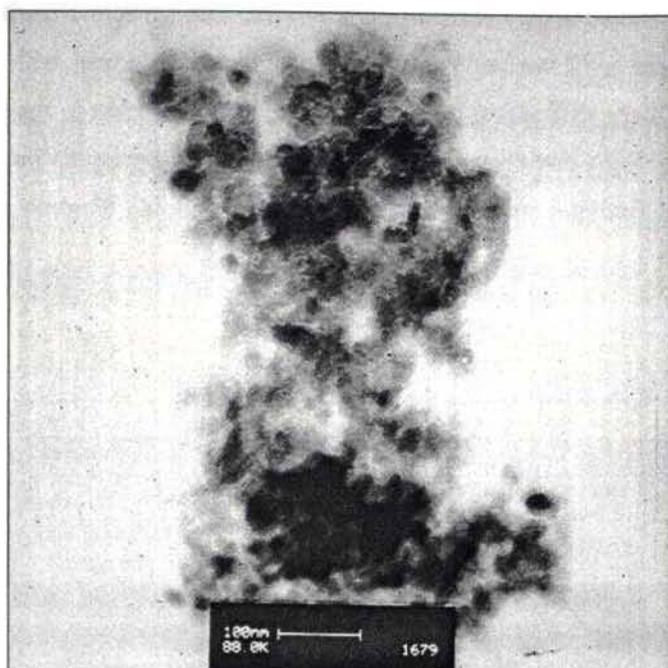


Figure 4.4: TEM of 120 minute milled zinc ferrite particles

4.4 Scanning electron microscopy

Scanning electron microscopy (SEM) gives a good idea about the surface morphology of the crystallites. In figure 4.5, 4.6 and 4.7 the SEM pictures of zinc ferrite particles are shown, which are Unmilled, 30 min milled and 120 min milled respectively. For readying the sample for scanning electron microscopy, the powder samples were compacted in the form of pellets by pressing uniaxially in a hydraulic pellet making press to a size of 12 mm in diameter and 1.5 to 1.8 mm thickness. These pellets were further sintered at 600°C for better compaction and surface was polished with emery paper.

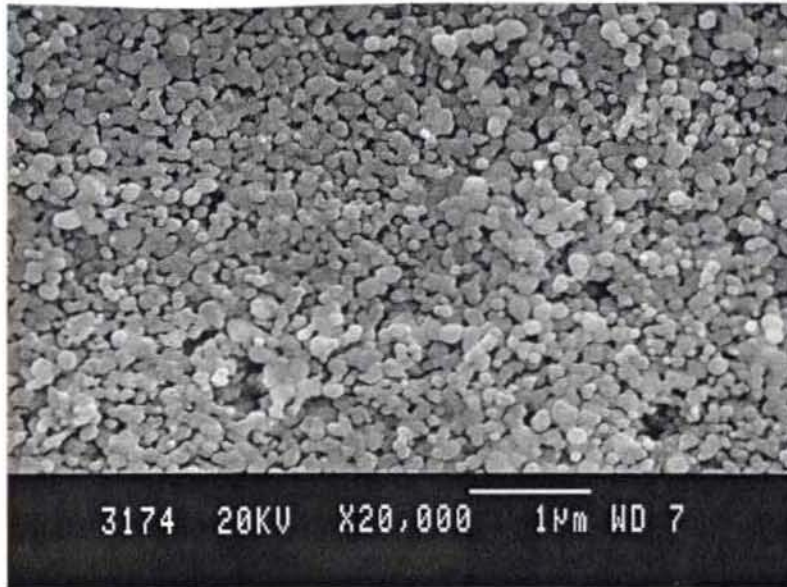


Figure 4.5: SEM micrograph of unmilled zinc ferrite powder

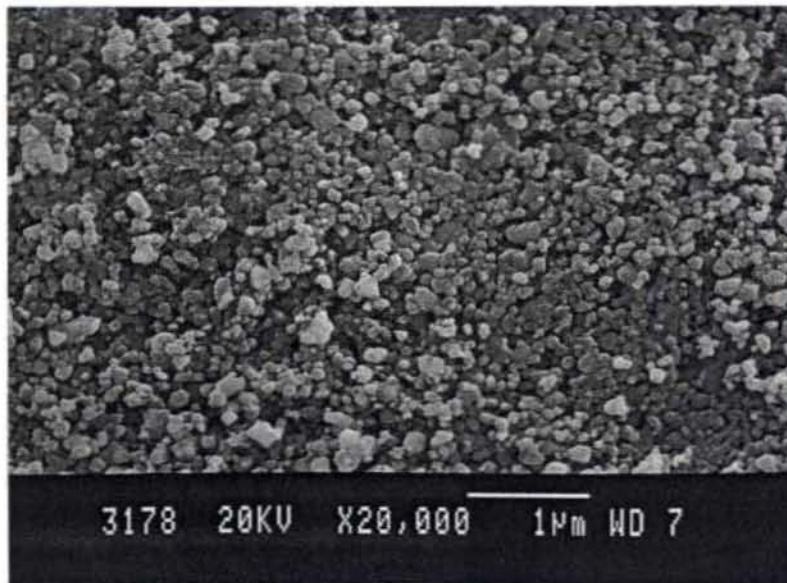


Figure 4.6: SEM micrograph of 30 min milled zinc ferrite powder

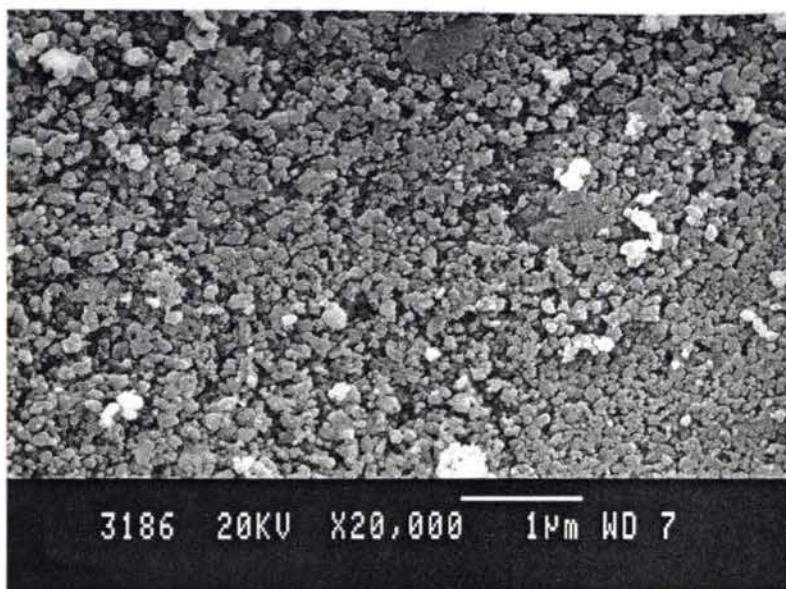


Figure 4.7: SEM micrograph of 120 min milled zinc ferrite powder

Unmilled zinc ferrite samples show a near perfect spherical shape as evident from the micrographs. A tendency of coalescence of particles can be observed from the micrographs and this is due to the effect of compaction and sintering. The 30 min milled samples also show not much change in shape and particles are still coalesced and particle clusters can be observed in the picture. However the 120 min milled sample shows a noticeable change in their shape. Due to high energy mechanical attrition during ball-milling the particles are broken into pieces and have deviated from the spherical shape. The size of the particles are slightly larger than what is observed in TEM. The sintering of the pellets for achieving compaction must have facilitated growth of grains and hence the increase in grain size [16,17].

An exactly similar observation can be made from the SEM of cadmium ferrite particles shown as figure 4.8, 4.9 and 4.10 which are unmilled, 30 min milled and 120 min milled samples. The compaction and sintering had been carried out on these samples exactly as in the case of cadmium ferrite samples. The particles of cadmium ferrite appear larger than that of zinc ferrite and this is as expected from the XRD studies. 120 min milled cadmium ferrite particles appear to be more uniform in particle size distribution.

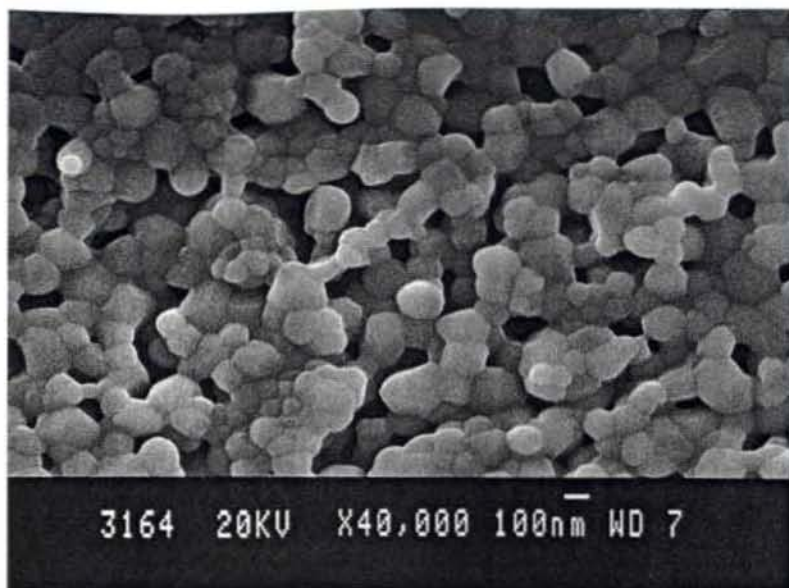


Figure 4.8 SEM micrograph of unmilled cadmium ferrite powder

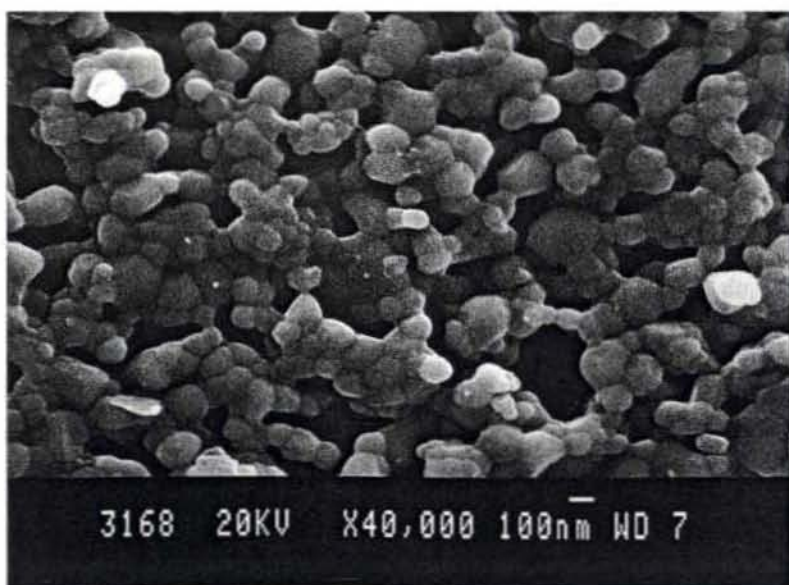


Figure 4.9 SEM micrograph of 30 min milled cadmium ferrite powder

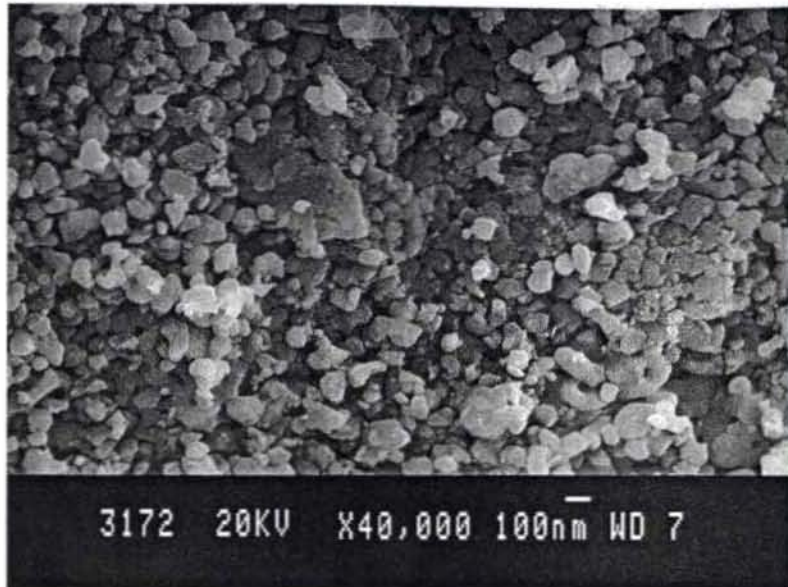


Figure 4.10: SEM micrograph of 120 min milled cadmium ferrite powder

4.5 Magnetic properties

Both unmilled and milled samples of zinc ferrite and cadmium ferrite were subjected to magnetic measurements using vibrating sample magnetometer (EG&G PAR 4500) at room temperature. Magnetic hysteresis was recorded and plotted for applied field varying from 0 to 15000 Oe at intervals of 300 Oe.

The most important feature in the magnetic behaviour of these two ball-milled ferrite systems is that they are perfectly identical. Even at 15000 Oe, the unmilled samples of cadmium and zinc ferrite do not show any saturation of magnetization. The magnetization curve is a straight line with a positive slope passing through the origin for both zinc ferrite and cadmium ferrites. The samples are perfectly paramagnetic justifying the formation of a normal spinel structure. Pure zinc ferrite and cadmium ferrite does not have any magnetic ordering in their structure since these two ferrites crystallize in the normal spinel structure and the paramagnetism originates from the isolated and non-interacting atomic magnetic moments of Fe atoms [1]. A-O-B superexchange interaction is absent in both ferrite systems and Fe ions remain non-interacting

and the individual moments align with the applied field resulting in a paramagnetic behaviour. At an applied field of 15000 Oe zinc ferrite shows a magnetization of 1.55 emu/g and cadmium ferrite exhibits 0.97 emu/g. The crystal size of cadmium ferrite is larger than that of zinc ferrite and Fe ions are more isolated in cadmium ferrite because of this. This could be the reason for smaller magnetization in cadmium ferrite.

But on high energy ball milling and on subsequent reduction of particle size both the samples exhibit a clear superparamagnetic behavior and a well defined magnetization loop was obtained with very small or negligible coercivity. However, perfect saturation is absent for these samples even at an applied field of 15000 Oe and magnetization curve shows a positive slope (this effect is further verified by SQUID magnetization studies at still higher magnetic fields) indicating that the magnetization will attain saturation at an higher applied field. The magnetization at any applied field shows a steady increase with milling time. Maximum magnetization is shown by 120 minute milled samples in both cases. The magnetic hysteresis loops of the zinc ferrite samples are shown in the figure 4.11 and that of cadmium ferrite samples are shown in figure 4.12

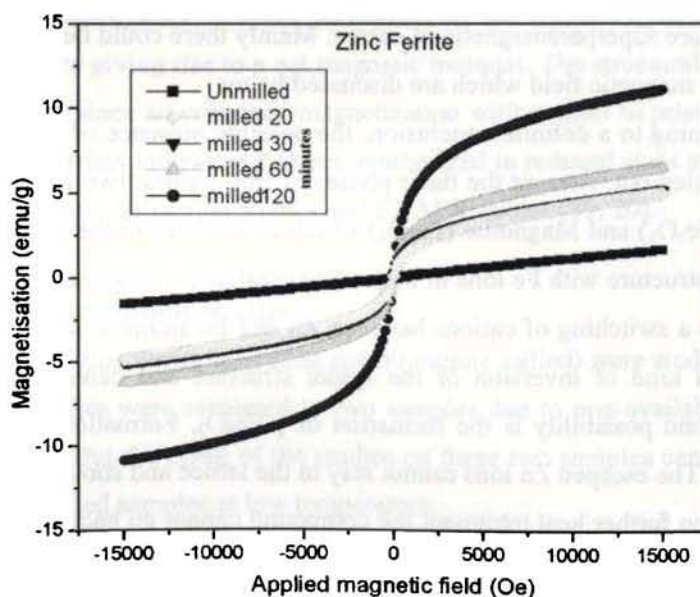


Figure 4.11: Hysteresis behaviors of ball-milled zinc ferrite particles

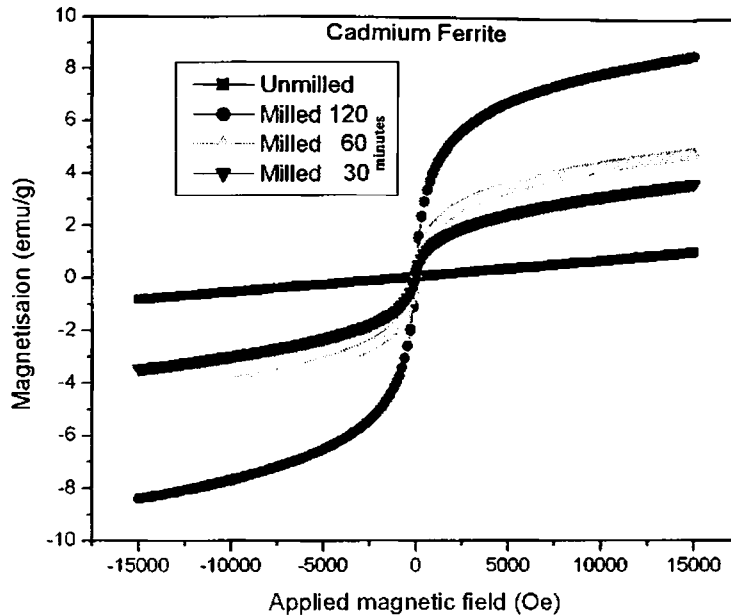


Figure 4.12: Hysteresis behaviors of ball-milled cadmium ferrite samples

The coercivity of the samples in all the cases is below 8 Oe and it can be safely assumed that these samples are superparamagnetic in nature. Mainly there could be a couple of reasons for such an increase in magnetic field which are discussed below

Before coming to a definite conclusion, the possible presence of impurity phases of iron oxides has to be ruled out. Among the three phases of iron oxides, two are magnetic [18]. They are Magnetite ($\gamma\text{-Fe}_2\text{O}_3$) and Magnetite (Fe_3O_4) which crystallizes in the inverse spinel structure. Fe_3O_4 has a spinel structure with Fe ions in both tetrahedral and octahedral sites. The formation of this phase requires a switching of cations between Zn and Fe atoms in some of the formula unit cells and this is a kind of inversion of the spinel structure and cannot be considered as an impurity. The second possibility is the formation of $\gamma\text{-Fe}_2\text{O}_3$. Formation of this phase requires escape of Zn ions. The escaped Zn ions cannot stay in the lattice and should be expelled out of the crystal lattice. So on further heat treatment the compound cannot go back to the zinc ferrite state. But it has been observed that after re-calcination of the ball-milled sample at 700 °C it retains its paramagnetic characteristics and shows the same behaviour of unmilled zinc ferrite giving the same magnetization per unit mass (1.5 emu/g for zinc ferrite and 0.95 emu/g for cadmium ferrite).

The other possibility is the formation of Haematite (α - Fe_2O_3) which is antiferromagnetic in nature. On XRD analysis this sample does not show any phase other than zinc ferrite. This clearly proves the presence of Zn cations in the lattice itself and rules out the formation of Fe_2O_3 phases. Further, no ZnO phase is observed in the XRD pattern of milled samples. Thus the formation of γ - Fe_2O_3 does not appear to be a possibility.

Having ruled out the presence of iron oxide and zinc oxide impurities it is imperative that the possibility of a magnetic ordering is to be examined. The origin of magnetic ordering upon high energy ball-milling can be explained by assuming a change in the cation distribution in the crystals. In normal spinels all Fe ions are in the octahedral sites and Zn or Cd atoms are in the tetrahedral sites. Such an arrangement cannot give any net magnetic moment in any antiferromagnetic ordering and that is evident in the pure unmilled samples. High energy ball-milling have two effects in the crystallites. The size of the crystallites are reduced to a very great extend and this is clearly evident in the X-ray diffraction pattern and in TEM micrographs. This may produce an increased surface to volume ratio and cause an increase in magnetic moment of the sample. But the magnitude of the increase suggests that some other mechanism has caused the enhancement in magnetic moment. A possible explanation is the change in the cation distribution in the crystals. A small percentage of the crystals must have undergone an inversion in the structure giving rise to a net magnetic moment. The structural inversion can be a result of size reduction, since an enhanced magnetization with respect to pristine zinc ferrite has been reported in zinc ferrites samples which are synthesized in reduced sizes and cation inversion was established by neutron diffraction studies and EXAFS studies [19, 20].

4.6 SQUID magnetization studies

Two samples of zinc ferrite (unmilled and 30 minute milled) were studied using a SQUID magnetometer. The studies were restricted to two samples due to non-availability of instrument time for other samples. But the result of the studies on these two samples can throw light on the magnetization of the milled samples at low temperature.

Figure 4.13 depicts the m - H (magnetization vs. applied field) curve of unmilled zinc ferrite measured with a maximum applied field of 60000 Oe. Even at such a high applied field the unmilled zinc ferrite remains paramagnetic, giving a strict linear relation between m and H . Neel

Chapter 4

temperature of zinc ferrite is reported to be at 10 K as mentioned previously [21]. Below 10K the material becomes antiferromagnetic and can give a shear

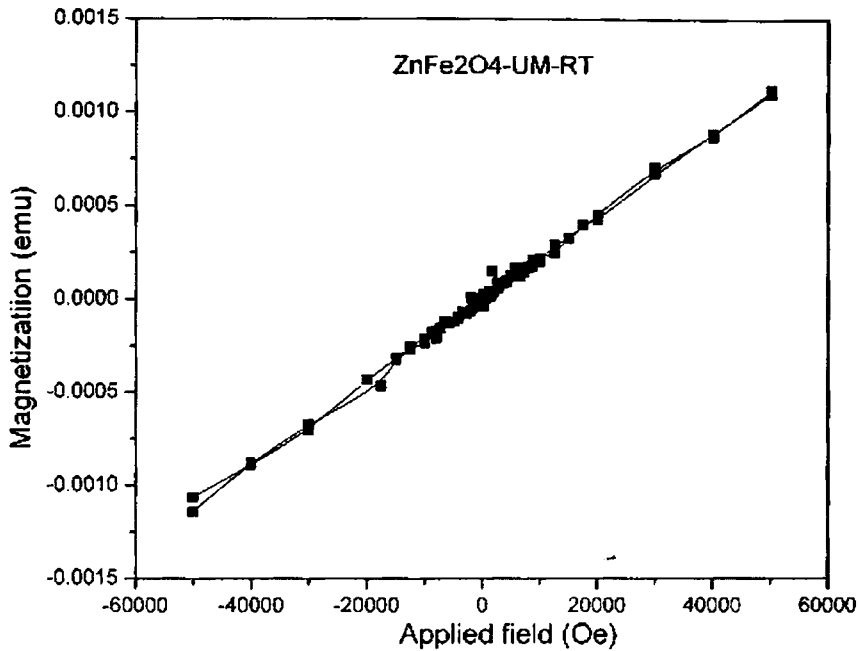


Figure 4.13: Magnetization vs. applied field of unmilled zinc ferrite measured in SQUID magnetometer

in the magnetization curve as the magnetization tends to saturate. Figure 4.14 shows the m-H graph at 6 K. At 6 K the sample has ferrimagnetic behaviour. The B-O-B superexchange interaction energy overcomes the thermal energy at this temperature facilitating ferrimagnetic ordering [22]

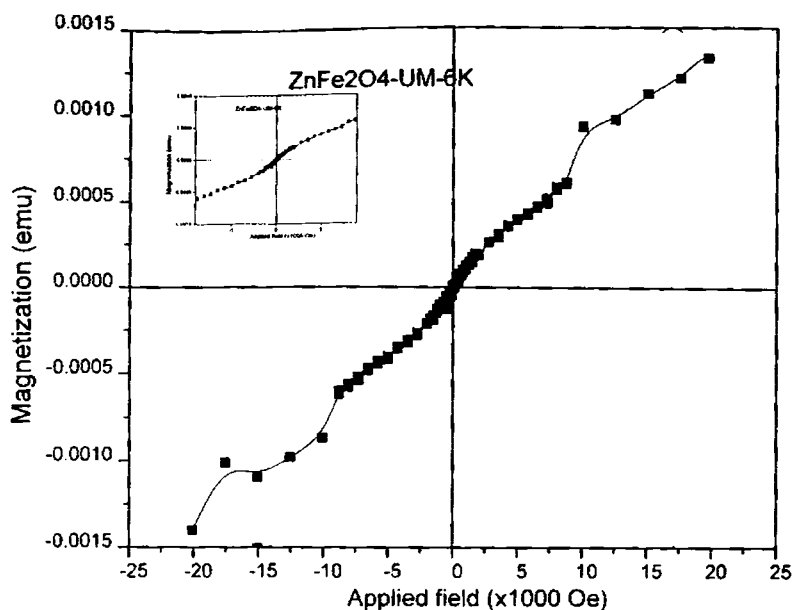


Figure 4.14: m-H graph of unmilled zinc ferrite at 6K

The milled zinc ferrite particles show a clear tendency to saturate but do not get saturated under an applied magnetic field of 15000 Oe (figure 4.15). It is evident that there are two components in the sample, of which one is purely paramagnetic and the other is ferrimagnetic. This is similar to the result obtained in VSM studies. At room temperature this sample does not show any coercivity and particles can be treated as superparamagnetic. Figure 4.16 shows the magnetization of the same sample at 6K. In terms of magnetization the sample gives more or less the same kind of behaviour but the coercivity has increased significantly. It suggests that the blocking temperature is somewhere in between room temperature and 6K. It is well established that the coercivity of particles showing superparamagnetic behaviour increases below the blocking temperature [23, 24]. This is pointing to the single domain nature and high shape anisotropy of ball-milled zinc ferrite particles [25,26].

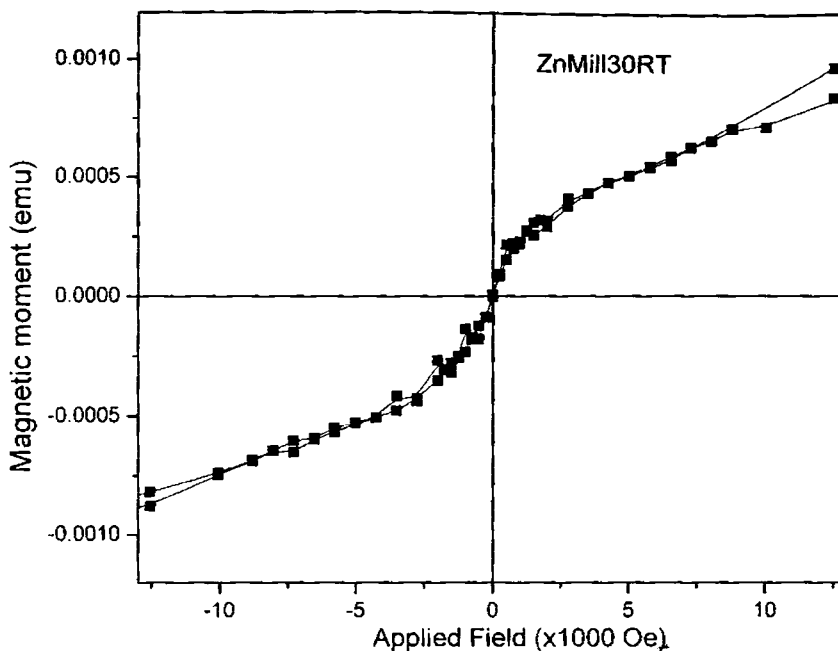


Figure 4.15: *m-H* graph at room temperature

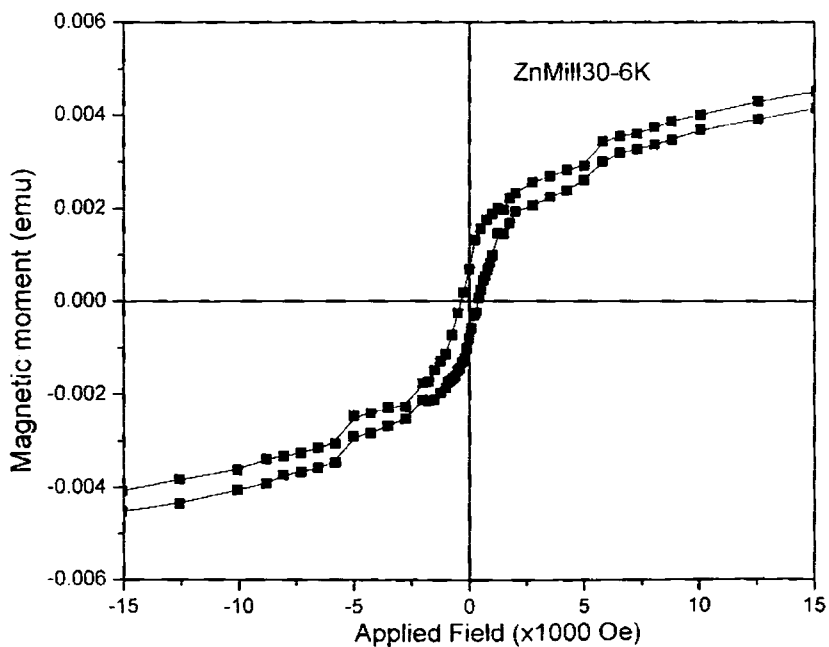


Figure 4.16: *m-H* graph at 6 K of 30 minute milled sample

Evaluation of the magnetization with temperature (m-T graph) can shed light on the magnetic ordering in a material. The m-T graph of unmilled sample at a field of 1 T is shown in figure 4.17. The graph shows a non-linear increase in magnetization with decrease in temperature. The rate of increase of magnetization decreases with increase in temperature. This is a clear signature of a paramagnetic material [21]. A cusp is formed at about 18K. This is the region of antiferromagnetic to ferrimagnetic transition of zinc ferrite (Neel temperature). However the shift of Neel temperature from the previously reported 10 K to 18 K is not well understood. Figure 4.18 shows the m-T graph of milled sample (30 min). Though there is steady increase in magnetization with increase in temperature, the shape of the graph is different from that obtained for unmilled sample. There appears to be a paramagnetic component super-imposed on a ferrimagnetic component. The inward curvature of the unmilled sample is totally compensated in the milled sample. The ferrimagnetic component could have a superparamagnetic behaviour. And the blocking temperature should be near 150K where the concave shape of the curve is completely compensated. The cusp appears at a temperature of 23K now. Thus the presence of ferrimagnetic component is established beyond doubt from these studies.

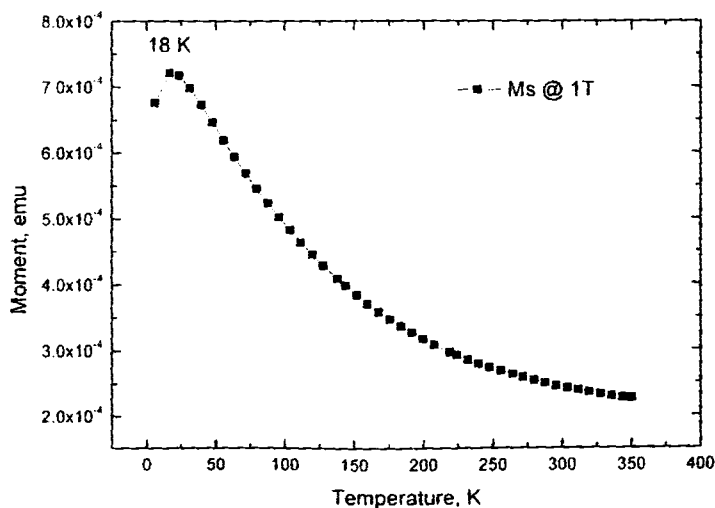


Figure 4.17: m-T graph of unmilled zinc ferrite

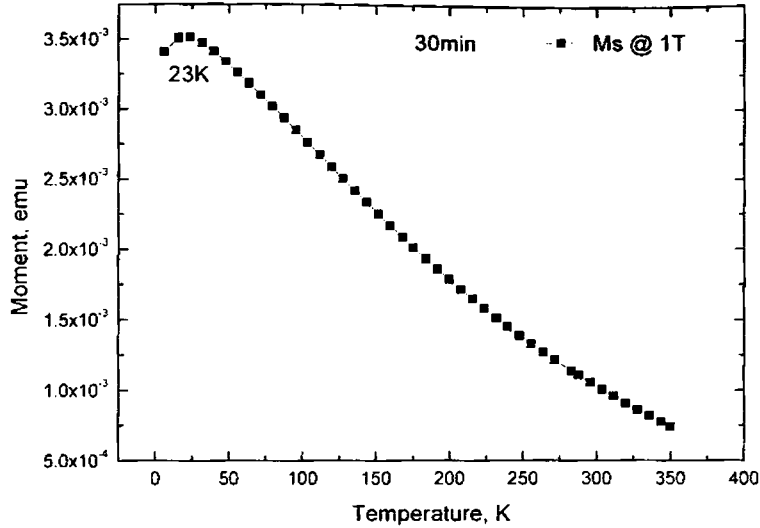


Figure 4.18: *m-T graph of 30-minute milled zinc ferrite*

4.7 Superparamagnetic behaviour and Langevin fit

The magnetization curve of a superparamagnetic material follows the Langevin function [22]

$$m = m_s \left(\coth y - \frac{1}{y} \right) \quad (4.1)$$

$$y = \frac{\mu H}{k_B T} \quad (4.2)$$

Here μ is the saturation magnetization of a single grain in the sample, H is the magnetizing field expressed in Tesla, k_B is the Boltzmann's constant and T is the temperature. In ball milled samples of zinc and cadmium ferrites, we have assumed that the net magnetic moment is due to the structural inversion that results when they are milled. So the total magnetic moment of a ferrite particle can depend on two factors. One is the total grain size, which goes on decreasing with the milling time. The second factor is the degree of inversion and which on the other hand, goes on increasing with milling time. Due to these two contradicting factors, the net magnetic moment cannot be calculated from the grain size alone. In addition to this, not all particles must have undergone inversion in equal amounts. It is evident from the SEM pictures that in milled samples certain grains have not undergone any breaking and some grains are well

broken. It is apparent from the magnetization curves that the samples do not attain magnetic saturation even at the maximum applied field of 15000 Oe. So the saturation magnetization of samples has to be determined before attempting the Langevin fit of the magnetization curve. Also it appears that there exists a permanent paramagnetic component in the samples, arising out of the un-reacted zinc and cadmium ferrites. This component is to be subtracted from the total magnetization before attempting any theoretical fitting of the data.

Assuming that the paramagnetic component remains a constant, the magnetization values of unmilled samples are subtracted from the total magnetization to get the corrected magnetization. The saturation magnetization is calculated by plotting the reciprocal of the applied field (H) against the magnetization, and by extrapolating the graph to $1/H=0$ assuming that at infinite applied field the sample is at saturation as depicted in figure 4.20. Figure 4.19 shows the correction applied on cadmium ferrite sample (as an example).

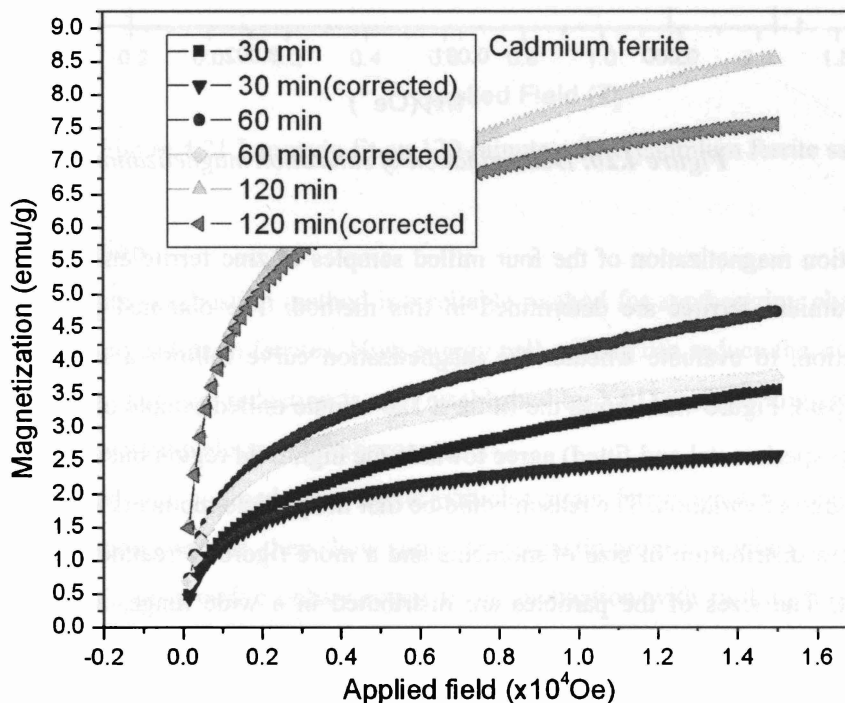


Figure 4.19: Magnetization graphs after applying correction for the paramagnetic components

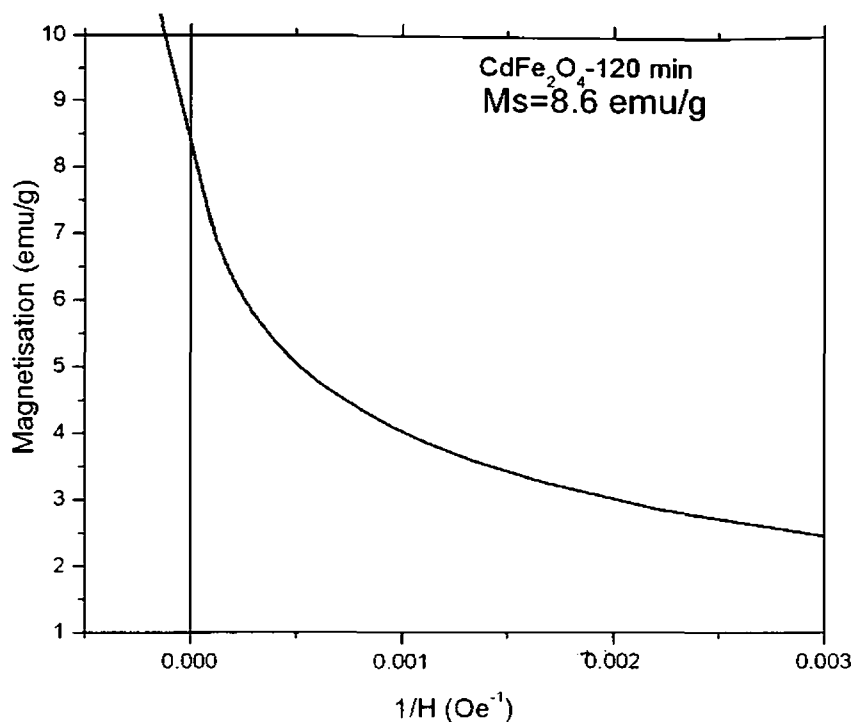


Figure 4.20: Determination of saturation magnetization

Saturation magnetization of the four milled samples of zinc ferrite and the three milled samples of cadmium ferrites are determined in this method. The obtained graph is fitted to Langevin function, to evaluate whether the magnetization curve follows a superparamagnetic magnetization path. Figure 4.21 shows the fit for a 120-minute milled sample of cadmium ferrite. The two plots (experimental and fitted) agree towards the high field region but at low fields there is a marked degree of variation. The reason could be that the particle moments are not a constant. There could be a distribution of size of moments and a more rigorous treatment is necessary to get a better fit. The sizes of the particles are distributed in a wide range, and the degree of inversion can vary from particle to particle. Still the fitted and experimental curves are in agreement at higher magnetic field where the contribution is from particles with larger magnetic moments.

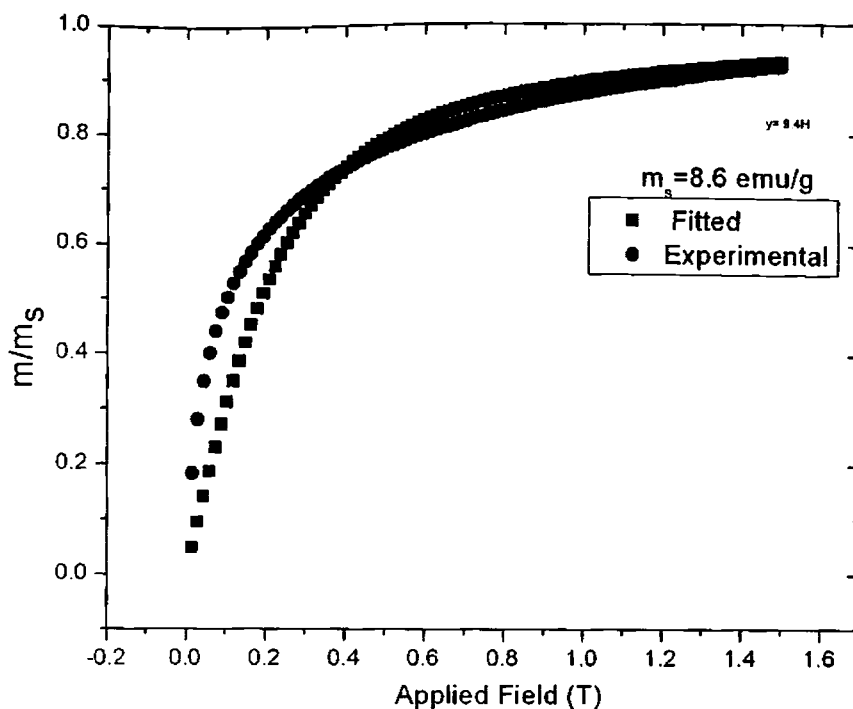


Figure 4.21 Langevin fit on 120-minute milled cadmium ferrite sample

4.8 Conclusion

Sol-gel auto-combustion method is a reliable method for synthesizing phase pure mixed oxides like zinc and cadmium ferrites. High energy ball-milling can reduce the size of the ferrite particles to 14 nm. The size reduction is well established by XRD analysis, transmission electron microscopy and scanning electron microscopy.

Ball-milled zinc and cadmium ferrite particles attain ferrimagnetic properties and being the particles at nanometer size, they show superparamagnetic properties when a magnetic field is applied. There is a progressive enhancement in magnetization with milling time. Inversion of spinel structure is attributed to the magnetic behaviour. But the formation of a amorphous impurity phase of iron oxides cannot be completely ruled out.

Further studies are required to give a clear cut picture about the mechanism in play of the enhancement of magnetic properties in ball-milled zinc and ferrite samples. Neutron diffraction studies and X-ray magnetic circular dichroism studies (XMCD) can give a conclusive

Chapter 4

evidence for the cause of the phenomenon because the former can reveal the existence of inversion in spinel structure and latter the presence of impurity presence of iron oxides in amorphous form.

References:

- 1 B. Viswanathan, V. R. K. Murthy, Ferrite Materials-Science and Technology, Narosa Publishing House, (1990) New Delhi
- 2 Katsuhisa Tanaka, Seisuke Nakashima, Koji Fujita, Kazuyuki Hirao, *J. Phys.: Condens. Matter* 15 (2003) L469
- 3 M. Yokoyama!, E. Ohta, T. Sato, T. Sato, *J. Mag. Mag. Mater.* 183 (1998) 173
- 4 T. Sato, K. Haneda, M. Seki, T. Iijima, *Appl. Phys. A* 50 (1990) 13
- 5 T. Kamiyama, K. Haneda, T. Sato, S. Ikeda, H. Asano, *Solid State Commun.* 81 (1992) 563
- 6 M K Roy, BidyutHaldar, H C Verma, *Nanotechnology* 17 (2006) 232–237
- 7 H. H. Hamdeh and J. C. Ho, S. A. Oliver, R. J. Willey, *J. Applied Phys.* 81 (1997), 1851
- 8 Z H Zhou , J M Xue, H S O Chan, *J. Appl. Phys.* 90 (2001) 4169
- 9 S A Oliver , H H Hamdeh, J C Ho, *Phys.Rev. B* 60 (1999) 3400
- 10 R. Valenzuela, *Magnetic Ceramics*, Cambridge University Press, 1994
- 11 Xiao-lan Song, Xi He, Hai-ping Yang, Yi-xin Qu, Guan-zhou Qiu, *Chin. J. Chem. Phys.* 21, (3), 2008, 205 (DOI:10.1088/1674-0068/21/03/295-300)
- 12 Jianjun Liu, Gongxuan Lu, Hongliang He, Hua Tan, Tao Xu, Kang Xu, *Mater. Res. Bull.*, 31 (9), (1996), 1049
- 13 Roman Klimkiewicz et al, *Mater. Res. Bull.* 44, (1), (2009), 15
- 14 J. R. Baker, U. S. Patent No. 3951869, 1976
- 15 C. Suryanarayana, M. G. Norton, *X-ray Diffraction-A Practical Approach*, Plenum Press, (1998), New York
- 16 Shanyi Du, Lin Xu, Xinghong Zhang, Ping Hu, Wenbo Han, *Mater. Chem. Phys.*, 116, (1), (2009), 76
- 17 K Kawano, M Hachiya, Y Iijima, N Sato, Y Mizuno, *J. Mag. Mag. Mater.*, 321, (16), (2009), 2488

- 18 U Schwertmann, R.M Cornell, *The Iron Oxides: Structure, Properties, Reactions, Occurrences and Uses*, Wiley-VCH, (2003) p. 81-92
- 19 C. N. Chinnasamy, A. Narayanasamy, N. Ponpandian, K. Chattopadyah, H. H Gu'erault, J. M. Greneche, *J. Phys. Condens. Mater.* 12 (2000) 7795
- 20 S. D. Shenoy , P. A. Joy, M. R. Anantharaman, *J. Magn. Magn. Mater.* 269, (2004) 217
- 21 Soshin Chikazumi, *Physics of Magnetism*, John Wiley and Sons, Inc (1964), New York
- 22 Stephen Blundell, *Magnetism in Condensed Matter*, Oxford University Press (2001) Oxford
- 23 B. D. Cullity, *Introduction to Magnetic Materials*, Addison Wesley Publishing Company (1972), London , p. 412
- 24 X. Gang et al, *Chin. Phys. Lett.*, 18, (5), (2001) 692
- 25 Jin Du, Yongqian Gao, Lanlan Chai, Guifu Zou, Yue Li, Yitai Qian, *Nanotechnology* 17, (2006) 4923
- 26 Subarna Mitra, K. Mandal, P. Anil Kumar, *J. Mag. Mag. Mater.*, 306 (2) (2006), 254

Chapter 5

Synthesis and characterization of nickel nanoparticles



5.1. Introduction

The synthesis of metal powders in nano phase has gained much importance in recent times. Sub micron and nano phased metal powders find wide applications in catalysis, as optical and magnetic recording media, superconductors, high performance engineering materials, dyes, pigments, adhesives, photographic suspensions, media for drug delivery etc [1-5]. Nanoparticles exhibit physical properties which are absent in the bulk material because of their high surface area to volume ratio. Smaller number of atoms in each particle modifies the energy band structure and thereby the absorption spectra. Magnetic metallic nanoparticles are of special interest since they are widely used in magnetic devices, and for numerous other applications [6-9]. Nickel nanoparticles can find applications in magnetic recording devices, catalysis, and paint industry. Single domain nickel particles dispersed in a suitable matrix show the tendency to form chains under the influence of a magnetic field altering the electrical conductivity of the matrix and this phenomenon can find application in fabricating magnetic field probes. Various techniques are employed for the production of metal nanoparticles like gas evaporation, sputtering, co-precipitation, sol-gel synthesis, hydrothermal synthesis, micro emulsion method and so on. Over the last two decades a great amount of work has been carried out on the synthesis of magnetic metallic nanoparticles owing to their unusual physical and chemical properties and their technological importance. Nickel nanoparticles assume a special importance in the regime of magnetic metallic nanoparticles. Many methods are available for the preparation of metal particles.

Chapter 5

Though many methods are available for the synthesis of nickel nanoparticles, not all can be adopted for the bulk synthesis. So emphasis was laid in developing a novel method which can be carried out in an ordinary laboratory and at the same time that can be scaled up to produce larger quantities of nickel particles. The method developed and going to be described here in this chapter is one such technique. This is carried out with an aim to synthesize chemically stable nickel particles which can be further employed for the preparation of rubber composites based on nickel and rubber. This chapter describes a novel method for the preparation of nickel nanoparticles. For continuity and clarity a report on the various methods of preparation of nickel particles is outlined in this chapter.

Reduction of nickel salts in aqueous solutions by suitable reducing agent is the most widely used method for the preparation of nickel particles. Metal particles are precipitated in the solution. Sodium borohydride and hydrazine hydrate are the common reducing agents used for the preparation of the nickel particles in precipitation methods. A suitable salt of nickel is dissolved in an organic solution like ethylene glycol and the control of pH is usually achieved by adding NaOH solution or liquid ammonia. Size control can be achieved by adding a surfactant like poly vinyl pyrrolidone and nickel particles as small as 10nm have been synthesized by this method. Size control of the precipitated particles can also be achieved by allowing the chemical reaction to take place in a micro-emulsion of oil in water [10, 11]

Polyol method is another commonly used method for the synthesis of nickel nanoparticles. In polyol method ethylene glycol acts as a solvent as well as a reducing agent. Again, particles of size smaller than 10nm are synthesized in polyol method also. Reflexion of the solution for long time, typically four to six hours, is required to complete the reaction in polyol method of synthesis [12].

There are quite a few reports on the preparation of nickel nanoparticles in spray pyrolysis method. A fine spray of nickel nitrate salt is sent to a reducing atmosphere like gaseous hydrogen or nitrogen, or a combination of both. This method is useful if a large quantity of nickel particles is required. A continuous production of nickel particles is possible in this method. A similar technique is employed in the gas-phase reduction synthesis of nickel nanoparticles from

nickel chloride. Some of the important methods in gas-phase reduction are laser assisted gas-phase photonucleation and hydrogen plasma metal reduction [13, 14].

In radiolytic reduction metal nano-clusters are induced by ion beam irradiation in aqueous solution as reported by Remita and Mostafavi [15]. They have prepared monometallic silver from aqueous solution of silver chloride by irradiating with C^{6+} ions. Formation of nanoclusters can be promoted by the irradiation of gamma rays and electron beams also. The reduction process yielding metallic nanoparticles is supported by the energy transfer between the incident ions and the reactants in the solution in which the precipitation of metal particles takes place. Similarly the reduction process to produce metal nanoparticles can be supported by electromagnetic radiation. Jose' H. Hodak et al reported the formation of metal nanoparticles induced by the irradiation using a laser beam in a reduction synthesis [16]. This kind of a process is known as photolytic reduction synthesis and silver and gold particles of the size 20 nm can be prepared by this technique. Reduction assisted by ultrasonic irradiation of solutions of metal salts is another widely used method for the synthesis of metal nanoparticles. Yoshiteru Mizukoshi et al reported the synthesis of metal nanoparticles by this sonochemical method and in this experiment an ultrasonic source of 200 KHz with a power of 200 W was used for irradiating the reactants [17]. Solvent extraction reduction method is another technique used for the production of metal nanoparticles.

Microemulsion technique is employed extensively for the preparation of nanoparticles in general [18, 19]. For this, microemulsions of water in oil are commonly used. This technique can well be used for the purpose of synthesizing nickel nanoparticles as well. D. Chen et al reported the preparation of nickel particles of the size of below 5 nm in this technique [20]. For this purpose two microemulsions of nickel chloride and hydrazine hydrate are separately prepared and these two microemulsions had been thoroughly mixed to allow the reduction reaction takes place. The size of the water particle forming the emulsion determines the size of the resulting particle.

The solution combustion method is very widely used for the synthesis of simple or mixed metal oxides. Recently a method very similar to the solution combustion method is reported by Ranjan K Sahu et al for the synthesis of nickel particles. In this method nickel powder is formed

Chapter 5

as a product of a microwave assisted combustion process using urea as the fuel for combustion. This is different from other methods since the nickel particles are not formed as a precipitate (21).

5.2 Experimental:

0.1 mole of $\text{Ni}(\text{NO}_3)_2 \cdot 6\text{H}_2\text{O}$ (Merck) was dissolved in 20 ml of ethylene glycol to form a concentrate solution at 50°C . The precursor was heated to boiling point on a hot plate, maintained at a temperature of 250°C placed in a fume cupboard. The temperature of the hot plate plays a key role in the rate of heating and a lower temperature result in the formation of nickel oxides. Ethylene glycol boils resulting in the formation of a gel and this gel expands and undergoes a violent exothermic reaction and a spongy gray material was formed in the beaker. The resulting material is a highly porous sponge like formation of metallic nickel. This nickel sponge was separated and ground in an agate mortar. They are characterized using various techniques like XRD, TEM, SEM, EDS, VSM and SQUID magnetometry.

5.3 X-ray Diffractometry

The X-ray diffraction measurements of the nickel sample were recorded on an X-ray diffractometer (Rigaku D-max-C) using $\text{Cu K}\alpha$ radiation ($\lambda=1.5406\text{\AA}$). The diffraction pattern is depicted in figure 5.1. The diffraction pattern is characteristic of an fcc phase of metallic nickel. Four characteristic peaks can be observed in the XRD pattern at $2\theta = 44.58, 51.9, 76.54$ and 93.2 and these values are matching with the reported XRD pattern of fcc structured nickel crystals [22]. Their corresponding miller indices are also indexed in figure 5.1 as 111, 200, 220 and 311. This result reveals that the nanoparticles resulted in the synthesis are pure nickel particles. The particle size was calculated from the value of full width at half maximum using Debye-Scherrer relation and it was found that the average particle size is 23.3 nm. The lattice constant of the sample was calculated using four main peaks in the XRD spectrum and it shows a slight contraction of the bonds compared to the reported values. Lattice constant of FCC structured nickel is 3.523 A as reported in ICDD database and our sample is showing a lattice constant of 3.517 A. Due to nanometer size, the co-ordination number of the surface atoms of the

nanocrystals decreases and this can result in a contraction of bonds and a decrease in the lattice constant. All peaks and peak-widths were determined by Providing Gaussian fit to the plotted curve at appropriate points using Microcal Origin, which is popular commercial software for plotting and analysis of graphs.

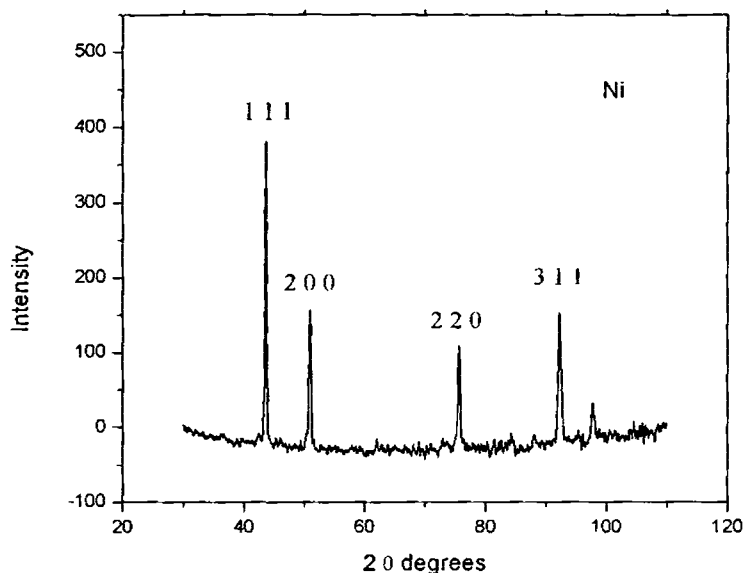


Figure 5.1:

X-ray diffraction pattern of the nickel nanoparticles

5.3 Magnetization studies

For the investigation of the magnetic properties of the nickel nanoparticles magnetic measurement were carried out on a Super-conducting Quantum Interface Device (SQUID) magnetometer at room temperature. Hysteresis loops were traced under a maximum applied field of 50000 Oe. Temperature dependent magnetization studies were conducted in the same equipment between from 5 K to 300 K at a field of 30 mT. The resulting hysteresis behaviour of the sample is as depicted in Figure 5.2. It can be observed from the hysteresis loop that the magnetization of the sample saturates at around an applied field of 7000 Oe as the curve becomes nearly parallel to the x-axis.

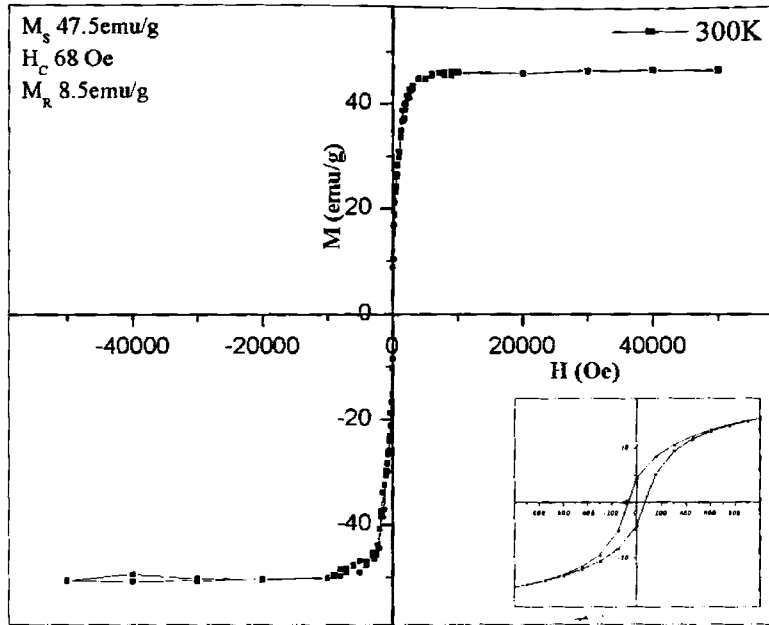


Figure 5. 2:

Magnetization versus magnetic field of nickel nanoparticles at 300 K

The sample at room temperature shows a saturation magnetization of 47.5 emu/g and this value of the saturation magnetization is nearly about 87 % of that of bulk nickel sample reported elsewhere [23]. The coercivity of the sample is found to be 68 Oe and the sample shows a remanence of 8.5 emu/g. The decrease in the saturation magnetization in nanosized samples is consistent with previous reports [24]. A number of reasons can be attributed for this phenomenon. Decrease in particle size increase the specific surface area of the particles. The disordered structure at interfaces can have less magnetic moment compared to the ferromagnetic core regions and thereby resulting a dead layer on the surface. Also the thermal fluctuations can reduce the magnetic moment as the magnetic energy of the nanoparticle becomes comparable to the thermal energy of the particles [25].

The coercivity of ferromagnetic nanoparticles has dependence on particle size. As the particle size increases the coercivity increase initially and then decreases after some critical

particle size [26]. This means that coercivity of nickel particle has a peak around this critical size where the particles undergo transition from single-domain to the multidomain nature. The critical size of nickel is 21.2 nm which had been calculated on the basis of the multidomain theory [27]. The average size of the particles is larger than the critical size for maximum coercivity and it can be assumed that the particles are not single domain particles. Comparatively smaller value of coercivity is justified due to this reason. Coercivity also has a dependence on the deviation of the particles from spherical shape. Due to the randomness in shape it will be difficult to calculate the exact contribution to anisotropy arising from the deviation of the nanoparticles from sphericity. The remnant magnetization of the sample is found to be 8.5 emu/g and this also agrees with previous published results [28].

5.4 Temperature dependent magnetization

For zero field cooled (ZFC) measurements the sample was cooled to 5 K before applying any magnetic field and magnetization of the sample was recorded in increasing temperature with a constant field of 30 mT. The field cooled (FC) measurements also were carried out in the same field. A magnetic cooling effect is evident from the graphs of ZFC and FC measurements Figure 5.3). The ZFC magnetization increases with temperature almost in a linear fashion, but the FC magnetization is almost a constant throughout in the temperature range with a slight tendency of decreasing magnetization with temperature. In ZFC magnetization a change of slope is observed below 150 K and this rate difference in rise of magnetization with temperature is typical of ferromagnetic nanoparticles [29]. The broad peak observed can be attributed to the antiferromagnetic ordering of the NiO coating formed on the nickel particles. The blocking temperature of these nickel particles is well above room temperature as it is evident from the high coercivity observed at room temperature. Zero field cooled magnetization studies on nickel particles by some researchers revealed that the blocking temperature increases with particle size and a size of 13 nm can give a blocking temperature of 338 K [28]. It is clear that the blocking temperature of the nickel particle studied is higher than this.

5.5 Transmission Electron Microscopy and EDS

The transmission electron micrograph of the nickel particles is given in figure 5.4. Due to the magnetic nature of the particles, they are agglomerated and a bundle like formation is observed in the micrograph. But uniform dispersion of particles can be observed within the bundle as can be clearly seen in the figure 5.4. Using a hard copy of the TEM picture the sizes of the particles are manually determined. Particles larger than the size of 45 nm are virtually absent and most of the particles are lying in the range of 15-40 nm. The particle distribution is represented in a bar diagram as shown as fig 5.6. The average particle size of the particles is determined by giving a Gaussian fit to the distribution and found to be 24 nm. This value is in very close agreement with the size determined from the XRD analysis.

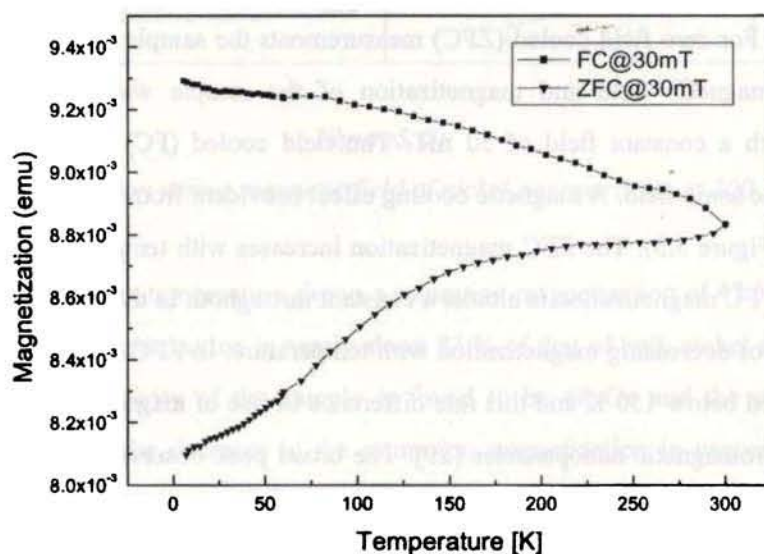


Figure 5.3:

Magnetization versus temperature of the nickel nanoparticles

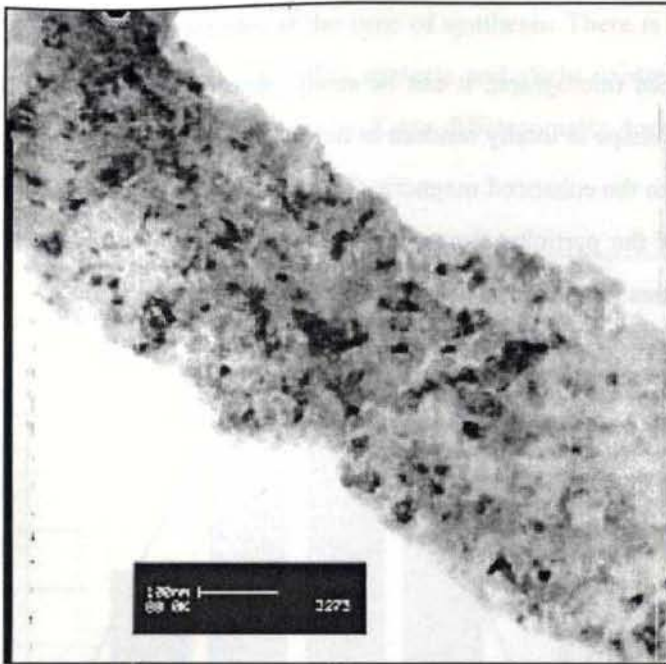


Figure 5.4:
Transmission Electron Micrograph of the nickel nanoparticles

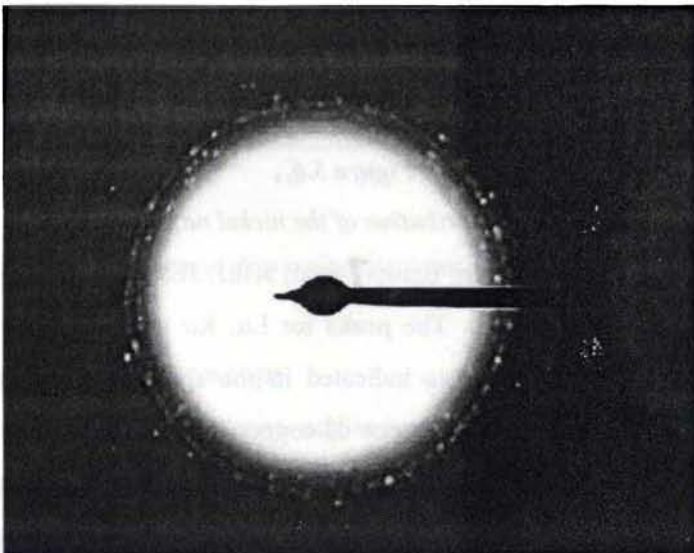


Figure 5.5: *Electron diffraction pattern of the nickel nanoparticles*

From the TEM micrograph, it can be easily observed that the particles are lacking any definite shape. Their shape is totally random in nature and as already mentioned this randomness in shape contributes to the enhanced magnetic coercivity of the nickel nanoparticles. The electron diffraction pattern of the particles shows well formed continuous circular rings as depicted in figure 5 which indicates that the particles are of nanometric sizes [24].

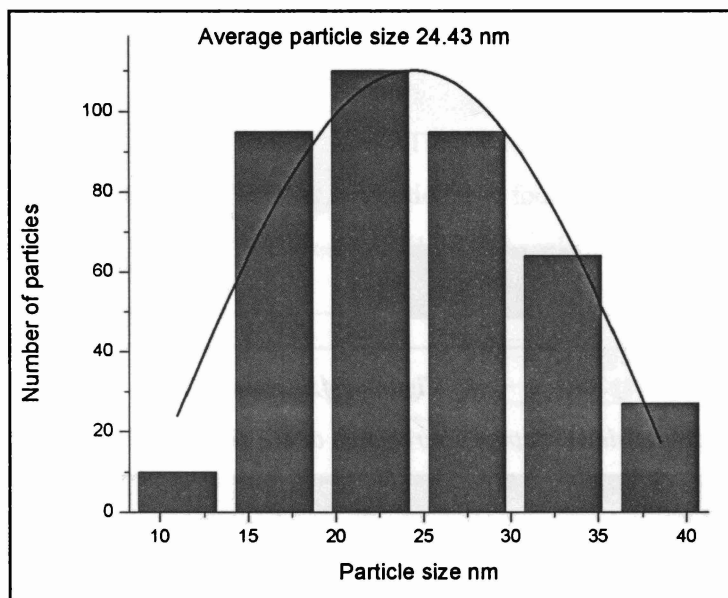


Figure 5.6

Particle size distribution of the nickel nanoparticles

The EDS spectrum presented in figure 7 from JOEL JEM 2200 FS Electron microscope clearly indicates the purity of sample. The peaks for $L\alpha$, $K\alpha$ and $K\beta$ lines of nickel is very prominent in the figure. Other elements indicated in the spectrum are Copper, Carbon and Oxygen in very small quantities. The presence of copper is from the copper grid in which the particles are suspended and carbon is from the organic medium in which the particles are suspended when the grids are prepared to be used in the electron microscope. The presence of oxygen, even though in very small quantity, might have arisen due to the presence of nickel oxide as a thin coating on the surface of nickel nanoparticles. Also there is the possibility of oxidation of nickel particles as they are exposed to air. A thin coating of nickel oxide in the form of NiO

might have formed on the nickel particles at the time of synthesis. There is a time gap of about two months between the synthesis and the EDS analysis and slight oxidation might have taken place by this time. But repeated analysis by X-ray diffractometry does not give any phases of oxides in the samples.

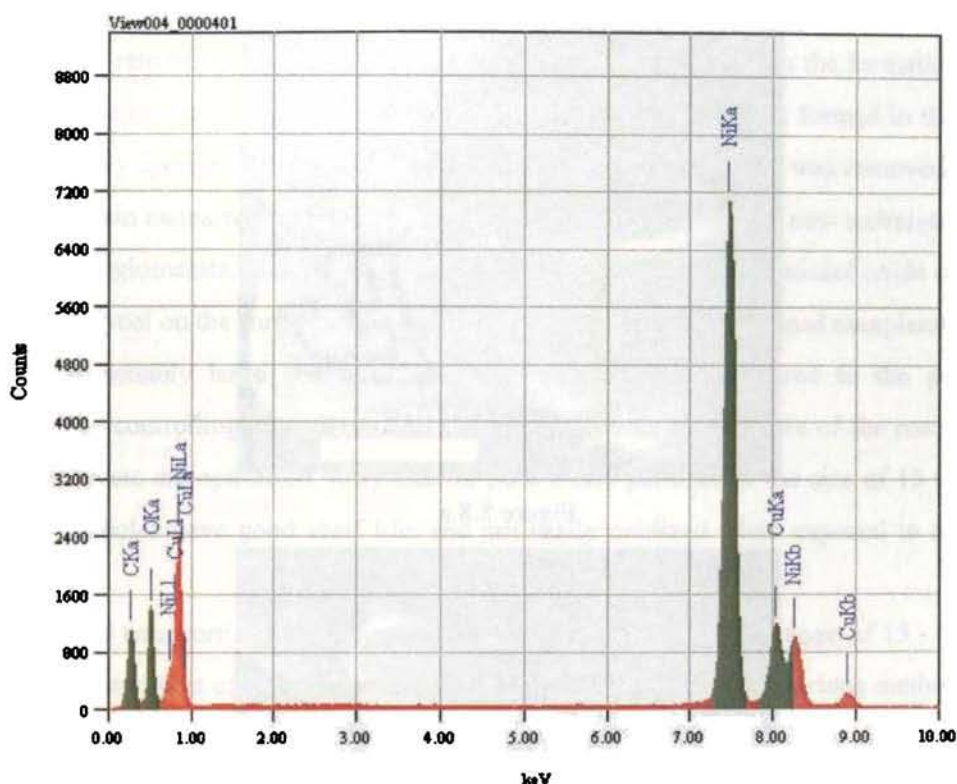


Figure 5.7: Electron dispersive spectrum of nickel nanoparticles

5.6 Scanning electron microscopy

The scanning electron microscopy studies were carried out on a Field emission scanning electron microscope (FESEM) JSM 6335 FESEM at 50 kV. Nickel particles were pressed to form thin metallic flakes for the SEM analysis. The SEM pictures are shown as figure 8a and 8.b. The shapes of the nickel particles are irregular as observed from the pictures. The particle sizes observed in SEM is a little higher than what obtained in the TEM pictures, and the reason for this

Chapter 5

increase in size may be that the particles were a little hard-pressed and flattened at the time of making them into pellets.

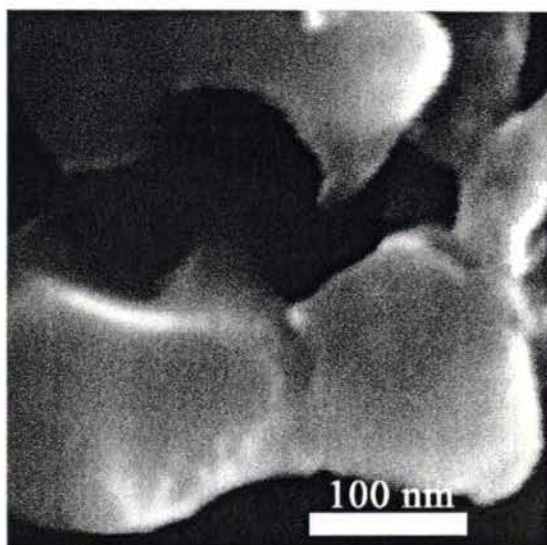


Figure 5.8.a

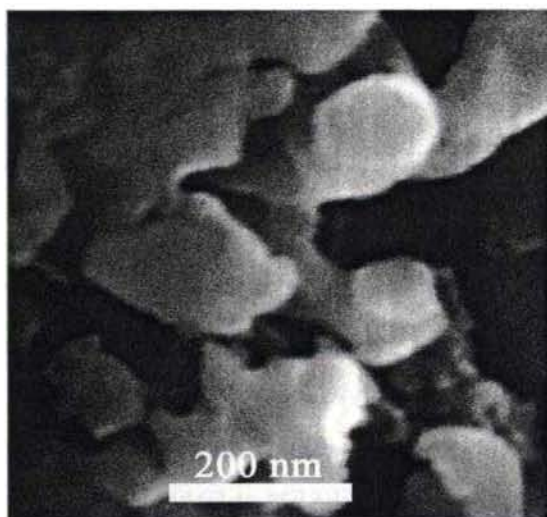


Figure 5.8.b

Figure 5.8.a and 5.8.b: Scanning electron micrographs of the nickel nanoparticles

5.7 Conclusion

Here is a modified method of combustion synthesis for the synthesis of nickel nanoparticles, in which ethylene glycol is used as the fuel for combustion and the method is comparatively simpler and does not require the assistance of microwaves. The key factor in this method is the rate of heating and a reduced rate of heating can result in the formation of nickel oxide. The separation of nickel particles is quite easy because nickel is formed in the form of a low density dry sponge with a lot of free space within and this sponge was removed and finely ground to obtain nanosized particles. These particles synthesized via the new technique shows no tendency to agglomerate, may be due to the formation of a thin layer of nickel oxide or a coating of ethylene glycol on the surface of the grains. This new method, developed completely in house, can give reasonably large quantities of nickel nanoparticles compared to the precipitation methods. The controlling parameters like pH of the solution, temperature of the reaction, initial concentration etc are optimized, to synthesize pure nickel particles of the size of 15 to 40 nm in size. The particles have good shelf life, and not easily oxidized when exposed to atmospheric oxygen.

Nickel nanoparticles were synthesized with particle size in the range of 15 - 40 nm by a novel, simple and cost effective chemical method. Characterizations by various methods confirm that the size of the nickel particles is in nano regime and they are crystalline in nature with face centered cubic structure. EDS analysis indicates that the particles are pure with only very small content of oxygen. Magnetic studies show that the sample is ferromagnetic with slightly decreased saturation magnetization in comparison to the bulk nickel sample and smaller coercivity and remnant magnetization. The method is very simple and can be reproduced easily and it opens up scope for further modification and bulk synthesis.

Chapter 5

References:

1. T. Hyeon : Chem. Commun. (2003), 927
2. A. P. Weber, M. Seipenbusch, G. J. Kasper: Nanoparticle Res.(2003), 5, 293
3. Guo, Q. Huang, X. Li, S. Yang: Phys. Chem. Chem. Phys.(2001) 3, 1661
4. X. W. Teng, H. Yang: J. Am. Chem. Soc.(2003), 125, 14559
5. Y. He, X. Li, M. T. Swihart: Chem. Mater., (2005), 17 (5), 1017
6. E. E. Crpender J. Magn. Magn. Mater.(2001), 225, 17
7. J. Shi, S. Gider, Babcock, D. D. Awschalom: Science (271) (1996), 937
8. S. A. Majetich, Y. Jin: Science 284 (1999), 470
9. L. Friebe, K. Liu, B. Obermeier, S. Petrov, P. Dube, I. Manner: Chem. Mater. 19 (10) (2007) 2630
10. Szu-Han Wu, Dong Hwang Chen, Journal of colloid and interface science 259 (2003) 282
11. Jung Woo Park, Eun H. Chae, Sang H. Kim, Jong Ho Lee, Jeong Wook Kim, Seon Mi Yoon, Jae-Young Choi, Materials chemistry and physics 97 (2006) 371
12. S. Ayyappan, G.N. Subbanna, R. Srinivasa Gopalan, C.N.R. Rao, Solid state ionics 84 (1996) 271
13. Yong Jae Suh, Hee Dong Jang, Han Kwon Chang, Dae Won Hwang, Heon Chang Kim Materials research bulletin 40 (2005) 2100-2109
14. Wei-Ning Wang, Yoshifumi Itoh, I Wuled Lenggaoro, Kikuo Okuyama, Materials science and engineering B 111 (2004) 69-76
15. H. Remita, I. Lampre, M. Mostafavi, E. Balanzat, S. Bouffard, Radiation Physics and Chemistry, 72 (5), 2005, 575
16. J. H. Hodak, A. Henglein, M. Giersig, G. V. Hartland, J. Phys. Chem. B 104 (2000) 11708
17. Y. Mizukoshi, K. Okitsu, Y. M. Takao, A. Yamamoto, R. Oshima, Y. Nagata, , J. Phys. Chem. B 101 (1997) 7033
18. D.E.Zang, X.M. Ni, H.G. Zheng, Y. Li, X.J.Zhang, Z.P Yang, Materials Letters 59 (2005), 2001 2014
19. I. Capek, Advances in colloid and interface science 110 (2004) 49-74

20. D. Chen, Szu-Han Wu, *Chem. Mater.*, 12 (5) (2000), 1354
21. R. K Sahu, A.K. Ray, S.K. Das, A.J. Kailath, L.C.Pathak, *J. Mater. Res.* 21 (7) 2006
22. JCPDS database, file no.03-1051
23. Gray D E: *American Institute of Physics Handbook* (1972) (McGraw Hill, New York)
24. C. Dong-Hwang, W. Szu-Han, *Chem. Mater.* 12 (2000), 1354
25. O. Masala , R. Seshadri: *Chem. Phys. Lett.* 402 (1-3) (2005) 160
26. B. D. Cullity, *Introduction to Magnetic Materials*, Addison Wesley Publishing Company (1972), London
27. Soshin Chikazumi: *Physics of Magnetism* p. 240, John Wiley , (1964) New York
28. Hanyu Wang, Xiuling Jiao, Dairong Chen: *J. Phys. Chem. C*, 112 (48) (2008), 18793
29. C. Prados, P. Crespo, J. M. González, A. Hernando, J. F. Marco, R. Gancedo, N. Grobert, M. Terrones, R. M. Walton, H. W. Kroto: *IEEE Trans. On Magnetics.* 37(4) (2001) 2117

Chapter 6

Preparation and cure, mechanical and magnetic studies on rubber-nickel nanocomposites

In this chapter the preparation and characterization of rubber-nickel nanocomposites is described in detail. Extensive studies have been conducted on the preparation and characterization of rubber-ferrite composites of natural and synthetic rubber, some of them by my co-researchers [1-4]. It has been proved beyond doubt that they are suitable for many potential applications like, microwave absorbers, flexible magnetic materials, magnetostrictive materials and high dielectric material. But not much work has been conducted on the metal rubber composites till date. The main constraint has been the difficulty in synthesizing stable metal nanoparticles in bulk quantities. A novel method for synthesizing nickel nanoparticles has been developed and the details were discussed in the previous chapter. This method is very simple, inexpensive and efficient. Nickel nanoparticles can be prepared in large quantities using this method [5].

In this work, nickel particles in the size range 15-40 nm are synthesized using a chemical method and their rubber composites are prepared using a specific recipe evolved by trial and error. Two elastomer matrixes are selected for the preparation of the composites. One is the natural rubber, as it is a commonly and cheaply available natural elastomer in the locality and the other is a particular variety of synthetic elastomer called neoprene. The synthetic rubber used in this study was chloroprene rubber grade W which is commonly known as neoprene. This is the rubber widely used for making O rings for air sealing and this particular rubber has superior mechanical properties when compared to natural rubber [6, 7].

6.1 Compounding recipes

Composites are prepared with blank rubber (gum vulcanazite) sample and for five different loadings of nickel nanoparticles from 20 phr (part per hundred rubber by weight) to 100 phr for both type of rubber. Selecting appropriate ingredients for curing rubber is important for preparing good quality rubber composites. The compounding recipe consists of chemicals which facilitate cross-linking of the polymer chains of the elastomers and agents which accelerate the cross-linking process. The most suitable recipes are evolved over time by trial and error. The recipes for compounding both varieties of rubber are given below in a tabular form (table 6.1). The mass of various ingredients are given for 100 g of rubber.

| Natural rubber | | Neoprene | |
|----------------|----------|------------------|----------|
| Ingredients | Weight g | Ingredients | Weight g |
| Natural rubber | 100 | Synthetic rubber | 100 |
| Zinc oxide | 4 | MgO | 4 |
| Steiric acid | 2 | Stearic acid | 1 |
| CBS | 1 | Filler (Ni) | phr |
| Filler (Ni) | phr | NA22 | 0.5 |
| Sulpher | 2.5 | ZnO | 5 |

Table 6.1: Compounding recipe

6.2 Mixing

Natural-rubber-nickel composites (NRNCs) as well as neoprene-rubber-nickel composites (NNCs) were prepared using the synthesized nickel powder and appropriate raw gum rubber samples. Appropriate recipes were chosen for both natural rubber and neoprene. The initial blending of the various ingredients with gum was done in a Brabender Plasticoder. A plasticoder is also called a torque rheometer, since it is used to measure the torque generated inside a polymer material, when the material is subjected to mastication, due to resistance [8]. Such measurements can be done under varied conditions of temperature and pressure. Plasticoder

is widely used in mixing, blending and for processability studies of polymers. It consists of a jacketed mixing chamber of approximately 40 cc of volume (model PL3S), fitted with two horizontal split rotors connected to a rotating shaft. A dynamometer balance shows the resistance offered by the test material undergoing mastication inside the jacketed mixing chamber. The speed of the rotors are controlled and displayed electronically and the temperature variation is achieved by a heating coil and controlling electronics. The rotors can be changed according to the nature and strength of the polymer used. The mixing of the rubber and the compounding materials was done according to the sequence prescribed by ASTM (ASTM D 3182, 1982). Rubber gum was charged into the mixing chamber and after the disappearance of the nerve of the rubber other compounding ingredients were added to the rubber. Both for natural rubber and neoprene composites, the mixing temperature was maintained at 60° C and at an angular speed of 50 rpm. The compound material is removed from the mixing chamber and further homogenization was carried out in a two-roll mill operated with a friction ratio of 1: 1.25. The compound was passed endwise six times through the two-roll mill, with a tight nip and finally rolled into a sheet by keeping the nip at a separation of 3 mm. These sheets are kept for 24 hours before evaluating the cure characteristics.

6.3 Cure analysis

The cure characteristics of the mixed composite were determined using circular sheets of the homogenized compounds cut in specific size placed in a rubber processing analyzer (RPA). RPA is a completely automated and highly sophisticated mechanical and rheological analyzer which can be used to determine the properties of polymers before, during and after the process of curing [8]. By measuring visco-elastic properties of rubber and other polymeric elastomers, RPA can provide key information on the processability of the compounds, their cure characteristics and of cured samples. Automatic temperature control with an accuracy of 0.5° C and homogeneous heat distribution is available inside the cure chamber. Shearing strain is applied on the circular sample using a pair of biconical dies, placed below and above the sample. The lower biconical die is oscillated using a direct drive servo motor system, whose frequency and angle of oscillation can be varied through a wide range of values. Throughout the experiment the frequency of the oscillation was kept at 50 Hz. The torque produced in the specimen due to the oscillation of the

Chapter 6

lower die through a small deforming angle is transmitted to the upper biconical die and a torque transducer on the upper die senses the torque accurately and passes on to a computer controlled measuring system for analysis. RPA can be used to make measurements of the properties of the samples under varied conditions such as fixed or varied strain, and all the conditions for measurements can be pre-programmed and automated. The data is used for real time display of the parameters in a graphical format using a computer program and also stored in the memory for future analysis.

In the present study cure characteristics of the composites were determined using a Rubber Processing Analyzer (RPA 2000 of α - technology), at a temperature of 150°C for natural-rubber composites and 160°C for neoprene-rubber by measuring modulus and torque against time at a pre-programmed strain. Different cure parameters outputs from the RPA are listed below.

- Minimum torque (D_{max})
Torque obtained by mix after homogenizing at the test temperature and before the onset of cure.
- Maximum torque (D_{min})
Maximum torque recorded at the completion of cure.
- Optimum cure time, t_{90}
This is the time taken for obtaining 90% of the maximum torque
- Scorch time, t_{10}
It is the time taken for two unit rise above minimum torque (i.e. about 10% vulcanization)
- Cure rate index
Cure rate index is calculated from the following equation

$$\text{Cure rate index} = \frac{100}{t_{90} - t_{10}}$$

Figure 6.1 shows a representative cure characteristic of nickel-rubber composites. The solid line is the cure rate curve and the broken line is the cure graph. Typically the torque decreases a little initially, for a very short duration and this is due to the decrease in viscosity through heating. On the onset of cross-linking, the torque starts to increase as the material becomes more resistant to shearing and torque reaches a maximum value. From the maximum

value of the torque, it decreases by very small amounts when the curing is complete. The cure time of the sample is given by time taken to reach 0.9 times the maximum torque. This is the time the sample is to be cured for preparing the rubber-nickel composites. The cure time may increase or decrease with the loading. In certain cases the filler material may act as a catalyst for the chemical reaction taking place during curing and in such cases the cure time decreases as the percentage of filler material increases in the composite. .

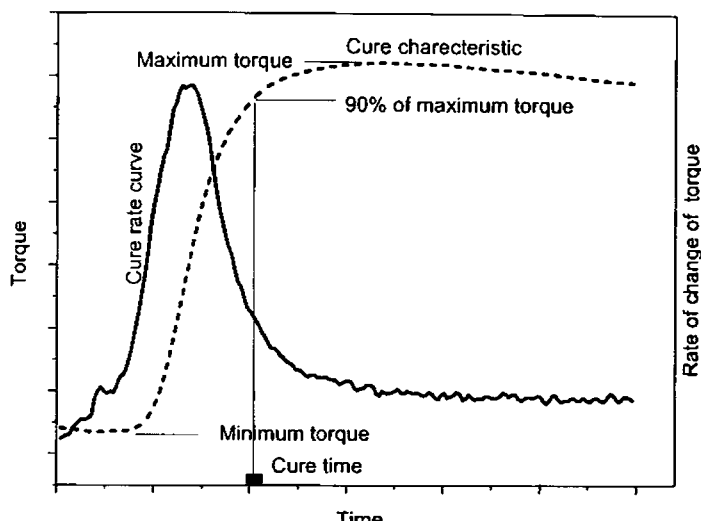


Figure 6.1 Typical cure characteristic of an elastomer

6.4 Cure characteristics of NRNCs

Figure 6.2 shows the cure characteristics of NRNCs for different loadings of nickel nanoparticles from 0 to 100 phr. There is a progressive increase in the maximum torque attained by the samples as the content of the nickel in the samples increases. The interaction between filler and matrix is better understood by analyzing the cure characteristics obtained from the RPA.

The cure parameters are shown in table 6.2. The maximum torque, that represents the shear modulus of the fully vulcanized rubber composites, increases with increase in loading of nickel. At the time of mixing due to the effect of high shearing forces the elastomer breaks down facilitating active sites on the molecules [9]. Rubber bound nickel particles formed by the

Chapter 6

interaction with active sites on polymer molecules cause the enhancement of shear modulus of the composites. This is a clear indication that the presence of nanometer sized nickel particles has a

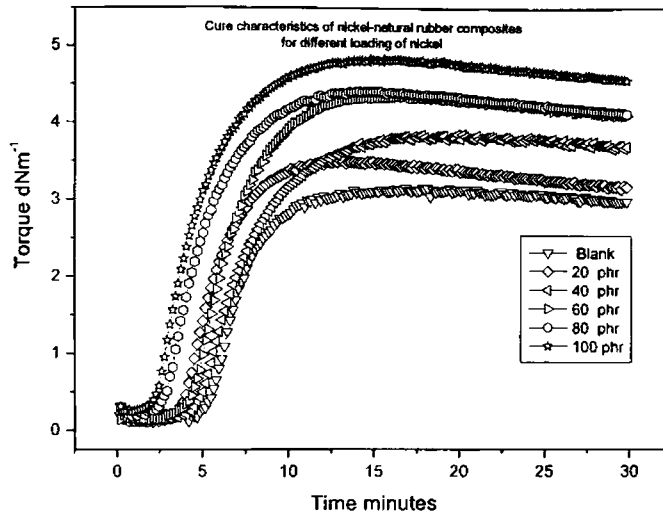


Figure 6.2: Cure characteristics of nickel-natural rubber composites

reinforcing effect in the natural rubber matrix. Minimum torque of the rubber compound is a measure of viscosity of the compound. In NRNC, the minimum torque remains almost steady up to filler loading of 60 phr and after that it registers an increase. The absence of large variations in minimum torque indicates that the processability of rubber is not hindered due to the addition of nickel nanoparticles. At higher filler ratios, the occlusion of rubber within and between filler aggregates may take place and causes immobility of elastomer layers resulting in an increase in minimum torque.

| Filler loading (phr) | 0 phr | 20 phr | 40 phr | 60 phr | 80 phr | 100 phr |
|----------------------|-------|--------|--------|--------|--------|---------|
| Minimum torque (dNm) | 0.153 | 0.101 | 0.127 | 0.13 | 0.179 | 0.251 |
| Maximum torque (dNm) | 3.095 | 3.4 | 3.8 | 4.32 | 4.4 | 4.8 |
| Scorch time (min) | 3.82 | 3.53 | 3.16 | 2.85 | 1.91 | 1.62 |
| Cure time (min) | 9.3 | 7.83 | 7.39 | 6.32 | 5.47 | 5.2 |

Table 6.2: Cure parameters of Natural rubber nickel composites

Torque variation in gum and filled compounds can be analyzed with the help of an equation proposed by Wolf and Westlinning [10, 11]. According to them the relative torque difference between minimum and maximum torques of the gum and filled compounds is directly proportional to the filler loading. The Wolf and Westlinning equation can be written as

$$\frac{D_{\max} - D_{\min}}{D_{\max}^0 - D_{\min}^0} - 1 = \alpha_F \frac{m_f}{m_p} \quad (6.1)$$

where D indicates the torques with the subscripts \max and \min for maximum and minimum and the superscript 0 for the blank rubber samples. The masses of filler and polymer in the compound are indicated by m_f and m_p respectively and α_F is a specific constant whose value can give some

indications about the final state of filler in the composites. The plot of $\frac{D_{\max} - D_{\min}}{D_{\max}^0 - D_{\min}^0} - 1$ against

$\frac{m_f}{m_p}$ is depicted in figure 6.3. The slope of this curve gives α_F and we have obtained a near

straight line graph passing closely through the origin and α_F is found to have an average value of 0.550 with an error of only 0.042. The variation in α_F is minimal and this indicates that the dispersion of nickel particles in the natural rubber matrix is uniform. The presence of nickel nanoparticles as filler in the natural rubber matrix does not produce any chemical interaction and the observed increase in maximum torque is purely because of physical reasons.

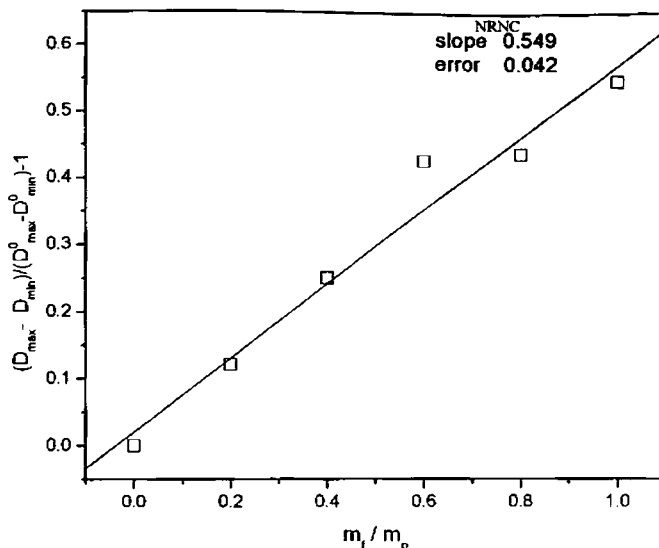


Figure 6.3: Wolf and Westlinning plot of NRNCs

The plot of difference in torque (Δ torque) with filler loading (figure 6.4) is also a near perfect straight line, again a clear indication of chemically non-interacting filler in the matrix. Due to low volume ratio of nickel particles resulting from its high density, inter particular attachments of polymer chains may be absent at all loadings, and this can be another reason for the linear variation of torque difference with the filler loading.

The cure time of NRNC shows a steady and linear decrease with filler loading as given in table 6.2. The cure time for gum compound was found to be 9.3 minutes and for the compound with 100 phr, the cure time decreases to 5.2 minutes. It was observed that, though the maximum torque increases with filler loading, the time taken to reach the maximum torque decreases sharply. Nickel is a well-known catalyst used in many organic chemical reactions [12]. The presence of fine particles of nickel appears to activate the process of cross-linking of natural rubber and the observed decrease in cure time is due to the catalytic action of nickel particles in the curing reaction. The cure rate index (CRI) of the NRNC compounds is depicted in figure 6.5 and shows a sharp increase initially, up to a filler loading of 60 phr and afterwards it shows a decrease. A decrease in CRI is because of the wetting of the surface of filler particles by the elastomer molecules [8, 13]. The volume fraction of nickel particles is small as already pointed out and the

wetting effect cannot produce any significant decrease in CRI in the initial stages. The decrease in CRI at higher filler loadings is an indication of such wetting becoming significant when the volume fraction increases. The variation of scorch time with filler loading is given in table 6.2 1 and the decrease in scorch time is mainly due to the activation in cross-linking reaction by the presence of fine particles of nickel.

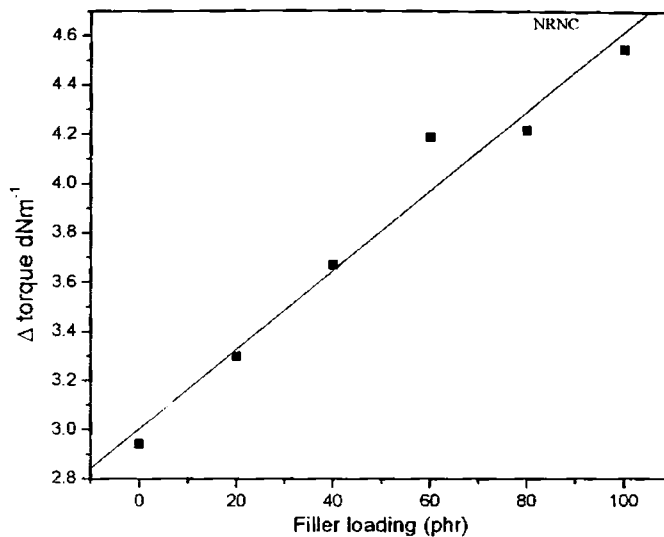


Figure 6.4: Variation of torque difference with filler loading (NRNCs)

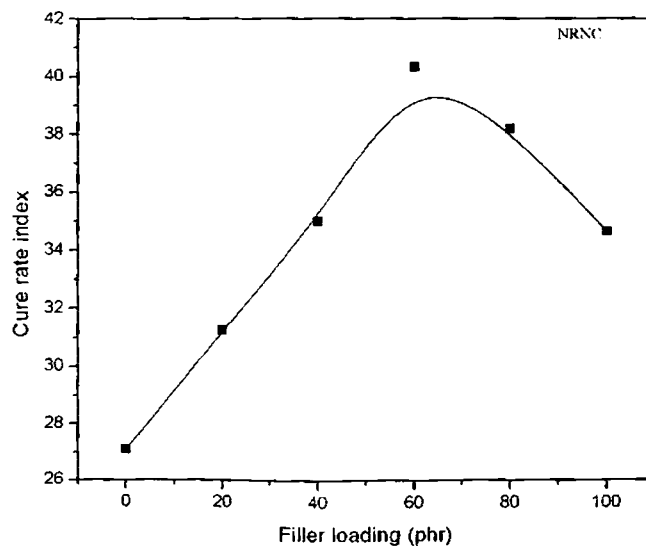


Figure 6.5: Variation in cure rate index with filler loading (NRNCs)

6.5 Cure characteristics of NNCs

As shown in figure 6.6 there is progressive increase in the maximum torque in the case of nickel-neoprene composites also. There is a rapid increase in the maximum torque from 60 phr of nickel onwards. The maximum torque shows a complete saturation in 0, 20 and 40 phr samples only. Other samples do not show saturation of torque but show a slight positive slope even after a time of 30 minutes. There is a progressive increase in the cure time with the percentage of nickel content.

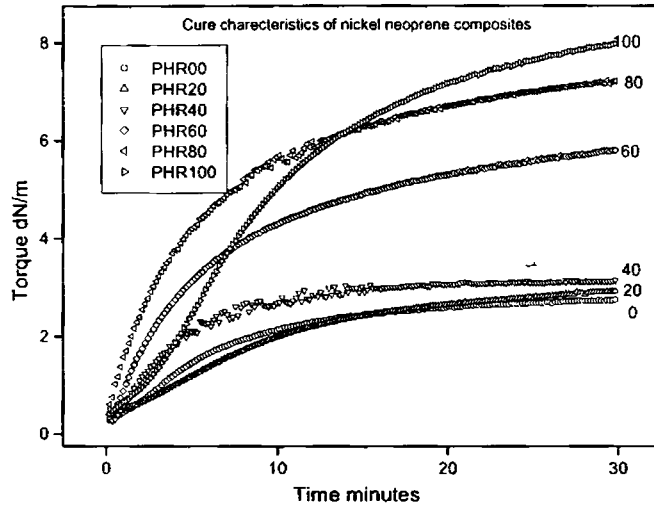


Figure 6.6: Cure graphs of NNCs

The main features of the cure characteristics of NNC are presented in table 6.3. The variation of minimum torque and maximum torque of the NNC during the process of curing is shown in this table. The maximum torque increase steadily with nickel loading and in neoprene rubber matrix also the fine particle nickel act as a reinforcing agent. But at 100 phr loading, maximum torque drops slightly and this may due to the effect of agglomeration at high volume fraction of filler. The minimum torque also increases with the loading of filler particles and the effect is almost similar to NRNCs. The steady increase in minimum torque can be attributed to the immobilization of elastomer chains at the surface of the filler particles.

| | | | | | | |
|----------------------|-------|--------|--------|--------|--------|---------|
| Filler loading (phr) | 0 phr | 20 phr | 40 phr | 60 phr | 80 phr | 100 phr |
| Minimum torque (dNm) | 0.275 | 0.29 | 0.422 | 0.425 | 0.53 | 0.536 |
| Maximum torque (dNm) | 3.161 | 4.399 | 4.929 | 5.815 | 7.845 | 7.24 |
| Scorch time (min) | 0.99 | 1.03 | 0.88 | 1.11 | 1.01 | 0.75 |
| Cure time (min) | 11.16 | 15.27 | 16.08 | 19.02 | 21.13 | 22.3 |

Table 6.3 Cure parameters of Neoprene-rubber nickel composites

The plot of $\frac{D_{\max} - D_{\min}}{D_{\max}^0 - D_{\min}^0} - 1$ against $\frac{m_f}{m_p}$ as depicted in figure 6.7 is a straight line

passing very nearly through the origin (zero). The average value of the constant α_f is 1.46 with

an error of only around 0.2. The linear behaviour of the plot between $\frac{D_{\max} - D_{\min}}{D_{\max}^0 - D_{\min}^0} - 1$ against

$\frac{m_f}{m_p}$ is a clear indication of non interacting filler particles. As in the case of NRNC samples the

plot of Δ torque with loading also is a straight line and is given in figure 6.8

The variation of cure behaviour of neoprene rubber composites is totally different from that of natural rubber composites. The cure time in NNC steadily increases with the filler content. In NNCs there is a steady increase in the maximum torque with the increase in filler loading. It is obvious that the cross-linking process in neoprene is not catalysed by nickel. The maximum torque and the cure time increases almost in the same ratio since the time taken to reach maximum torque increases as there is enhancement in maximum torque. Cure rate index (CRI) of neoprene composites shows a decrease with the increase in the filler content as depicted in figure 6.9 The wetting of surface of the particles is more effective in neoprene in comparison to natural rubber. The neoprene polymer chains are smaller than that of natural rubber and this may be a reason for the enhanced wetting of particles by the polymer in the case of neoprene.

Chapter 6

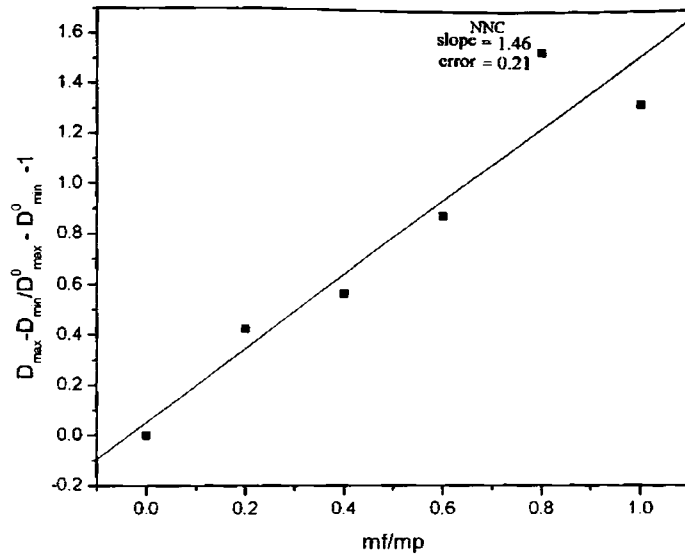


Figure 6.7 Wolf and Westlinning plot of Neoprene-rubber nickel composites

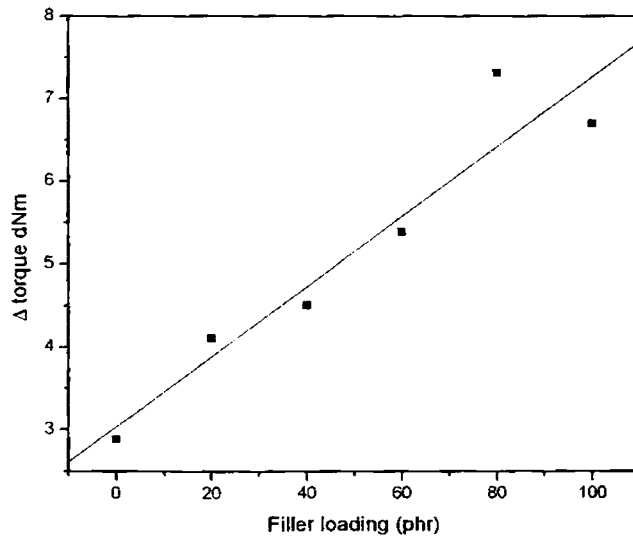


Figure 6.8 Variation of torque difference with filler loading (Neoprene-rubber nickel composites)

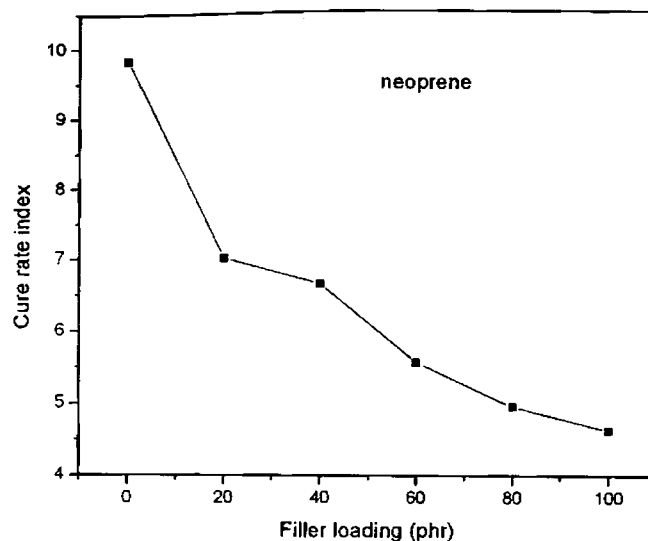


Figure 6.9: Variation in cure rate index with filler loading (Neoprene-rubber nickel composites)

6.6 Moulding of the composites

Nickel rubber composites are moulded in the form of thin sheets of 10cm x 7.5cm x 2 mm size using dies made of stainless steel. An electrically heated hydraulic press is used for the compression moulding and curing of the test specimens. This hydraulic press has platens of size 45 x 45 cm and a pressure of 140 kg cm⁻² was applied on the rubber sheets undergoing curing and moulding. The natural rubber composites had been moulded at a temperature of 150°C and the neoprene samples at 160°C. On completion of the required cure time, as determined from the cure time analysis, the pressure was released and the sheet was removed off from the mould and suddenly cooled by dipping into cold water and stored in a cool dark place. Twelve specimens were prepared in all; six in each category of rubber and these specimens were used for the subsequent analysis and characterization.

6.7 X-ray diffractometry

Twelve samples of rubber-nickel composites were prepared, six in each type of rubber, from varying loading percentages from 0 phr to 100 phr. The rubber-nickel composite samples were subjected to structural characterization immediately after they were moulded into sheets

Chapter 6

using X-ray diffractometry and the resulting XRD patterns are shown in figure 6.10 (NRNCs) and in figure 6.11 (NNCs). The characteristic peaks of nickel are clearly visible in all the samples [13]. In the sample of 0 phr (blank rubber) a broad peak centered approximately at 22° of 2θ is observed in both types of samples and this is due to the short range orientation of polymer molecules of cured rubber [14, 15]. Diffraction peaks marked 1 to 5 are due to various curing agents remaining unreacted in the blank rubber. The broad peak at 22° vanishes as we increase the content of nickel since the large diffraction peaks of crystalline nickel with fcc structure becomes predominant. There are no shifts in the positions of the diffraction peaks of the nickel and this indicates that no structural change has occurred to the nickel particles due to the heat treatment. Peaks corresponding to NiO are present in the pattern and this indicates the presence of trace amounts of NiO which had arisen due to the heat treatment at 150°C and 160°C or the heat generated while mixing. But this presence of NiO did not affect the magnetic properties of the composites in any significant manner.

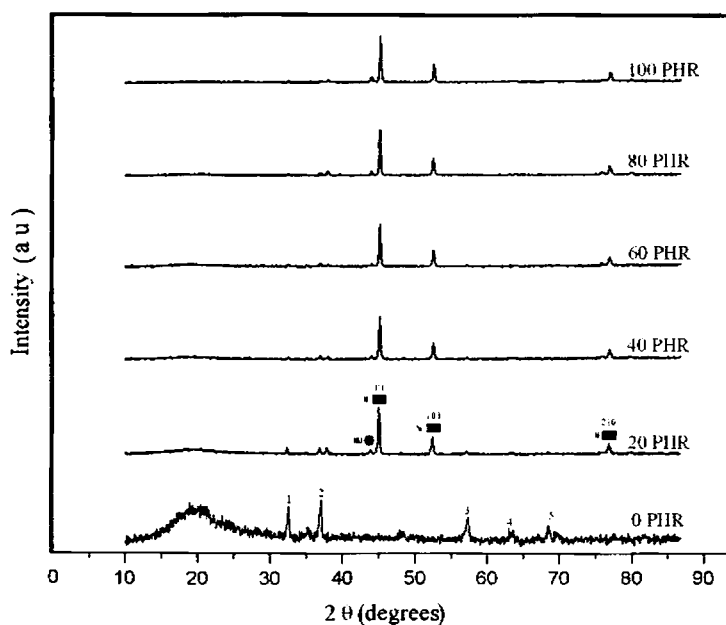


Fig 6.10: XRD pattern of Natural rubber nickel composites

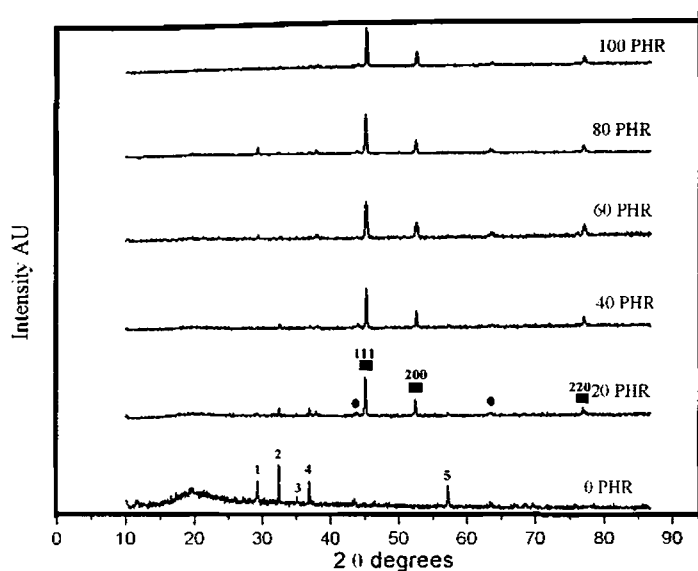


Fig 6.11: XRD pattern of Neoprene-rubber nickel composites

6.8 Mechanical properties

Evaluation of the mechanical properties of the rubber-nickel composites are carried out using a UTM (universal testing machine), model Instron 4500. Dumb-bell shaped sample pieces are cut using a sharp die with a cross section of 2mmx2mm. Parameters namely tensile strength, modulus at different strains and elongation at the breaking point, which are some of the most important indications of the mechanical strength of the material were determined and the variations in these properties with loading were studied for both natural rubber and neoprene composites. An evaluation of these properties of NRNCs and NNCs is given in the following sections.

The restoring stress developed inside the material for a particular strain is a good indication of its mechanical strength. In figure 6.12 the stress of NRNCs for different strains are shown for various filler loadings [15, 16-18].

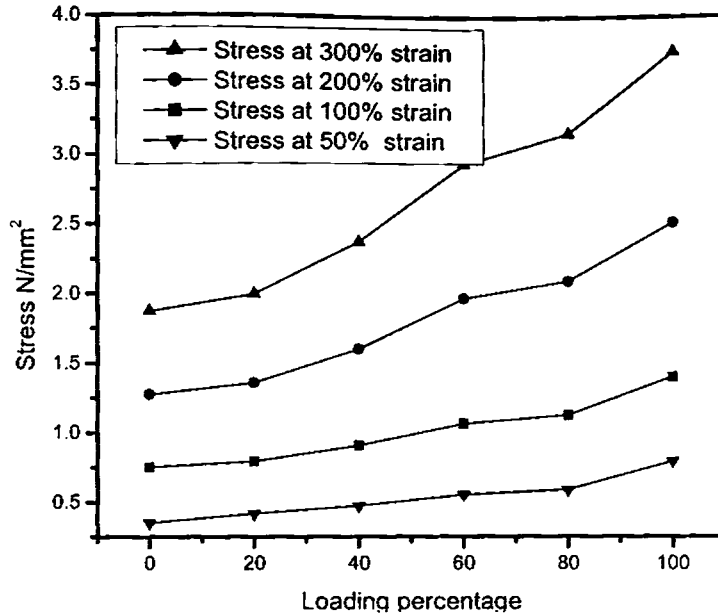


Fig 6.12 Elastic properties of nickel natural rubber composites for different loading of nickel

It can be observed that the stress increases with the filler loading for all strains starting from 50% elongation of the original length to 300% elongation. So it is clear that the incorporation of nickel nanoparticles in natural rubber matrix enhances its mechanical property. But there is a steady decrease of stress at the breaking point (breaking stress) with the filler percentage as indicated in figure 6.13. The reason for this may be the microscopic discontinuities introduced in the matrix material due to the presence of the filler material. But the materials are not strained to the breaking point in its ordinary applications, and the lowering of breaking stress is not a flaw for the material in comparison to the increased elastic properties at different strains, from 50% to 300%. Again, from figure 6.14 it is clear that the strain at breaking point also decreases with the filler loading. But even at the minimum strain (for the 100 phr sample) the sample can be stretched to a length of 7.5 times the original length. The decrease in breaking stress is actually due to the fact that at higher loadings the composite breaks at lower elongations. Formations of agglomerations of nickel inside the composite material can be a reason for breaking at lower elongations

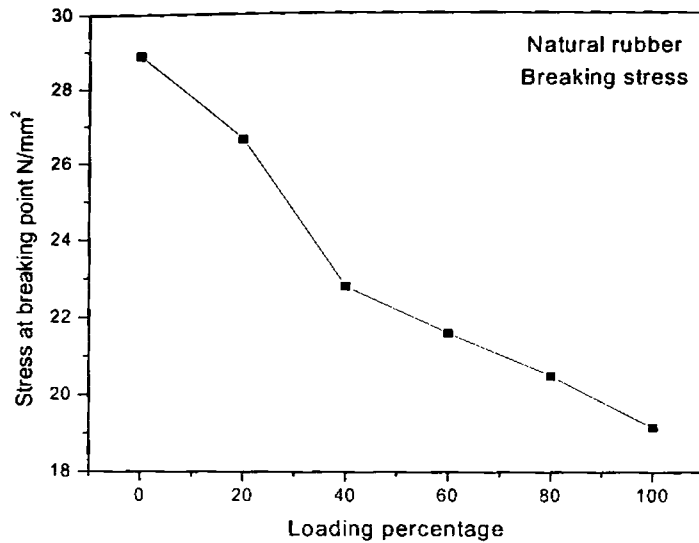


Figure 6.13: Variation of breaking stress with loading

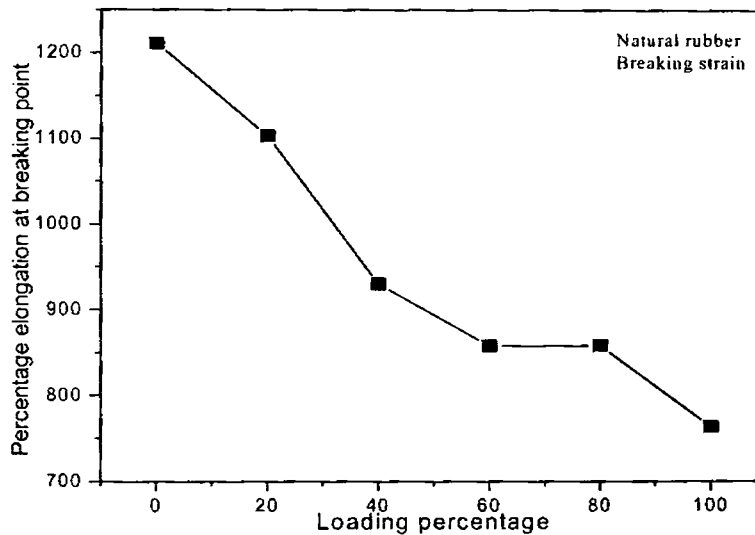


Figure 6.14: variation of breaking strain with loading in nickel-natural rubber composites

The mechanical properties of NNCs are more or less similar to the properties of NRNCs. If we examine the stress at different elongations (figure 6.15) it can be seen that it increases with the loading. As in the case of natural rubber, the presence of nickel in the matrix reinforce the

matrix and enhance elastic modulus. Neoprene-rubber sheets become mechanically strong as the percentage of nickel nanoparticles increases in it. At the same time the breaking stress and breaking strain decrease with the percentage of nickel nanoparticles in the composites (figures 6.16 and 6.17). All the reasons proposed for the nickel natural rubber composites can be attributed to neoprene rubber too. But it is clear that these changes in the mechanical properties are actually determined by nickel nanoparticles as filler rather than the matrix material since the same kind of behavior is observed in both matrixes.

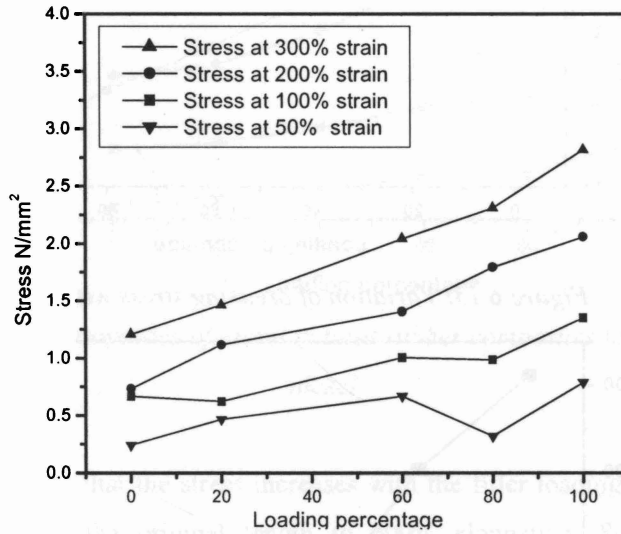


Fig 6.15: Elastic properties of NNCs for different loading of nickel

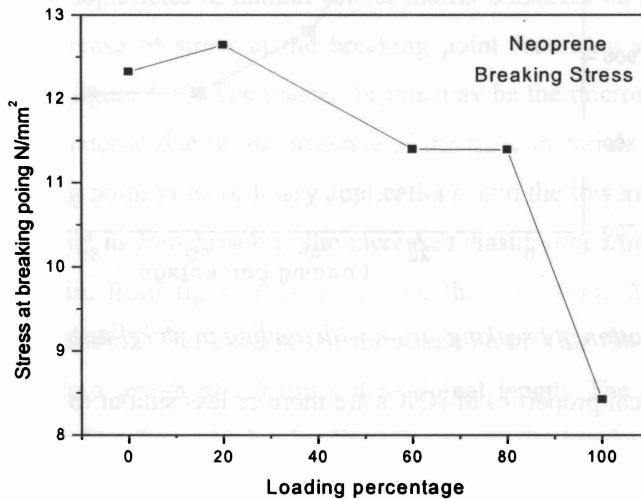


Figure 6.16: Breaking stress of NNCs with filler loading

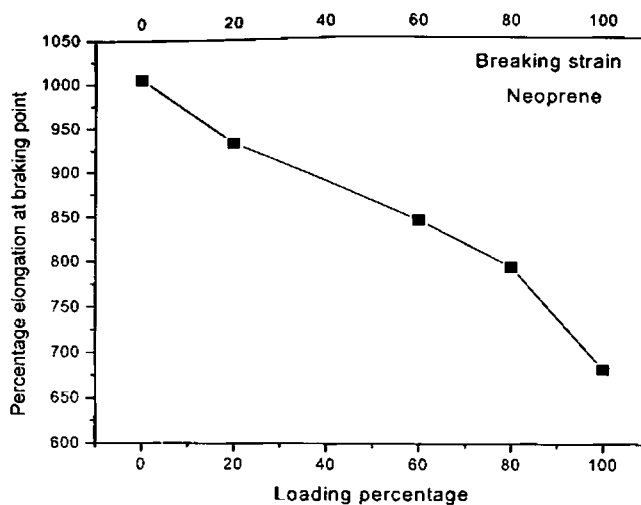


Figure 6.17: Variation of breaking strain with loading of Neoprene-rubber nickel composites

6.9 Magnetic properties of NRNCs and NNCs

The magnetic properties of the nanocomposites were determined by an EG&G PAR 4500 Vibrating Sample Magnetometer at room temperature with a maximum magnetic field of 15000 Oe with increments of 150 Oe. Hysteresis loops are plotted for all the samples.

The magnetic properties of cured rubber samples clearly indicate that the ferromagnetic characteristics of nickel particles are retained in the NRNC and NNC samples. Figure 6.18 and 6.19 depict the magnetic hysteresis of NRNC and NNC samples respectively. A steady increase in saturation magnetization with increase in filler fraction can be observed in both composite samples from the magnetization curves and the magnetic properties are identical in both types of composites.

The magnetic properties of NRNCs and NNCs were evaluated under similar conditions. It was observed that the coercivity of the samples did not show any variation with the concentration of nickel particles in the composites. Further the coercivity values remain nearly the same in both series of composites as depicted in figure 6.20 and 6.21 which are the enlarged central region of the magnetic hysteresis loop. The reason for a small enhancement in the coercivity observed in NRNCs is not clear. However it could be due to the higher shear modulus

of natural rubber compared to neoprene rubber. The remanent magnetization keeps a linear variation with the increase in concentration of nickel nanoparticle again keeping exactly the same characteristics in both composite types.

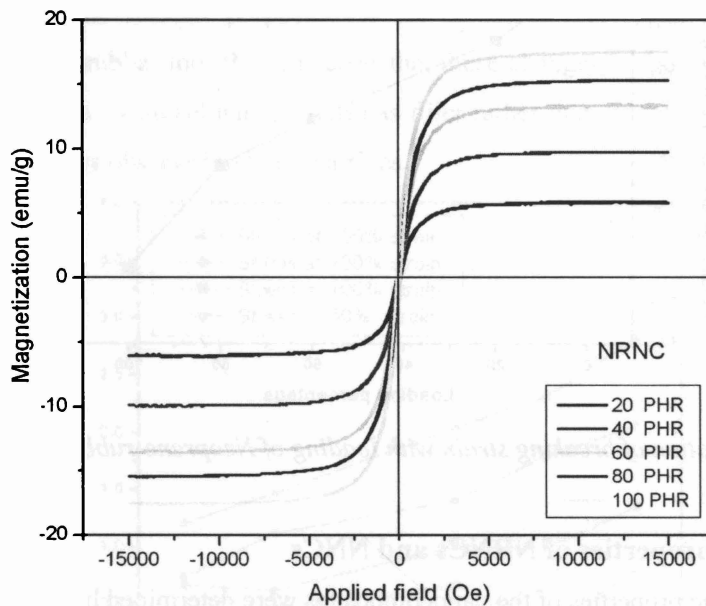


Figure 6.18: Magnetic hysteresis of Natural rubber nickel composites

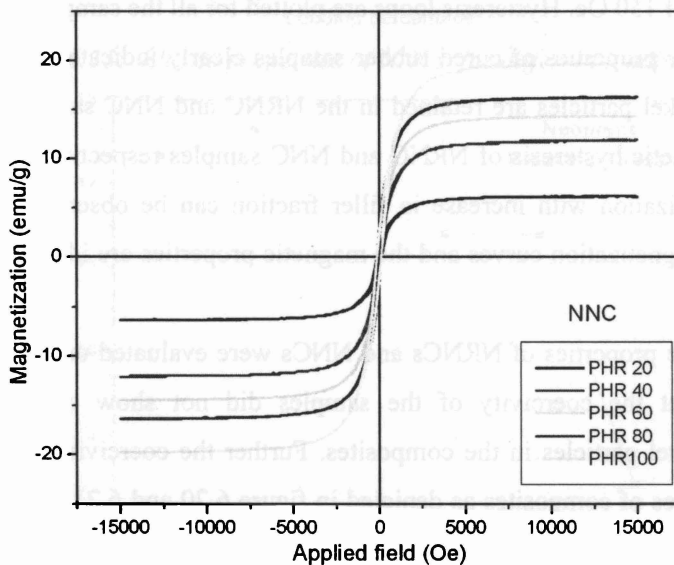


Figure 6.19: Magnetic hysteresis of NNC samples

| Sample phr (mass of nickel in 100g rubber) | Total mass (Nickel + rubber + curing agents) | Calculated magnetization emu/g | Observed magnetization emu/g |
|--|--|-----------------------------------|---------------------------------|
| 20 | 129.5 | 7.4 | 7 |
| 40 | 149.5 | 12.8 | 11 |
| 60 | 169.5 | 16.9 | 14 |
| 80 | 189.5 | 20.2 | 17 |
| 100 | 209.5 | 22.9 | 20 |

Table 6.4: The calculated and observed saturation magnetizations of NRNC samples

| Sample phr (mass of nickel in 100g rubber) | Total mass (nickel + neoprene + curing agents) | Calculated magnetization emu/g | Observed magnetization emu/g |
|--|--|-----------------------------------|---------------------------------|
| 20 | 130.5 | 7.4 | 7.1 |
| 40 | 150.5 | 12.8 | 11.6 |
| 60 | 170.5 | 16.9 | 14.3 |
| 80 | 190.5 | 20.2 | 18.2 |
| 100 | 210.5 | 22.9 | 20.7 |

Table 6.5: The calculated and observed saturation magnetizations of Neoprene- rubber nickel composites

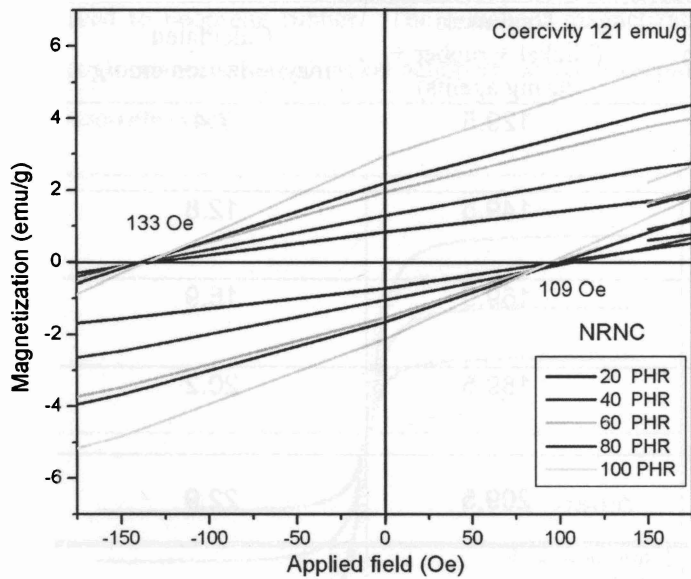


Figure 6.20: Central region of the magnetic hysteresis of Natural rubber nickel composites showing the coercivity and remanant magnetizations

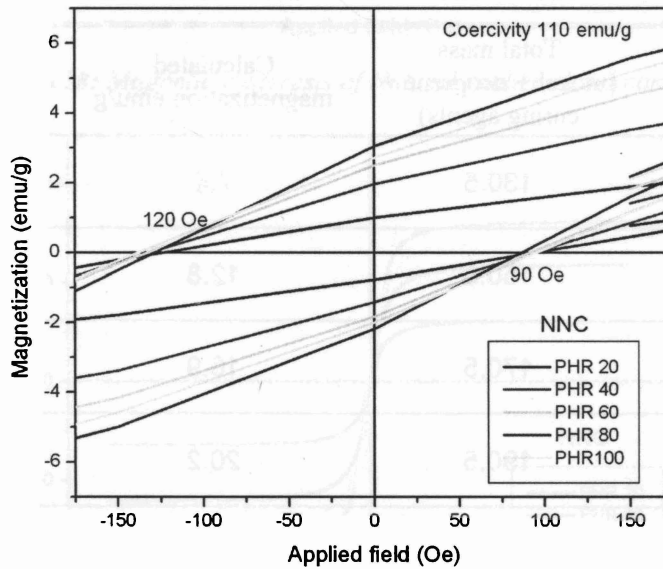


Figure 6.21: Central region of the magnetic hysteresis of Neoprene-rubber nickel composites showing the coercivity and remanant magnetizations

Evaluation of the magnetic properties of the nickel-rubber and nickel-neoprene composites reveals that the magnetic properties of the filler particles are completely retained in the composites. The calculated values of saturation magnetizations in composites are presented in Table 6.4 and 6.5 (NRNCs and NNCs respectively) along with the measured saturation magnetization of each sample of composites. It can be observed that these two values are in good agreement. These composites can act as flexible magnetic materials and can be permanently magnetized.

6.10 Conclusion

. The cure characteristics of natural-rubber-nickel and neoprene-nickel nanocomposites were evaluated and the cure properties of these two series of composites were compared. There is an increase in the maximum torque values in both series of composites and this establishes the reinforcing effect of nanoparticles of nickel in elastomeric matrices. The variation in Wolf and Westlinning constant is minimal in both the composites and this shows that the dispersion of nickel in natural rubber and neoprene rubber matrices is uniform and filler elastomer interaction is totally absent. The presence of nickel nanoparticles in the matrices doesn't produce any chemical interaction and the observed increase in maximum torque is purely due to certain physical reasons. The curing process of natural rubber appears to be catalysed by the presence of nickel particles and such an effect is not observed in neoprene rubber composites. Incorporation of nickel nanoparticles had improved the elastic modulus of both natural rubber and neoprene band nanocomposites. The saturation magnetization and the remanence of the composites increase in a linear fashion with the concentration of nickel particles. The coercivity of the samples remains a constant in all samples in both of the series of composites. Thus incorporation of nickel nanoparticles in matrices like natural rubber and neoprene rubber can result in magnetic nanocomposites with the required mechanical and magnetic properties. This can be achieved by tuning the loading of the fillers. Further they can also be potential materials for microwave absorbers.

Chapter 6

References

1. Anantharaman, M.R.; Sindhu, S.; Jagathesan, S.; Malini, K.A.;Kurian, P: J. Phy. D. Appl. Phy. 1999, 32, 1801
2. Mohammed, E.M.; Malini, K.A.; Joy, P.A.; Kulkarni, S.D.; Date, S.K.; Kurian, P.; Anantharaman, M.R: Plas. Rubb. Comp. 2002, 31 (3), 106
3. M.A Soloman, P. Kurian, M. R. Anantharaman, P. A. Joy: Polymer-Plastics Tech. Eng. 2004, 43 (4), 1013
4. K A. Malini E. M. Mohammed, S. Sindhu P. A. Joy, S. K. Date, S. D. Kulkarni P. Kurian, M. R. Anantharaman: J. Mat. Sci. 2001, 36, 5551
5. This thesis, Chapter I
6. K. H. Prema ; P. Kurian ; P. A. Joy ; M. R. Anantharaman, Polymer-Plastics Technology and Engineering, 47:2, 137 – 146
7. Morton, M. Rubber Technology, 3rd Ed., Van Nostrand Reinold Company: New York, Chapter 12, 1995
8. K. H. Prema, Ph. D. Thesis, Department of Polymer Science and Rubber Technology, Cochin University of Science and Technology (2007)
9. Laurent, E. Kay, J. Appl. Phys. 65, 1717 (1989)
10. H.M. da Costa, L. L.Y. Visconte, R.C.R. Nunes, and C.R.G. Furtado, International Journal of Polymeric Materials, 53 (2004), 475.
11. H. Westlinning and S. Wolf, Kautsch. Gummi Kunstst., 19 (1966) 470.
12. W. A. Bonner, R. A. Grimm: J. Org. Chem. 31: (12) (1966) 4304
13. S. Wolf, Chemical aspects of rubber reinforcement by fillers, Rub. Chem. Tech. 69: 3 (1996) 325
14. N. H. H. Abu Bakar, J. Ismail, M. Abu Bakar, Mater. Chem. Phy 480 (2007) 276

15. E. M. A. Jamal, P. A. Joy, P. Kurian, M. R. Anantharaman: *Mater. Scien. Engg. B* 153 (2009) 24
16. G. V. Salmoria, C.H. Ahrens, V.E. Beal, A.T.N. Pires, V. Soldi: *Mater. & Design*, 30 (3) (2009) 758
17. P. Compston, J. Schiemer, A. Cvetanovska: *Composite Structures*, 86 1-3 2008 22
18. Q. Liu, Y. Zhang, H. Xu, *Applied Clay Scien.* 42 (1-2) (2008), 232

Chapter 7

Dielectric properties of rubber-nickel nanocomposites in radio-frequencies

Lossy dielectrics are considered to be good microwave absorbers, however tuning the band width of absorption for different applications often necessitate the incorporation of a magnetic filler with an appropriate permeability in the composite. The combined effect of an appropriate permittivity and permeability often leads to a good absorber. Thus characteristics of an absorber can be modeled by surface impedance equations and the optimum thickness of the microwave absorber can then be pre-determined. So composites based on rubber and metallic nanoparticles are considered ideal for such applications. Hence preparation of composites based on rubber and nickel nanoparticles assume significance and the evaluation of their dielectric properties in the different frequency regions attract commercial applications. This chapter deals with the evaluation of the dielectric properties of the natural rubber nickel and neoprene-rubber nickel nanocomposites in the radio frequency regime in frequency range of 100 KHz to 8 MHz.

7.1 Properties of composites

It is well known that the dielectric properties of an insulating medium can be modified by dispersing electrically conducting particles in the medium [1-4]. The insulating host material can in turn be made conducting or semi-conducting, depending on the amount of filler particles dispersed in it [5]. Though magnetic fillers are incorporated in a rubber matrix to impart magnetic properties, they also alter the dielectric properties of the host matrix.[6-8]. Elastomers are flexible materials and composites of these materials can find many useful technological applications mainly due to their flexibility and mouldability [8]. Natural rubber is a commonly available elastomer and there exist reports on the studies on electrical properties of composites based on

Chapter 7

natural rubber with ferrite particles as fillers [7, 8]. However reports on the dielectric properties of natural rubber dispersed with metal particles are not very abundant in literature.

Nickel filled rubber composites possess magnetic as well as dielectric properties. If the volume ratio of filler is below the percolation threshold these composites become purely dielectric materials. Nickel, being metallic can alter the dielectric properties of rubber and at the same time, being ferromagnetic can impart high magnetic properties too. Rubber is inexpensive, and the possibility of synthesizing materials capable of absorbing electromagnetic radiation from rubber assumes importance because of its cost effectiveness. Evaluation of the magnetic and dielectric properties of the material is equally important to assess the usability of the material in applications. In addition to the structural, magnetic, morphological and mechanical properties, described in the previous chapter, a detailed evaluation of the dielectric properties of the composites in the frequency range of 100 kHz to 8 MHz is done here. The evaluation of the dielectric behaviour in the radio frequency regime assumes importance from the point of view of using these materials in low frequency electronic components. These studies can also reveal the influence of interfacial polarization in determining the dielectric permittivity of composite materials, and the influence of metallic inclusions in altering the dielectric permittivity in elastomers like natural rubber and neoprene rubber.

There are many factors which influence the dielectric and conducting properties of insulator-metal composites [5, 9]. The most important of these is the ratio of the filler particles to the host material. At lower volume ratios, the composites are good dielectric materials, but the conductivity of the material can increase sharply at some critical value of the volume ratio. This is due to the formation of conductive paths at the percolation threshold of the filler particles [10]. But within the percolation threshold, these materials are good insulators, and their dielectric properties can be tuned by the volume ratios of the filler material. The investigations of dielectric properties of metal elastomer composites thus assume importance under these circumstances. Elastomer nickel composites were synthesized using natural rubber and neoprene rubber and nanosized nickel particles. The details of synthesis of these composites are described in chapter 6. The volume ratio of the nickel nanoparticles was so chosen that they did not exceed the percolation threshold and the composites are dielectric materials.

7.2 Dielectric studies in radiofrequency range

Circular discs were cut out from the cured sheets of composites with a diameter of 12 mm for dielectric studies. These studies were carried out using an HP impedance analyzer model 4285 A in the frequency range of 100 KHz to 8 MHz by varying the temperature from 30°C to 120°C. The samples were inserted between two copper plates of the same diameter to form a capacitor in a home-made dielectric cell whose fabrication details are reported elsewhere [13]. Using the impedance analyzer the capacitance and loss tangent were recorded at intervals of 100 KHz using an automated measurement set-up. The measurement was automated by interfacing the impedance analyzer with a personal computer through a GPIB cable IEEE488. A commercial interfacing and automation software LabVIEW was used for the acquisition of data. The program for data acquisition was written in the language G which is a graphical language much suitable for data acquisition applications as described in chapter 2. With this 20000 data points can be acquired in a matter of 5 minutes and transported to a file. The dielectric permittivity (ϵ'_r) of the sample was calculated using the relation [7]

$$\epsilon'_r = \frac{C.d}{\epsilon_o A} \quad (7.1)$$

and the dielectric loss (ϵ''_r) by the relation

$$\epsilon''_r = \epsilon'_r \tan \delta \quad (7.2)$$

where C is the capacitance of the capacitor formed by inserting the sample between two metal plates, d is the thickness of the sample, ϵ_o the permittivity of free space, A is the area of cross section of the sample and δ is the loss tangent.

7.3 Results and Discussions

7.3.1 Dielectric properties of natural-rubber-nickel composites

In figure 7.1 the typical variation of dielectric permittivity of the samples within a frequency range of 100 KHz to 8 MHz at temperatures starting from 40°C to 120°C is shown. The dielectric permittivity decreases almost linearly with frequency. At the lower side of the frequency the variation is slow and after about 2 MHz there is comparatively sharper variation

and these variations are of the same nature at all temperatures. The graph shown as figure 7.1 is of 60 phr sample and the entire range of samples exhibit a closely similar

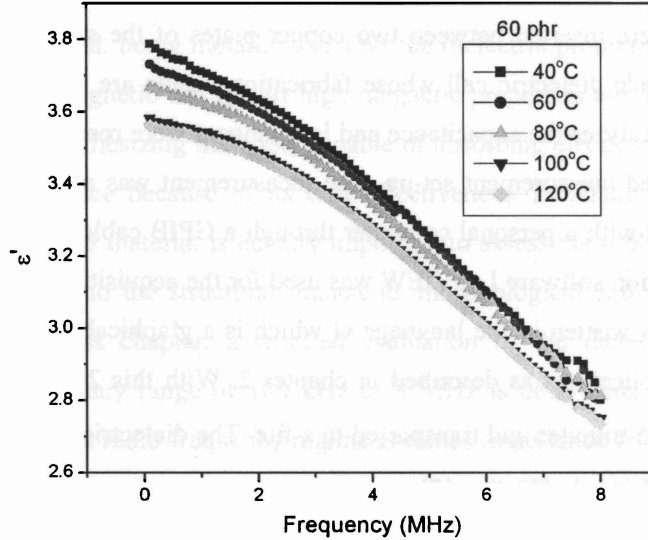


Figure 7.1: Variation of real part of dielectric permittivity with frequency

behavior. The drop in dielectric permittivity with increasing applied frequency is understood on the basis of Debye model of dielectric relaxation [17]. The behaviour of the dielectric constant of materials with a single relaxation mechanism can be represented by the relation of the form

$$\varepsilon^*(\omega) - \varepsilon_\alpha = \frac{\varepsilon_s - \varepsilon_\alpha}{1 + i\omega\tau} \quad (7.3)$$

where $\varepsilon^*(\omega)$ is the complex permittivity at the frequency ω , ε_s is the static permittivity, ε_α is the permittivity at infinite frequencies and τ is the relaxation time of the relaxation mechanism present in the material. Equation (7.3) can be written as real and imaginary parts separated as

$$\varepsilon'(\omega) = \varepsilon_\alpha + \frac{\varepsilon_s - \varepsilon_\alpha}{1 + \omega^2\tau^2} \quad (7.4)$$

and
$$\varepsilon''(\omega) = (\varepsilon_s - \varepsilon_\alpha) \frac{\omega\tau}{1 + \omega^2\tau^2} \quad (7.5)$$

Equations (7.4) and (7.5) are known as Debye equations since they were derived by Debye on a molecular basis [17]. The drop in dielectric permittivity with increase in applied frequency is understood according to equation (7.4). Electronic polarization which is attributed to the dielectric polarization in materials has a relaxation time of the order of 10^{-14} s [18]. Such a small relaxation time does not produce dielectric dispersion at the radio frequency (rf) range where the dielectric measurements were made. It is clear that the kind of relaxation mechanism operating in the frequency regime is different and has a higher relaxation time. Many researchers have attributed the dielectric dispersion in rf regime to interfacial polarization [9, 19]

In figure 7.2 the variation of dielectric permittivity (ϵ') with the nickel content in the composite is plotted for four different frequencies at temperature of 40°C.

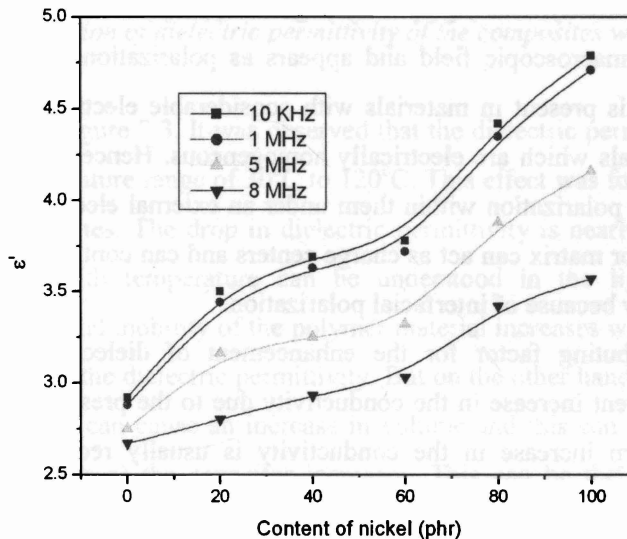


Figure 7.2: Variation of permittivity with content of nickel in the composites

Permittivity increases with filler loading almost linearly with all frequencies. The same kind of behaviour is exhibited by the composites at all temperatures. Metallic inclusions in any insulating material enhance the dielectric permittivity of the material as predicted by many theoretical models and verified by experimental results [9, 18, 19]. Increase in permittivity in rubber-nickel nanocomposites is nearly linear with the percentage of loading of nickel particles. It

Chapter 7

is possible to tune the dielectric permittivity to a desired value, and the dielectric loss in the material with nickel loading is small, and this material can be potential candidates for making capacitors, owing to the possibility of moulding rubber as very thin sheets or films.

The enhancement of dielectric permittivity in metal polymer composites can be understood on the basis of three possible mechanisms. They are the interfacial polarization, enhancement of electrical conductivity and formation of internal barrier layer capacitor (IBLC). Interfacial polarization is always present in materials comprised of more than one phase like a metal elastomer composite. This kind of polarization arising at the interfaces is due to the migration of charge carriers through different phases of the composite material resulting in differential charge accumulation at the interfaces [20]. When these charges are made to move by the application of an external electric field, the motion will be hindered at various points of the composite material differently, causing space charge to appear. The appearance of such space charge can distort the macroscopic field and appears as polarization to an external observer. Interfacial polarization is present in materials with considerable electrical heterogeneity and is totally absent in materials which are electrically homogeneous. Hence composite materials will exhibit large interfacial polarization within them under an external electric field. Metal particles embedded in an insulator matrix can act as charge centers and can contribute to the enhancement of dielectric permittivity because of interfacial polarization.

Another contributing factor for the enhancement of dielectric permittivity in such composites is the apparent increase in the conductivity due to the presence of metal particles in the matrix. But a sharp increase in the conductivity is usually recorded at the percolation threshold of these composites. And below the percolation threshold the increase in conductivity is only moderate or small [10]. However the observed increase in the dielectric permittivity can be a combined effect of these two mechanisms. The enhancement in permittivity can also be due to the formation of IBLC as reported in many systems [21, 22]. The occurrence of very high value of dielectric permittivity (of the order of 1000) was purportedly explained on the basis of IBLC. Even though such an effect was reported in certain polycrystalline ceramics and perovskite materials, IBLC is not a plausible mechanism governing the permittivity in metal elastomer composites since there is no possibility of formation of IBLC in them. The variation of dielectric constant with temperature is plotted for various filler loadings at a representative frequency of 4

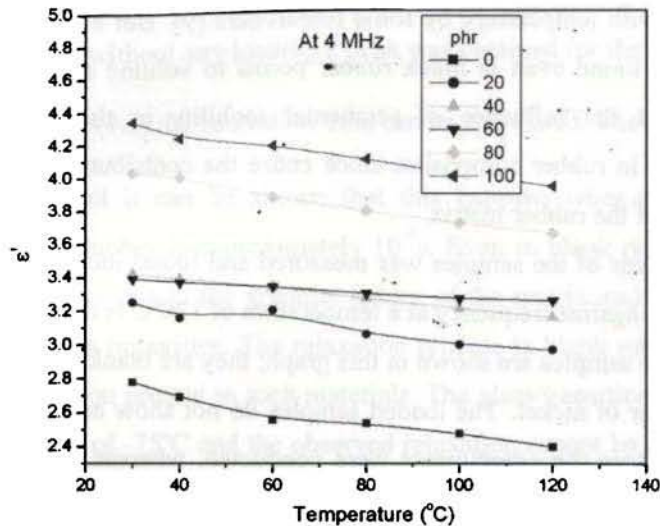


Figure 7.3: Variation of dielectric permittivity of the composites with temperature

MHz and is depicted in figure 7.3. It was observed that the dielectric permittivity decreased with temperature in the temperature range of 30°C to 120°C. This effect was found in the blank rubber as well as in the composites. The drop in dielectric permittivity is nearly linear. The change in dielectric permittivity with temperature can be understood in the light of two competing mechanisms. The segmental mobility of the polymer material increases with temperature and this can lead to an increase in the dielectric permittivity. But on the other hand, the thermal expansion of the elastomer material can cause an increase in volume and this can affect the measurement condition as the thickness of the capacitor increases. This can be the cause of the measured decrease in the dielectric permittivity at higher temperatures. The average decrease in the dielectric permittivity over a temperature range of 90°C is around 7 percent of the value at room temperature. The linear expansivity of natural rubber is $220 \times 10^{-6}/^{\circ}\text{C}$ [23]. The volume expansivity of natural rubber therefore is 660 parts per million (ppm) per °C. Over the temperature range of 90°C the possible volume expansions is about 6 percent. This estimation agrees well with the observed decrease in the dielectric permittivity with increase of temperature. Differential thermal expansion between the metallic inclusions and the rubber matrix and the resulting disruption of metal clusters had been suggested as a possible reason for the drop in the

Chapter 7

dielectric permittivity with temperature by some researchers [9]. But a drop in permittivity with increasing temperature found even in blank rubber points to volume expansion as the possible reason. It appears that the influence of segmental mobility in the variation of dielectric permittivity is minimal in rubber composites since entire the contribution appears to arise from the volume expansion of the rubber matrix.

The dielectric loss of the samples was measured and found increasing with temperature. A plot of dielectric loss against frequency at a temperature of 120°C is depicted in figure 7.4. The dielectric losses of three samples are shown in this graph; they are blank rubber and rubber loaded with 40 phr and 100 phr of nickel. The loaded samples do not show any dielectric relaxation in the frequency range where the experiments were conducted, whereas the blank rubber sample displays a relaxation at about 2.25 MHz.

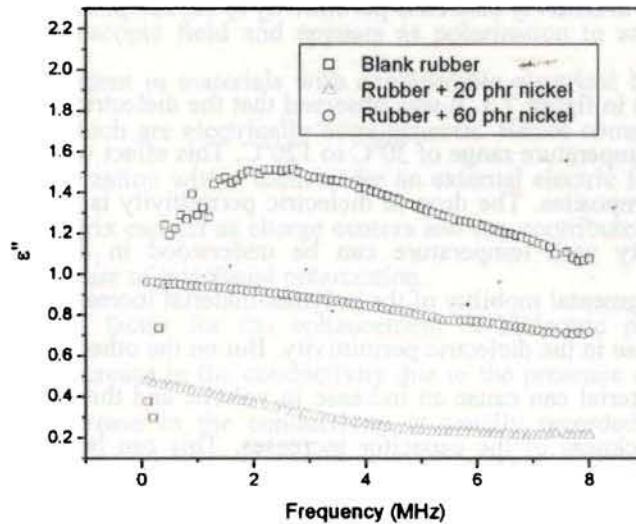


Figure 7.4: Variation of dielectric loss with frequency of three samples of composites at a temperature of 120°C

In equation (7.5) ϵ_{α} can be considered equal to the value of dielectric constant obtained at microwave frequencies. Electronic polarization becomes significant at higher frequencies and the value of ϵ_{α} remains a constant. The value of ϵ_s can be determined by extrapolating the dielectric dispersion curve to lower frequencies. Even though we have not attempted to determine the values of ϵ_{α} and ϵ_s it is evident that the quantity $\epsilon_s - \epsilon_{\alpha}$ is a constant for a given material

and the variation of dielectric loss depends on the relaxation time and the applied frequency only. For blank rubber samples without any loading a peak was obtained for the dielectric loss nearly at 2.25 MHz. From equation (7.5) the relaxation time can be calculated. The quantity $\frac{d\varepsilon''}{d\omega}$ vanishes when ε'' is maximum and it can be shown that this happens when $\omega\tau = 1$. The calculated relaxation time of blank rubber is approximately 10^{-7} s. Even in blank rubber sample interfacial polarization can be present due to the granular nature of the matrix and due to the presence of unreacted curing agents as impurities. The relaxation process in blank rubber is attributed to the weak interfacial polarization present in such materials. The glass transition temperature of natural rubber is at a temperature of -75°C and the observed relaxation cannot be due to such a transition [23]. The inclusion of metallic fillers increases the relaxation time of composites, and the peaks go undetected within the frequency range in which the experiments were conducted. It is evident that interfacial polarization suggested by Maxwell-Wagner is responsible for the dielectric dispersion exhibited by these samples in this frequency range. It is evident from fig 7.4 is that a relaxation peak may be observed at some lower frequencies.

In figure 7.5 the dielectric loss is plotted for blank rubber for three temperatures to show its variation with temperature. It can be observed from the graph that the loss increases with the increase in temperature. But the relaxation peak does not shift noticeably from the 2.25 MHz as indicated by the graphs. It appears that the relaxation time in blank rubber is unaffected by temperature. The samples loaded with nickel did not show any relaxation as the dielectric loss was found decreasing with increase in frequency. It is reasonable to assume that the relaxation time of blank rubber gets enhanced when nickel nanoparticles were incorporated in the matrix and relaxation peaks appear at a frequency lower than 100 kHz. Further studies are required to establish the nature of the relaxation process in nickel loaded samples at frequencies lower than 100 kHz. Further, at 120°C the dielectric loss corresponding to the relaxation peak is about 1.5 but it decreased sharply when the temperature is 80°C to about 0.9. As the frequency increases the loss falls considerably as observed in figure 7.5. So for any frequency beyond 3 MHz both blank rubber and nickel rubber composite can be considered as low loss materials.

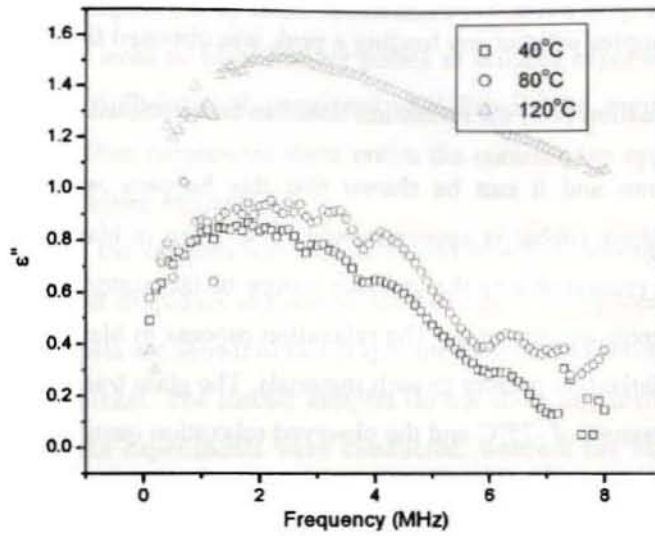


Figure 7.5: Graph showing the dielectric loss at temperatures 40°C, 80°C and 120°C of blank rubber

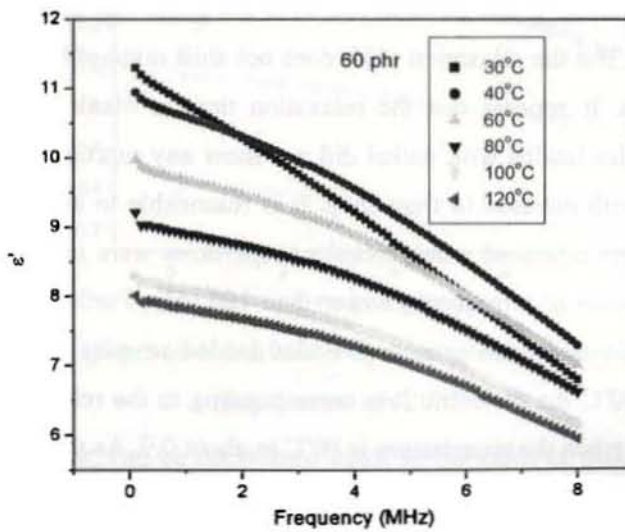


Figure 7.6: Variation of real part of dielectric permittivity on neoprene-nickel composites with frequency

7.3.2 Dielectric properties of neoprene-rubber-nickel composites

Dielectric permittivity and dielectric loss tangent of the composites in the frequency range of 100 KHz to 8 MHz from 30°C to 120°C were determined and was found that the dielectric behaviour of them are identical to that of natural rubber nickel composites. All samples including the blank neoprene sample exhibit a steady decrease in dielectric permittivity with the increase of frequency. The variation is nearly linear as observed in figure 7.6. Here the composite containing 60 phr nickel is taken as a representative sample for depicting the variations since all samples show exactly the same kind of behaviour. Neoprene has high permittivity compared to natural rubber due to the polar nature of its molecules [24]. The decrease in dielectric permittivity with frequency is attributed to the interfacial polarization which causes a low frequency relaxation process similar to natural rubber-nickel composites. Even in blank neoprene the material is granular in nature, providing large amount of grains and grain boundaries and charge accumulation at these interfaces could be the cause of interfacial polarization.

It was found that the dielectric permittivity increased with increase of nickel concentration in the matrix at all frequencies. A representative graph plotted at 3 MHz is shown in figure 7.7. As we have already seen in the case of natural-rubber-nickel composites the increase in permittivity with increase in filler loading can be understood on the basis of two possible reasons, the increase in interfacial area in the composite and the resulting enhancement in the interfacial polarization and the increase in the conductivity of the sample due to the presence of metallic fillers. IBLC doesn't appear to be a reason for enhancement of permittivity in these composites as explained in an earlier part of this chapter.

The variation of dielectric loss with frequency is plotted for all the samples at room temperature in figure 7.8. For blank neoprene sample without any loading a peak have been obtained the loss-frequency graph nearly at 6 MHz and the estimated relaxation time from this is 2.65×10^{-8} s. The inclusion of metallic fillers increases the relaxation time of samples, and the peaks get shifted towards the low frequency side progressively as observed in figure 7.9. The 100 phr sample shows a sharp relaxation peak at 2.5 MHz of applied signal frequency and for the 80 phr sample the peak is shifted to the position of 4 MHz.

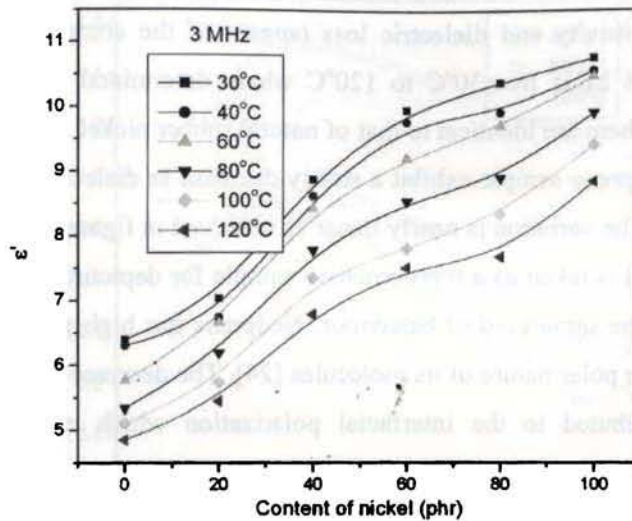


Figure 7.7: Variation of dielectric permittivity of neoprene-nickel composites with nickel content

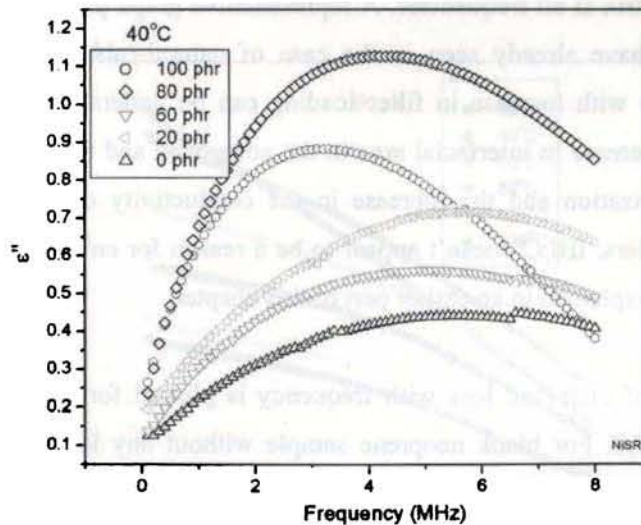


Figure 7.8: Variation of dielectric loss of neoprene-nickel composites with frequency

The increase in filler loading increases the interfacial area inside the composites and accumulation and removal of charges from the interfaces, caused by the applied field, takes more

time to complete and will lag behind the applied field. The shift in the peaks in the loss-frequency graphs towards the lower frequency side with increase in filler content is a clear indication for the presence of interfacial polarization suggested by the Maxwell-Wagner theory in metal filled polymer samples

The effect of temperature on the dielectric permittivity of neoprene-nickel composites is depicted in figure 7.9. The dielectric permittivity decreases in general with increase in temperature. But at higher frequencies it is observed that the dielectric permittivity increases in the temperature range of 30-40°C and then decreases. This can be well understood on the basis of two competing factors influencing the dielectric behaviour of polymers [19]. One is the segmental mobility of the molecules of the polymer material and other is the thermal expansion of the elastomer matrix as explained during the discussion of natural-rubber-nickel composites. The segmental mobility of the

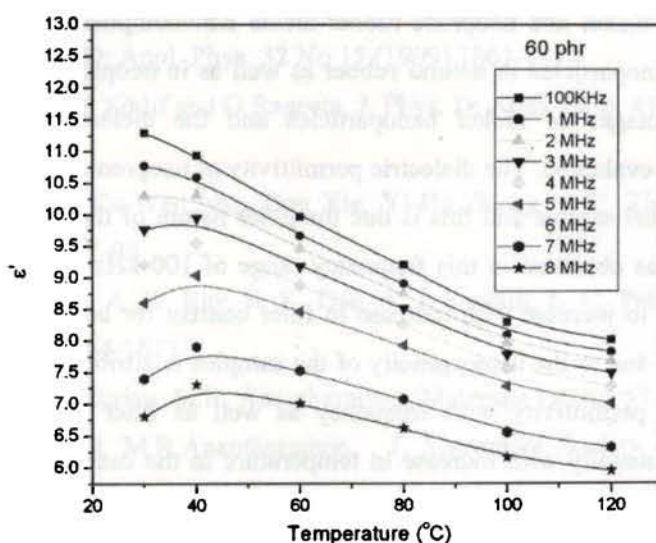


Figure 7.9: Variation of dielectric permittivity of neoprene-nickel composites with temperature

polymer material increases with temperature and this can enhance the polarization leading to an increase in the dielectric permittivity. But on the other hand, the expansion of the neoprene matrix can affect the measurement conditions by an apparent increase in the thickness of the neoprene disc resulting in a decrease in the measured capacitance. The enhanced segmental mobility

Chapter 7

appears to be predominant at lower temperatures up to 40°C since the composites show an increase in permittivity. A decrease thereafter indicates the effects due to volume expansivity that comes in to play after this temperature. Also it can be observed from the plots in figure 7.9 that this gradual ascent descent effect is totally absent in the frequency range up to 1 MHz suggesting that the segmental mobility is not much affected by the temperature at frequencies below 1 MHz and a rise in temperature enhances segmental mobility above this frequency which is a clear indication that the segmental mobility has a dependence on the applied frequency. Above 40°C volume expansivity of the matrix becomes more significant and results in a drop in permittivity. Figure 7.9 is that of the 60 phr sample and all samples exhibit a similar behaviour at all frequency regimes in which the present studies were carried out.

7.4 Conclusion

Natural-rubber-nickel and neoprene-rubber-nickel nanocomposites were synthesized by incorporating nickel nanoparticles in natural rubber as well as in neoprene rubber matrixes with varying weight percentages of nickel nanoparticles and the dielectric properties in radio frequency regime were evaluated. The dielectric permittivity of neoprene-nickel samples is higher than that of rubber-nickel sample and this is due the polar nature of the neoprene molecules. A dielectric dispersion was observed in this frequency range of 100 kHz to 8 MHz and dielectric permittivity was found to increase with increase in filler content for both the series of samples. Interfacial polarization due to the heterogeneity of the samples is attributed as the reason for the variation of dielectric permittivity with frequency as well as filler concentration. Dielectric permittivity decreases steadily with increase in temperature in the case of natural-rubber-nickel samples and high volume expansivity of rubber matrix can be the cause for such a phenomenon. But in neoprene-rubber-nickel samples the dielectric permittivity first increases with temperature up to 40°C and then decreases. This may be because the influence of segmental mobility is predominant at lower temperature. Dielectric loss of the composites was determined and in the case of rubber-nickel composites relaxation peaks were observed only in blank rubber. The impregnation of nickel particles might have shifted the relaxation peaks to a frequency lower than 100 kHz and have gone unobserved. In neoprene-nickel composites the peaks are observed in all samples and they shift to the lower frequency side with the increase in filler loadings.

References:

- 1 T.Tanaka, G.C.Montanari, R.Mulhaupt, IEEE Tran. Dielectrics and Electrical Insulation; vol. II, No 5; (2004), 763-784
- 2 G.M. Tsangaris, G.C. Psarras, A.J. Kontopoulos, J. Non-Crystalline Solids 131-133 (1991) 1164-1168
- 3 G.C.Psarras, E. Manolakaki, G.M. Tsangaris, Composites Part A 33 (2002) 375-384
- 4 G.C.Psarras, composites Part A 37 (2006) 1545-1553
- 5 P.S.Neelakanta, Handbook of electromagnetic materials .CRC Press; 1995
- 6 Baoshan Zhang, Yong Feng, Jie Xiong, Yi Yang, Huaixian Lu, IEEE Trans. On Magnetism, 42, 7, (2006), 1778-1781
- 7 S Sindhu, M. R. Anantharaman, Bindu P Thampi, K. A. Malini, Philip Kurian, Bull. Mater. Sci. 25, 7, (2002), 599-607
- 8 M R Anantharaman, S Sindhu, S Jagatheesan, K A Malini, P Kurian J. Phys. D: Appl. Phys. 32 No 15 (1999) 1801-1810
- 9 Z M Elimat, A M Zihlif and G Ragosta, J. Phys. D: Appl. Phys. 41 (2008) 165408
- 10 [Zhi-Min Dang, Ce-Wen Nan, Dan Xie, Yi-He Zhang, S. C. Tjong, App Phys Lett 85 (2004) 97-99
- 11 Ranjan. K. Sahu, A. K. Ray, S. K. Das, A. J. Kailath, L. C. Pathak J. Mater. Res., 21, (2006) No. 7, 1664-1673
- 12 K.A. Malini, P. Kurian, M.R. Anantharaman, Materials Letters 57 (2003) 3381– 3386
- 13 E.M. Mohammed, M.R.Anantharaman, , J. Instrument Society of India, Vol. 32., No.3 (2002), 165
- 14 H. V. Keer, Principles of Solid State Physics, Wiley Eastern Ltd, New Delhi, (1998)
- 15 W. Gong, H. Li, Z. Zhao, J. Chen, J. Appl. Phys. 69, (1991), 5119
- 16 N.H.H. Abu Bakar, J. Ismail, M. Abu Bakar, Materials Chemistry and Physics, 104, (2007), 276-283
- 17 I.I. Perepechko, An Introduction to Polymer Physics, Mir Publishers, Moscow, 1981
- 18 B.Tareev, Physics of Dielectric Materials, MIR Publishers, Moscow, 1975
- 19 Musameh. S. M, Zihlif. A, Ragosta G., Mater. Sci. Eng. B. 10, 29-33

Chapter 7

- 20 H.A. Pohl, Dielectrophoresis, Cambridge University Press, London, 1978
- 21 Derek C. Sinclair, Timothy B. Adams, Finlay D. Morrison, Anthony R. West, Applied Physics Letters, 80, 2153, (2002)
- 22 Pradip Kumar Jana, Sudipta Sarkar, H. Sakata, Tsunco Watanabe, B. K. Chaudhuri, J. Phys. D. Appl. Phys. 41 (2008), 65403
- 23 C. M. Blow, C. Hepburn, Rubber Technology and Manufacture, second edition, page 347, Butterworths, London, 1982 p.
- 24 Morton, M. Rubber Technology, 3rd Ed., Van Nostrand Reinold Company: New York, Chapter 12, 1995.
- 25 Z M Elimat, A M zihilif, G Ragosta, J. Physics.D.Applied. Phys.(41) (2008) 165408

Chapter 8

Dielectric permittivity and magnetic permeability studies on rubber-nickel composites in the S and X band microwave frequencies

It has been pointed out in the previous chapter that the evaluation of dielectric permittivity and magnetic permeability of composites based on rubber and nickel nanoparticles in the S (2 to 4 GHz) and X (7 to 12 GHz) band is a major step in characterizing these samples for possible microwave absorbing applications. The evaluation of these parameters and the subsequent modeling of the surface impedance equations is attempted here. The findings are presented in this chapter.

The interest in electromagnetic absorbers in the microwave region has increased in recent times due to the significant expansion in applications using electromagnetic waves in this frequency band. There are numerous electronic gadgets operating in the microwave frequencies like mobile phones, wireless local area networks, radar systems etc and the problem of electromagnetic interference has worsened significantly, demanding the use of microwave absorbers [1-3]. A good absorber has to have low or negligible reflection, sufficiently large attenuation and good heat dissipation characteristics because the absorbed energy is converted to heat within the material [4]. In stealth technology, which is another important field of application of microwave absorption, especially in aerospace applications, total absorption of electromagnetic waves without any reflection is essential since the device should go undetected by radar signals.

8.1 Microwave absorbers

The complex dielectric permittivity and magnetic permeability of a material together defines its electromagnetic wave absorbing characteristics and this emphasizes the importance of

Chapter 8

magnetic dielectric materials. Various kinds of magnetic dielectric materials have been developed over the years to find application as microwave absorbers such as ferrites, ferrite-polymer composites and composites containing metallic magnetic particulates [5-14]. In comparison to ferrites, metallic magnetic composites have several advantages like high saturation magnetization, tunability of magnetic permeability by controlling the volume fraction of metallic particles and mechanical flexibility of the host material of the composite. One major disadvantage of metallic magnetic composite is the drop in magnetic permeability at higher applied frequencies due to skin effect and eddy current loss developed in the particulates [15]. However this drawback can be overcome by using particles of size smaller than the skin-depth of the metal with respect to the frequency of operation. The skin depth of iron in gigahertz frequencies has been estimated to be about 1 μm and that of nickel about 500 nm [5, 15, 16]. Iron and nickel particles below these critical size limits dispersed in suitable dielectric materials therefore are potential candidates as microwave absorbers.

The investigations on the complex dielectric and magnetic properties of composites prepared by impregnating nanometric sized nickel particles in two different elastomer matrixes namely natural rubber and neoprene rubber are described in this chapter. Natural rubber is an easily available and inexpensive material and neoprene is a synthetic rubber with several superior physical properties compared to natural rubber such as better resistance to harsh chemicals, tough flame resistance and resistance to salinity. The ease with which they can be moulded into any complex shapes and size can give both these materials an extra edge in stealth applications. The complex dielectric permittivity and magnetic permeability of these composites are evaluated in the S band (2 to 4 GHz) and X band (7 to 12 GHz) microwave frequencies using cavity perturbation technique. The details of this technique are already described in detail in chapter 2.

8.2 Cavity perturbation method

For a rectangular cavity, real part of the dielectric permittivity can be calculated from the relation [17, 18]

$$\frac{\Delta f}{f_s} = 2 \frac{V_s}{V_c} (\epsilon' - 1) \quad (8.1)$$

Where Δf is the shift in resonance frequency on introduction of the sample into the cavity and V_s and V_c are the volume of the sample and cavity respectively.

The imaginary part of the dielectric permittivity is given as

$$\left[\frac{1}{2Q_s} - \frac{1}{2Q_c} \right] = 2 \frac{V_s}{V_c} \epsilon_r'' \quad (8.2)$$

Q_s and Q_c are the quality factors of the cavity with and without sample, given by

$$Q_s = \frac{f_s}{\Delta f}, \quad Q_c = \frac{f_c}{\Delta f} \quad (8.3)$$

Magnetic permeability was measured by perturbing the cavity by the samples at positions where the electric field is zero. X band measurements were possible only for even modes since this cavity was provided with a hole at the centre of the cavity. The real and imaginary parts of the complex permeability of composite samples were determined using the relations

$$\mu_r' - 1 = \frac{(\lambda_g^2 + 4a^2)}{8a^2} \left(\frac{\Delta f}{f_s} \right) \frac{V_c}{V_s} \quad (8.4)$$

$$\mu_r'' = \frac{(\lambda_g^2 + 4a^2)}{16a^2} \left(\frac{1}{Q_s} - \frac{1}{Q_c} \right) \frac{V_c}{V_s} \quad (8.5) \quad \text{and}$$

$$\lambda_g = \frac{2l}{p} \quad (8.6) \quad \text{where } p \text{ is the}$$

number of mode in which the cavity is excited for a particular measurement.

8.3 Measurements in the S band

Measurements in the S band were carried out by a two port network analyzer (ZVB4, Rohde & Schwaz) with the help of an S band rectangular cavity having dimensions 3.4cm x 7.2cm x 30.8cm by employing cavity perturbation technique. The rectangular S-band cavity operating in TE₁₀ mode was fabricated with a narrow line slot (3mmx180mm) to insert the sample material into the cavity. Calibration was performed by the method of through-open-short-match (TOSM) before carrying out the measurements. Within the frequency range of 2 GHz to 4 GHz,

Chapter 8

the cavity resonates at five different frequencies corresponding to the TE_{10n} modes. The cavity was perturbed at these frequencies using rectangular composite strips. The entire set-up was calibrated using FR4 glass epoxy, a standard material with known dielectric properties in microwave band. Dielectric permittivity and dielectric loss of the composite were determined by measuring the resonant frequency (f_r) and the quality factor (Q) of the microwave cavity when perturbed by inserting sample in the form of strips into the cavity at a position where electric field is found to be at a maximum.

8.4 Measurements in the X band

Rectangular strips of about 5 cm in length and 2mm x 2 mm cross section were cut from the sheets of composites and the dielectric measurements in the X band microwave frequencies were done by cavity perturbation method using an Agilent 4 port network analyzer with a rectangular cavity of dimensions 1cm x 2.3cm x 15.1 cm. The cavity has a precision cut hole at the centre (along the 2.3cm side) through which the sample can be introduced and dielectric measurements were carried out at odd modes (Electric field forms an anti-node at the centre) and permeability measurements at even modes (Electric field forms a node at the centre) [19]. The equations used for determining the complex permittivity and permeability are given in the section 8.2. The complex dielectric permittivity values are determined for four different frequencies in the X-band. These four frequencies are nearly 7.224 GHz, 8.239 GHz, 9.559 GHz and 11.067 GHz corresponding to the TE_{103} to TE_{109} modes of the cavity used for the measurements. The magnetic permeability was measured at five frequencies which are nearly 6.8746 GHz, 7.676 GHz, 8.8621 GHz, 10.283 GHz and 11.861 GHz corresponding to the TE_{102} to TE_{1010} modes of the cavity.

8.5 Complex dielectric permittivity of natural-rubber-nickel composites

The variation of dielectric permittivity (ϵ_r') of the composites for five different frequencies in the S band is depicted in figure 8.1. It was observed that the dielectric permittivity of a particular sample remains nearly a constant in the entire frequency range. Blank rubber shows a permittivity of 2.61 at a frequency of 2.304 GHz and shows a maximum of 2.67 at

dielectric permittivity between 6.03 and 6.16 in the frequency range. Within the error limits, it can be assumed that the permittivity remains unchanged within the frequency range of S band. This is consistent with a number of previous results [20,21] The increase in permittivity with the nickel content can be attributed to the presence of interfacial polarization, the formation of internal barrier layer capacitance (IBLC) or the increase in the electrical conductivity of the samples [22]. The presence of interfacial polarization can be ruled out in the GHz frequencies because it is a slower relaxation process, generally with relaxation times of the order of 10^{-3} s [23]. Metallic fillers can enhance the conductivity of the samples and this can be the reason for the increase in permittivity. The increase is found to be very sharp and much more than what predicted by the mathematical models suggested by Bruggman or Baziard [20,26,27] for composites with metallic fillers. An empirical relation of the form

$$\epsilon_r^* = \frac{\epsilon_r'}{(1-y)^8} \quad (8.7)$$

is used to fit the experimentally observed values and is in close agreement with the model. Here, ϵ_r^* , ϵ_r' and y are the effective permittivity of the composite, permittivity of the polymer host material and the volume ratio of the metallic filler respectively. The variations of permittivity according to various models are shown in figure 8.2. The reason for such a sharp increase in.

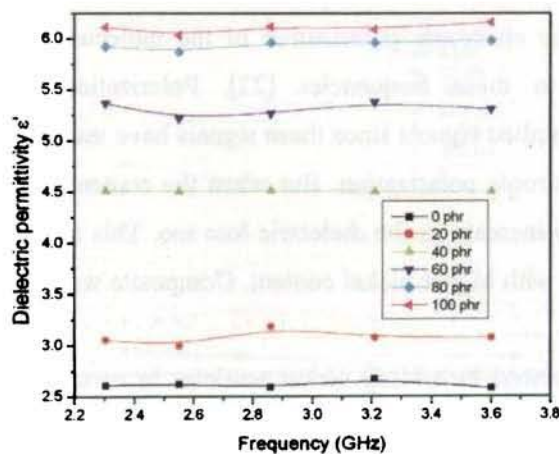


Figure 8.1: Variation of dielectric permittivity of natural rubber based composites with frequency in the S band

permittivity is not known. It is possible that more than one factor is at work which contribute to the increase in the permittivity like enhancement of electrical conductivity or internal barrier layer capacitance

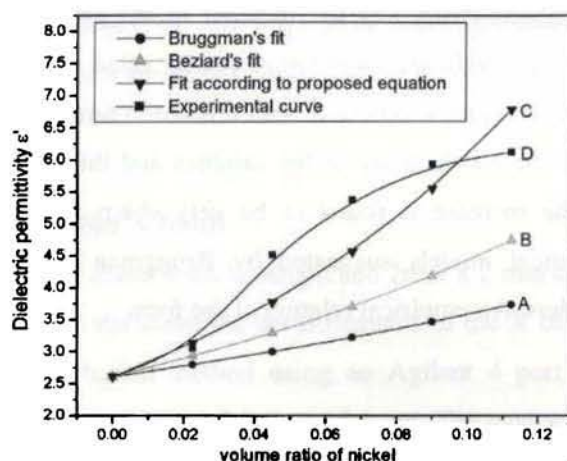


Figure 8.2: Variation of dielectric permittivity with volume ratio of nickel in the S band compared with different models (natural rubber based composites)

The dielectric loss of the material in the S band is shown in figure 8.3. The loss remains nearly a constant for the entire range of 2 GHz to 4 GHz. The loss in the case of blank rubber lies in the range of 0.012 and 0.014. A flat curve indicates the absence of any relaxation process in this frequency regime. The electronic polarization of the molecules can only be the relevant polarization mechanism in these frequencies [23]. Polarization of the molecules is in synchronization with the applied signals since these signals have much lower period compared to the relaxation time of electronic polarization. But when the content of nickel in the composites increases, there is a steady increase in the dielectric loss too. This may be due to the increase in the reflectance of material with higher nickel content. Composite with 100 phr nickel content has maximum dielectric loss which is almost 9 times the loss of the blank rubber. It is evident that the dielectric loss can be enhanced by adding nickel particles in natural rubber and this opens up scope for developing materials for absorption of electromagnetic waves in microwave frequencies.

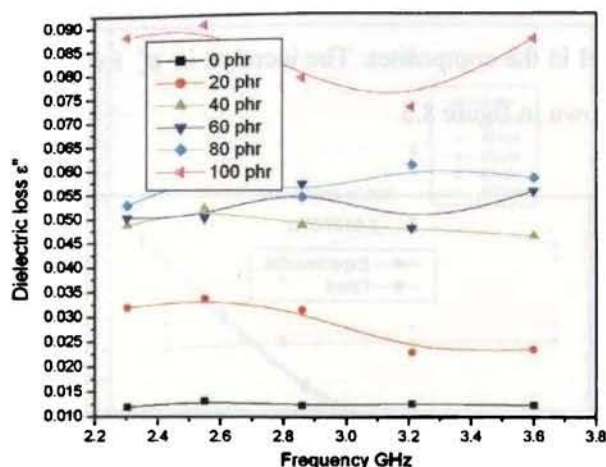


Figure 8.3: Dielectric loss with frequency in the S band (natural rubber based composites)

8.6 Complex dielectric permittivity of neoprene-rubber-nickel composites

It was observed from the rf dielectric studies that neoprene rubber possesses a higher dielectric permittivity compared to natural rubber [chapter 7]. This enhancement in ϵ'_r was observed in S band microwave frequency also. Figure 8.4 depicts the variation of ϵ'_r with frequency and as observed in the case of natural rubber, there is a steady increase in ϵ'_r with

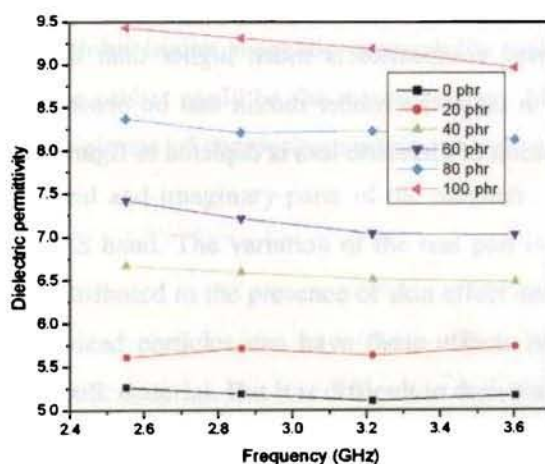


Figure 8.4 Variation of dielectric permittivity of neoprene-rubber based composites with frequency in the S band

Chapter 8

increase in content of nickel in the composites. The increase in ϵ' follows the empirical relation suggested by Baziard as shown in figure 8.5.

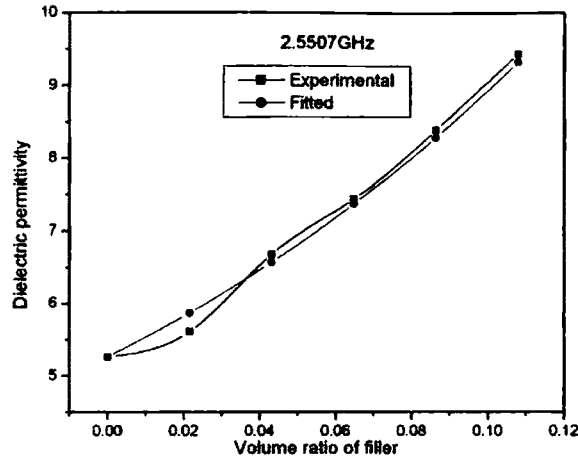


Figure 8.5: Variation of dielectric permittivity with volume ratio of nickel in the S band compared with Baziard's model (neoprene-rubber based composites)

The behaviour of dielectric loss in neoprene based composites is different from that of natural rubber based composites. Dielectric loss of all the composite samples increases steadily with frequency and shows saturation towards the higher edge of the s band. Further, the dielectric loss in neoprene rubber based composites is much higher than that in natural rubber based composites. This high loss in neoprene rubber matrix can be observed in all frequency ranges from rf to X band. The variation of dielectric loss is depicted in figure 8.6

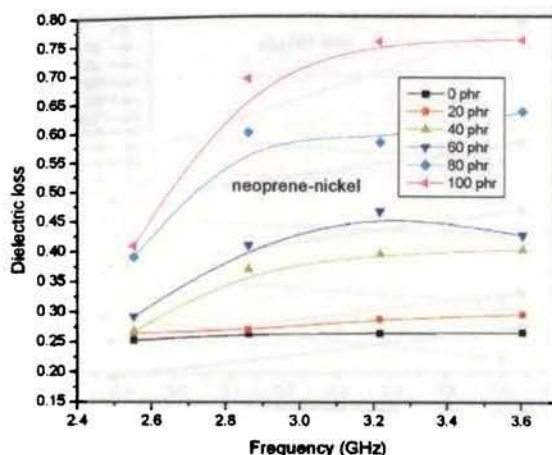


Figure 8.6: Dielectric loss with frequency in the S band (neoprene-rubber based composites)

8.7 Magnetic permeability of the composites

The magnetic permeability of both natural rubber and neoprene rubber based composites were measured at two frequencies in the S band. Magnetic permeability decreases with frequency. The studies reveal that the variations in magnetic permeability behaviour of both types of composites are identical as depicted in figure 8.7 and 8.8. The origin of magnetic permeability is from the embedded ferromagnetic nickel nanoparticles in the matrix and the elastomer matrix does not offer any contribution towards the magnetic properties. It was observed that the natural rubber based composites exhibit higher magnetic permeability and higher elastic modulus of natural rubber over neoprene rubber could be the reason for this. Magnetic loss also shows the same kind of change in both classes of composites samples as shown in figures 9 and 10. Due to instrument limitations the real and imaginary parts of the magnetic permeability are plotted for only two frequencies in the S band. The variation of the real part is as expected and it shows a steady decrease and this is attributed to the presence of skin effect and eddy current loss in nickel particles. Even nanometer sized particles can have these effects in a reduced scale, if not as prominent as in the case of bulk material. But it is difficult to derive any conclusion about the true nature of magnetic loss from the observed data.

Chapter 8

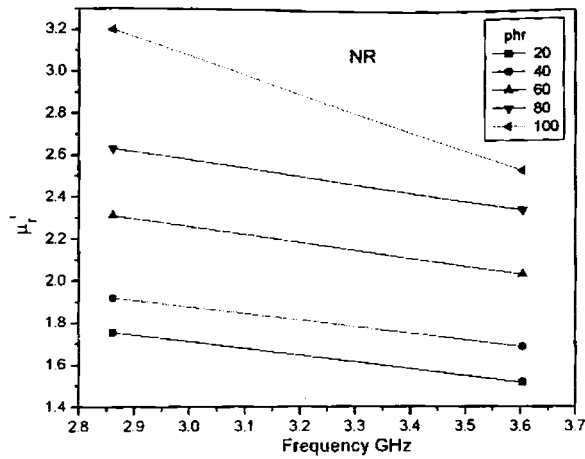


Figure 8.7: Variation of magnetic permeability in the S band (natural rubber based composites)

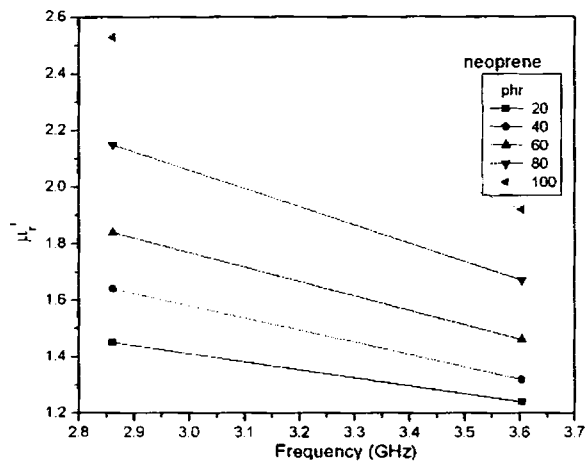


Figure 8.8: Variation of magnetic permeability with frequency in the S band (neoprene-rubber based composites)

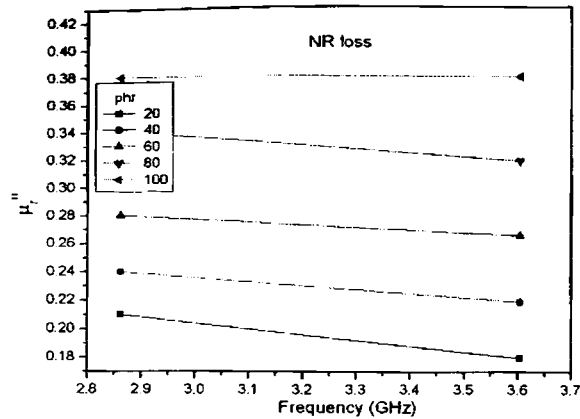


Figure 8.9: Variation of magnetic loss with frequency in the S band (natural rubber based composites)

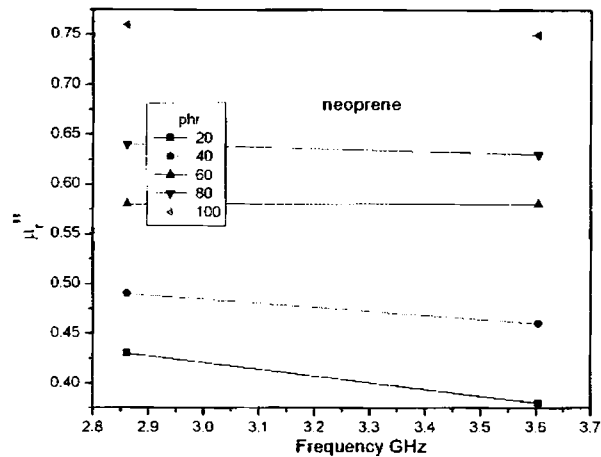


Figure 8.10: Variation of magnetic loss with frequency in the S band (neoprene-rubber based composites)

8.8 Complex dielectric permittivity in X band

The variation of the real part of the relative dielectric permittivity (ϵ'_r) of natural-rubber-nickel composites is depicted in figure 8.11 and that of neoprene-rubber-nickel composites in figure 8.12. It can be observed that, in both types of composites, the permittivity of a particular composite sample remains constant for the entire frequency range of 7 – 12 GHz. Frequency dependant dispersion of permittivity is completely absent in the X band frequency. The polarization mechanism operating in the gigahertz frequency is purely electronic or orientational

Chapter 8

with relaxation times smaller than the time period of the applied signals. Interfacial polarization, which is the basic reason for the dispersion at radio frequency (rf) regime, has no role to play in the microwave frequencies as it does not produce dispersion in ϵ'_r because of its much smaller relaxation time. But ϵ'_r was found to increase with the increase of mass ratio of filler in the composite as evident from figure 8.11 and figure 8.12. This phenomenon of increase in ϵ'_r with filler concentration can be attributed to the enhancement of electrical conductivity of the composites due to the incorporation of metal particles as filler.

It can be observed from figure 8.11 and figure 8.12 that the dielectric permittivity of neoprene rubber composites is much higher than that of natural rubber composites for a given filler concentration. Neoprene rubber is made of polar molecules and the polar nature of the molecules is retained even after the cross-linking of the molecular chains. Polar molecules of neoprene can undergo orientational polarization and can give rise to enhanced polarization compared to the molecules of natural rubber and this explains its higher dielectric permittivity.

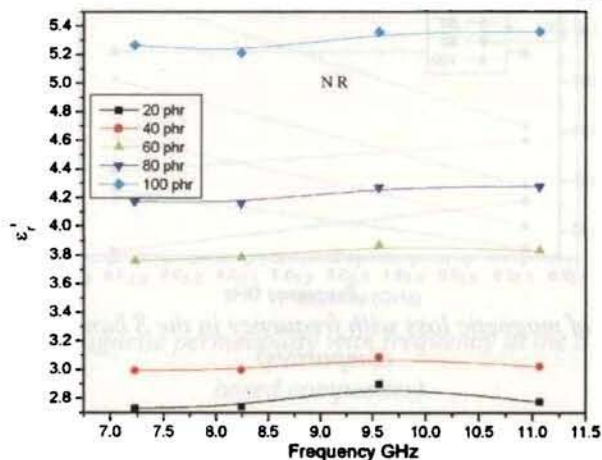


Figure 8.11: Variation of dielectric permittivity of natural rubber based composites with frequency in the X band

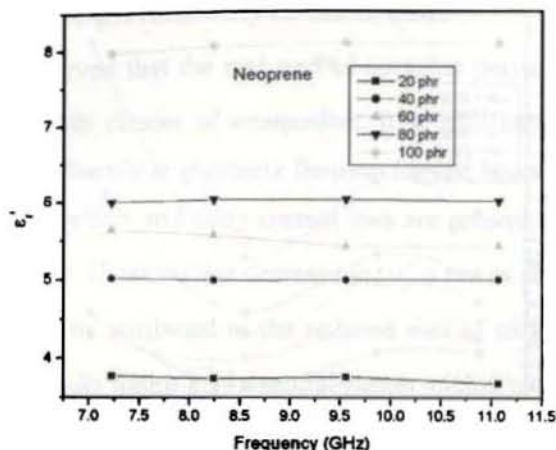


Figure 8.12: Variation of dielectric permittivity of neoprene- rubber based composites with frequency in the X band

Figure 8.13 and figure 8.14 depict the variation in dielectric loss (ϵ_r'') with frequency of natural-rubber-nickel and neoprene-rubber-nickel composites respectively.

In neoprene-rubber-nickel composites, as frequency increases ϵ_r'' registers a steady increase and this phenomenon is observed in all the five samples. This can be attributed to interfacial polarization and the resulting energy loss due to relaxation polarization. Even though the absence of interfacial polarization was confirmed from the absence of frequency dispersion in ϵ_r' , small amount of charge accumulation may be present around metal particles even at GHz frequencies. The electric conductance loss may also be contributing at higher frequencies and this could be the reason for enhanced loss for 100 phr sample towards the higher edge of the frequency band [24]. Also there is a steady increase in ϵ_r'' with the increase in the concentration of nickel in the composites suggesting the presence of electrical conductance loss.

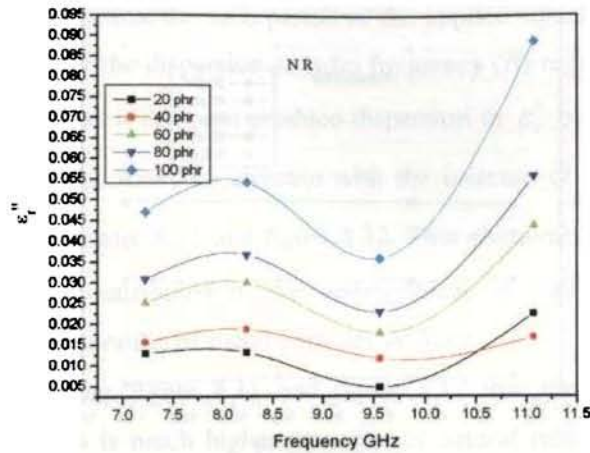


Figure 8.13: Variation of dielectric loss with frequency in natural rubber based composites in the X band

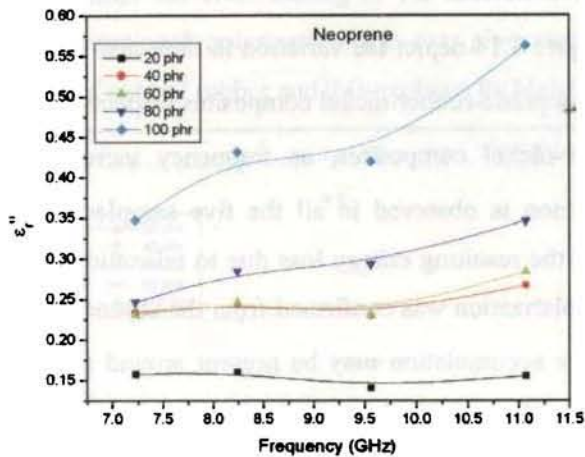


Figure 8.14: Variation of dielectric loss with frequency in neoprene-rubber based composites in the X band

Natural-rubber-nickel composites show a similar kind of variation in dielectric loss but at 8.25 GHz, there appears a relaxation peak. Orientational polarization of the polymer chains of natural rubber may have a relaxation times close to this frequency and causing the relaxation peak. But the dielectric loss increases towards the higher frequency side and increases sharply at higher loading fractions. Conductance loss due to the presence of metallic inclusions is attributed to this enhancement in dielectric loss.

8.9 Complex magnetic permeability in the X band

It was observed that the real part of complex permeability (μ'_r) decreases with increase in frequency in both classes of composites. It is well-known that the permeability of ferromagnetic nickel drops sharply at gigahertz frequencies and becomes close to unity at 10 GHz [20]. The influence of skin effect and eddy current loss are present in nanometer sized particles also, in a reduced magnitude. However the decrease in μ'_r is not as sharp as the reported behavior of bulk nickel and this can be attributed to the reduced size of nickel particle. The variation of μ'_r with frequency is shown in figure 8.15 (natural-rubber-nickel composites) and in figure 8.16 (neoprene-rubber-nickel composites).

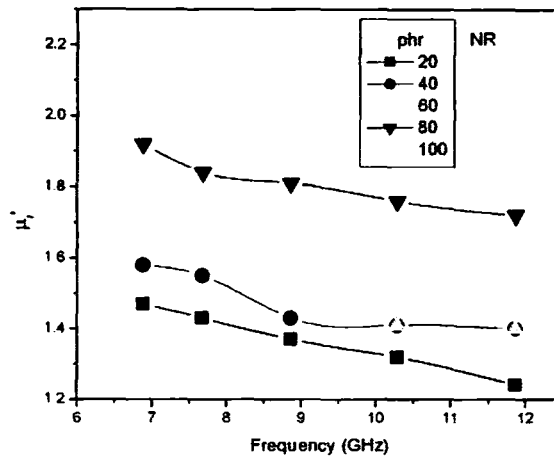


Figure 8.15: Variation of magnetic permeability with frequency of the natural rubber based composites in the X band

The magnetic loss (μ''_r) increases initially and both composites show a peak at about 8 GHz and then drops slightly (figures 8.17 and 8.18). This is due to the resonant vibration of the nickel particles in the oscillatory magnetic field [24]. Further, the loss is more pronounced in neoprene based composites, even though the pattern of variation remains the same, as evident from the graphs. It appears that the neoprene matrix offers less resistance to resonant vibrations of nickel particles on application of an oscillatory electromagnetic field.

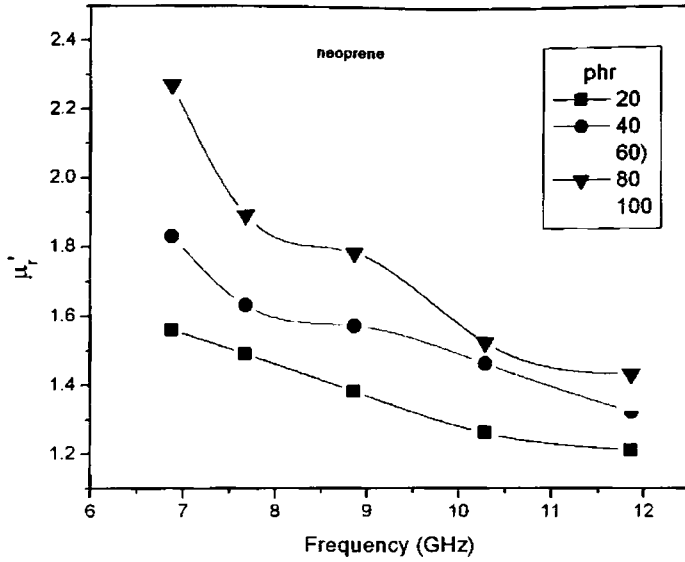


Figure 8.16: Variation of magnetic permeability with frequency of neoprene-rubber based composites in the X band

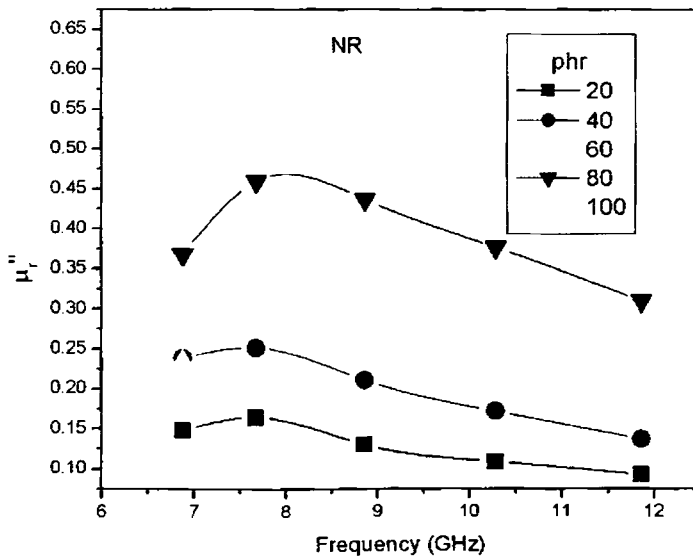


Figure 8.17: Variation of magnetic loss with frequency of the natural rubber based composites in the X band

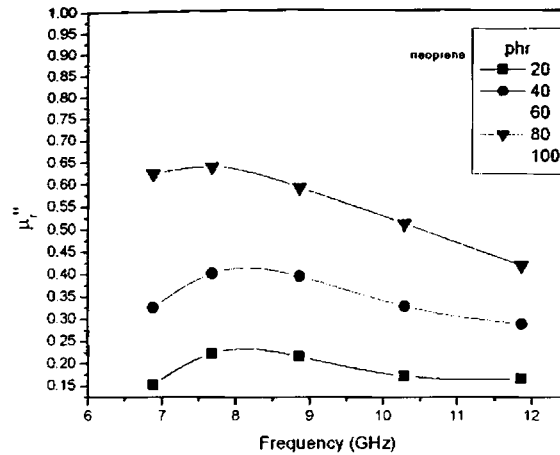


Figure 8.18: Variation of magnetic loss with frequency of the natural rubber based composites in the X band

8.10 Input impedance and reflection loss

The microwave absorption characteristics of a material are analyzed on the basis of its complex permittivity and permeability. Good absorbers should have low reflection coefficient and good absorption coefficient. Electromagnetic waves entering a material are absorbed effectively if there is a good impedance matching between the material and the free space and the condition for which can be written down as follows [24]

$$\frac{\mu'}{\varepsilon'} = 1 \quad (8.9)$$

The neoprene-nickel composites in these studies show that ε'_r varies between 2.5 and 5 with respect to different loadings and ε''_r varies between 1.2 and 2.2 and it is difficult to meet the condition given by equation (6) for any particular sample or in any given frequency. The propagation constant γ of electromagnetic waves in a material is given by the relation

$$\gamma = \alpha + i\beta \quad (8.10)$$

where α is the attenuation constant and β is the phase constant. In terms of the complex permittivity and permeability the propagation constant is expressed by the relation

Chapter 8

$$\gamma = j \frac{2\pi.f}{c} \sqrt{\mu_r \varepsilon_r} \quad (8.11)$$

Separating the real and imaginary parts of equation (11) gives the attenuation constant α and phase constant β . [25] as

$$\alpha = \frac{\sqrt{2}}{c} \pi.f \times \sqrt{(\mu_r'' \varepsilon_r'' - \mu_r' \varepsilon_r') + \sqrt{(\mu_r'' \varepsilon_r'' - \mu_r' \varepsilon_r')^2 + (\varepsilon_r' \mu_r'' + \varepsilon_r'' \mu_r')}} \quad (8.12)$$

and
$$\beta = \frac{\sqrt{2}}{c} \pi.f \times \sqrt{(\mu_r' \varepsilon_r' - \mu_r'' \varepsilon_r'') + \sqrt{(\mu_r'' \varepsilon_r'' - \mu_r' \varepsilon_r')^2 + (\varepsilon_r' \mu_r'' + \varepsilon_r'' \mu_r')}} \quad (8.13)$$

The input impedance of a wave absorber (Z_{in}) with a single layer, backed by a metallic reflector is given by the relation

$$Z_{in} = Z_0 \sqrt{\frac{\mu_r}{\varepsilon_r}} \tanh(\gamma.t) \quad (8.14)$$

Where Z_0 is the impedance of free space, and the reflection coefficient is given by the relation

$$\Gamma = \frac{Z_{in} - Z_0}{Z_{in} + Z_0} \quad (8.15)$$

and reflection loss expressed in decibel (R) is given as

$$R = 20.\log_{10}|\Gamma| \text{ dB} \quad (8.16)$$

The electrical wavelength (λ) in the material can be calculated from the phase constant β for any given frequency as

$$\lambda = 2.\pi / \beta \quad (8.17)$$

At the air material interface total cancellation of reflected wave can occur by interference between the incident and the reflected waves. The condition for this can be deduced by assuming that the dielectric loss in the medium is small compared with the dielectric permittivity [25]. The equation can be expressed as

$$t_0 = \frac{c}{4.f} \frac{1}{\sqrt{\mu_r' \varepsilon_r'}} \left(1 + \frac{1}{8} \tan^2 \delta_\mu \right)^{-1} \quad (8.18)$$

where δ_μ is the magnetic loss tangent.

Based on the equations given above, the propagation constant of the composites was calculated and from which the reflection loss at various frequencies were estimated. In this study the permeability and permittivity were not measured for the same frequencies, since the measurements were carried out at even and odd resonating modes of the cavity. The real part of the permittivity of a particular sample nearly remains a constant in the entire frequency range of X band and the average value of this permittivity was assumed to be valid for all frequencies and used in the calculations. The values of ϵ_r'' , μ' and μ'' were estimated for the entire range of X band in steps of 0.1 GHz by interpolating the plots with the help of a commercial computer software for extrapolation and interpolation of graphs.

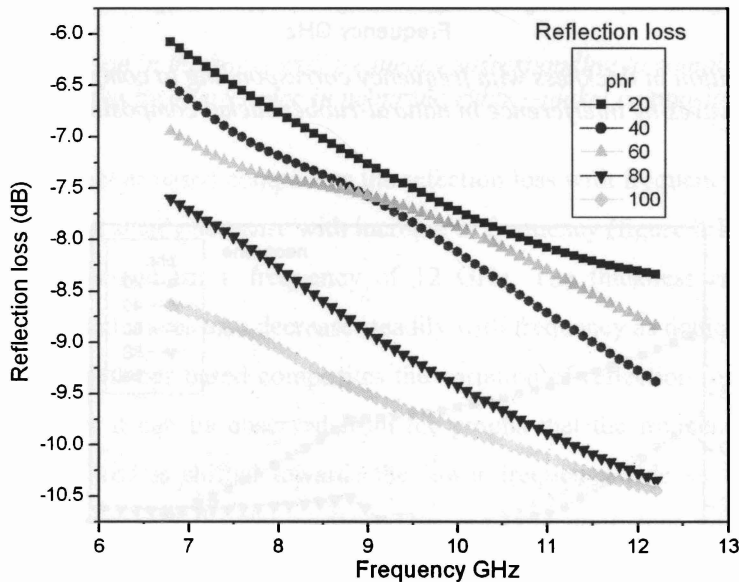


Figure 8.19: Reflection loss with frequency in natural-rubber-nickel composites

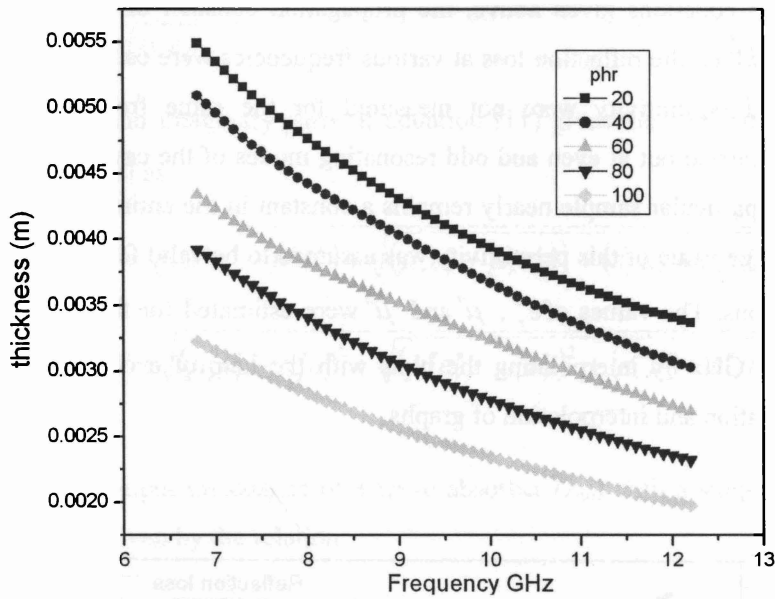


Figure 8.20: Variation in thickness with frequency corresponding to complete cancellation of waves by interference in natural-rubber-nickel composites

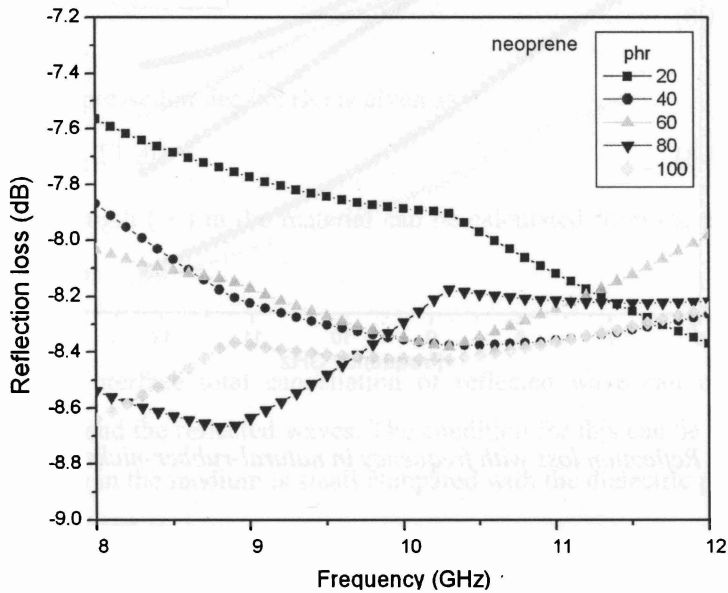


Figure 8.21: Reflection loss with frequency in neoprene-rubber-nickel composites

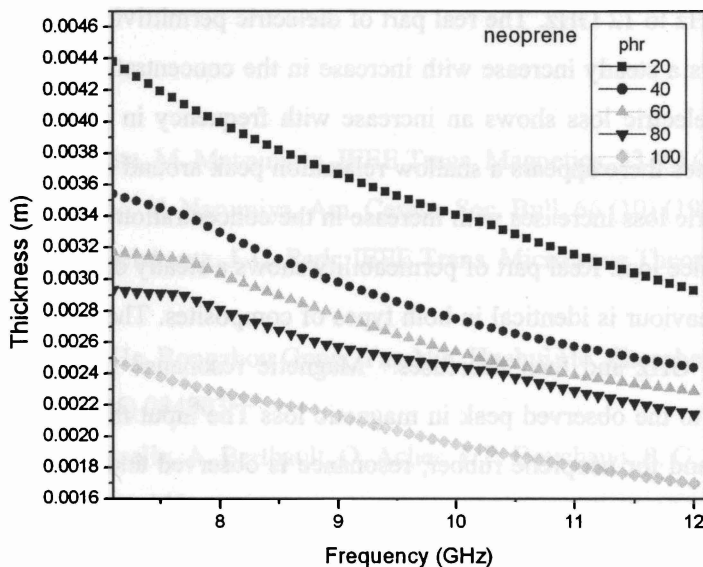


Figure 8.22: Variation in thickness with frequency corresponding to complete cancellation of waves by interference in neoprene-rubber-nickel composites

For natural rubber based composites the reflection loss with frequency does not show any resonance and shows a steady decrease with increase of frequency (figure 8.19). A maximum of -10.5 dB loss is registered for a frequency of 12 GHz. The thickness corresponding to the cancellation of reflected waves also decrease steadily with frequency as depicted in figure 8.20

For neoprene-rubber based composites the variation of reflection loss with frequency is shown in figure 8.21. It can be observed from the graphs that the frequency corresponding to maximum reflection loss is shifted towards the lower frequency side as the concentration of nickel particles increases in the composites. This result is consistent with previous reports.

The thickness for cancellation of reflected wave is calculated and the results are shown in figure 8.22. There is a steady decrease in thickness corresponding to total annihilation of waves by interference.

8.11 Conclusion

The complex dielectric permittivity and magnetic permeability of natural-rubber-nickel and neoprene-rubber-nickel nanocomposites were evaluated in the X-band of microwave

Chapter 8

frequencies from 7 GHz to 12 GHz. The real part of dielectric permittivity does not change with frequency but registers a steady increase with increase in the concentration of loading of nickel nanoparticles. The dielectric loss shows an increase with frequency in general and for natural rubber based composites there appears a shallow relaxation peak around 8.25 GHz. In both these of composites, dielectric loss increases with increase in the concentration of filler which could be the result of conductance loss. Real part of permeability shows a steady decrease with increase of frequency and the behaviour is identical in both types of composites. The magnetic loss shows a small relaxation at 8 GHz and then decreases. Magnetic resonance of ferromagnetic nickel particles is attributed to the observed peak in magnetic loss. The input impedance and reflection loss were calculated and for neoprene rubber, resonance is observed and found to shift towards higher frequency side with the increase in concentration of nickel nanoparticles.

References:

1. Y. Miyata, M. Matsumoto, IEEE Trans. Magnetics, 33 (5) (1997) 3427-29
2. K. Ishino, Y. Narumiya, Am. Ceram. Soc. Bull. 66 (10) (1987) 1169
3. P. S. Neelakanta, J. C. Park, IEEE Trans. Microwave Theory Tech 43 (6) (1995) 1381
4. Yanfei He, Rongzhou Gong, Yan Nie, Huahui He, Zhensheng Zhao J. App. Phys. 98 (2005) 084903
5. D. Rousselle, A. Berthault, O. Acher, J. P. Bouchaud, P. G. Zerah, J. Appl. Phys. 74 (1993) 475
6. S. Sugimoto, T. Maeda, D. Book, T. Kagotani, K. Inomata, M. Homma, H. Ota, Y. Houjou, R. Sato J. Alloys Compd 330 (2002) 301
7. Jiu Rong Liu, Masahiro Itoh, Takashi Horikawa, Ken-ichi Machida, J. App. Phys. 98 (2005) 054305
8. Bao-Wen Li, Yang Shen, Zhen-Xing Yue, Ce-Wen Nan. App. Phys. Lett. 89 (2006) 132504
9. A. Bahadoor, Y. Wang, M. N. Afsar J. Appl. Phys. 97 (2005) 10F105
10. Sung-Soo Kim, Sun-Tae Kim, Yeo-Choon Yoon, Kyung-Sub Lee, J. Appl. Phys (2005) 10F905
11. M.C. Dimri, S. C. Kashyap, D. C. Dube, Ceramics International, 30 (2004) 1623-1626
12. N. Gupta, M. C. Dimri, S. C. Kasyap, D. C. Dube, Ceramics International (2004) 3123-27
13. N. Gupta, S. C. Kashyap, D. C. Dube J. Mag. Mag. Mater (2004)
14. K. P. Surendran, P. V. Bijumon, P. Mohanan, M. T. Sebastian, Applied Physics A, 81 (2005), 823-826
15. Stepan L. PIERS online, (4), 6, (2008), 686-690
16. D. D. L. Chung, *Composite Materials: Science and Applications, Functional Materials for Modern Technologies*, p. 93, Springer (2003).

Chapter 8

17. Y. Ye, A. Sklyuyev, C. Akyel, P. Ciureanu, *IEEE Proc. Instrumentation and Measurement Technology Conference, IMTC (2007)* 1-6, DOI: 10.1109/IMTC.2007.379006
18. Mi Lin, Yong Wang; M.N Afsar, *IEEE Proc. 13th International Conference on Terahertz Electronics, Infrared and Millimeter Waves . IRMMW-THz 2005.* 1, 19-23 (2005) 62 - 63 1 DOI: 10.1109/ICIMW.2005.1572407
19. A. Sklyuyev, M. Ciureanu, C. Akyel, P. Ciureanu, D. Menard, A. Yelon, *IEEE Proc. Canadian Conference on Electrical and Computer Engineering, (2006)* CCECE-2006 1486-1489 DOI:10.1109/CCECE.2006.277824
20. J. E. Atwater, *Appl. Phys. A, (2002)* 75, 555-558
21. D. Y. Kim, Y. C. Chung, T. W. Kang, H. C. Kim, *IEEE Tans. on Magnetics, 32 (2), (1996)* 555-558
22. Chapter 7, this thesis
23. C. J. F. Bottcher, *Theory of Electric Polarization (1952)* Elsevier, New York
24. Y. B. Feng, T. Qui, C. Y. Shen, X. Li, *IEEE Trans. Magnetics, 42, 3, 2006,* 363-368
25. B. Zhang, Y. Feng, J. Xiong, Y. Yang, H. Lu, *IEEE Trans. Magnetics 42 (7) (2006)* 1778
26. Z. M. Elimat, A. M. Zihlif, G. Ragosta, *J. Phys. D. Applied Phys. 41 (2008)* 165408
27. Baziard. Y, Breton. S, Toutain. S, Gourdena. A, *Eur. Polym. Journal, 24 (1988)* 521

Chapter 9

Conclusion

The development of material science is always associated with advancement made in materials. So synthesis and characterization of materials assume great importance in the realm of material science. New and novel methods of synthesis also are important from a pure science perspective. These materials often provide a template for the proper understanding of the physics at the macro and micro dimensions. The emergence of nanoscience and nanotechnology augur very well for research in material science. Novel preparation techniques like sol-gel, auto-combustion and other cold precipitation techniques enabled researchers to synthesize nanosized particles so preparation of materials using these techniques is all the more important. Composites are very vital for many applications, because the best of the matrix and filler can be advantageously utilized for tailoring the properties. Magnetic nanocomposites are found to play an important role in many devices. So preparation and characterization of these nanocomposites also assume significance. This particular work which is basically on the synthesis and characterization of precursor for composites and synthesis of composites using these precursors is such an attempt in realizing the objectives of synthesizing precursors, nano composites and the investigations on their various physical properties in order to understand the basic physics.

Both ceramic and metal nanoparticles play an important role in the modern day science and technology. Testing and fine tuning synthetic techniques for both these kinds of particles is thus of prime importance. For ceramic nanoparticles the sol-gel auto-combustion method is much promising because of its ability to yield phase pure nanoparticles. Unlike in conventional ceramic technique which yields micron sized particles, sol-gel method of synthesis are suitable for large scale production of nanosized particles. In this study, phase pure ceramic nanoparticles were successfully synthesized and the method was optimized effectively. Zinc and cadmium ferrite

Conclusion

nanoparticles with grain sizes of ~ 50 nm were synthesized by sol-gel technique and its phase purity and particles size were established using various characterization tools like XRD, TEM and SEM. The evaluation of dielectric permittivity of these materials revealed that they exhibit dielectric dispersion at radio frequencies. The studies of a. c. conductivity of these ferrites provided insights about the kind of conduction mechanism which may be present in these materials. These two ferrites systems behaved identically with respect to dielectric properties.

The finite size effects on the magnetic properties of normal spinel ferrite are an interesting area of research work for over a decade. Zinc ferrite and cadmium ferrite are purely antiferromagnetic systems with no apparent magnetization at room temperature. If synthesized in nanometric size they exhibit ferrimagnetic ordering as revealed by many research findings. In this study it was established beyond doubt that even at a particle size of around 50 nm phase pure zinc and cadmium ferrite do not show any magnetic properties at room temperature and ferrimagnetic ordering in these ferrites systems becomes observable only at temperatures as low as 10 K. But on further reduction of size by high energy ball-milling-(HEBM) these particles exhibited ferrimagnetic properties contrary to the early belief that normal ferrites are antiferromagnetic. The energy exchange between crystal lattice and milling system plays a major role in deciding the magnetic properties of these ferrites. The second important finding in this study is that , when started from low grain size materials , the same effect produced by prolonged milling of tens of hours can be achieved by ball-milling for shorter duration (maximum a couple of hours) if the starting grain size is small. This study hypothesizes the inversion in the spinel structure as a reason for the observed ferrimagnetic ordering in the ferrites. The third finding is that the two systems which were under investigation were exactly identical in dielectric as well as magnetic properties.

The low temperature studies conducted on unmilled zinc ferrite revealed beyond doubt that the material undergoes a magnetic phase transition at around 18 K which is slightly higher than what was observed earlier. This deviation is attributed to reduced particle size. The low temperature magnetization measurements of 30 min milled sample clearly showed two components of magnetic ordering, one is purely paramagnetic and the other is ferrimagnetic. Cation redistribution accounts for the observed ferrimagnetism exhibited by these ferrites.

Conclusion

However these findings are inconclusive and there is scope for further investigations. Neutron scattering experiments can shed light on the magnetic structure of these ferrites. Since FC/ZFC experiments cannot establish the origin of superparamagnetism in these compounds, advanced experiments using an ac susceptometer can establish whether the observed magnetism at finite sizes is due to spin glass like behaviour or entirely due to ordering resulting out of a cation redistribution. Studies employing magnetic circular dichroism (MCD) can be useful for delving into the origin of magnetism at the nano level exhibited by the normal spinels.

The second part of this research work focuses on the preparation of nanonickel particles and preparation and characterization of nanocomposites based on nanonickel and rubber. Magnetic metal nanoparticles are much sought after materials in the modern day world of technology. A novel technique was developed for the bulk synthesis of nickel nanoparticles. It was established that nickel nanoparticles synthesized using the new method is pure and is in the size range of 15-40 nm. They find numerous applications and efforts are on in the laboratory to synthesize metal-particle based ferrofluids using nickel nano particles in this method. Preparation of ferrofluid using these nickel precursors can lead to thermally conducting fluids.

Composites based on metal particles embedded in polymer matrices have been gaining a lot of interest in recent times. Rubber-nickel composites based on natural rubber and neoprene rubber were successfully synthesized and thoroughly characterized. The cure characteristics of these two composites show similarities and differences. There is considerable improvement in the mechanical properties of both composites and the reinforcing nature of metallic nickel particle in these two polymer matrices was established beyond doubt. They are flexible magnetic materials and have the potential of being used in a number of technological gadgets. It was not possible to conduct the low temperature magnetic properties of the composites. Nickel based composites can be developed using a number of other matrices like polymers, silica and ceramics and the physical characteristics of these nanocomposites can be interesting from a technological point of view. Further, the magnetic properties of such composites can be investigated at room temperature and low temperatures because any change in magnetic properties of nickel particles when embedded in a polymer matrix will be of fundamental interest.

The investigations on the dielectric properties of the composites in the rf regime revealed some very interesting findings. The dielectric permittivity of pristine neoprene is higher than that

Conclusion

of natural rubber. On loading with nickel nanoparticles both composites exhibited enhancement in the dielectric permittivity and this enhancement is found to follow some empirical relationship. Natural rubber is a low loss material and nano nickel embedded composites can find applications in rf electronic devices owing to the tunability of dielectric properties. The dielectric loss in neoprene based composites is comparatively larger.

Microwave properties of the rubber nickel composites in the S and X bands of microwave frequencies revealed some interesting findings. The real part of the complex permittivity remained a constant for any particular composite suggesting the absence of high frequency relaxation processes in the material. Neoprene-rubber based composites always exhibited higher dielectric permittivity and higher dielectric loss compared to natural rubber. The characteristics of complex magnetic permeability of both composites are identical with real part of permeability decreasing with increase in frequency and drops off towards the end of the X band. Even the magnetic relaxation effects revealed by the imaginary part of the magnetic permeability are identical in nature. The magnetic properties are only influenced by the presence of nickel particles in the composites and the rubber matrix has no role to play in it.

These composites are reasonably good microwave absorbers with reflection loss reaching up to 11 dB in the X band. There is further room for more such investigations in improving the microwave absorption characteristics by incorporating carbon black along with nanonickel in rubber. Such a combination of a magnetic filler and absorbing filler like carbon black can tune the bandwidth of absorption. These composites can also serve as good sensing elements for pressure sensing. Such a study could not be carried out.

Annexure

On the structural, optical and dielectric properties of zinc aluminate nanoparticles

1. Introduction

Zinc aluminate, a mixed oxide of aluminium and zinc, is a naturally available mineral commonly called as gahnite with a normal spinel structure having all zinc cations in the tetrahedral and all aluminium cations in the octahedral voids of fcc lattice of oxygen anions. Zinc aluminate is a widely used catalyst employed in chemical reactions namely synthesis of methanol and synthesis of styrenes from acetophenones [1,2] (vaan der Laaga et al 2004; Xiuhua Wei et al 2006). In addition to this, zinc aluminate is used as a catalyst support owing to its high thermal stability. Recently the optical properties of zinc aluminate is being investigated and it was reported that polycrystalline zinc aluminate has an optical band gap nearly equal to 320 nm and is highly reflective at wavelengths less than 300 nm [3, 4] (Ciupina. V. et al 2004; Ravindra Pandey et al 1999). Thus zinc aluminate may find applications in opto-electronic devices operated in the ultraviolet region. Studies on the optical and catalytic properties of zinc aluminate nanoparticles were carried out by many researchers, but reports on the dielectric properties of this material is very rarely found in literature. Zinc aluminates resembles zinc ferrite structurally, and it has been found recently that zinc ferrite in the nano-regime show anomalous magnetic properties in that zinc ions instead of occupying tetrahedral (A) sites occupies octahedral (B) sites partially when prepared in the nano-regime [5] (Roy. M. K et al 2006). Zinc aluminate can be considered as the non-magnetic counterpart of zinc ferrite and an ideal template to test the hypothesis on the migration of zinc ions to the B sites as a consequence of the size reduction as the standard property. This article describes the synthesis of zinc aluminate nanoparticles in a sol-gel combustion method, the characterization of the material and the evaluation of its dielectric

Annexure

properties in a frequency range of 100 kHz to 8 MHz. Synthesis of zinc aluminate nanoparticles in sol-gel combustion method was taken as an example for the synthesis of spinel structured mixed oxide nanoparticles in general and it was attempted to understand the various chemical and physical phenomena involved in the process of synthesis with analysis carried out in each stage of the preparation by various analytical tools.

2. Experimental details

Zinc nitrate hydrate and aluminium nitrate hydrate taken in 2:1 molar ratio were dissolved in ethylene glycol, by adding ethylene glycol in small quantities, to form a saturated solution. The solution was heated at 70°C with constant stirring on a magnetic stirrer for several hours until gel formation had taken place following a chemical reaction. The gel was heated at a temperature of 180°C placed on a heating mantle until combustion had taken place forming slightly rose colored fine powder. This powder was analyzed using X-ray diffractometry and it was found that the phase of zinc aluminate was not yet formed. This powder was calcinated at different temperatures starting from 350°C and had been analyzed using XRD after each calcination trials to study the structural details. Calcination at 700°C for six hours yielded phase pure zinc aluminate nano particles.

The gel formed at 70°C had been analyzed by means of differential scanning calorimetry (DSC) (Mettler Toledo DSC 822e) and thermo gravimetric analysis (Perkin Elmer, Diamond TG). zinc aluminate nanocrystallites thus formed were characterized using X-ray diffractometry (XRD) (Rigaku Dmax C with Cu K α X-ray source), transmission electron microscopy and energy dispersive spectra (EDS) (Joel JEM-2200 FS electron microscope operated at 200 KV), UV-Vis NIR spectroscopy (Jasco V 530 spectrophotometer) and Fourier Transform Infrared spectroscopy (FTIR) (Thermo Nicolet Avatar 370).

Dielectric and ac conductivity studies of zinc aluminate were carried out using HP Impedance analyzer model 4285 A and a home-made dielectric cell under a vacuum of 10⁻³ mbar and at temperatures varying from 30 °C to 120 °C. The fabrication details of the dielectric cell are cited elsewhere. [6](Mohammed. E. M et al 2002). Nanoparticles of zinc aluminate were pressed into pellets of size 12 mm in diameter and approximately 2 mm in thickness. These pellets were

sintered at a temperature of 700°C for 24 hours to achieve maximum compaction of the particles. In the dielectric cell a capacitor is formed by keeping the pellet in between two copper discs of the same diameter and the capacitance was measured in the impedance analyzer. Temperature was measured with a Cryocon temperature controller with platinum resistance (PT-100) sensor. The measurements of the capacitance of the capacitor were carried out in a frequency range of 100 kHz to 8 MHz. The instrument we used is capable of capacitance measurements up to 30 MHz, but we had limited the measurements only to 8 MHz, because of the limitations of the co-axial cable used in our experiments. The dielectric permittivity of the material was calculated from the values of capacitance using the relation

$$\varepsilon' = \frac{C.d}{\varepsilon_0 A} \quad (1)$$

and dielectric loss of the material using the equation

$$\varepsilon'' = \varepsilon' \tan \delta \quad (2)$$

where, ε' is the dielectric permittivity of the sample (the real part), C is the capacitance of the capacitor formed by inserting the sample between two metal plates, d is the thickness of the sample, ε_0 the permittivity of free space and A is the area of cross section of the sample. The ac conductivity of the sample was determined from the loss tangent by using the relation

$$\sigma_{ac} = 2.\pi.f.\varepsilon_0.\varepsilon'.\tan \delta \quad (3)$$

where f is the applied frequency [7] (Tareev. B 1975)

3 Results and Discussion

3.1 DSC and TGA

Figure 1 shows the heat flow diagram of the differential scanning calorimetry performed on the gel. Two exothermic peaks are observed at temperatures 183°C and 422°C. The first exothermic peak at 183°C corresponds to the combustion of the Gel at this temperature to form the powder. The second peak can be attributed to the formation of the spinel phase about 400°C. The calcination trials indicated that the phase formation takes place in this temperature range. The crystallites go to a lower energy state by the formation stable spinel structure through an

Annexure

exothermic stage. In sol-gel synthesis of $ZnAl_2O_4$ there is an intermediate crystalline phase as indicated in the XRD diagram (figure 3). This intermediate phase has a non-cubical structure and closely resembles a phase of Aluminium hydroxide. It appears that this intermediate phase is a mixture of aluminium hydroxide and zinc hydroxide.

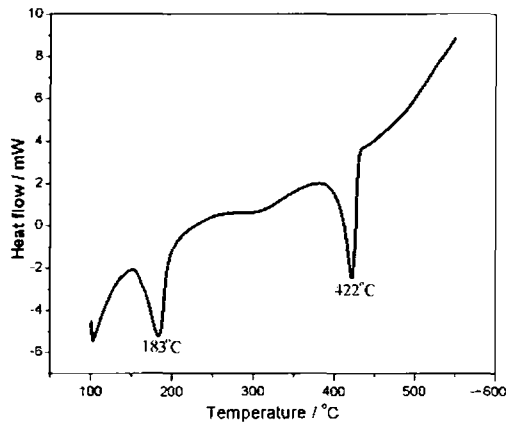


Figure 1: Heat flow diagram obtained by differential scanning calorimetry of the gel

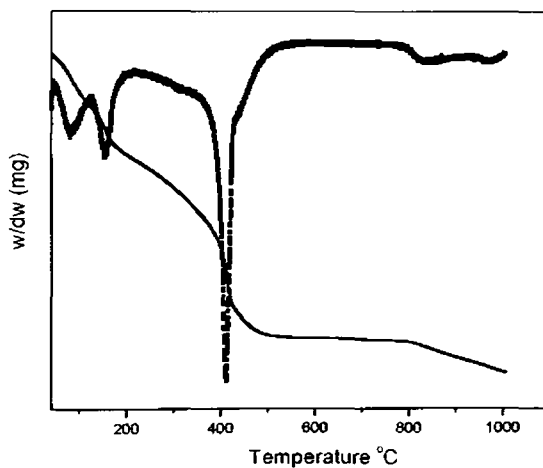


Figure 2 TGA and DTGA curves of the gel

Figure 2 depicts the TGA of the gel before calcination. Both the variation of mass of the compound with the temperature and its rate of variation with temperature (differential coefficient of mass variation with respect to temperature) are shown in the diagram as separate plots. A sudden fall in mass of the compound is evident at two positions, close to 200°C and 400°C. The first one is attributed to the expulsion of the organic solvent in the gel and the formation of the powder hydroxides of zinc and aluminium. The second position can be assigned to the formation of spinel phase structure from the hydroxides of the metals. This result is consistent with what was observed in the DSC analysis.

3.2 Structural studies

Figure 3 is the XRD diagram of the intermediate phase formed at 180°C. This compound seems to be a mixture of aluminium hydroxides and zinc hydroxide with a non-cubical structure. Figure 4 shows the XRD diagrams of the compound calcinated at 350°C, 500°C, 700°C and 800°C. It can be seen that the phase formation is complete at 700°C and further increase in calcination temperature doesn't improve the crystallinity of the compound. All peaks are well defined pointing to the high crystalline nature of the sample. The XRD pattern was compared with JCPDS files (file no. 74-1138) and all the diffraction peaks are in good match with the reported result and the peaks were indexed with the help of these reported patterns. Rietveld refinement was carried out to verify the formation of spinel phase and also to determine the cation distribution or displacement of zinc ion from A site to B site. It can be observed that excellent matching is obtained in terms of the peak positions and peak intensity between the theoretical and observed data as depicted in figure 5. The lattice parameter obtained from the Rietveld analysis is

Annexure

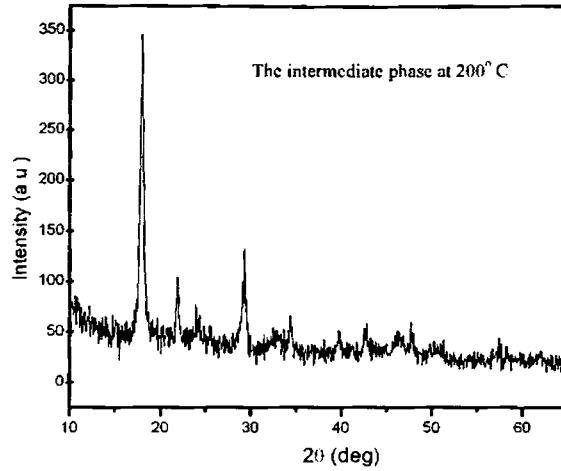


Figure 3: XRD pattern of the intermediate phase

8.098 Angstroms. The reported value of lattice parameter is 8.099 Å according to the JCPDS data and this close agreement indicates the phase purity of the zinc aluminate particles obtained in the sol-gel technique. The particle size was determined from the XRD data using the Debye Scherrer equation for the average particle size D

$$D = \frac{0.9\lambda}{\beta \cdot \cos\theta} \quad (4)$$

where λ is the wavelength of the X-ray source, β is the full width at half maximum (FWHM) of the diffraction peak and 2θ is the diffraction angle [8] (Keer H. V 1998). The FWHM was determined by giving Gaussian fit to the diffraction peaks with the help of a software package. The average particle size of the particles was found to be 40 nm.

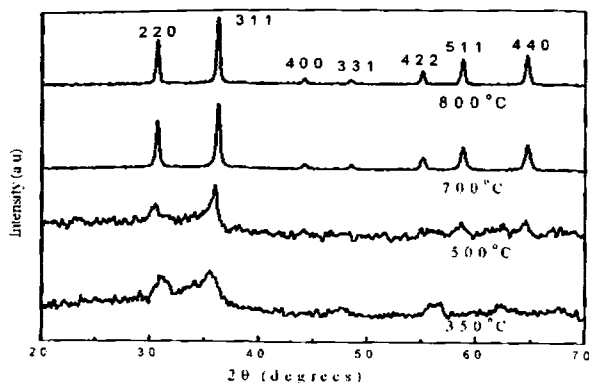


Figure 4: XRD pattern of the zinc aluminate particles fired at temperatures starting from 350°C to 800°C

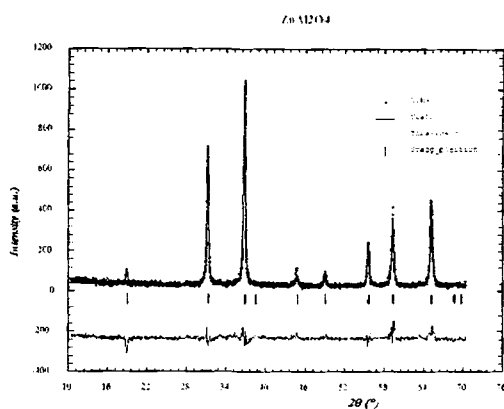


Figure 5: Rietveld analysis of XRD of zinc aluminate particles

3.3 FTIR spectroscopy

The FTIR spectrum is presented in figure 6 the curves named A, B and C are corresponding to of the gel, the intermediate phase and the final spinel phase of the compounds formed during the sol-gel synthesis. In plot A, a broad absorption band centered at 3470 cm^{-1} is visible and this corresponds to OH group, and this is contributed by the water content. The bands at 1630 cm^{-1} and 1386 cm^{-1} can be attributed to the OH group in the metal alkoxides present in the gel. An intermediate phase is formed at 180°C and the infrared absorption of this material is

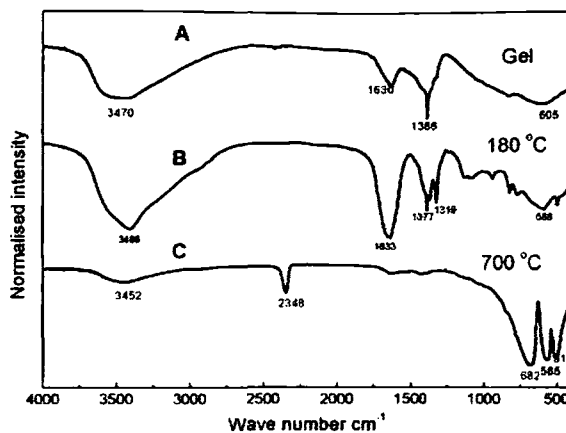


Figure 6: FTIR spectrum of compounds at various stages of synthesis of zinc aluminate nanoparticles

shown in plot B. It can be seen that the bands at 1630 cm^{-1} and 1386 cm^{-1} are still present with a little splitting and this can be explained due to the formation of metal hydroxides as an intermediate compound before the formation of the zinc aluminate spinel. In plot C, which is of the calcinated zinc aluminate, the band at 3408 is almost absent and a small shallow band is indicated by the slight water content in the crystallites. Three sharp absorption bands visible in plot C at 682 , 565 and 510 cm^{-1} arise from the stretching vibrations of tetrahedral and octahedral bonds in the spinel. The peak observable at 2348 cm^{-1} can be attributed to the presence of oxygen-oxygen bonds in the fcc crystal lattice of oxygen atoms. This peak is detectable in all spinel compounds and can be treated as a characteristic feature of spinel structured crystallites. In plot B the metal bonds start to appear indicating the beginning of the formation of spinel phase.

3.4 TEM and EDS analysis

Figure 7 depicts the TEM image of the particles calcinated at 700°C . The sizes of all particles lie in the range of 25 to 60 nm. The size distribution is narrow. It is evident from the micrograph that the shape of the particles is very nearly spherical. The average size of 40 nm obtained from the XRD analysis is in consistent with this result.

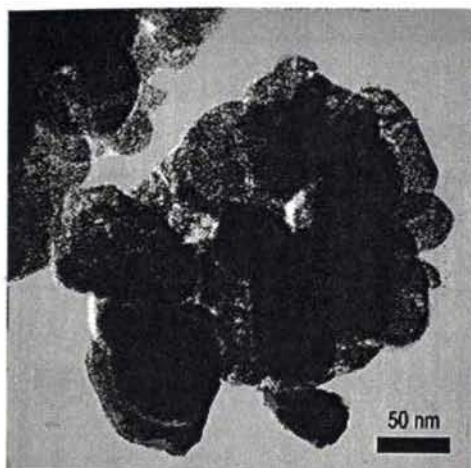


Figure 7: TEM micrograph of zinc aluminate nanoparticles

The energy dispersive spectrum of the particles is depicted in figure 8. The counts corresponding to C and Cu are from the organic solvent in which the particles are dispersed and from the copper grid respectively. The $K\alpha$ lines of Al and Zn can be clearly noticed in the spectrum. An exact quantitative estimate of the content of these elements was not carried out but from the number of counts it appears that the number of atoms of Zn is half the atoms of Al.

3.5 Optical Measurements

The absorption spectra of zinc aluminate particles in transmission mode was recorded by dispersing the particles uniformly in liquid paraffin, in the wavelength range of 225 nm to 800 nm. For a direct band gap semi conducting material the absorption coefficient near the band edge is given by

$$\alpha = \frac{A}{h\nu} (h\nu - E_g)^{\frac{1}{2}} \quad (5)$$

Where α is the absorption coefficient, $h\nu$ the photon energy E_g the energy gap and A is constant depending on the type of transition. Equation 5, for any energy can be rearranged and written in the form

$$(\alpha h\nu)^2 = A^2 (h\nu - E_g) \quad (6)$$

Annexure

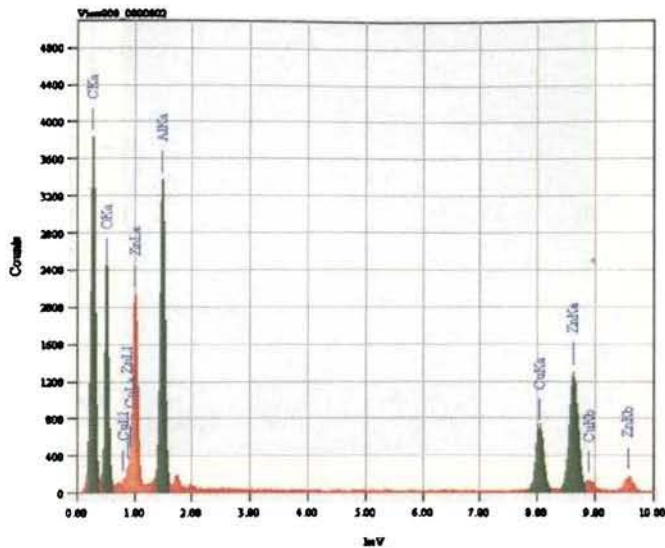


Figure 8: EDS spectrum of zinc aluminate nanoparticles

From equation (6), it is clear when $h\nu = 0$, $E_g = h\nu$. The Energy gap is determined by plotting $(\alpha h\nu)^2$ against $h\nu$ and finding the intercept on the $h\nu$ axis by extrapolating the plot to $(\alpha h\nu)^2 = 0$ as shown in figure 9. A band-gap energy of 3.84 eV was observed which is slightly higher than the reported band gap of bulk zinc aluminate suggesting a blue shift which can be attributed to the quantum confinement due to small size of zinc aluminate particles [Turton.R 2000].

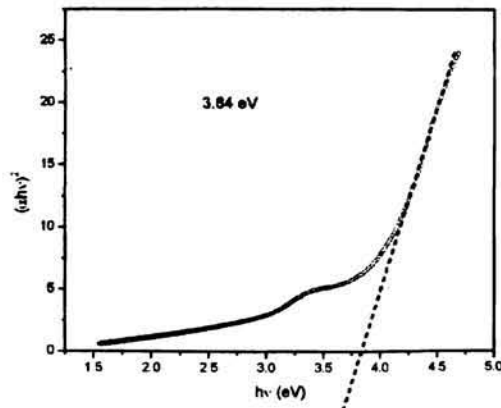


Figure 9: Tauc plot to determine the optical band-gap from UV-Vis absorption spectrum

3.6 Dielectric studies

The variation in dielectric permittivity (ϵ') with applied frequency is presented in figure 10 as a semi log plot in which log of the frequency is in the x-axis and ϵ' is in y-axis. It can be observed that there is a steady decrease in ϵ' with applied frequency. This phenomenon can be understood on the basis of Maxwell-Wagner model of interfacial polarization and Koop's phenomenological theory [9, 10] (Koops. C. G, 1951; Wagner. K.W 1993). The zinc aluminate pellets used in the study was made of pressed nanoparticles. The band gap studies of the sample already

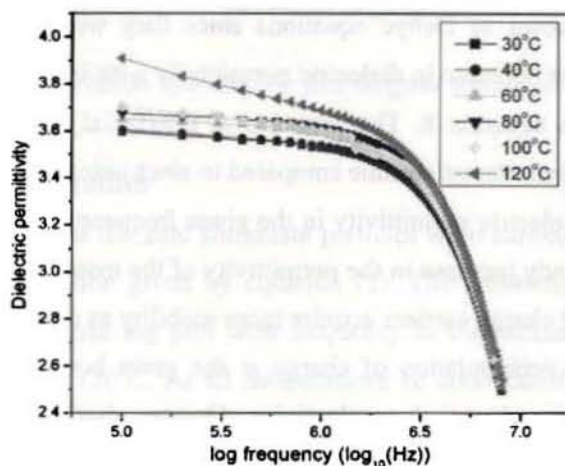


Figure10: Variation of dielectric permittivity of zinc aluminate with applied frequency at temperatures ranging from 30°C to 120 °C

revealed that the sample has semi-conducting nature. Every grain of the pellets can be considered having a perfect crystalline characteristics and therefore having low electrical resistance compared to the grain boundaries. This is exactly the model presented in Koop's theory. Maxwell-Wagner type interfacial polarization exists in the grain boundaries around the grains, by accumulation of charges in these high resistance regions. This kind of polarization exists in all poly-crystalline condensed matter samples which are heterogeneous in composition. Considering

Annexure

that the material has a single relaxation time in the frequency regime under test it is possible to write the equations for complex dielectric permittivity as

$$\varepsilon^*(\omega) - \varepsilon_\alpha = \frac{\varepsilon_s - \varepsilon_\alpha}{1 + i\omega\tau} \quad (7)$$

where $\varepsilon^*(\omega)$ is the complex permittivity at the frequency ω and ε_α is the permittivity at optical frequencies. Equation 7 can be written as real and imaginary parts separated as

$$\varepsilon'(\omega) = \varepsilon_\alpha + \frac{\varepsilon_s - \varepsilon_\alpha}{1 + \omega^2\tau^2} \quad (8)$$

$$\text{and } \varepsilon''(\omega) = (\varepsilon_s - \varepsilon_\alpha) \frac{\omega\tau}{1 + \omega^2\tau^2} \quad (9)$$

Equations 8 and 9 are known as Debye equations since they were derived by Debye on a molecular basis [17]. The decrease in dielectric permittivity with increase in applied frequency is understood according to equation 8. The presence of interfacial polarization gives rise to a relaxation process with a high relaxation time compared to electronic or dipolar polarization. This causes a decrease in the dielectric permittivity in the given frequencies. It can be observed from figure 10 that there is a steady increase in the permittivity of the material at all frequencies. With the increase of temperature charge carriers acquire more mobility as a result of thermal activation and this can increase the accumulation of charge at the grain boundaries, because the grain boundaries exhibit a lower electrical conductivity. Greater charge accumulation at higher temperatures in the interfaces of grains gives rise to enhanced dielectric permittivity.

It can be observed that the dielectric permittivity of zinc aluminate is smaller than some of the other members in the spinel family. Zinc ferrite and manganese ferrite has larger values of dielectric permittivity [11,12] (Veena et al 2008; Devan R S et al 2006). Zinc aluminate has a smaller crystal size compared to ferrites. The smaller the size the smaller is the electronic charge separation in the crystals when an electric field is applied. The component of electronic polarization is smaller in zinc aluminate compared to ferrites. Dielectric loss tangent is plotted against applied frequency in figure 11. The loss tangent decreases with the increase of applied frequency. As the temperature increases the loss tangent increases steadily and shows shallow relaxation peaks centered about 2 MHz

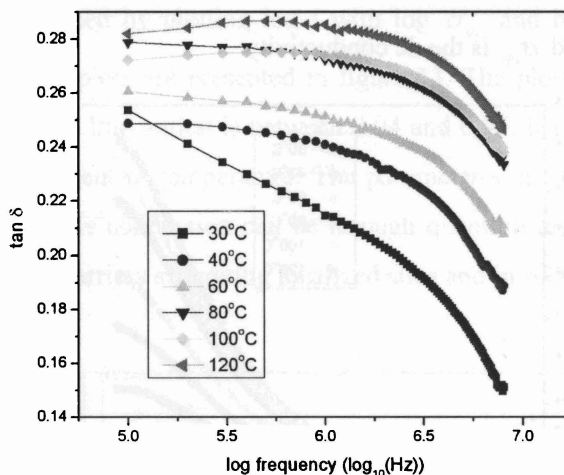


Figure 11: Variation of dielectric loss tangent with applied frequency

3.7 Ac conductivity studies

Studies on ac conductivity of the zinc aluminate particles were carried out from the loss tangent data by employing the relation given by equation (2). The variation of the ac conductivity is plotted in Figure 12 as a semi log plot with frequency in the horizontal axis for temperatures starting from 30°C through 120°C. At all temperatures ac conductivity shows a steady increase with the increase of frequency. In a dielectric material there are no free charge carriers and therefore there cannot be any dc conduction by means of the movement of free charges. The ac conduction in the material is through a hopping mechanism of bound charges, in which charges hop back and forth between well defined bound states. Electrons undergo hopping between bound states through a tunneling process from one site to other. The hopping mechanism is supported by the increase in frequency and ac conductivity increases at higher frequencies. Even though an ideal dielectric material doesn't have any free charge carriers, there can be small amount of free charges in them and the measured conductivity arises from the two contributing factors, namely the ac and dc conduction. In general the measured ac conductivity is represented by the relation

$$\sigma_{ac}(\omega)_m = \sigma_{ac}(\omega) + \sigma_{dc} \quad 10$$

where $\sigma_{ac}(\omega)_m$ is the total frequency dependant conductivity and $\sigma_{ac}(\omega)$ is the contribution from the ac conductivity and σ_{dc} is the dc conductivity.

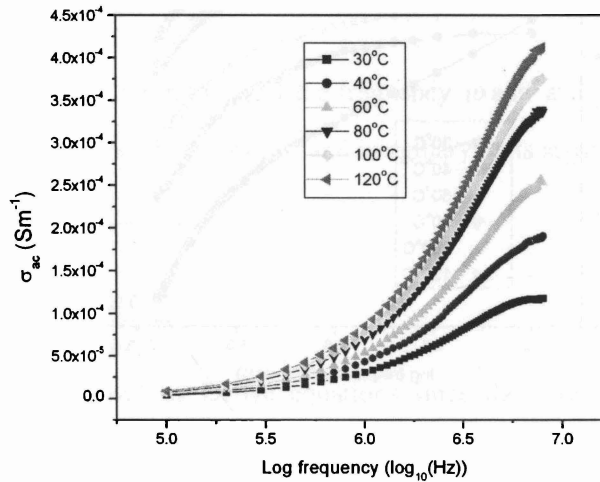


Figure 12: Variation of ac conductivity of zinc aluminate with applied frequency at temperatures ranging from 30°C to 120 °C

The total conductivity and ac conductivity are dependant on the angular frequency ω of the applied signal. From figure 12 it can be observed that the total conductivity is very small at 100 kHz compared to that at higher frequencies. So the static contribution from the dc conductivity is negligible in the total conductivity of the sample at all temperatures. Further the angular frequency dependence of the ac conductivity can be represented in the form

$$\sigma_{ac} = \sigma_{dc} + Af^s \quad 11$$

where A and s are coefficients and f is the applied frequency [13] (Ghosh A. et al 2008) . Since the dc conductivity is found to be negligible equation 11 can be written in the form

$$\sigma_{ac} = Af^s \quad 12$$

The values A and s can be determined by plotting log of ac conductivity against log frequency. The plot is a straight line, since

$$\log \sigma_{ac} = \log A + s \log f \quad 13$$

Equation 13 is the equation of a straight line with a slope s . The values of s for different temperatures were determined by plotting $\log f$ with $\log \sigma_{ac}$ and by finding the slope of the resulting straight line. The plots are presented in figure 13. The plots are parallel to each other and the slope of the straight line region is between 0.94 and 0.95. It is reasonable to assume that the parameter s is independent of temperature. The parameter s can throw light on two distinct conduction mechanisms. The conduction can be through quantum mechanical tunneling (QMT) of charge carriers through barriers separating localized sites and in such a case the parameter s is

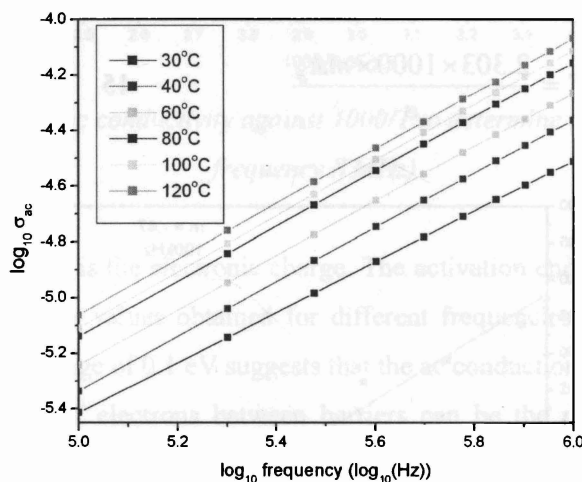


Figure 13: Plots of log of ac conductivity against log frequency

independent of temperature [14] (El-Samanoudy 2002). Another possible mechanism of conduction is the correlated barrier hopping (CBH) in the same barrier. In CBH a decrease in the parameter s is expected with increase of temperature. For zinc aluminate particles the decrease in s is only minimal. The values of A were calculated by substituting the value of s in equation 12. The calculated values of A and s are given in table 1.

The ac conductivity of zinc aluminate was found to increase with temperature. Absorption of heat energy increases the mobility of electrons taking part in the hopping conduction. The variation of ac conductivity with temperature can be understood on the basis of Arrhenius equation given in the form

Annexure

$$\sigma_{ac} = \sigma_o \exp\left(\frac{-E}{k_B T}\right) \quad 14$$

Where σ_o is the pre-exponential factor, E is the activation energy, k_B is the Boltzmann's constant and T is temperature in Kelvin [15] (Elimat Z. M et al 2008). Activation energy of zinc aluminate particles was estimated by plotting $\log_{10}(\sigma_{ac})$ against $1000/T$ and by finding the slope of the straight line obtained by least square linear fit to the data points. The plots and straight line fits are presented in figure 14 and 15 for frequencies 100 kHz and 8 MHz. The activation energy in eV is given by the equation

$$E = \frac{2.303 \times 1000 \times m \cdot k_B}{e} \quad 15$$

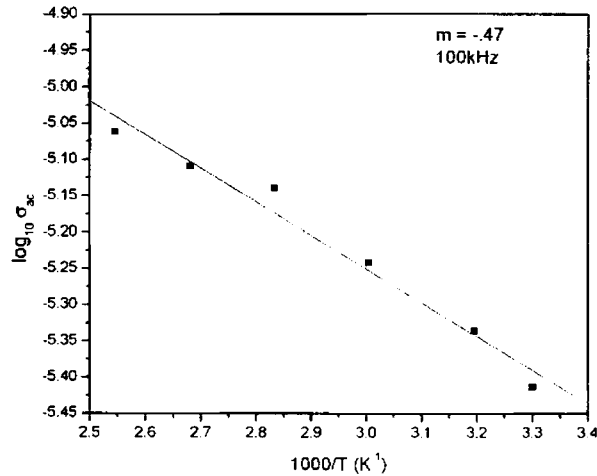


Figure 14: Plot of log of ac conductivity against $1000/T$ to determine the activation energy (for frequency 100 kHz)

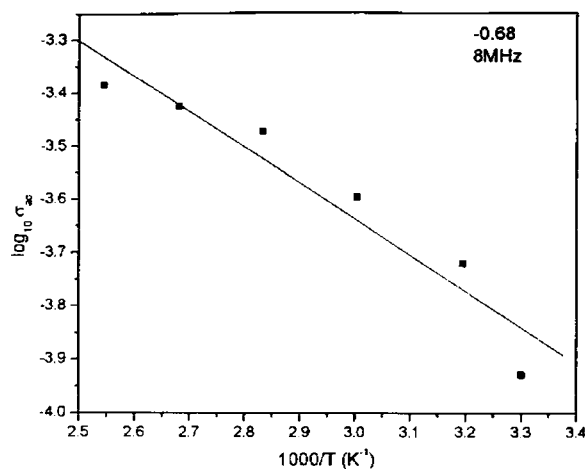


Figure 15: Plot of log of ac conductivity against $1000/T$ to determine the activation energy (for frequency 8 MHz)

where m is the slope and e is the electronic charge. The activation energy was found to increase with the frequency and the values obtained for different frequencies are presented in table 2. Activation energy in the range of 0.1 eV suggests that the ac conduction in the material is realized through electrons. QMT of electrons between barriers can be the possible mechanism of ac conduction in zinc aluminate particles because there is no appreciable change in the parameters with temperature. .

| Temperature °C | s | A (Sm^{-1}) |
|----------------|------|------------------------|
| 30 | 0.95 | 9.5626E-12 |
| 40 | 0.95 | 1.4144E-11 |
| 60 | 0.95 | 1.8019E-11 |
| 80 | 0.94 | 2.7784E-11 |
| 100 | 0.94 | 3.0792E-11 |
| 120 | 0.94 | 3.4037E-11 |

Table 1 Frequency exponent factor s and pre-exponent factor A for different temperatures

Annexure

| Frequency MHz | Activation Energy eV |
|------------------|-------------------------|
| 0.1 | 0.093 |
| 1 | .110 |
| 2 | .117 |
| 3 | .121 |
| 4 | .123 |
| 5 | .125 |
| 6 | .127 |
| 7 | .131 |
| 8 | .135 |

Table 2

Activation energy of ac conductivity of zinc aluminate nanoparticles at different frequencies

4. Conclusion

The formation of spinel structured zinc aluminate nanoparticle with average size of 40 nm was accomplished through a sol-gel combustion process. It was found that an intermediate phase possibly of a mixture of aluminium hydroxide and zinc oxide is formed at 180°C. The spinel phase was formed at a temperature close to 400°C and this was established by calcination trials from 350°C to 800 °C. The optical bandgap of the material is found to be 3.84 eV, slightly greater than that of bulk material and this is attributed to the quantum confinement due to small size of zinc aluminate particles. The dielectric permittivity of the material exhibits dispersion in the low frequency region and interfacial polarization of Maxwell-Wagner type could be the reason for this phenomenon. Ac conductivity increases with frequency. The frequency exponent factor was found to be nearly unity and it didn't show any appreciable variation with temperature. This is attributed to ac conduction through hopping of electron between sites by means of quantum mechanical tunneling. The zinc aluminate is a normal spinel and no evidence for cation redistribution is found from Rietveld analysis. Therefore it is to be assumed that the non-magnetic

counterpart of zinc ferrite in the nano-regime is not susceptible to size effects and the cation distribution does not undergo any change as evident from XRD and Rietveld analysis. However high surface area zinc aluminate can be synthesized and optical studies indicate that they can be suitable for other optical applications. The size effect on the optical properties can be an interesting piece of investigation for further studies.

References:

- 1 van der Laaga. N. J, M.D. Snela. M. D, Magusinb. P. C. M. M, de Wit. G, J. Eur. Ceram. Soc. 24 (2004) 2417–2424 1
- 2 Xiuhua Wei, Donghua Chen, Materials Letters 60 (2006) 823–827 2
- 3 Ciupina. V, Carazeanua. I, Prodan. G, Journal of Optoelectronics and Advanced Materials Vol. 6, No. 4, (2004), p. 1317 – 1322 3
- 4 Ravindra Pandey, Julian D. Gale, Suresh K. Sampath, and Jose M. Recio J. Am. Ceram. Soc., **82** [12] 3337–41 (1999) 4
- 5 Roy. M. K, Haldar. B, Verma. H. C. Nanotechnology , 17 (2006) 232-237 5
- 6 Mohammed E, M , Anantharaman. M. R, J. Instrument Society of India, Vol. 32., No.3 (2002), (165–171 6
- 7 Tareev. B, Physics of Dielectric Materials, MIR Publishers, Moscow, 1975 7
- 8 Keer H.V., Principles of Solid State Physics, Wiley Eastern Ltd., NewDelhi, 1998. 8
- 9 Koops. C.G, Phys. Rev. 83, 1, 1951, 9
- 10 Wagner K W 1993 Ann. Phys. 40 817 10
- 11 E. Veena Gopalan, K A Malini, S Saravanan, D Sakthi Kumar, Yasuhiko Yoshida and M.R Anantharaman, *J. Phys. D: Appl. Phys.* **41**, 18 (2008) 185005 11
- 12 Devan R. S, Y DKolekar and BKChougule *J. Phys.: Condens. Matter* 18 (2006) 9809 12
- 13 Aloka Ghosh¹, S Bhattacharya², D P Bhattacharya¹, A Ghosh^{2,3}, *J. Phys.: Condens. Matter* 20 (2008) 035203 13
- 14 El-Samanoudy. M. M, *J. Phys.: Condens. Matter* 14 (2002) 1199–1212 PII: S0953-8984 (02) 26167-6
- 15 Elimat. Z. M, Zihlif A. M, Ragosta. G, *J. Phys. D: Appl. Phys.* 41 (2008) 165408. 470